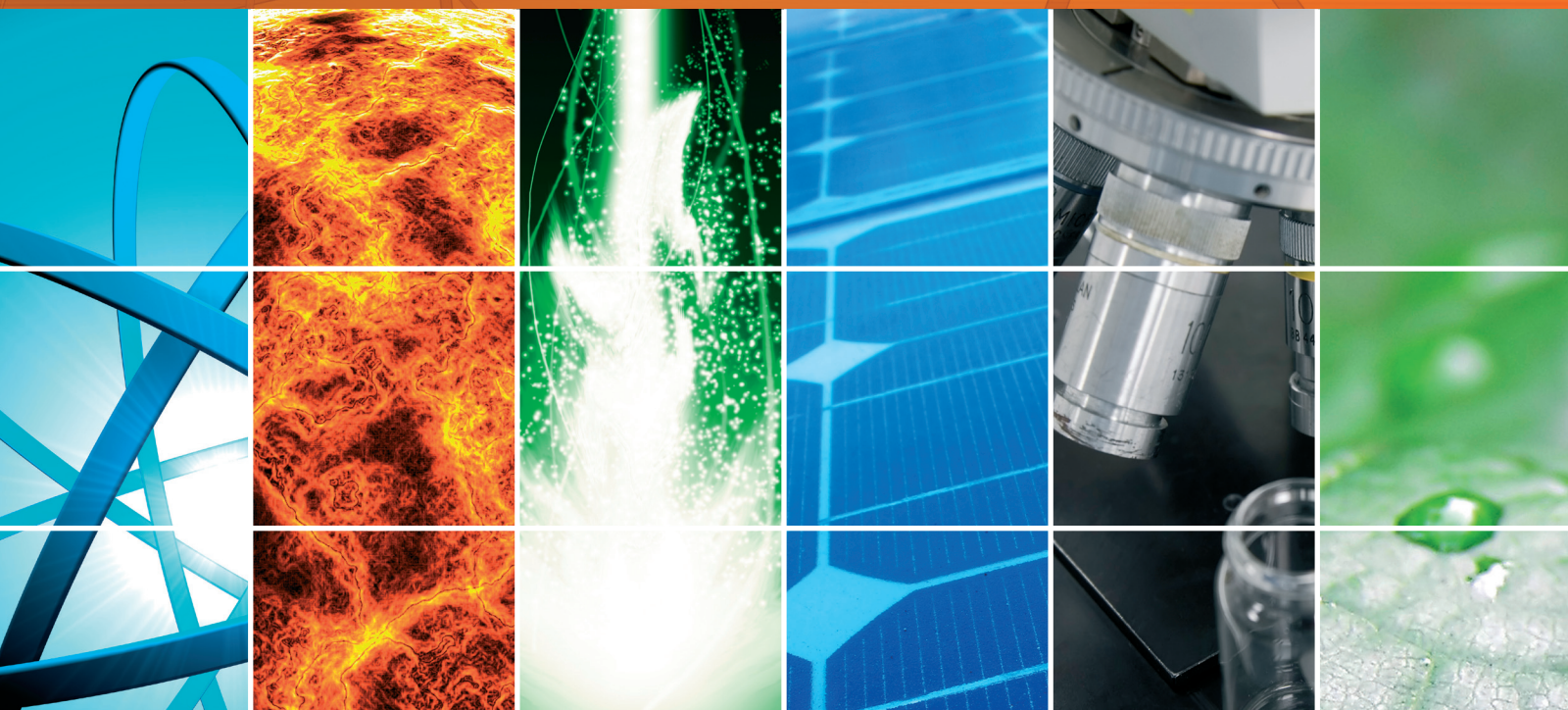


International Journal of Photoenergy

# Nanostructured Solar Cells

Lead Guest Editor: Pushpa Raj Pudasaini

Guest Editors: Sanjay K. Srivastava, Yaohui Zhan, Francisco R. Zepeda,  
and Bill Pandit





---

# **Nanostructured Solar Cells**

International Journal of Photoenergy

---

## **Nanostructured Solar Cells**

Lead Guest Editor: Pushpa Raj Pudasaini

Guest Editors: Sanjay K. Srivastava, Yaohui Zhan,  
Francisco R. Zepeda, and Bill Pandit



---

Copyright © 2017 Hindawi. All rights reserved.

This is a special issue published in "International Journal of Photoenergy." All articles are open access articles distributed under the Creative Commons Attribution License, which permits unrestricted use, distribution, and reproduction in any medium, provided the original work is properly cited.

## Editorial Board

M. S.A. Abdel-Mottaleb, Egypt  
Angelo Albini, Italy  
Alberto Álvarez-Gallegos, Mexico  
Vincenzo Augugliaro, Italy  
Detlef W. Bahnemann, Germany  
Simona Binetti, Italy  
Fabio Bisegna, Italy  
Thomas M. Brown, Italy  
Joaquim Carneiro, Portugal  
Yatendra S. Chaudhary, India  
Věra Cimrová, Czech Republic  
Juan M. Coronado, Spain  
P. Davide Cozzoli, Italy  
Dionysios D. Dionysiou, USA  
Abderrazek Douhal, Spain  
Mahmoud M. El-Nahass, Egypt  
Polycarpos Falaras, Greece  
Chris Ferekides, USA  
Paolo Fornasiero, Italy  
Manuel Fuentes Conde, Spain

Germà Garcia-Belmonte, Spain  
Elisa Isabel Garcia-Lopez, Italy  
Mohammed Ashraf Gondal, KSA  
Giulia Grancini, Switzerland  
Pierluigi Guerriero, Italy  
Michael D. Heagy, USA  
Wing-Kei Ho, Hong Kong  
Jürgen Hüpkens, Germany  
Tariq Iqbal, Canada  
Adel A. Ismail, Kuwait  
Chun-Sheng Jiang, USA  
Cooper H. Langford, Canada  
Manuel Ignacio Maldonado, Spain  
Dionissios Mantzavinos, Greece  
Santolo Meo, Italy  
Claudio Minero, Italy  
Antoni Morawski, Poland  
Fabrice Morlet-Savary, France  
Mohammad Muneer, India  
Maria da Graça P. Neves, Portugal

Tsuyoshi Ochiai, Japan  
Kei Ohkubo, Japan  
Leonardo Palmisano, Italy  
Thierry Pauporté, France  
Philippe Poggi, France  
Francesco Riganti Fulginei, Italy  
Leonardo Sandrolini, Italy  
Jinn Kong Sheu, Taiwan  
Zofia Stasicka, Poland  
Elias Stathatos, Greece  
Jegadesan Subbiah, Australia  
K. R. Justin Thomas, India  
Nikolai V. Tkachenko, Finland  
Ahmad Umar, KSA  
Thomas Unold, Germany  
Mark van Der Auweraer, Belgium  
Wilfried G.J.H.M. Van Sark, Netherlands  
Xuxu Wang, China  
Yanfa Yan, USA  
Jiangbo Yu, USA

# Contents

---

## **Nanostructured Solar Cells**

Pushpa Raj Pudasaini, Sanjay K. Srivastava, Yaohui Zhan, Francisco Ruiz-Zepeda, and Bill Pandit  
Volume 2017, Article ID 1289349, 2 pages

## **Hole-Transporting Layer Treatment of Planar Hybrid n-Si/PEDOT:PSS Solar Cells with Power Conversion Efficiency up to 14.5%**

Chenxu Zhang, Yuming Zhang, Hui Guo, Zeyulin Zhang, and Chunfu Zhang  
Volume 2017, Article ID 3192197, 7 pages

## **A Dye-Sensitized Solar Cell Using a Composite of PEDOT:PSS and Carbon Derived from Human Hair for a Counter Electrode**

Klitsada Moolsarn, Apishok Tangtrakarn, Adulphan Pimsawat, Kornrawit Duangsa, Charusporn Mongkolkachit, Wasan Maiaugree, and Vittaya Amornkitbamrung  
Volume 2017, Article ID 1064868, 11 pages

## **Nanostructured Dielectric Layer for Ultrathin Crystalline Silicon Solar Cells**

Yusi Chen, Yangsen Kang, Jieyang Jia, Yijie Huo, Muyu Xue, Zheng Lyu, Dong Liang, Li Zhao, and James S. Harris  
Volume 2017, Article ID 7153640, 6 pages

## **Organic Dyes Containing Coplanar Dihexyl-Substituted Dithienosilole Groups for Efficient Dye-Sensitized Solar Cells**

Ciaran Lyons, Neelima Rathi, Pratibha Dev, Owen Byrne, Praveen K. Surolia, Pathik Maji, J. M. D. MacElroy, Aswani Yella, Michael Grätzel, Edmond Magner, Niall J. English, and K. Ravindranathan Thampi  
Volume 2017, Article ID 7594869, 14 pages

## **Influence of the Porosity of the TiO<sub>2</sub> Film on the Performance of the Perovskite Solar Cell**

Xiaodan Sun, Jia Xu, Li Xiao, Jing Chen, Bing Zhang, Jianxi Yao, and Songyuan Dai  
Volume 2017, Article ID 4935265, 10 pages

## **Impedance Spectroscopic Investigation of the Degraded Dye-Sensitized Solar Cell due to Ageing**

Parth Bhatt, Kavita Pandey, Pankaj Yadav, Brijesh Tripathi, and Manoj Kumar  
Volume 2016, Article ID 8523150, 9 pages

## **Photoelectric Properties of DSSCs Sensitized by Phloxine B and Bromophenol Blue**

Penghui Ren, Yuanzuo Li, Yuehua Zhang, Hongshuai Wang, and Qungui Wang  
Volume 2016, Article ID 2135847, 11 pages

## Editorial

# Nanostructured Solar Cells

**Pushpa Raj Pudasaini,<sup>1,2</sup> Sanjay K. Srivastava,<sup>3</sup> Yaohui Zhan,<sup>4</sup>  
Francisco Ruiz-Zepeda,<sup>5</sup> and Bill Pandit<sup>6</sup>**

<sup>1</sup>*Department of Materials Science and Engineering, The University of Tennessee, Knoxville, USA*

<sup>2</sup>*Center for Nanophase Materials Science, Oak Ridge National Laboratory, Oak Ridge, TN, USA*

<sup>3</sup>*Inorganic Photovoltaic Devices Group, CSIR-National Physical Laboratory, Dr. K.S. Krishnan Marg, New Delhi 110012, India*

<sup>4</sup>*School of Optoelectronic Information Science and Engineering, Soochow University, No. 1, Shizi Street, Suzhou, Jiangsu 215006, China*

<sup>5</sup>*Department for Materials Chemistry, National Institute of Chemistry, Hajdrihova 19, 1000 Ljubljana, Slovenia*

<sup>6</sup>*Department of Chemistry, Northwestern University, Evanston, IL, USA*

Correspondence should be addressed to Pushpa Raj Pudasaini; ppudasai@utk.edu

Received 15 May 2017; Accepted 15 May 2017; Published 12 November 2017

Copyright © 2017 Pushpa Raj Pudasaini et al. This is an open access article distributed under the Creative Commons Attribution License, which permits unrestricted use, distribution, and reproduction in any medium, provided the original work is properly cited.

Nanostructured materials, such as nanowires, nanorods, and quantum dot structures, are being studied and developed for solar cell applications since they have enabled the fabrication of high efficient and low-cost devices. It is believed that there are mainly two approaches to reduce the cost per kilowatt-hour of electrical energy generated by solar cell devices. Firstly, one can aim to increase the efficiency of the device, usually by pursuing new cell designs that can take full advantage of high-quality absorber materials. Secondly, one can pursue cost reductions while maintaining the efficiency of the device, often done by exploring novel manufacturing approaches but also sometimes with new cell designs and perhaps by exploiting lower-quality, cost attractive materials and processes. From either perspective, nanostructuring of inorganic solar cells offers the possibility of reducing the cost of photovoltaics by allowing smaller amounts of lower-grade photovoltaic semiconductor materials to be used or improving the photoelectric conversion efficiency by making more light and charge carriers to be harvested. The device physics, including carrier/exciton separation, charge extraction, and recombination, is strongly influenced by the nanostructure. Research in various fabrication methods and their influence on the device physics has also provided insight on how to increase efficiency limits. Additionally, the synthesis of solar cells by solution-based methods or fabrication pathways

using less traditional, abundant materials is identified as a promising route to wide-scale photovoltaic electricity generation. Nanostructured solar cell geometries are highlighted as essential in this approach.

The use of dyes as sensitizers in solar cells has also been the target of current active research, due to the low production cost, adaptable optical properties, and high performance. However, several issues are still to be solved regarding long-term stability, and an expected improvement in the conversion efficiency is also needed so they can be suitable for large-scale applications.

This special issue selects 7 papers about different nanostructured solar cells. It consists of 4 papers on dye-sensitized solar cells (DSSC) addressing its variety of material properties such as dyes, electrodes, and others, the photoelectric properties, and the ageing effect by the impedance spectroscopic method. The issue also covers perovskite solar cells, n-Si/PEDOT:PSS organic-inorganic heterojunction-based hybrid solar cells, and nanostructured ultrathin silicon solar cells covering a variety of related aspects towards achieving efficient and stable nanostructured PV devices.

For example, P. Bhatt et al. discussed the effect of ageing on the performance of dye-sensitized solar cells (DSCs). Based on a detailed degradation study of DSC by

electrochemical impedance spectroscopy (EIS), they suggested that the DSC should be used under low illumination conditions and around room temperature for a longer life.

Y. Chen et al. demonstrated a new approach to design, simulate, and fabricate whole-wafer nanostructures on a dielectric layer on a thin c-Si solar cell for effective light trapping. By employing periodic nanostructured dielectric arrays on 40  $\mu\text{m}$  thin c-Si, they could suppress the reflection loss below 5% over a wide spectra and angular range and demonstrated 32% improvement in short circuit current and 44% relative improvement in energy conversion efficiency in a crystalline silicon solar cell with only a 2.9  $\mu\text{m}$  ultrathin absorber layer.

C. Lyons et al. synthesized a new chromophore containing a coplanar dihexyl-substituted dithienosilole (CL1) and displayed an energy conversion efficiency of 6.90% under AM 1.5 sunlight irradiation in dye-sensitized solar cells. Similar fill factor and open-circuit voltage are presented for a new synthesizer with N719. The charge transfer resistances are presented comparable, indicative of similar recombination rates by the oxidised form of the redox couple. Using time-dependent density functional theory, studies are performed to ascertain the absorption spectrum of the dye and assess the contribution of various transitions to optical excitation. Good agreements are reported between experimental and calculated results.

While X. Sun et al. reported that an increase in the porosity of the mesoporous  $\text{TiO}_2$  (mp- $\text{TiO}_2$ ) film leads to an improvement in the performance of the perovskite solar cells (PSCs), P. Ren et al. employed phloxine B and bromophenol blue as the sensitizers of dye-sensitized solar cells, and the devices were characterized using UV-Vis spectra, FT-IR spectra, fluorescence spectra, and current-voltage characteristics. K. Moolsarn et al. employed carbonized hair/PEDOT:PSS composites (CxP) with varied carbon contents from  $x=0.2$  to 0.8 g, as counter electrode (CE) for a dye-sensitized solar cell (DSSC). And last but not least, C. Zhang et al. demonstrated that annealing temperature has a great influence on the PEDOT:PSS material properties and the corresponding device performance. By optimizing the annealing temperature, the conductivity of the PEDOT:PSS film doped with Triton X-100 and EG could be enhanced by a factor of more than three orders.

The objective is to provide an opportunity for interdisciplinary researchers to share their latest research achievements in nanostructured solar cells and let the potential readers learn some insightful concepts in this exciting field of photovoltaic energy concepts. We hope this research progress can inspire more advanced ideas for the future development of such novel concepts of PV devices. We would like to extend our heartiest gratitude to all the authors who submitted their work for consideration in our special issue and to the reviewers for their critical feedback.

*Pushpa Raj Pudasaini*  
*Sanjay K. Srivastava*  
*Yaohui Zhan*  
*Francisco Ruiz-Zepeda*  
*Bill Pandit*

## Research Article

# Hole-Transporting Layer Treatment of Planar Hybrid n-Si/PEDOT:PSS Solar Cells with Power Conversion Efficiency up to 14.5%

Chenxu Zhang,<sup>1</sup> Yuming Zhang,<sup>1</sup> Hui Guo,<sup>1</sup> Zeyulin Zhang,<sup>2</sup> and Chunfu Zhang<sup>1</sup>

<sup>1</sup>Wide Bandgap Semiconductor Technology Disciplines State Key Laboratory, School of Microelectronics, Xidian University, Xi'an 710071, China

<sup>2</sup>School of Textiles and Materials, Xi'an Polytechnic University, Xi'an 710048, China

Correspondence should be addressed to Hui Guo; guohui@mail.xidian.edu.cn and Chunfu Zhang; cfzhang@xidian.edu.cn

Received 15 February 2017; Accepted 13 April 2017; Published 13 June 2017

Academic Editor: Pushpa Pudasaini

Copyright © 2017 Chenxu Zhang et al. This is an open access article distributed under the Creative Commons Attribution License, which permits unrestricted use, distribution, and reproduction in any medium, provided the original work is properly cited.

A systematical investigation was carried out into the effects of the hole-transporting layer treatment of poly(3,4-ethylenedioxythiophene):poly(styrenesulfonate) (PEDOT:PSS) on the performance of planar hybrid n-Si/PEDOT:PSS solar cells. Triton X-100 and ethylene glycol (EG) were chosen to improve the conductivity and surface morphology of the PEDOT:PSS film. It was found that the annealing temperature has a great influence on the PEDOT:PSS material properties and the corresponding device performance. By optimizing the annealing temperature, the conductivity of the PEDOT:PSS film doped with Triton X-100 and EG could be enhanced by a factor of more than three orders. And the corresponding device also shows record power conversion efficiency as high as 14.5% with an open circuit voltage of 0.627 V, a short circuit current of 32.6 mA/cm<sup>2</sup>, and a fill factor of 70.7%.

## 1. Introduction

The solar cell is an efficient way to convert solar energy to electric power [1]. Presently, the mono- and multicrystalline silicon solar cells still dominate more than 90% of the PV market owing to their materials abundance and mature fabrication techniques. However, compared to the conventional energy sources, the cost of silicon solar cells is still too high because those devices are based on the p-n junctions which are generally formed by a high-temperature dopant diffusion process. Their high thermal budget accounts for ~30% of the total manufacturing cost of silicon (Si) solar cells [2]. To reduce the fabrication cost, the low-temperature solar cell concepts based on the organic/inorganic hybrid heterojunctions, particularly the Si/poly(3,4-ethylenedioxythiophene):poly(styrenesulfonate) (Si/PEDOT:PSS), have attracted significant research interest in recent years [3–6]. Si has a strong absorption ability in a very wide spectrum range and very excellent carrier transport ability. And PEDOT:PSS is a water-soluble polymer which has high conductivity, a

transmission window in the visible spectral range, and an excellent chemical and thermal stability [7]. This type of Si/PEDOT:PSS hybrid solar cell combines the superior absorption property of Si in a wide spectrum range and the advantage of aqueous solution-based processes for PEDOT:PSS [4], which avoids an expensive high-temperature process and promises a low-cost photovoltaic technique with the potential to realize a power conversion efficiency (PCE) as high as 22% in theory [5].

Since the first crystalline n-Si/PEDOT:PSS hybrid solar cell was reported in 2010 [4], great efforts, including the interface engineering [6, 8], treatment of PEDOT:PSS [9, 10], doping of the Si substrate [11], passivation on the device surface [12], nanoparticles [13, 14], and nanostructured surfaces [15–17], have been devoted to improve the device performance. Among these strategies, the treatment of the hole-transporting layer of PEDOT:PSS is a very simple and effective method.

Figure 1 shows the band structure of a hybrid Si/PEDOT:PSS cell concept, and it could be concluded that the

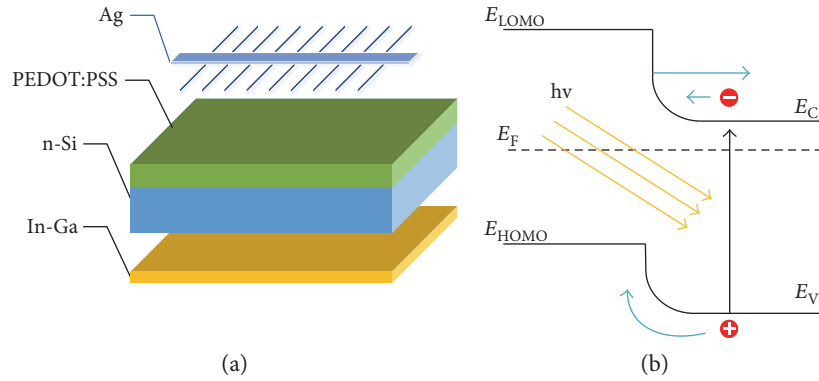


FIGURE 1: (a) Schematic structure of n-Si/PEDOT:PSS solar cell. (b) Schematic energy band diagrams of the device.

device performance greatly depends on the hole-conducting layer of PEDOT:PSS. Price et al. [18] made a comparison between hybrid Si/PEDOT:PSS heterojunctions and all-inorganic Si/Au Schottky junctions and found that the unfavorable electron injection rate from Si into PEDOT:PSS is three orders of magnitude smaller compared to that from Si into Au, which could result in high open circuit voltages ( $V_{OC}$ ) in the corresponding device. Besides the interface properties, the holes must transport across the PEDOT:PSS layer before they could be collected by the electrode. Thus, the material properties of PEDOT:PSS could greatly affect the device characteristics [18].

The basic building block of PEDOT is thiophene. By adding stabilizing side groups, this material has a high thermal and chemical stability. Its conductivity could be enhanced by oxidizing the thiophene backbone with sodium peroxydisulfate, and thus, the polymer characteristics could be converted from a chromophoric to a metallic behavior. Recent results have shown that the additive in the liquid state may provide space for the reorientation of PEDOT:PSS chains [19] and is important for further conductivity enhancement. Several methods have been reported to enhance the conductivity of PEDOT:PSS. Kim et al. reported that addition of a high dielectric solvent into an aqueous solution of PEDOT:PSS can enhance the conductivity of the resulting PEDOT:PSS film by more than one order of magnitude as a result of weakening of the coulombic attraction between the counter ions and the charge carriers [20]. Sorbitol, ethylene glycol (EG), and other alcohols comprise another set of inert secondary dopants that can enhance the conductivity [20]. The exact principle of the enhancement has not been recognized, and several mechanisms have been proposed. It is generally believed that the solvent optimizes the morphology of the films, providing good percolating paths among the PEDOT:PSS domains (PEDOT-rich regions) and transforming the molecular structure. Xia et al. proposed that the additive does not only act simply as a plasticizer but also change the conformation in the PEDOT:PSS film [4]. All these studies mainly focused on the material properties instead of their influence on the solar cells. However, compared to the many reports about the material researches about the conductivity modulation of PEDOT:PSS, the systematic studies about the treatment of

PEDOT:PSS on the corresponding performance of hybrid Si/PEDOT:PSS cell are still lacking.

The aim of the current study is to systematically investigate the effects of the hole-transporting layer treatment of PEDOT:PSS on the performance of planar hybrid n-Si/PEDOT:PSS solar cells. In this work, the conductivity and surface morphology of PEDOT:PSS film were improved by adding the Triton and EG in the aqueous PEDOT:PSS solution. It was found that the annealing temperature has a great influence on the PEDOT:PSS material properties and the corresponding device performance. By optimizing the annealing temperature, the conductivity of the PEDOT:PSS film doped with Triton and EG could be enhanced by a factor of more than three orders. And the corresponding device also shows a recorded PCE as high as 14.5% with a  $V_{OC}$  of 0.627 V, a short circuit current ( $J_{SC}$ ) of 32.6 mA/cm<sup>2</sup>, and a fill factor (FF, the ratio of maximum obtainable power to the product of  $V_{OC}$  and  $J_{SC}$ ) of 70.7%.

## 2. Experimental

**2.1. Film Formation and Device Fabrication.** n-type Si/PEDOT:PSS hybrid heterojunction solar cells were fabricated on the sequence below: n-type Si (100) wafers with a thickness of 300  $\mu\text{m}$  and a resistivity of 0.05–0.1  $\Omega\text{-cm}$  was cut into  $1.5 \times 1.5 \text{ cm}^2$  for solar cell fabrication and ultrasonically cleaned in acetone, isopropyl alcohol, and ionized water sequentially for 10 min. The native oxide on the silicon surface (about 4 nm) was etched by dipping the sample into hydrofluoric acid (5% HF for 30 s) and then drying by  $\text{N}_2$  for later use. In order to improve wettability and to form a uniform PEDOT:PSS film on a Si substrate, Triton X-100 is added as a surfactant. PEDOT:PSS (PH1000, Heraeus Clevios) was filtered with polyvinylidene fluoride membrane (0.45  $\mu\text{m}$  porosity) to remove agglomerations. To increase the conductivity of the PEDOT:PSS film, the optimized 7 vol% EG were added to the PEDOT:PSS solution and Triton X-100 (1%) was then added to it. The solution was spin coated on the HF-treated Si substrate at a speed of 2500 rpm for 60 s. The samples were annealed on a hot plate at 190°C for 15 min to remove the solvent to form a uniform and conductive p-type organic thin film. A 150 nm thick Ag film was thermally evaporated to form a grid. Finally, the

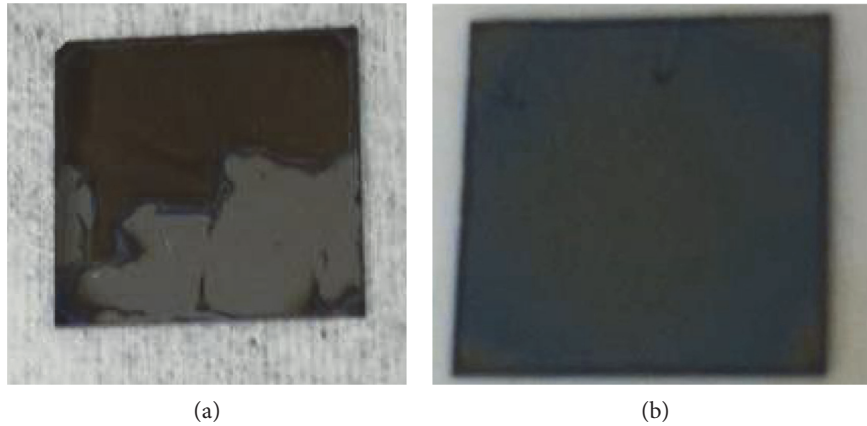


FIGURE 2: Photos (a) before and (b) after Triton X-100 treatment.

eutectic In-Ga fully covered the rear side of the Si substrates to form an ohmic contact.

**2.2. Device Characterization.** The morphology measurements of the PEDOT:PSS films was measured by atomic force microscopy (AFM). The UV-visible reflection spectra were recorded with UV-visible spectrophotometer (Perkin-Elmer Lambda 950). Photovoltaic parameters were measured by using a Keithley 2400 source meter under simulated sunlight from XES-70S1 solar simulator matching the AM 1.5G standard with an intensity of  $100 \text{ mW/cm}^2$ . The system was calibrated against a NREL-certified reference solar cell. All the measurements of the solar cells were performed under ambient atmosphere at room temperature without any encapsulation.

### 3. Results and Discussion

The n-Si/PEDOT:PSS hybrid solar cell is structured as In-Ga eutectic/n-Si/PEDOT:PSS/Ag as shown in Figure 1(a). There is a type III hybrid interface between Si and PEDOT:PSS as shown in Figure 1(b). The device operation is based on a charge-selective interface, where the PEDOT:PSS and the n-Si act as hole- and electron-transport layers, respectively. Lights are illuminated from the top of the cell, where the PEDOT:PSS film is more than 90% transparent at such a thickness in the visible spectral range. Therefore, most of the light is absorbed by n-Si. Due to the high conductivity of the PEDOT:PSS layer, a depletion region in Si near the interface of n-Si/PEDOT:PSS is formed. As shown in Figure 1(b), the LOMO level of the PEDOT:PSS is much higher than the conductance band of the n-Si, so the electrons under illumination would be blocked from flowing into the PEDOT:PSS layer. On the other hand, the HOMO level of PEDOT:PSS is closely aligned with the valence band of n-Si, allowing holes in the n-Si to flow into the PEDOT:PSS film. The depletion region separates the photogenerated carriers in n-Si to the opposite direction, which suggests that electrons can be transported to the rear side of the n-Si and collected by the cathode. At the same time, the holes are transported to the anode through the PEDOT:PSS layer.

The thickness of the PEDOT:PSS film was measured by AFM and found to be about 55 nm.

The silicon surface has highly hydrophobic properties after etching by HF solution. It is not easy to form a uniform PEDOT:PSS film on such a surface by spin coating the aqueous PEDOT:PSS solution. To overcome this problem and ensure proper wetting of PEDOT:PSS on the Si substrates, Triton X-100 is added in the PEDOT:PSS solution. Figures 2(a) and 2(b) show the pictures of PEDOT:PSS films before and after the addition of Triton X-100. The PEDOT:PSS film without Triton addition was quite rough and cannot cover all of the substrate. By adding the Triton X-100, the adhesion of PEDOT:PSS conjugated polymer on hydrophobic n-Si has been improved, resulting in an efficient suppression of defect generation at the n-Si/PEDOT:PSS interface.

In order to improve the conductivity of the PEDOT:PSS films, EG is chosen to be added in the aqueous PEDOT:PSS solution since it can improve the electrical conductivity due to phase separation of the hydrophilic conductive PEDOT and the hydrophobic insulating PSS, which leads to an increase in the hole mobility. Figure 3(a) shows  $J$ - $V$  characteristics of the fabricated n-Si/PEDOT:PSS cells. All the devices were fabricated by the same procedures except for the different annealing temperatures. DMSO is also added in the aqueous PEDOT:PSS solution as the reference and its device parameters is summarized in Table 1. In solar cells, where the PEDOT:PSS films are doped by DMSO-Triton (100:5 v/v), EG-Triton (100:7 v/v) is represented as the DMSO cell and EG cell. The  $J$ - $V$  characteristics of PV cells can be approximately described by the Shockley equation

$$J = J_0 \left( \exp \left( \frac{q(V - R_s J)}{nk_B T} \right) - 1 \right) + \frac{V - R_s J}{R_{sh}} - J_{ph}, \quad (1)$$

where  $J_0$  is the saturation current,  $J_{ph}$  the photocurrent,  $R_s$  the series resistance,  $R_{sh}$  the shunt resistance,  $n$  the ideality factor,  $q$  the electron charge,  $k_B$  the Boltzmann constant, and  $T$  the temperature. By using (1) with our proposed explicit analytic expression method [21], the experimental data can be well rebuilt as shown in Figure 3(a), which

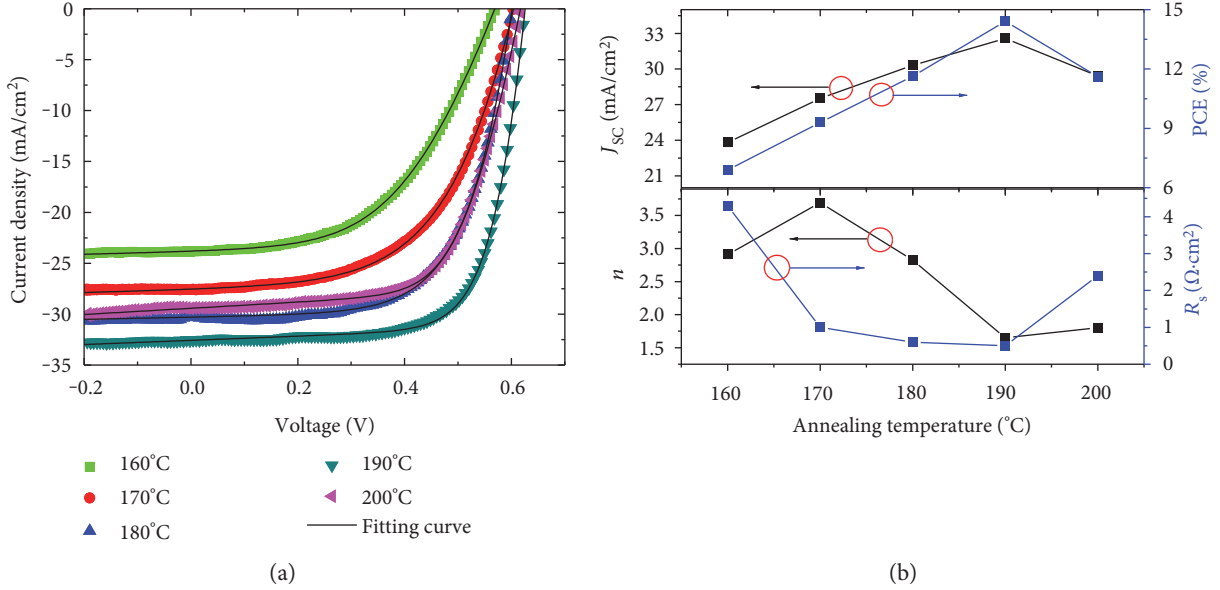


FIGURE 3: (a) Illuminated  $J$ - $V$  characteristics of the solar cells annealing on different temperatures. The  $J$ - $V$  experimental data are fit by (1). (b) The cells' parameters with different annealing temperatures.

TABLE 1: Photovoltaic performance of n-Si/PEDOT:PSS solar cells under AM 1.5G illumination (100 mW/cm<sup>2</sup>).

	$V_{oc}$ (V)	$J_{sc}$ (mA/cm <sup>2</sup> )	FF (%)	PCE (%)
DMSO cell	0.598	25.6	57.4	8.8
EG cell 160	0.569	23.8	50.9	6.9
EG cell 170	0.604	27.5	55.9	9.3
EG cell 180	0.602	30.3	63.8	11.6
EG cell 190	0.627	32.6	70.7	14.5
EG cell 200	0.617	29.4	64.0	11.6

confirmed the validity of the extracted parameters. Table 1 summarizes the device performance parameters. The device with the DMSO addition exhibits a  $J_{sc}$  of 25.6 mA/cm<sup>2</sup>, a  $V_{oc}$  of 0.598 V, and a FF of 57.4%, leading to a corresponding PCE of 8.8%, and its performance is relatively constant with different annealing temperatures. The performance is comparable to the reported results with a similar device structure [19]. It is obvious that the low  $J_{sc}$  is the main factor that limits the PCE. Compared with the DMSO cells, the EG cells have significantly improved in performance with a proper annealing temperature as shown in Figures 3(a) and 3(b). When the annealing temperature is 160°C, the performance of the device is low with a  $J_{sc}$  of 23.8 mA/cm<sup>2</sup>, a  $V_{oc}$  of 0.569 V, and a FF of 50.9%, resulting in a PCE of 6.9%. With the increase of the annealing temperature, all of  $J_{sc}$ ,  $V_{oc}$ , and FF improved. When the annealing temperature is 190°C, the optimized device is achieved.  $J_{sc}$  increased to 32.6 mA/cm<sup>2</sup>,  $V_{oc}$  increased to 0.627 V, FF increased to 70.7%, and the overall PCE improved to 14.5%. It is inferred that the EG can help enhance the uniformity and conductivity of PEDOT:PSS film with a proper annealing temperature

and thus improve the device performance. Beyond 190°C, the device performance decreased with a higher annealing temperature. From Figure 3(b), it also could be seen that the annealing temperature could greatly affect the ideality factor and the series resistance. When the annealing temperature is 160°C,  $n$  is 2.91 and  $R_s$  is 4.3 Ω·cm<sup>-2</sup>. When the annealing temperature is increased to 190°C,  $n$  decreases to 1.65 and  $R_s$  is 0.5 Ω·cm<sup>-2</sup>, which means that an optimized annealing temperature could greatly improve the conductivity of the hole-transporting layer and thus enhance the device performance. The reason maybe that proper temperature could evaporate the water of the PEDOT:PSS solvent as well as have a positive effect in PEDOT:PSS chain reforming to a high conductive state. The conductivity measurement also shows that the optimized annealing temperature could enhance the conductivity of the PEDOT:PSS film with Triton and EG addition from 0.2 to over 200 S/cm, and this is consistent with the  $J$ - $V$  characteristics of the hybrid solar cells. The same trend of the influence of annealing temperature on the hybrid GaN/PEDOT:PSS solar cells is also reported in one previous work [22]. It is shown that the annealing could affect the work function and conductivity of PEDOT:PSS. XPS measurements and  $J$ - $V$  characteristics analysis indicate that the change of the  $V_{oc}$  can be due to the work function variations of the PEDOT:PSS and the barrier height of the Schottky contact, while the change of the  $J_{sc}$  can be ascribed to the competition between the enhancement of the conductivity and the thermal degradation of the PEDOT:PSS. Thus, there is an optimized annealing temperature so that almost all the device parameters could be improved. For our case, the optimized annealing temperature is 190°C.

Figure 4 shows AFM images of PEDOT:PSS films annealed at different annealing temperatures and their corresponding root-mean-square (RMS) value variation with the different annealing temperatures. When the annealing

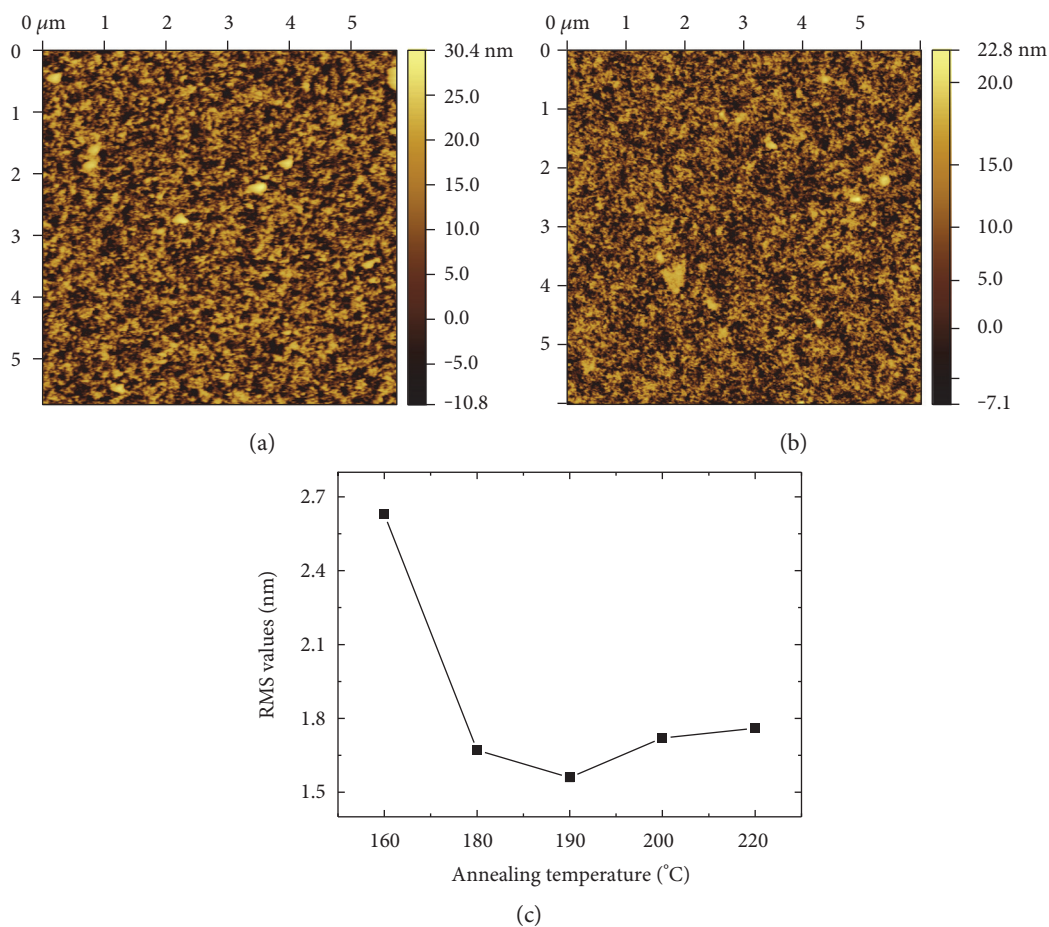


FIGURE 4: AFM images of PEDOT:PSS films annealed at (a) 160°C and (b) 190°C. (c) RMS value variation of PEDOT:PSS films with the different annealing temperatures.

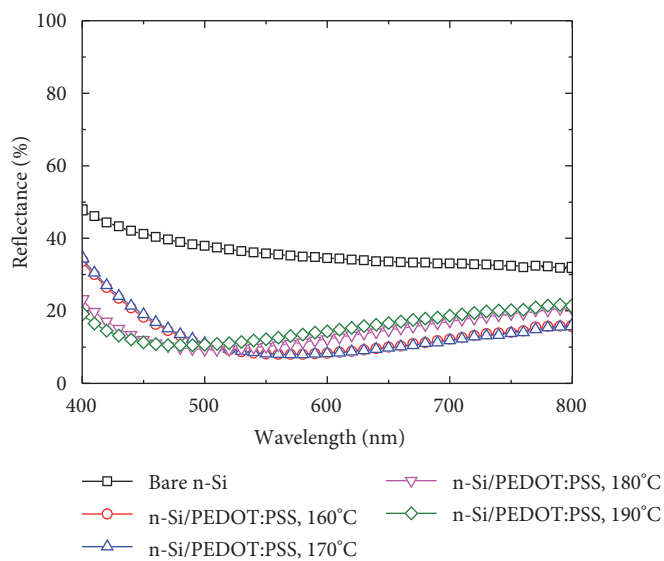


FIGURE 5: Reflectance spectra of n-Si/PEDOT:PSS samples annealed at different temperatures from 160°C to 190°C, and the reflectance spectrum of the polished bare n-Si is also shown for a reference.

temperature is 160°C, a relatively rough surface of PEDOT:PSS film is obtained with a root-mean-square (RMS) value of 2.63 nm as shown in Figure 4(a). For the optimized annealing temperature of 190°C, a relatively smooth surface is obtained with a RMS value of 1.56 nm as shown in Figure 4(b). The annealing temperature could greatly affect the roughness of PEDOT:PSS films. The variation of RMS values with different annealing temperatures as shown in Figure 4(c) matched the performance variation of devices as shown in Figure 3(b). A uniform hole-transparent layer could suppress the recombination on the junction and promote the hole current by enhancing the carrier collection ability. This may be one reason for the higher device performance annealed at the optimized temperature of 190°C.

We also investigate how the annealing temperature affects the optical properties of n-Si/PEDOT:PSS structures by measuring the reflectance spectra. Figure 5 shows the variation of the reflectance spectra of n-Si/PEDOT:PSS structures with the annealing temperatures from 160°C to 190°C. The reflectance spectrum of the polished bare n-Si is also shown in Figure 5 for a reference. The planar polished bare n-Si exhibits a reflectance of more than 30% over a wavelength range from 400 nm to 800 nm, while all the samples with n-Si/PEDOT:PSS structures show a reduced reflectance. This means that the PEDOT:PSS film could help to improve the overall light absorption ability. Comparing the samples with n-Si/PEDOT:PSS structures annealed at different temperatures, it could be found that the sample with the 190°C annealing temperature shows a relatively larger reflectance compared to the sample with a relatively low annealing temperature such as 160°C for the wavelength range from 500 nm to 800 nm. This means that there is no absorption improvement for the device with the 190°C annealing temperature. The enhanced device performance for the optimized annealing temperature of 190°C should result from the improved carrier collection ability instead of the absorption improvement. The device performance could be further improved by enhancing the optical absorption ability with the antireflective film or the textured Si surface.

#### 4. Conclusion

In summary, doping PEDOT:PSS with EG and Triton is an effective method to improve the conductivity of PEDOT:PSS films and at the same time there is great influence of the annealing temperature on the final film properties. The proper annealing temperature could improve the film morphology, increase the film conductivity, and decrease the device series resistance. Compared with the devices with the different annealing temperatures, the planar hybrid Si/PEDOT:PSS solar cell annealed at 190°C shows the optimized performance and PCE reaches as high as 14.5% with a  $J_{SC}$  of 32.6 mA/cm<sup>2</sup>, a  $V_{OC}$  of 0.627 V, and a FF of 70.7%. A further improvement is expected by enhancing the optical absorption ability with the antireflective film or the textured Si surface.

#### Conflicts of Interest

The authors declare that there is no conflict of interest regarding the publication of this paper.

#### Acknowledgments

The authors thank the Natural Science Foundation of China (61604119), Young Talent fund of University Association for Science and Technology in Shaanxi, China (20150103), Fundamental Research Funds for the Central Universities (Grant nos. JB151406, JB161101, and JB161102), and class general financial grant from the China Postdoctoral Science Foundation (Grant no. 2016M602771).

#### References

- [1] W. Hoffmann, "PV solar electricity industry: market growth and perspective," *Solar Energy Materials & Solar Cells*, vol. 90, no. 18, pp. 3285–3311, 2005.
- [2] S. B. Darling, "Block copolymers for photovoltaics," *Energy Environment Science*, vol. 2, no. 12, pp. 1266–1273, 2009.
- [3] S. C. Shiu, J. J. Chao, S. C. Hung, C. L. Yeh, and C. F. Lin, "Morphology dependence of silicon nanowire/poly(3,4-ethylenedioxythiophene):poly(styrenesulfonate) heterojunction solar cells," *Chemistry of Materials*, vol. 22, no. 10, pp. 3108–3113, 2010.
- [4] Y. Xia, H. Zhang, and J. Ouyang, "Highly conductive PEDOT : PSS films prepared through a treatment with zwitterions and their application in polymer photovoltaic cells," *Journal of Materials Chemistry*, vol. 20, no. 43, pp. 9740–9747, 2010.
- [5] J. Sheng, K. Fan, D. Wang et al., "Improvement of the SiOx passivation layer for high-efficiency Si/PEDOT:PSS heterojunction solar cells," *ACS Applied Materials & Interfaces*, vol. 6, no. 18, pp. 16027–16034, 2014.
- [6] S. Jäckle, M. Liebhaber, J. Niederhausen et al., "Unveiling the hybrid n-Si/PEDOT:PSS interface," *ACS Applied Materials & Interfaces*, vol. 8, no. 13, pp. 8841–8848, 2016.
- [7] L. Groenendaal, F. Jonas, D. Freitag, H. Pielartzik, and J. R. Reynolds, "Poly (3, 4-ethylenedioxythiophene) and its derivatives: past, present, and future," *Advanced Materials*, vol. 12, no. 7, pp. 481–494, 2000.
- [8] M. Pietsch, S. Jackle, and S. Christiansen, "Interface investigation of planar hybrid n-Si/PEDOT:PSS solar cells with open circuit voltages up to 645 mV and efficiencies of 12.6%," *Applied Physics A: Materials Science & Processing*, vol. 115, no. 4, pp. 1109–1113, 2014.
- [9] J. Ouyang, Q. Xu, C. W. Chu, Y. Yang, G. Li, and J. Shinar, "On the mechanism of conductivity enhancement in poly(3,4-ethylenedioxythiophene):poly(styrene sulfonate) film through solvent treatment," *Polymer*, vol. 45, no. 25, pp. 8443–8450, 2004.
- [10] C. S. Pathak, J. P. Singh, and R. Singh, "Effect of dimethyl sulfoxide on the electrical properties of PEDOT:PSS/n-Si heterojunction diodes," *Current Applied Physics*, vol. 15, no. 4, pp. 528–534, 2015.
- [11] S. Jäckle, M. Mattiza, M. Liebhaber et al., "Junction formation and current transport mechanisms in hybrid n-Si/PEDOT: PSS solar cells," *Scientific Reports*, vol. 5, article 13008, 2015.
- [12] P. Yang, D. Xie, Y. Zhao et al., "NO<sub>2</sub>-induced performance enhancement of PEDOT:PSS/Si hybrid solar cells with a high

- efficiency of 13.44%," *Physics Chemical Chemical Physics*, vol. 18, no. 10, pp. 7184–7189, 2016.
- [13] T. Song, S. T. Lee, and B. Sun, "Prospects and challenges of organic/group IV nanomaterial solar cells," *Journal of Materials Chemistry*, vol. 22, no. 10, p. 4216, 2010.
- [14] Z. Xia, T. Song, J. Sun, S. T. Lee, and B. Sun, "Plasmonic enhancement in hybrid organic/Si heterojunction solar cells enabled by embedded gold nanoparticles," *Applied Physics Letters*, vol. 105, no. 24, pp. 18–22, 2014.
- [15] K. T. Park, H. J. Kim, M. J. Park et al., "13.2% efficiency Si nanowire/PEDOT:PSS hybrid solar cell using a transfer-imprinted Au mesh electrode," *Scientific Reports*, vol. 5, article 12093, 2015.
- [16] L. He, Rusli, D. Lai, and H. Wang, "Highly efficient Si-nanorods/organic hybrid core-sheath heterojunction solar cells," *Applied Physics Letters*, vol. 99, no. 2, pp. 3–6, 2011.
- [17] S. Jeong, E. C. Garnett, S. Wang et al., "Hybrid silicon nanocone-polymer solar cells," *Nano Letters*, vol. 12, no. 6, pp. 2971–2976, 2012.
- [18] M. J. Price, J. M. Foley, R. A. May, and S. Maldonado, "Comparison of majority carrier charge transfer velocities at Si/polymer and Si/metal photovoltaic heterojunctions," *Applied Physics Letters*, vol. 97, no. 8, article 83503, 2010.
- [19] M. Pietsch, M. Y. Bashouti, and S. Christiansen, "The role of hole transport in hybrid inorganic/organic silicon/poly(3,4-ethylenedioxy-thiophene): poly(styrenesulfonate) heterojunction solar cells," *The Journal of Physical Chemistry C*, vol. 117, no. 18, pp. 9049–9055, 2013.
- [20] J. Y. Kim, J. H. Jung, D. E. Lee, and J. Joo, "Enhancement of electrical conductivity by a change of solvents," *Synthetic Metals*, vol. 126, no. 2, pp. 311–316, 2002.
- [21] C. Zhang, J. Zhang, Y. Hao, Z. Lin, and C. Zhu, "A simple and efficient solar cell parameter extraction method from a single current-voltage curve," *Journal of Applied Physics*, vol. 110, no. 6, Article ID 064504, 2011.
- [22] Q. Feng, K. Du, Y. Li, P. Shi, and F. Qing, "Effect of annealing on performance of PEDOT:PSS/n-GaN Schottky solar cells," *Chinese Physics B*, vol. 23, no. 7, article 077303, 2014.

## Research Article

# A Dye-Sensitized Solar Cell Using a Composite of PEDOT:PSS and Carbon Derived from Human Hair for a Counter Electrode

**Klitsada Moolsarn,<sup>1</sup> Apishok Tangtrakarn,<sup>1,2,3,4,5</sup> Adulphan Pimsawat,<sup>2</sup> Kornrawit Duangsa,<sup>1</sup> Charusporn Mongkolkachit,<sup>6</sup> Wasan Maiaugree,<sup>2</sup> and Vittaya Amornkitbamrung<sup>2,3,4,5</sup>**

<sup>1</sup>Materials Science and Nanotechnology Program, Department of Physics, Faculty of Science, Khon Kaen University, Khon Kaen 40002, Thailand

<sup>2</sup>Department of Physics, Faculty of Science, Khon Kaen University, Khon Kaen 40002, Thailand

<sup>3</sup>Integrated Nanotechnology Research Center, Khon Kaen University, Khon Kaen 40002, Thailand

<sup>4</sup>Nanotec-KKU Center of Excellence on Advanced Nanomaterials for Energy Production and Storage, Khon Kaen University, Khon Kaen 40002, Thailand

<sup>5</sup>Thailand Center of Excellence in Physics, Commission on Higher Education, Bangkok 10400, Thailand

<sup>6</sup>National Metal and Materials Technology Center, 114 Paholyothin Road, Klong 1, Klong Luang, Pathumthani 12120, Thailand

Correspondence should be addressed to Apishok Tangtrakarn; [nateta@kku.ac.th](mailto:nateta@kku.ac.th)

Received 18 January 2017; Revised 15 March 2017; Accepted 22 March 2017; Published 13 June 2017

Academic Editor: Yaohui Zhan

Copyright © 2017 Klitsada Moolsarn et al. This is an open access article distributed under the Creative Commons Attribution License, which permits unrestricted use, distribution, and reproduction in any medium, provided the original work is properly cited.

Carbon derived from hair is interesting because it has good electrocatalytic activity due to the existence of innate heteroatom dopants especially nitrogen and sulfur. In this study, a carbon catalyst containing high nitrogen contents (9.47 at.%) was fabricated without using any harsh chemicals. Moreover, the carbonization temperature was only 700°C. Carbonized hair/PEDOT:PSS composites ( $C_xP$ ) with varied carbon contents from  $x=0.2$  to 0.8 g were tested as a counter electrode (CE) for a dye-sensitized solar cell (DSSC). This type of DSSC CE has scarcely been investigated. A DSSC with a  $C_{0.6}P$  CE provides the best efficiency ( $6.54 \pm 0.11\%$ ) among all composite CEs because it has a high fill factor (FF) and a high short-circuit current density ( $J_{sc}$ ). The efficiency of DSSC with  $C_{0.6}P$  CE is lower than Pt's ( $7.29 \pm 0.01\%$ ) since the Pt-based DSSC has higher FF and  $J_{sc}$  values. However,  $C_{0.6}P$  is still promising as a DSSC CE since it is more cost-effective than Pt.

## 1. Introduction

A renewable energy source such as a dye-sensitized solar cell (DSSC) has been intensively studied due to its simple fabrication process and high solar conversion efficiency [1]. To construct a DSSC with high efficiency, one approach is to use a counter electrode (CE) material with high conductivity and excellent electrocatalytic activity. Among leading candidates for a DSSC CE is Pt [2]. Unfortunately, since Pt is expensive, employing a cheaper substitute becomes a stringent requirement. So far, there are cheaper alternative materials that can rival with Pt in terms of electrocatalytic performance such as nitrides [3], sulfides [4], carbides [5], and carbon allotropes. Various types of carbons that can function well as CE catalysts include graphites, carbon nanotubes, graphenes,

reduced graphene oxides, activated carbons, carbon blacks, and biomass-derived charcoals (biochars) [6–13].

One of the procedures to produce a biochar catalyst for a DSSC application is to thermally carbonize biomass under reducing atmosphere at a high temperature of around 850°C [12, 13]. Furthermore, to improve the as-pyrolized carbon's electrocatalytic performance, additional chemical processing steps in order to increase the carbon's surface area may be required. Most of these chemical treatment processes involve the use of harsh chemicals [14–16], which can be a downside. Therefore, biomasses subjected to milder thermal/chemical treatment are of interest provided that each derived carbon still function as a good catalyst.

Human hair is a fascinating biochar source because it naturally contains nitrogen and sulfur atoms. It has been

known that carbon doped with heterodopants such as nitrogen and sulfur usually have high electrocatalytic activity [17, 18]. Yet, there were only a few reports involving applications of carbonized human hair as an electrochemical electrode. These reports demonstrated the use of carbonized hair as a supercapacitor electrode [19, 20] and as a CE of a quantum dot-sensitized solar cells (QDSSC) [13]. As for the QDSSC-related work, Sahasrabudhe et al. fabricated their QDSSC CEs by mixing carbonized-hair powder with a PVDF binder and an NMP solvent. Mechanical grinding was not used in their work because human hair was digested with concentrated sulfuric acid before carbonizing the human hair at 850°C for 6 h. Without further chemical treatment of the carbon, their optimized QDSSC reached an efficiency of 4.44% in a polysulfide electrolyte.

In this study, we demonstrated the use of DSSC CE made of human hair catalyst mixed with a PEDOT:PSS binder. PEDOT:PSS (PEDOT) conducting polymer is a good choice because it has high conductivity and exhibits electrocatalytic activity toward converting tri-iodide ( $I_3^-$ ) into iodide ( $I^-$ ) [21]. Consequently, DSSCs with CEs made of PEDOT composited with various types of carbon catalysts often show a high solar conversion efficiency [22–27]. Notably, human hair-derived carbon has rarely been tested as a DSSC CE.

Herein, the hair was carbonized at only 700°C, and none of harsh chemical treatment was used in any steps in order to retain heterodopant atoms and to lessen the burden of furnace sealing. The synergistic effects of combining carbonized hair at various loadings with PEDOT toward the electrochemical performance and solar conversion efficiency were studied. Our solar conversion efficiency of DSSC with only PEDOT CE is  $3.03 \pm 0.09\%$ . Interestingly, mixing carbon at the amount of 0.6 g with PEDOT significantly increases the efficiency of a DSSC to  $6.54 \pm 0.11\%$ , which was not far from those of DSSCs with a Pt CE ( $7.29 \pm 0.01\%$ ).

## 2. Experimental

**2.1. Preparation of a Working Electrode.** Blocking layers were prepared by soaking FTO glass in a boiling  $TiCl_4$  40 mM at 70°C for 30 min. Seven layers of PST-18NR (Catalysts and Chemical Industries Co., Ltd.) and one layer of PST-400 were screen printed on FTO glass. The films were then annealed in an oven at 500°C for 1 h and soaked in a N719 dye solution at a room temperature for 24 h.

**2.2. Preparation of a Counter Electrode.** Teenager's hair without hair dye from a local barber was thoroughly washed in alcohol and DI water. The hair was carbonized in an argon atmosphere at 700°C for 2 h. The carbon was then finely ground and mixed with PEDOT:PSS (Sigma-Aldrich). The different amount of carbonized hair contents were 0.2, 0.4, 0.6, and 0.8 g while PEDOT/DI ratio was fixed at 1:1. The composites were vigorously stirred and then sonicated for 1 h. Each composite paste was applied on FTO glass with a doctor blade through a Kapton tape mask to define an active area of  $0.5 \text{ cm}^2$ . Then, the films were heated in the oven at 80°C for 6 h. A Pt counter electrode was prepared by spin coating Pt solution on FTO glass. Pt solution was prepared

by mixing chloroplatinic acid hydrate ( $H_2PtCl_6 \cdot xH_2O$  5 mM) dissolved in DI water 5 mL with ethyl cellulose 0.2 g in ethanol 15 mL. Then the film was annealed at 500°C for 1.50 h.

**2.3. Preparation of an Electrolyte.** An electrolyte was prepared by mixing the following chemicals with one another: 0.05 M  $I_2$ , 0.10 M LiI, 0.60 M 1-methyl-3-popylimidazolium iodide (MPI), 0.50 M tetrabutylpyridine (TBP), and 0.0025 M  $Li_2CO_3$  in acetonitrile.

**2.4. Characterization and Measurements.** The surface area of carbonized hair was determined using a BET (Brunner-Emmett-Teller) method. The pore structures of the carbon were investigated by  $N_2$  (77 K) adsorption-desorption measurement with a Bel Sorp mini II adsorption analyzer (Bel, Japan). The samples were degassed at 200°C for 3 h. in a vacuum prior to the BET measurement. The morphologies of carbonized hair were characterized by using a scanning electron microscope (SEM, LEO 1450VP, England), a field emission scanning electron microscopy (FESEM, FEI Scios DualBeam, Germany) and a transmission electron microscope (TEM, FEI Tecnai G2, USA). The phase of carbonized hair was investigated with an X-ray diffractometer (XRD, PANanalytical Empyrean, Netherlands) under  $Cu \text{ K}\alpha$  radiation and a Raman spectroscopy (JOBIN YVON HORIBA, T64000) equipped with a 532 nm solid state laser. Synthetic graphite powder less than  $20 \mu\text{m}$  (Sigma-Aldrich) was used as a standard for a 2D-peak reference. The chemical compositions of sample surfaces were investigated using an X-ray photoelectron spectrometer (XPS; AXIS Ultra DLD, Kratos Analytical, UK). The base pressure in the XPS analysis chamber was about  $5 \times 10^{-9}$  torr. The monochromatic  $Al \text{ K}\alpha$  1,2 source at 1.4 keV was radiated over the spot area of  $700 \times 300 \mu\text{m}$ . X-ray was maintained at 15 kV and 10 mA (150 W). The electrochemical studies were carried out using an electrochemical station (Gamry Instrument Reference 3000, USA). Electrocatalytic activities of all CEs were measured with a cyclic voltammetry (CV) technique in a standard three-electrode setup at a scan rate of  $20 \text{ mVs}^{-1}$ . The impedance characteristics of CEs were determined using electrochemical impedance spectroscopy (EIS) at frequencies ranging from 0.1 to 100 kHz with an AC amplitude of 10 mV. The solar conversion efficiency of full DSSC cells were measured using a solar simulator (Class A, PEC-L11, Japan) under a standard illumination of  $100 \text{ mW cm}^{-2}$ .

## 3. Results and Discussion

**3.1. Surface and Structure of Carbonized Hair.** To understand the microstructure of carbonized hair, nitrogen sorption isotherm was recorded (Figure 1). A carbonized hair sample has type-II adsorption isotherm characteristics typically related to nonporous microstructures [28]. However, the subtle hysteresis loop, related to the minor difference pressure ratio ( $P/P_0$ ) between a pore filling cycle and an emptying one, should be attributed to the existence of mesopores [28]. This is confirmed by Barrett-Joyner-Halenda (BJH) analysis (Figure 1 inset); however, there are only small

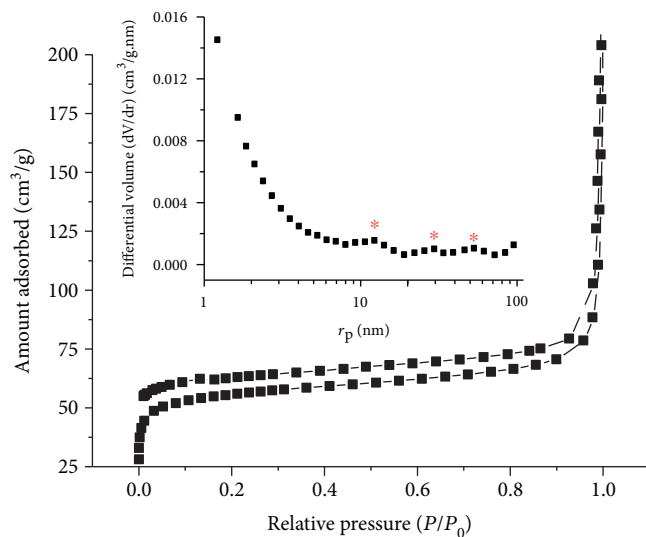


FIGURE 1: The  $N_2$  sorption isotherm and inset pore size distribution of carbonized hair.

differential volumic amount of certain pore sizes (noted with asterisk). Since pores are not prevalent, an average surface area of carbonized hair determined from BET technique is mere  $187.96 \text{ m}^2 \text{ g}^{-1}$ . This value was not exceptionally high as compared to Sahasrabudhe et al.'s because most carbon flakes were not etched with any chemicals and the carbonization temperature was only  $700^\circ\text{C}$ .

Figure 2 shows the SEM images of ground carbonized hair. Figures 2(a) and 2(b) show the morphology of carbon flakes at low magnification (1000x) and high magnification (10Kx), respectively. The sizes of most flakes are generally smaller than  $3 \mu\text{m}$ . A closer inspection with FESEM at 80Kx (Figure 2(c)) reveals the rough surface of carbonized hair platelets. Pores are not clearly observed at this magnification. According to TEM imaging (Figure 3(a)), smaller carbon nanoflakes ranging between 100 and 250 nm are also observed. Pore features are also not clearly resolved in TEM images.

A high-resolution TEM image of carbonized hair (Figure 3(b)) shows the mixture of some graphitic crystallites and an amorphous phase. The lattice fringes of the graphitic phase are approximately 0.33 nm corresponding to (002) graphitic planes. The selected area electron diffraction (SAED, Figure 3(b) inset) shows ring patterns which belong to (002) and (101) planes without spotted features, implying the presence of sparse short-range order crystallites in the amorphous phase. XRD was used to affirm the existence of crystalline phase in the carbonized hair powder. As shown in Figure 4, the background intensity of the XRD signals is rather high, which should come from the air scattering effect [29]. Moreover, two XRD peaks were observed at  $25.5^\circ$  and  $42.3^\circ$ . These peaks can be assigned to (002) and (101) planes, respectively [20, 30]. The presence of clear (002) and (101) peaks suggests that the carbonized hair already partially transforms into some turbostratic graphitic structure [30]. Figure 5 shows an example of Raman spectrum which belonged to the carbonized human hair.

Raman curve fittings were carried out using three- and two-peak models to determine the number, position, and area of each of carbon's signature peak. A disorder graphitic structure (D peak) and amorphous (A peak) and graphitic-like (G peak) features were identified in a three-peak model [31]. Note that the A peak was not fitted in the two-peak fitting scheme. Phase identification with Raman analysis is useful because both G peak and D peak are associated with the electrocatalytic reaction. The defective sites on graphitic edges related to G peak could help reduce the charge transfer resistance of the DSSC's CE [32]. Although the electrocatalytic activity occurs mostly at edge planes rather than the basal planes, the basal plane itself could benefit from the electron transfers in the CE. As for the D peak, its area and intensity increase with the increasing disorders in a carbon material, which can be affected by a particle size, a dopant, and others. When carbon particles become smaller, the D peak area and intensity increase. It was shown that a DSSC whose CE was made of smallest carbon black particles (20 nm) exhibited the highest solar conversion efficiency [33]. This nanocarbon, whose D peak is large, performs better than the larger ones since it has high surface areas and its disorder sites are electrochemically active in the material. Aside from the size effect, the introduction of heteroatom in carbon normally introduces disorder in a carbon material and consequently raises area ratio of D peak ( $I_D$ ) over G peak ( $I_G$ ) ( $I_D/I_G$ ). For example,  $I_D/I_G$  of reduced graphene oxide, when doped with nitrogen and phosphorous, increases from 0.94 to 1.15 [34]. The higher  $I_D/I_G$  ratio, associating with increasing degree of disorder, offers numerous active sites for electrocatalytic activity [35].

In this study, all peaks were fitted with asymmetric Lorentzian. The peaks are located at  $1335.47 \text{ cm}^{-1}$  (D),  $1509.37 \text{ cm}^{-1}$  (A), and  $1583.55 \text{ cm}^{-1}$  (G). The  $I_D/I_G$  ratio determined from the three-peak model is 1.36. For the two-peak model, the D peak and G peak obtained from asymmetric Lorentzian fitting are situated at  $1330.72 \text{ cm}^{-1}$  and  $1590.78 \text{ cm}^{-1}$ , respectively. From the two-peak model, the  $I_D/I_G$  ratio is 1.07 which is lower than that of the three-peak model. For our samples, the three-peak model should be more appropriated for fitting because a hidden shoulder peak related to the amorphous phase near G peak is clearly present. Based on the two- and three-peak models, our  $I_D/I_G$  is higher than Sahasrabudhe et al.'s work ( $650\text{--}850^\circ\text{C}$ ), meaning our carbon has higher degree of disorder.

Another useful information from Raman analysis is to detect an amorphous phase by considering the second-order two-phonon mode (2D). The absence of 2D peak could infer the presence of amorphous phase in the material [36]. From Figure 5(b), 2D peak of graphitic micropowder at  $\sim 2703 \text{ cm}^{-1}$  is sharp while that of carbonized hair is very broad and low. This could confirm the presence of amorphous phase as well as some small number of graphitic phase in the carbonized hair sample.

**3.2. Composition Analysis.** The building blocks of human hair comprise amino acid, keratin, melanin and protein. Therefore, basic elements found in hair are carbon, oxygen, nitrogen, hydrogen, and sulfur [37, 38]. Generally, burning

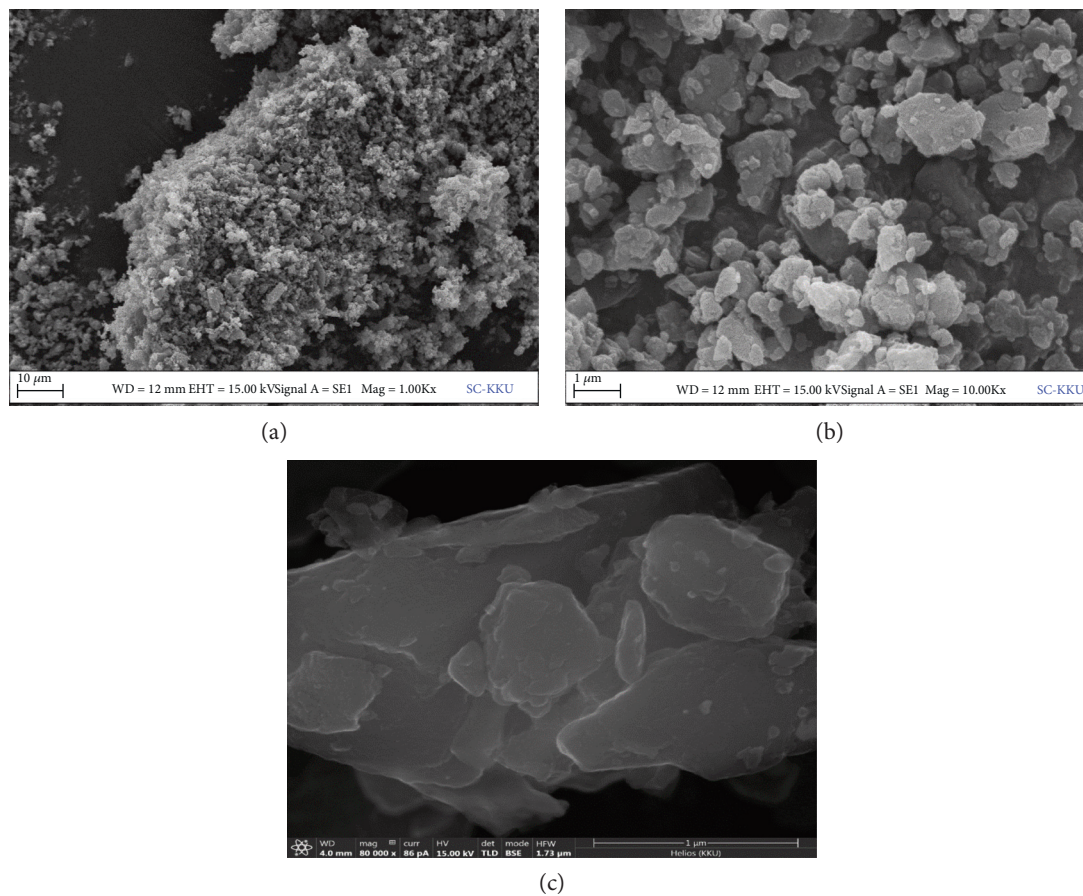


FIGURE 2: The SEM images of ground carbonized hair. (a) The morphology of carbon flakes at low magnification (1000x), (b) high magnification (10Kx), and (c) ultrahigh magnification (80Kx).

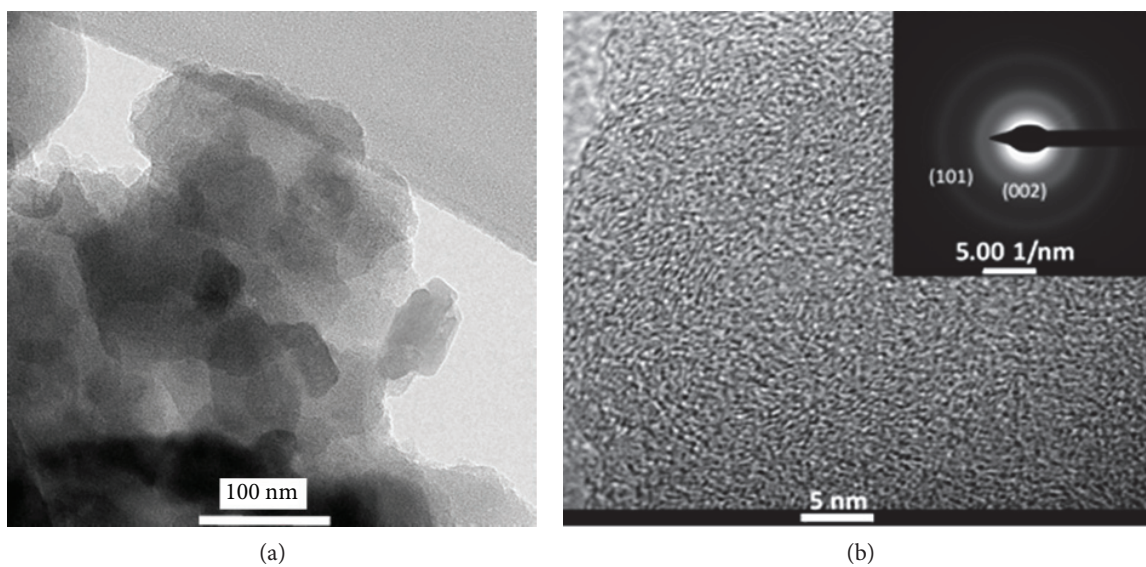


FIGURE 3: A TEM image of carbonized hair (a) low resolution, (b) high resolution, and inset SAED.

human hair in a certain oxygen-deficit condition will result in a carbon that contains remaining nitrogen, oxygen, and sulfur if the temperature is not high enough to expel these

heteroatoms. Since our carbonization temperature was lower than usual and no harsh chemical was used, it was speculated that many extant heteroatoms were present with the carbon.

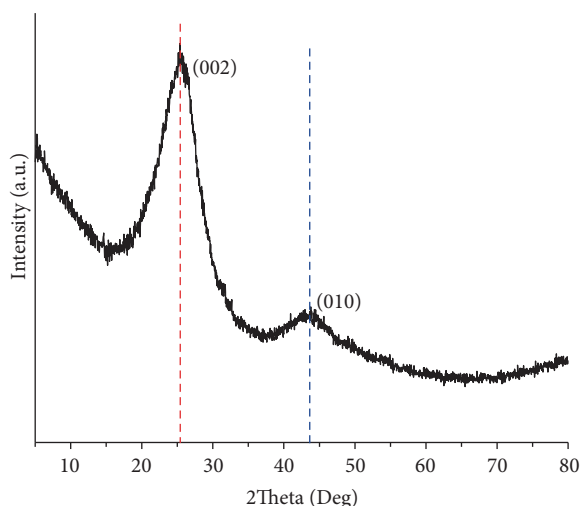
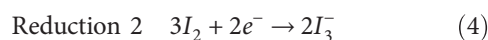
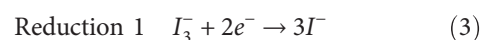
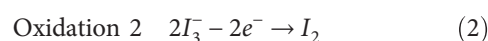
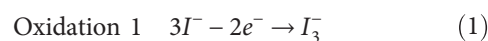


FIGURE 4: An XRD spectrum of carbonized hair.

XPS was used to identify the atomic binding states and the elemental compositions of carbonized hair surface. The XPS results were arranged in Table 1. The XPS peaks shown in Figures 6(a), 6(b), 6(c), 6(d), and 6(e) were indexed following NIST standard and various references [39–41]. The C 1s (C-C) peak at 284.9 eV corresponds to  $sp^2$  hybridized carbon commonly found in the carbon-based aromatic ring. The C 1s (C-C) shoulder peak at 286.2 eV reveals the presence of  $sp^3$  hybridized carbon. The C-N peak could overlap with the C-C peak. Another C 1s satellite peak at 287.6 eV is related to coincidence sum peak of carbonyl groups (C=O) and C=N while the one located at 288.8 eV corresponds to the ester group (O=C-O). The last peak at 290.4 eV is assigned to the carboxylic group (O=C-OH). The oxygen-carbon bonds also appear at 530.9 eV (C=O), 532.0 eV (O-C-O), 533.1 eV (O=C-O), and 534.3 eV (amide), respectively. There are three peaks representing nitrogen N 1s bonds which are located at 398.7 eV (pyridinic), 400.1 eV (pyrrolic), and 401.2 eV (quaternary). Apart from nitrogen, only a small amount of sulfur also appears in the form of thiopenic structures (C-S-C) whose peaks are situated at 163.9 eV (2p 3/2) and 164.9 eV (2p 1/2). The presence of C-N and C=N peaks confirms the doping of nitrogen into the carbon structure. The amount of nitrogen in the our carbon is 9.47 at.%, which is higher than Si et al.'s report (1–3%). The amount of oxygen and sulfur in our carbonized hair is 9.98 and 0.15 at.%, respectively. Such high amount of nitrogen could be of great help to increase the electrocatalytic activity of the carbon catalyst.

**3.3. Electrochemical Properties.** The electrochemical activities of all samples were investigated by cyclic voltammetry (CV). The CV results were shown in Figures 7(a) and 7(b). All samples have two oxidation peaks and two reduction peaks. The oxidation peaks are related to chemical reactions following (1) and (2) while the reductions reactions correspond to (3) and (4) [42]. It has been accepted that a DSSC performance is also governed by  $I_3^-/I^-$  redox reaction on the CE side [43]. Therefore, a catalyst on the CE side must be electrochemically active in  $I_3^-$  reduction activity. This is justified from

the value of cathodic current involving  $I_3^-$  reduction ( $I_{cr}$ ), which is located at more negative potential. Higher  $|I_{cr}|$  value indicates better electrocatalytic activity. All the  $I_{cr}$  values are shown in Figure 8. The absolute value of  $I_{cr}$  increases with the increasing carbon up to 0.6 g. Nevertheless, adding carbon beyond this optima results in the slight decrease in  $|I_{cr}|$ . This could be due to the reduction of catalytic activity induced by agglomerations that partially block some active sites. Based on CV results,  $C_{0.6}P$  should have the best electrocatalytic activity among  $C_xP$ . Nonetheless,  $I_{cr}$  value ( $2.53 \times 10^{-4}$  mA) of  $C_{0.6}P$  is still lower than that of Pt ( $4.77 \times 10^{-4}$  mA), implying that Pt is better than  $C_{0.6}P$  regarding the  $I_3^-$  reduction capability.



Apart from a CV technique, impedance measurements to determine a series resistance ( $R_s$ ), a transport resistance in PEDOT and carbon layer ( $R_{trp}$ ), and a charge transfer resistance at CE surface ( $R_{ct}$ ) were performed [44]. The electrochemical impedance spectra (EIS) of symmetric CE cells were shown in Figures 9(a), 9(b), 9(c), and 9(d). All the resistance values (Table 2) were derived by fitting the impedance data with an equivalent circuit [44].  $R_s$  is a combination of series resistances from FTO glass, test wires, and ohmic contacts between FTO glass and an electrocatalytic layer.  $R_s$  is related to the  $x$ -axis intercept of the 1st semicircle at high frequency. The  $R_{trp}$  is a real part within the 1st semicircle of PEDOT and  $C_xP$  except for Pt which has no semicircle related to the  $R_{trp}$ . As for the  $R_{ct}$  value,  $R_{ct}$  is a real part within the 2nd semicircle of PEDOT and the composites; however, in the case of Pt, the  $R_{ct}$  was determined from a high frequency peak (1st semicircle) [12, 45, 46]. The reason that Pt (Figure 9(b) (inset)) does not have  $R_{trp}$ -related semicircle is because Pt is highly conductive.

Furthermore, Pt has the lowest  $R_s$  (13.48  $\Omega$ ) among all samples, which also implies that spinning coating induces good adhesion between the Pt film and the FTO substrate. The  $R_s$  of PEDOT is 16.17  $\Omega$  while the highest one belonged to  $C_{0.8}P$  (17.13  $\Omega$ ). The additions of carbon from 0.2 to 0.6 g into PEDOT only slightly increase the  $R_s$  of PEDOT. This should be due to the slightly poorer adhesion between the film and FTO glass and the incremental series resistances when more carbon contents were added.

In the case of  $R_{trp}$ , PEDOT has the largest  $R_{trp}$  value (2.28  $\Omega$ ). Adding carbon at the amount of 0.2 and 0.4 g reduces  $R_{trp}$  to 1.43  $\Omega$  and 0.84  $\Omega$ , respectively. This is because carbon increases the conducting pathways in the composite. Additional carbon loadings (0.6 and 0.8 g) lead to slight increasing of  $R_{trp}$  (1.14 and 2.25  $\Omega$ ). The reason for this is that even though more carbons could further reduce the  $R_{trp}$  resistance, counteraction to such effect might come from accumulative carbon's resistances.

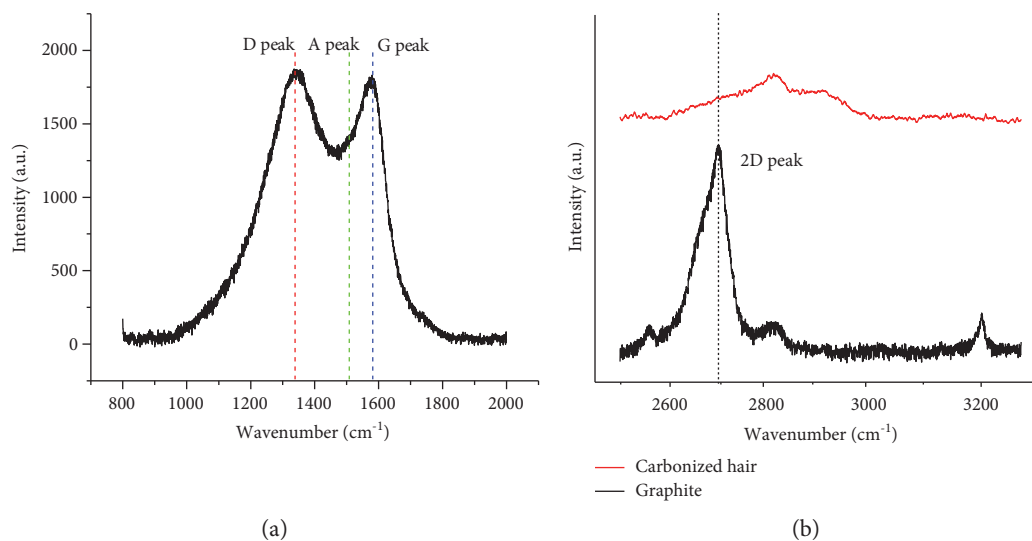


FIGURE 5: A Raman spectrum of (a) carbonized hair (from 800 to 2000  $\text{cm}^{-1}$ ) and (b) carbonized hair and graphite (from 2500 to 3200  $\text{cm}^{-1}$ ).

TABLE 1: The peak assignment and elemental composition derived from XPS spectra.

Peak	Binding energy (eV)	Assignment	Element composition (at.%)	Fraction of species (%)
C 1s	284.9	$\text{Sp}^2$ C-C	80.22	58.3
	286.2	$\text{Sp}^3$ C-C, C-N		23.1
	287.6	-C=O, C=N		8.8
	288.8	O=C-O		6.9
	290.4	O=C-OH		2.9
O 1s	530.9	C=O	9.98	30.0
	532.0	O-C-O		34.4
	533.1	O-C=O		29.1
	534.4	Amide		6.5
N 1s	398.7	Pyridinic N (N-6)	9.47	43.4
	400.1	Pyrrolic N (N-5)		36.8
	401.2	Quaternary N (N-Q)		19.8
S 2p	163.9	Thiophenic (C-S-C) 3/2	0.15	57.4
	164.9	Thiophenic (C-S-C) 1/2		42.6

The  $R_{\text{ct}}$  is the resistance at the interface between the CE surface and the electrolyte. Low  $R_{\text{ct}}$  denotes the high electrocatalytic activity of CE catalyst. PEDOT has the highest  $R_{\text{ct}}$  (152.08  $\Omega$ ) among all samples. For 0.2–0.6 g of carbon contents, the  $R_{\text{ct}}$  of the  $\text{C}_x\text{P}$  is decreasing with increasing amount of carbon, suggesting the enhancement in electrocatalytic activity. This is related to the rise of electrochemical active sites for  $\text{I}_3^-$  reduction, which is attributed to increasing in carbon catalysts and the PEDOT's surface areas as well as the ease of electrolyte access.

The lowest  $R_{\text{ct}}$  among the  $\text{C}_x\text{P}$  is realized for  $\text{C}_{0.6}\text{P}$  (7.11  $\Omega$ ). Yet, if the carbon content is 0.8 g, the  $R_{\text{ct}}$  escalates to 29.98  $\Omega$ . This might correspond to carbon agglomeration at high carbon loading and consequently leads to the decline in the active area of carbon and PEDOT. Note that the  $R_{\text{ct}}$  of  $\text{C}_{0.8}\text{P}$  (29.98  $\Omega$ ) is still lower than that of  $\text{C}_{0.4}\text{P}$  (54.39  $\Omega$ ). Compared with Pt, the  $R_{\text{ct}}$  of  $\text{C}_{0.6}\text{P}$  is higher than Pt's (4.58  $\Omega$ ). The trend of  $R_{\text{ct}}$  with varied carbon amount is reasonable because it goes inversely with  $|I_{\text{cr}}|$  [47].

The summation of resistances ( $R_s + R_{\text{trp}} + R_{\text{ct}}$ ) is shown in Table 2. These overall resistances impede the electrochemical activity and have negative effect toward solar efficiency.  $\text{C}_{0.6}\text{P}$  has the lowest overall resistance meaning that it should have the highest electrocatalytic activity among  $\text{C}_x\text{P}$ . However, its electrocatalytic activity is lower than that of Pt.

**3.4. Solar Efficiency.** The main parameters affecting a solar efficiency are an open-circuit voltage ( $V_{\text{oc}}$ ), a fill factor (FF), and a short-circuit current density ( $J_{\text{sc}}$ ). To gain high energy conversion efficiency, these three parameters must be as high as possible. The  $J$ - $V$  characteristics of selected samples of a DSSC with  $\text{C}_x\text{P}$  CE ( $\text{C}_x\text{P}$  DSSC) and a DSSC with Pt CE (Pt DSSC) were shown in Figure 10. All the photovoltaic parameters were summarized in Table 2. The  $V_{\text{oc}}$  is expressed as the difference between the  $\text{TiO}_2$ 's Fermi level and the electronic energy of  $\text{I}_3^-/\text{I}^-$  redox couple [48]. Therefore, the  $V_{\text{oc}}$  mostly depends on the  $\text{TiO}_2$ , a dye, and an electrolyte quality.

In this work,  $V_{\text{oc}}$  values of all  $\text{C}_x\text{P}$  DSSCs fall within 0.75–0.76 V, which are also close of Pt DSSC (0.74 V). This corresponds to the reproducible fabrication of the  $\text{TiO}_2$  photoanode films. As for the FF factor, this parameter depends on the whole processes essential for the operation of DSSC. On the CE side, such processes include  $\text{I}_3^-$  supply,  $\text{I}_3^-$  to  $\text{I}^-$  conversion activity, and  $\text{I}^-$  availability [49]. Therefore, the electrochemical activity and the resistances of CEs are useful for the interpretation of relationship between carbon content and the FF value. The fill factor

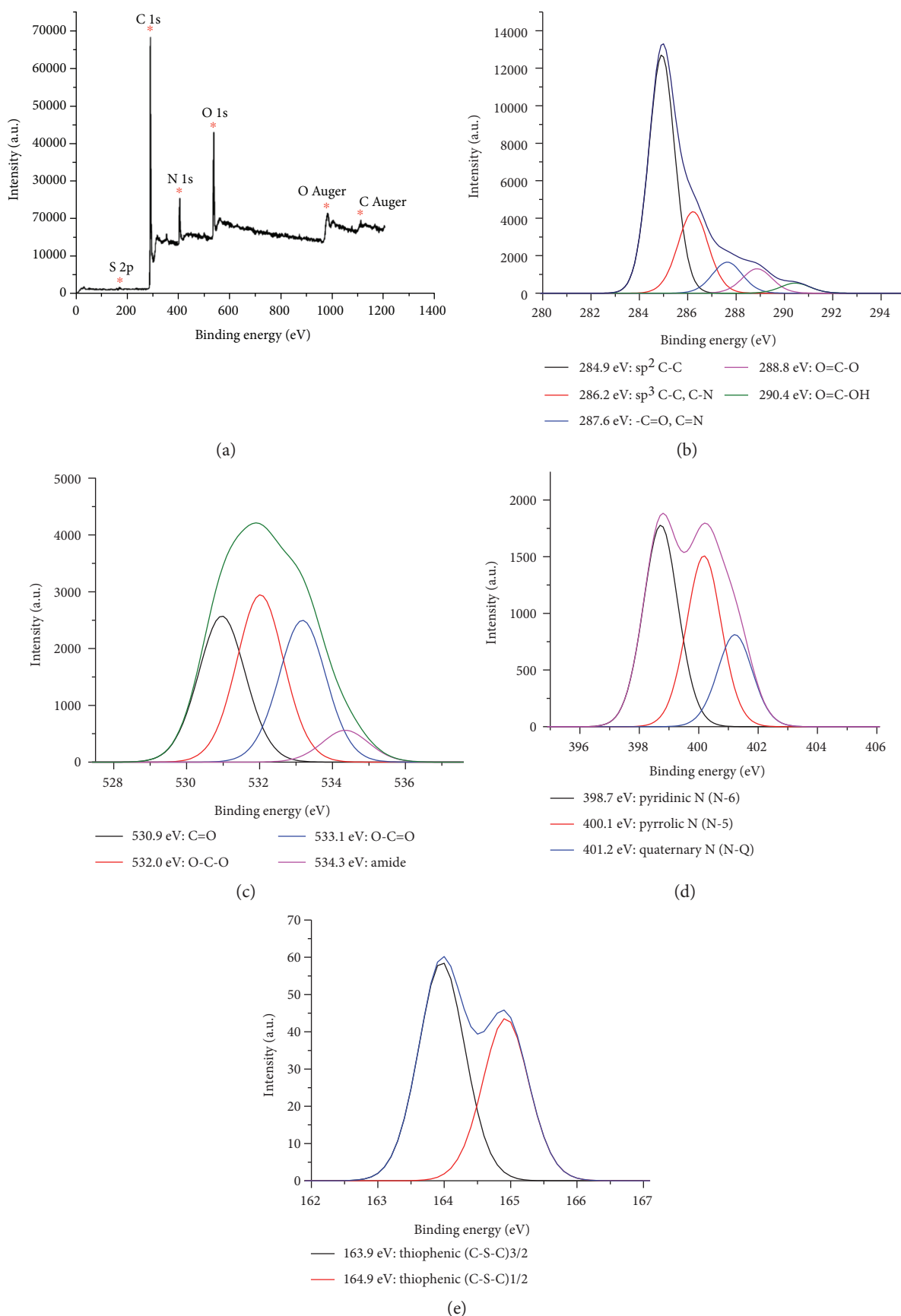


FIGURE 6: XPS spectra of carbonized hair. (a) XPS survey spectrum, (b) C 1s, (c) O 1s, (d) N 1s, and (e) S 2p.

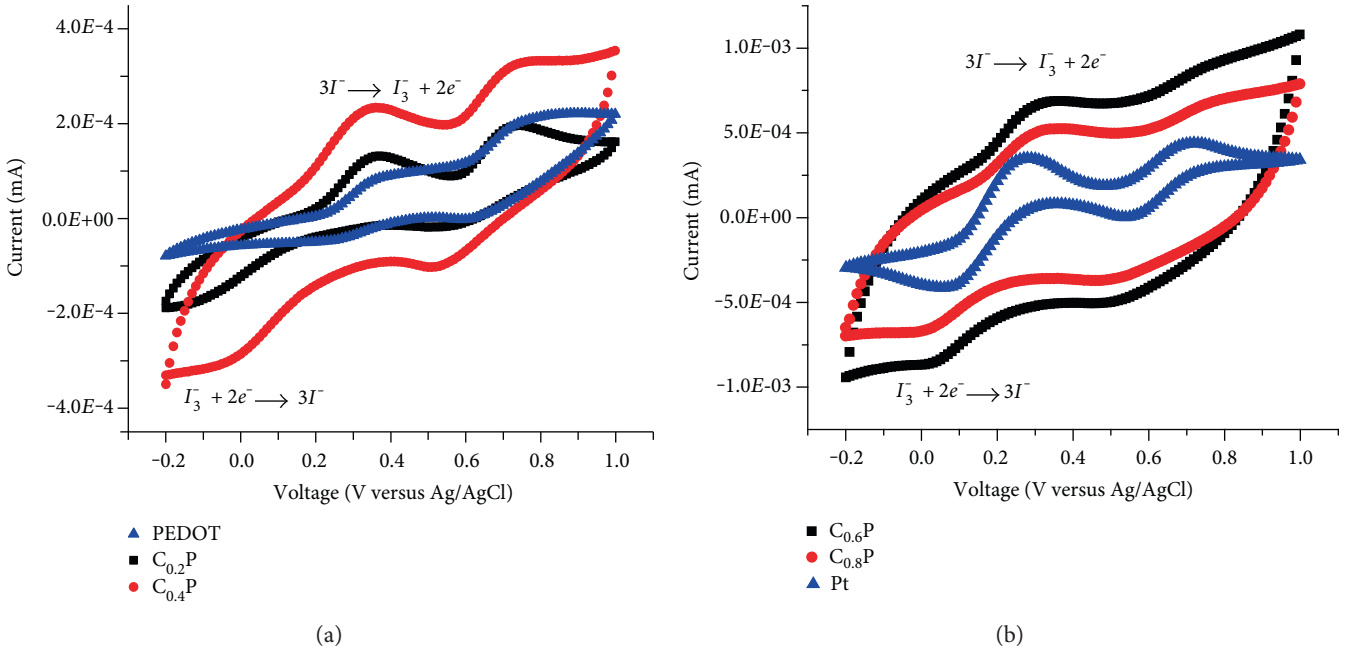


FIGURE 7: CV results of counter electrodes. (a) C<sub>0.2</sub>P, C<sub>0.4</sub>P, and PEDOT. (b) C<sub>0.6</sub>P, C<sub>0.8</sub>P, and Pt.

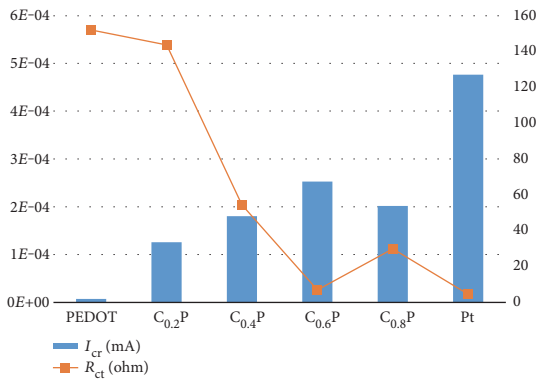


FIGURE 8: The relationship between  $I_{cr}$  and  $R_{ct}$ .

of PEDOT DSSCs is only  $0.31 \pm 0.01$ . PEDOT DSSC has low FF because PEDOT has the poorest electrocatalytic activity as verified from CV results. The FF value rises with the increasing carbon amount (0.2 to 0.6 g) due to increasing catalytic sites and reduction of total resistances. Nevertheless, when 0.8 g of carbon is added, the FF does not significantly increase as compared to that of C<sub>0.6</sub>P DSSC due to the increase in the overall resistances (Table 2). Among C<sub>x</sub>P DSSCs, the high FF value of  $0.58 \pm 0.01$  is obtained for C<sub>0.6</sub>P DSSC and C<sub>0.8</sub>P DSSC. However, their values are lower than that of Pt DSSC (0.63) because Pt's total resistance is the lowest.

The  $J_{sc}$  is a photocurrent density measured without any external loads under a short-circuit condition. Similar to FF,  $J_{sc}$  value is dictated by electrocatalytic activity and a total

resistance. That is, high electrocatalytic activity and low total resistance are required to ease electrochemical processes of CE side and so guaranteeing a high  $J_{sc}$  value [49]. With increasing carbon content from 0.2 to 0.4 g, the  $J_{sc}$  increases and reaches its maximum for carbon content of 0.6 g ( $14.85 \pm 0.03 \text{ mA cm}^{-2}$ ). However,  $J_{sc}$  decreases with increasing carbon content to 0.8 g ( $14.52 \pm 0.05 \text{ mA cm}^{-2}$ ) as electrocatalytic activity decrease for excessive carbon loading. This is explained by the sudden increase of total resistance of symmetric C<sub>0.8</sub>P DSSC as compared to that of C<sub>0.6</sub>P DSSC. The maximum  $J_{sc}$  belonged to Pt DSSC ( $15.64 \pm 0.02 \text{ mA cm}^{-2}$ ) as Pt DSSC has the lowest total resistance.

Among all samples, PEDOT has the lowest efficiency ( $3.03 \pm 0.09\%$ ) due to its low FF and  $J_{sc}$  values. Combining carbonized hair with PEDOT provides the synergistic catalytic effect for  $I_3^-$  reduction. The FF and  $J_{sc}$  values are increasing with the increasing carbon loadings from 0.2 to 0.6 g. Accordingly, the efficiency keeps increasing until the maximum efficiency is reached at  $6.54 \pm 0.11\%$  for C<sub>0.6</sub>P DSSC. Nonetheless, too high carbon loading (0.8 g) results in the reduction of DSSC's efficiency ( $6.31 \pm 0.11\%$ ). The efficiency of Pt DSSC ( $7.29 \pm 0.01\%$ ) is higher than that of C<sub>0.6</sub>P DSSC due to the higher FF and  $J_{sc}$  values achieved in Pt DSSC.

#### 4. Conclusion

Composite films made of PEDOT and nonactivated carbonized hair were tested as DSSC CEs. Though the carbon does not have exceptionally large specific surface area ( $187.96 \text{ m}^2 \text{ g}^{-1}$ ), it is effective enough for electrocatalytic reduction of  $I_3^-$ , which could be due to the contribution of nitrogen dopants (up to 9.47 at.%) and from graphitic-

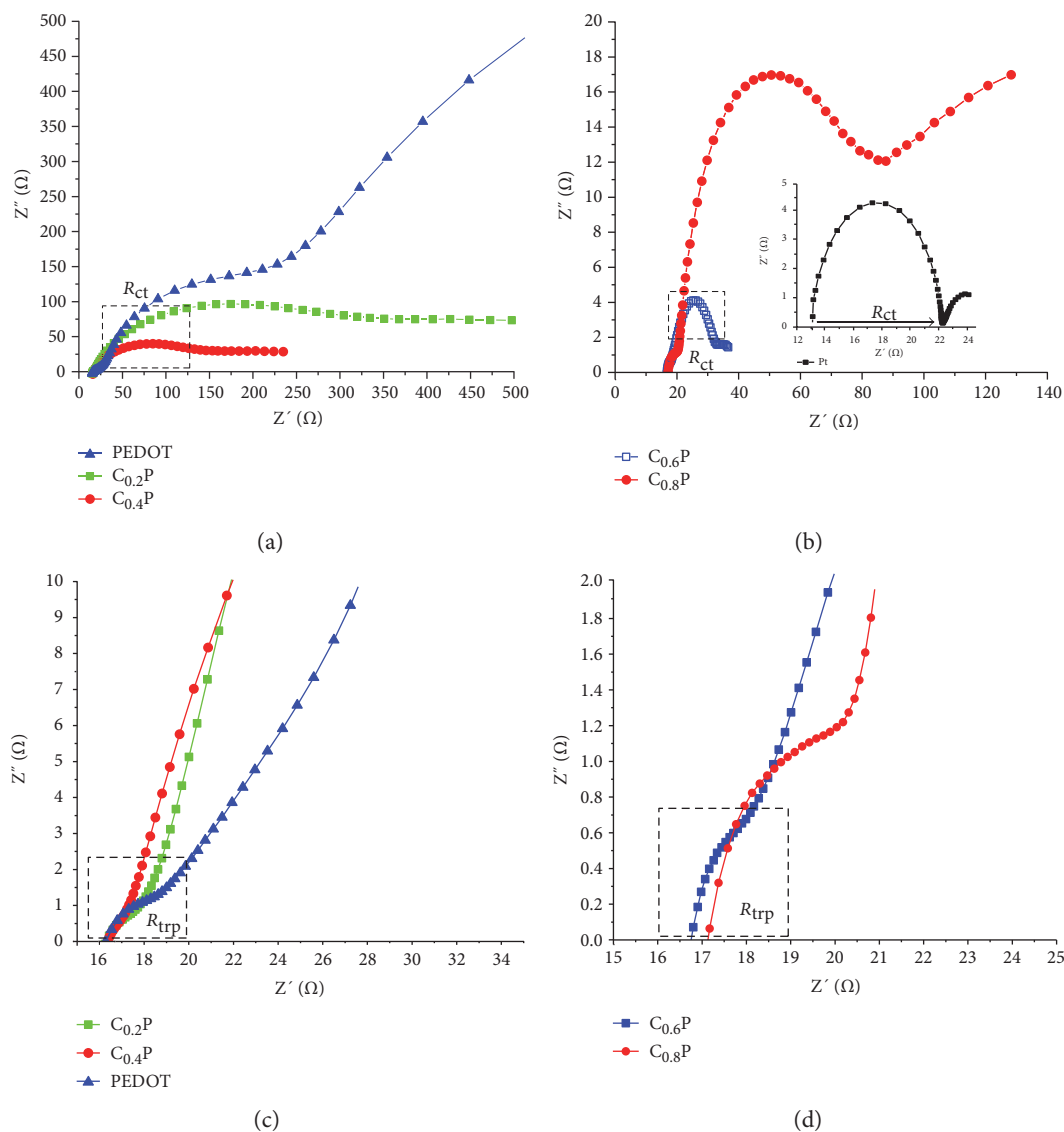


FIGURE 9: Impedance spectra of counter electrodes. (a)  $C_{0.2}P$ ,  $C_{0.4}P$ , and PEDOT; (b)  $C_{0.6}P$  and  $C_{0.8}P$ ; and inset Pt (c) zoom-in detail of 9(a) and (d) zoom-in detail of 9(b).

TABLE 2: Photovoltaic parameters and EIS resistances of different counter electrodes.

Counter electrodes	Photovoltaic parameters				Electrochemical impedance spectroscopy			
	$J_{sc}$ ( $\text{mA cm}^{-2}$ )	$V_{oc}$ (V)	FF	$\eta$ (%)	$R_s$ (Ω)	$R_{trp}$ (Ω)	$R_{ct}$ (Ω)	$R_{Total}$ (Ω)
PEDOT	$13.03 \pm 0.05$	$0.75 \pm 0.0028$	$0.31 \pm 0.01$	$3.03 \pm 0.09$	16.17	2.28	152.08	170.53
$C_{0.2}P$	$13.54 \pm 0.03$	$0.76 \pm 0.0019$	$0.46 \pm 0.00$	$4.73 \pm 0.02$	16.35	1.43	143.65	161.43
$C_{0.4}P$	$14.48 \pm 0.04$	$0.76 \pm 0.0025$	$0.55 \pm 0.02$	$6.05 \pm 0.22$	16.49	0.84	54.39	71.72
$C_{0.6}P$	$14.85 \pm 0.03$	$0.76 \pm 0.0018$	$0.58 \pm 0.01$	$6.54 \pm 0.11$	16.76	1.14	7.11	25.01
$C_{0.8}P$	$14.52 \pm 0.05$	$0.75 \pm 0.0029$	$0.58 \pm 0.01$	$6.31 \pm 0.11$	17.13	2.25	29.98	49.36
Pt	$15.64 \pm 0.02$	$0.74 \pm 0.0010$	$0.63 \pm 0.00$	$7.29 \pm 0.01$	13.48	—	4.58	18.06

like carbons as well as the disordered types. Without carbon, a PEDOT DSSC has the lowest efficiency ( $3.03 \pm 0.09\%$ ) due to its low FF and  $J_{sc}$ . Compositing carbonized hair with

PEDOT helps improve FF and  $J_{sc}$  values of DSSCs. The maximum efficiency of  $6.54 \pm 0.11\%$  was achieved for  $C_{0.6}P$  DSSC. Though the efficiency of  $C_{0.6}P$  DSSC is lower than

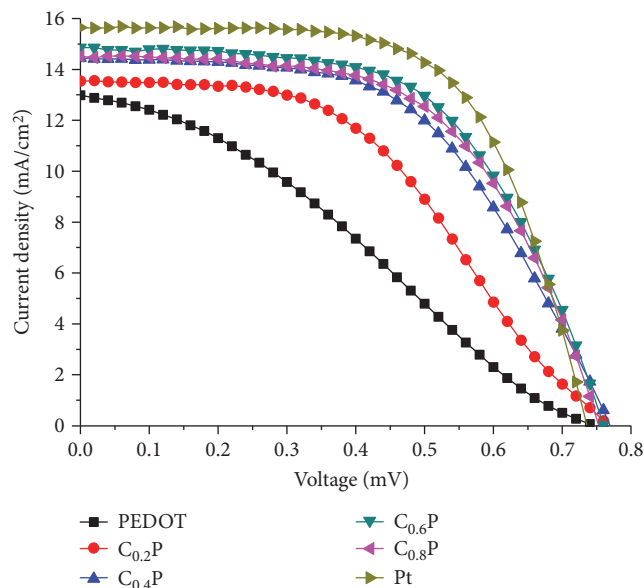


FIGURE 10:  $J$ - $V$  curves of counter electrodes.

Pt DSSC's ( $7.29 \pm 0.01\%$ ) due to its lower FF and  $J_{sc}$ , the carbon catalyst proposed here is still interesting for a DSSC application because our preparation steps involve no harsh chemical. Moreover, the selected carbonization temperature herein is only  $700^\circ\text{C}$ .

## Conflicts of Interest

The authors declare that they have no conflicts of interest.

## Acknowledgments

This work was supported by the Science Achievement Scholarship of Thailand (SAST); the Nanotechnology Center (NANOTEC), NSTDA, Ministry of Science and Technology, Thailand, through its program of Center of Excellence Network, Center for Alternative Energy Research and Development, Khon Kaen University; the Higher Education Research Promotion and National Research University Project of Thailand, Office of the Higher Education Commission, through the Advanced Functional Materials Cluster of Khon Kaen University; the Integrated Nanotechnology Research Center, Khon Kaen University, Thailand; and Thailand Center of Excellence in Physics, Commission on Higher Education.

## References

- [1] S. Mathew, A. Yella, P. Gao et al., "Dye-sensitized solar cells with 13% efficiency achieved through the molecular engineering of porphyrin sensitizers," *Nature Chemistry*, vol. 6, no. 3, pp. 242–247, 2014.
- [2] S. H. Park, B. K. Kim, and W. J. Lee, "Electrospun activated carbon nanofibers with hollow core/highly mesoporous shell structure as counter electrodes for dye-sensitized solar cells," *Journal of Power Sources*, vol. 239, pp. 122–127, 2013.
- [3] S. H. Park, Y. H. Cho, M. Choi et al., "Nickel-nitride-coated nickel foam as a counter electrode for dye-sensitized solar cells," *Surface & Coatings Technology*, vol. 259, pp. 560–569, 2014.
- [4] F. Yao, P. Sun, X. Sun et al., "One-step hydrothermal synthesis of ZnS-CoS microcomposite as low cost counter electrode for dye-sensitized solar cells," *Applied Surface Science*, vol. 363, pp. 459–465, 2016.
- [5] P. Vijayakumar, M. Senthil Pandian, S. P. Lim et al., "Facile synthesis of tungsten carbide nanorods and its application as counter electrode in dye sensitized solar cells," *Materials Science in Semiconductor Processing*, vol. 39, pp. 292–299, 2015.
- [6] H. Kim, G. Veerappan, and J. H. Park, "Conducting polymer coated non-woven graphite fiber film for dye-sensitized solar cells: superior Pt- and FTO-free counter electrodes," *Electrochimica Acta*, vol. 137, pp. 164–168, 2014.
- [7] W. Zheng, T. Qi, Y. C. Zhang, H. Y. Shi, and J. Q. Tianqing, "Fabrication and characterization of a multi-walled carbon nanotube-based counter electrode for dye-sensitized solar cells," *New Carbon Materials*, vol. 30, no. 5, pp. 391–396, 2015.
- [8] I. A. Sahito, K. C. Sun, A. A. Arbab, M. B. Qadir, and S. H. Jeong, "Graphene coated cotton fabric as textile structured counter electrode for DSSC," *Electrochimica Acta*, vol. 173, pp. 164–171, 2015.
- [9] L. Qiu, H. Zhang, W. Wang, Y. Chena, and R. Wang, "Effects of hydrazine hydrate treatment on the performance of reduced graphene oxide film as counter electrode in dye-sensitized solar cells," *Applied Surface Science*, vol. 319, pp. 339–343, 2014.
- [10] I. Y. Y. Bu and J. Zheng, "A new type of counter electrode for dye sensitized solar cells based on solution processed  $\text{SnO}_2$  and activated carbon," *Materials Science in Semiconductor Processing*, vol. 39, pp. 223–228, 2015.
- [11] C. C. Ting and W. S. Chao, "Efficiency improvement of the DSSCs by building the carbon black as bridge in photo electrode," *Applied Energy*, vol. 87, no. 8, pp. 2500–2505, 2010.
- [12] W. Maiaugree, S. Lowpa, M. Towannang et al., "A dye sensitized solar cell using natural counter electrode and natural dye derived from mangosteen peel waste," *Scientific Reports*, vol. 5, p. 15230, 2015.
- [13] A. Sahasrabudhe, S. Kapri, and S. Bhattacharyya, "Graphitic porous carbon derived from human hair as 'green' counter electrode in quantum dot sensitized solar cells," *Carbon*, vol. 107, pp. 395–404, 2016.
- [14] M. Pakula, S. Biniak, and A. Swiatkowski, "Chemical and electrochemical studies of interactions between iron (III) ions and an activated carbon surface," *Langmuir*, vol. 14, no. 11, pp. 3082–3089, 1998.
- [15] J. Guo and A. C. Lua, "Textural and chemical characterizations of activated carbon prepared from oil-palm stone with  $\text{H}_2\text{SO}_4$  and KOH impregnation," *Microporous and Mesoporous Materials*, vol. 32, no. 1, pp. 111–117, 1999.
- [16] O. Gercel, A. Ozcan, A. Safa Ozcan, and H. Ferdi Gercel, "Preparation of activated carbon from a renewable bio-plant of *Euphorbia rigida* by  $\text{H}_2\text{SO}_4$  activation and its adsorption behavior in aqueous solutions," *Applied Surface Science*, vol. 253, no. 11, pp. 4843–4852, 2007.
- [17] M. Chen, L. L. Shao, Y. P. Liu, T. Z. Ren, and Z. Y. Yuan, "Nitrogen-doped ordered cubic mesoporous carbons as metal-free counter electrodes for dye-sensitized solar cells," *Journal of Power Sources*, vol. 283, pp. 305–313, 2015.
- [18] W. Yang, X. Ma, X. Xu et al., "Sulfur-doped porous carbon as metal-free counter electrode for high efficiency dye-sensitized

- solar cells,” *Journal of Power Sources*, vol. 282, pp. 228–234, 2015.
- [19] W. Si, J. Zhou, S. Zhang, S. Li, W. Xing, and S. Zhuo, “Tunable N-doped or dual N, S-doped activated hydrothermal carbons derived from human hair and glucose for supercapacitor applications,” *Electrochimica Acta*, vol. 107, pp. 397–405, 2013.
- [20] Z. Guo, Q. Zhou, Z. Wu et al., “Nitrogen-doped carbon based on peptides of hair as electrode materials for supercapacitors,” *Electrochimica Acta*, vol. 113, pp. 620–627, 2013.
- [21] E. Tamburri, V. Guglielmotti, S. Orlanducci, and M. L. Terranova, “Structure and  $I_2/I^-$  redox catalytic behaviour of PEDOT-PSS films electro polymerized in aqueous medium: implications for convenient counter electrodes in DSSC,” *Inorganica Chimica Acta*, vol. 377, no. 1, pp. 170–176, 2011.
- [22] G. Yue, J. Wu, Y. Xiao, J. Lin, and M. Huang, “Low cost poly(3,4-ethylenedioxythiophene):polystyrenesulfonate/carbon black counter electrode for dye-sensitized solar cells,” *Electrochimica Acta*, vol. 67, pp. 113–118, 2012.
- [23] M. Belekoukia, M. S. Ramasamy, S. Yang et al., “Electrochemically exfoliated graphene/PEDOT composite films as efficient Pt-free counter electrode for dye-sensitized solar cells,” *Electrochimica Acta*, vol. 194, pp. 110–115, 2016.
- [24] C. P. Lee, C. A. Lin, T. C. Wei et al., “Economical low-light photovoltaics by using the Pt-free dye-sensitized solar cell with graphene dot/PEDOT:PSS counter electrodes,” *Nano Energy*, vol. 18, pp. 109–117, 2015.
- [25] A. Nikolakopoulou, D. Tasis, L. Sygellou, V. Dracopoulos, C. Galiotis, and P. Lianos, “Study of the thermal reduction of graphene oxide and of its application as electrocatalyst in quasi-solid state dye-sensitized solar cells in combination with PEDOT,” *Electrochimica Acta*, vol. 111, pp. 698–706, 2013.
- [26] H. J. Shin, S. S. Jeon, and S. S. Im, “CNT/PEDOT core/shell nanostructures as a counter electrode for dye-sensitized solar cells,” *Synthetic Metals*, vol. 161, no. 13–14, pp. 1284–1288, 2011.
- [27] J. Y. Lin, W. Y. Wang, and S. W. Chou, “Flexible carbon nanotube/polypropylene composite plate decorated with poly(3,4-ethylenedioxythiophene) as efficient counter electrodes for dye-sensitized solar cells,” *Journal of Power Sources*, vol. 282, pp. 348–357, 2015.
- [28] A. M. M. Santos and W. L. Vasconcelos, “Obtention of nanostructured silica glass by sol-gel process with incorporation of lead compounds,” *Materials Research*, vol. 2, no. 3, pp. 201–204, 1999.
- [29] S. J. V. Gaast and A. J. Vaars, “A method to eliminate the background in X-ray diffraction patterns of oriented clay mineral samples,” *Clay Minerals*, vol. 16, no. 4, pp. 383–393, 1981.
- [30] A. K. Kercher and D. C. Nagle, “Microstructural evolution during charcoal carbonization by X-ray diffraction analysis,” *Carbon*, vol. 41, no. 1, pp. 15–27, 2003.
- [31] T. Jawhari, A. Roid, and J. Casado, “Raman spectroscopic characterization of some commercially available carbon black materials,” *Carbon*, vol. 33, no. 11, pp. 1561–1565, 1995.
- [32] W. Kwon, J. M. Kim, and S. W. Rhee, “Electrocatalytic carbonaceous materials for counter electrodes in dye-sensitized solar cells,” *Journal of Materials Chemistry a*, vol. 1, no. 10, pp. 3202–3215, 2013.
- [33] J. M. Kim and S. W. Rhee, “Electrochemical properties of porous carbon black layer as an electron injector into iodide redox couple,” *Electrochimica Acta*, vol. 83, pp. 264–270, 2012.
- [34] X. Qiao, S. Liao, C. You, and R. Chen, “Phosphorus and nitrogen dual doped and simultaneously reduced graphene oxide with high surface area as efficient metal-free electrocatalyst for oxygen reduction,” *Catalysts*, vol. 5, no. 2, pp. 981–991, 2015.
- [35] L. Geng, S. Wu, Y. Zou et al., “Correlation between the microstructures of graphite oxides and their catalytic behaviors in air oxidation of benzyl alcohol,” *Journal of Colloid and Interface Science*, vol. 421, pp. 71–77, 2014.
- [36] X. Wu, X. Yu, Z. Lin et al., “Nitrogen doped graphitic carbon ribbons from cellulose as non noble metal catalyst for oxygen reduction reaction,” *International Journal of Hydrogen Energy*, vol. 41, no. 32, pp. 14111–14122, 2016.
- [37] C. R. Robbins and M. K. Bahl, “Analysis of hair by electron spectroscopy for chemical analysis,” *Society of Cosmetic Chemists*, vol. 35, pp. 379–390, 1984.
- [38] C. R. Robbins, *Chapter 2 Chemical Composition of Different Hair Types*, Springer-Verlag, Berlin Heidelberg, 2012.
- [39] T. Ujva’ri, A. Kolitsch, A. To’th, M. Mohai, and I. Berto’ti, “XPS characterization of the composition and bonding states of elements in CNx layers prepared by ion beam assisted deposition,” *Diamond and Related Materials*, vol. 11, no. 3, pp. 1149–1152, 2002.
- [40] G. M. Burke, D. E. Wurster, M. J. Berg, P. V. Pedersen, and D. D. Schottelius, “Surface characterization of activated charcoal by X-ray photoelectron spectroscopy (XPS): correlation with phenobarbital adsorption data,” *Pharmaceutical Research*, vol. 9, no. 1, pp. 126–130, 1992.
- [41] National Institute of Standards and Technology (NIST), “XPS database,” 2012, <http://srdata.nist.gov/xps/EnergyTypeValSrch.aspx/>.
- [42] A. I. Popov and D. H. Geske, “Studies on the chemistry of halogen and of polyhalides. XIII. Voltammetry of iodine species in acetonitrile,” *Journal of the American Chemical Society*, vol. 80, no. 6, pp. 1340–1352, 1958.
- [43] Z. Huang, X. Liu, K. Li et al., “Application of carbon materials as counter electrodes of dye-sensitized solar cells,” *Electrochemistry Communications*, vol. 9, no. 4, pp. 596–598, 2007.
- [44] W. Kwon, J. M. Kim, and S. W. Rhee, “A new equivalent circuit model for porous carbon electrodes in charge transfer reaction of iodide/triiodide redox couples,” *Electrochimica Acta*, vol. 68, pp. 110–113, 2012.
- [45] Q. Wang, S. Ito, M. Grätzel et al., “Characteristics of high efficiency dye-sensitized solar cells,” *Journal of Physical Chemistry B*, vol. 110, no. 50, pp. 25210–25221, 2006.
- [46] W. Maiaugree, A. Tangtrakarn, S. Lowpaa, N. Ratchapolthavisinb, and V. Amornkitbamrung, “Facile synthesis of bilayer carbon/Ni<sub>3</sub>S<sub>2</sub> nanowalls for a counter electrode of dye-sensitized solar cell,” *Electrochimica Acta*, vol. 174, pp. 955–962, 2015.
- [47] C. T. Li, C. T. Lee, S. R. Li et al., “Composite films of carbon black nanoparticles and sulfonatedpolythiophene as flexible counter electrodes for dye-sensitized solar cells,” *Journal of Power Sources*, vol. 302, pp. 155–163, 2016.
- [48] R. Katoh and A. Furube, “Electron injection efficiency in dye-sensitized solar cells,” *Journal of Photochemistry and Photobiology C*, vol. 20, no. 1, pp. 1–16, 2014.
- [49] M. Wu and T. Ma, “Platinum-free catalysts as counter electrodes in dye-sensitized solar cells,” *ChemSusChem*, vol. 5, no. 8, pp. 1343–1357, 2012.

## Research Article

# Nanostructured Dielectric Layer for Ultrathin Crystalline Silicon Solar Cells

Yusi Chen,<sup>1</sup> Yangsen Kang,<sup>1</sup> Jieyang Jia,<sup>1</sup> Yijie Huo,<sup>1</sup> Muyu Xue,<sup>2</sup> Zheng Lyu,<sup>1</sup> Dong Liang,<sup>3</sup> Li Zhao,<sup>2</sup> and James S. Harris<sup>1,3,4</sup>

<sup>1</sup>Department of Electrical Engineering, Stanford University, Stanford, CA 94305, USA

<sup>2</sup>Department of Material Science and Engineering, Stanford University, Stanford, CA 94305, USA

<sup>3</sup>Department of Physics, Stanford University, Stanford, CA 94305, USA

<sup>4</sup>Department of Applied Physics, Stanford University, Stanford, CA 94305, USA

Correspondence should be addressed to James S. Harris; [jharris@stanford.edu](mailto:jharris@stanford.edu)

Received 18 November 2016; Revised 5 March 2017; Accepted 22 March 2017; Published 16 May 2017

Academic Editor: Sanjay K. Srivastava

Copyright © 2017 Yusi Chen et al. This is an open access article distributed under the Creative Commons Attribution License, which permits unrestricted use, distribution, and reproduction in any medium, provided the original work is properly cited.

Nanostructures have been widely used in solar cells due to their extraordinary photon management properties. However, due to poor pn junction quality and high surface recombination velocity, typical nanostructured solar cells are not efficient compared with the traditional commercial solar cells. Here, we demonstrate a new approach to design, simulate, and fabricate whole-wafer nanostructures on dielectric layer on thin c-Si for solar cell light trapping. The optical simulation results show that the periodic nanostructure arrays on dielectric materials could suppress the reflection loss over a wide spectral range. In addition, by applying the nanostructured dielectric layer on 40  $\mu\text{m}$  thin c-Si, the reflection loss is suppressed to below 5% over a wide spectra and angular range. Moreover, a c-Si solar cell with 2.9  $\mu\text{m}$  ultrathin absorber layer demonstrates 32% improvement in short circuit current and 44% relative improvement in energy conversion efficiency. Our results suggest that nanostructured dielectric layer has the potential to significantly improve solar cell performance and avoid typical problems of defects and surface recombination for nanostructured solar cells, thus providing a new pathway towards realizing high-efficiency and low-cost c-Si solar cells.

## 1. Introduction

Nanostructures have been widely applied onto solar cells, as they demonstrate promising features for future high-efficiency and low-cost solar cells, such as antireflection and light trapping [1–7]. However, how to effectively realize the potential of nanostructured solar cells still remain a challenge. Compared with traditional commercial counterparts, nanostructured solar cells have lower energy conversion efficiency [8].

On the other hand, ultrathin crystalline silicon (c-Si) solar cells have attracted much interest, as they could potentially achieve high efficiency with low-cost manufacturing [9, 10]. However, due to the intrinsic optical properties of Si as an indirect bandgap material, light trapping using nanostructures is necessary for ultrathin c-Si solar cells to

achieve competitive efficiencies [11–14]. In order to get high efficiency, reducing recombination, especially surface recombination, is critical for ultrathin c-Si solar cells [11, 12]. However, typical nanostructured c-Si solar cells suffer from nanostructured pn junction with poor junction quality and high surface damage due the fabrication process, which result in a low  $V_{oc}$ , despite a relatively high short circuit current  $J_{sc}$  [11–14]. Consequently, the efficiencies of ultrathin c-Si cells are low.

Such problems can be solved in III-V solar cells by nanostructuring the semiconductor window layer with higher energy bandgap instead of nanostructuring the solar cell absorber. The nanostructured window layer could produce antireflection and light-trapping effect, while at the same time maintaining the pn junction quality and blocking the minority carriers from being recombined

at the surface [6]. Similarly, this concept could be applied to c-Si solar cells as well. Particularly, low-cost dielectric materials with large bandgap (above 3 eV) have already been widely used in c-Si solar cells, such as silicon nitride ( $\text{SiN}_x$ ), aluminum oxide ( $\text{Al}_2\text{O}_3$ ), and silicon dioxide ( $\text{SiO}_2$ ) [15]. In addition, these dielectric materials have been reported to provide excellent surface passivation for c-Si solar cells [16, 17]. Therefore, by nanostructuring those dielectric materials, antireflection and light trapping could be achieved without sacrificing the junction quality and surface passivation.

In this work, we present the design of nanostructured dielectric layer (NDL) of  $\text{SiN}_x$  on c-Si thin films for antireflection and light trapping. Simulation and experiment results are also provided and discussed. First, simulation results demonstrate the design robustness and the photon management performance of the NDL over a wide spectra and angular range. Second, NDL is applied onto a  $40\ \mu\text{m}$  c-Si thin film, which suppresses the overall reflection to below 5%. In the final part, the NDL is integrated with a c-Si solar cell with  $2.9\ \mu\text{m}$  ultrathin absorber layer, demonstrating 32% improvement in  $J_{sc}$  and 30 mV enhancement in  $V_{oc}$ .

## 2. Design and Simulation of Nanostructured Dielectric Layer

To study the antireflection effect of nanostructured dielectric layers, optical simulations were performed by finite-difference time-domain (FDTD) method in FDTD Solutions from Lumerical Inc. The simulated nanostructures were an array of nanocones with a 600 nm diameter at the base and 600 nm height, as illustrated in Figure 1. In this simulation, the light source was located above the nanostructures, which is incident normally into the nanostructures. The reflectance of each wavelength was calculated based on the ratio of reflected power and the total incident power. As we are only studying the antireflection effect, the c-Si layer under the NDL is assumed to be infinite. A 10 nm thick  $\text{SiO}_2$  (index of 1.6) passivation layer is also included beneath the  $\text{SiN}_x$  region. When the light comes through the NDL and into the solar cell, reflection occurs at the air/NDL and NDL/c-Si interfaces. The taper-shaped nanocones provide a gradually changing refractive index and eliminate the reflection at the air/NDL interface. On the other hand, although the index mismatch between dielectric and c-Si exists,  $\text{SiN}_x$  with refractive index  $\sim 2$  can suppress the reflectance to below 8%.

Figure 2(a) shows the simulated spectral reflectance of  $\text{SiN}_x$  NDL with refractive index ranging from 1.9 to 2.2. The predicted reflectance is below 10% over a wide portion of the solar spectrum. Another benefit of nanostructures is their wide acceptance angle. Figure 2(b) shows the comparison of simulated spectral averaged reflectance, which is the integrated reflectance weighted by the number of incident photons per wavelength over AM 1.5G, between the  $\text{SiN}_x$  NDL, single-layer antireflective coating (SLARC, 80 nm thick  $\text{SiN}_x$ ), and double-layer antireflective coating (DLARC). In the simulation, the SLARC was set to be single 80 nm thick

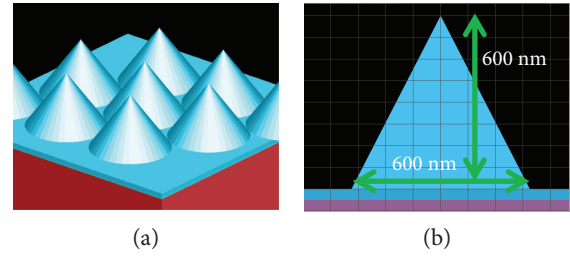


FIGURE 1: Schematics of simulated NDL on top of c-Si, including (a) top view and (b) cross section.

$\text{SiN}_x$  layer, and the DLARC was 140 nm thick  $\text{SiO}_2$  on top of 80 nm thick  $\text{SiN}_x$ . The  $\text{SiN}_x$  NDL with refractive index of 2.1 shows below 10% overall reflectance up to 60-degree incidence, which is better than any single-layer antireflective coating (SLARC) at all angles and outperforms double-layer antireflective coating (DLARC) when the incident angle is greater than 20 degrees. On the other hand, the antireflection performance does not change much for NDL with different refractive index from 1.9 to 2.2, which provides a good design robustness as  $\text{SiN}_x$  might have a variation in refractive index.

## 3. Fabrication of Nanostructured Dielectric Layer

The  $\text{SiN}_x$  NDL was fabricated using a nanosphere lithography method [18] as shown in Figure 3. First, 700 nm of  $\text{SiN}_x$  with 10 nm of  $\text{SiO}_x$  on top was deposited on the c-Si layer using plasma-enhanced chemical vapor deposition (PECVD) at  $350^\circ\text{C}$ . It should be noted that the 10 nm of  $\text{SiO}_x$  is crucial here for the etching uniformity during the nanosphere lithography process. Next, 600 nm silica nanospheres were assembled into monolayer closed-pack film on top of the  $\text{SiO}_x$  via Langmuir–Blodgett (LB) coating method [19]. Later, with the silica nanospheres as etch masks, electron cyclotron resonance plasma etching with  $\text{CF}_4$  and  $\text{O}_2$  gas ( $\text{CF}_4:\text{O}_2=10:1$ ) is used to etch down the  $\text{SiN}_x$  and produce the nanocone arrays. To achieve isotropic etching for the nanostructures, a high chamber pressure of 40 to 50 mTorr was used [20, 21]. Finally, silica nanosphere residues were removed in 50:1 hydrofluoric acid. The shape of nanostructures can be controlled by the ratio between etchant gas and the bias applied during plasma etching. Scanning electron microscope (SEM) images in Figure 4 shows the fabricated nanocone array with different shapes.

## 4. Nanostructured Dielectric Layer on $40\ \mu\text{m}$ c-Si Layer

To evaluate the antireflection and light-trapping effect, a  $\text{SiN}_x$  NDL layer was applied onto a  $40\ \mu\text{m}$  c-Si thin layer that was prepared using the epi-lift-off (ELO) kerfless Si technique. The NDL layer was fabricated using the method described in Section 3 and has the nanodome shape as in Figure 4(a). The reflectance measurements were performed using a standard integrating sphere system, and the characterization results are shown in Figure 5. Figure 5(a) shows the FDTD

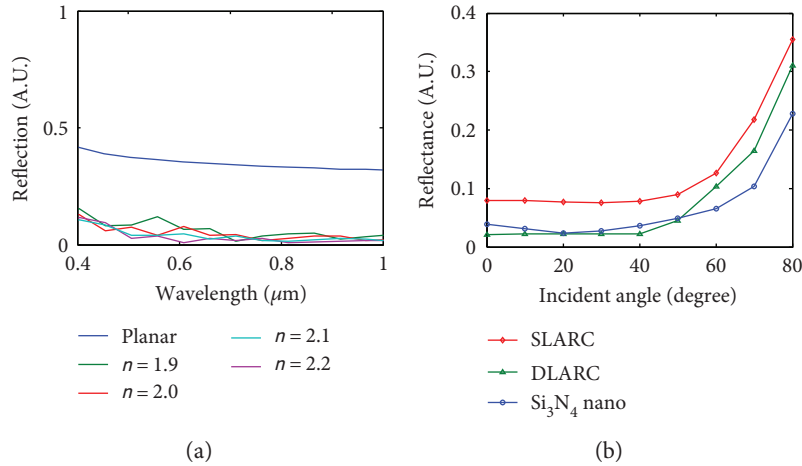


FIGURE 2: Simulated antireflection properties of  $\text{SiN}_x$  NDL. (a) Spectral reflectance of  $\text{SiN}_x$  NDL with refractive index from 1.9 to 2.1 and normal incident light from 300 nm to 900 nm. (b) Simulation result of integrated overall angular reflectance under AM 1.5G of SLARC (red), DLARC (green), and  $\text{SiN}_x$  NDL with reflective index of 2.1 (blue).

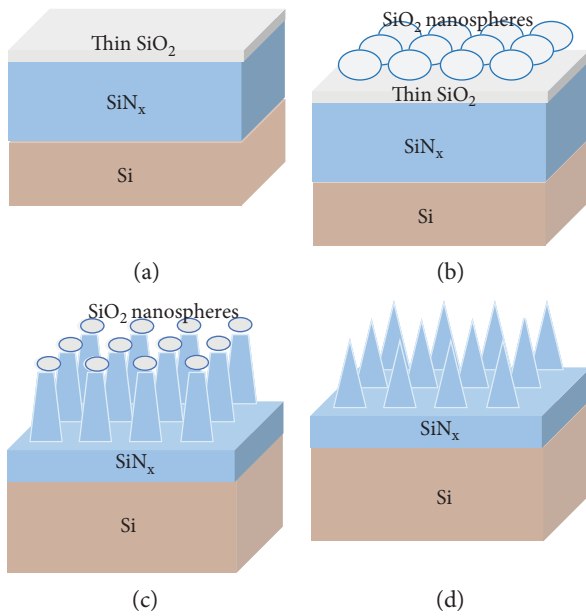


FIGURE 3: Fabrication process of the  $\text{SiN}_x$  NDL. (a) Deposit the  $\text{SiN}_x$  layer on the c-Si, with a thin layer of  $\text{SiO}_x$  ( $\sim 10$  nm) on top using PECVD; (b) assemble a monolayer of silica nanospheres on top using LB coating method; (c) dry etch the  $\text{SiN}_x$  with the silica nanospheres as etching masks; and (d) remove the remaining silica nanospheres and  $\text{SiO}_x$  using wet etch.

simulation and experimental measurement results of reflectance on top of the  $40\ \mu\text{m}$  c-Si thin layer with NDL. The incident light is under normal direction with wavelength ranging from 400 nm to 1000 nm. From Figure 5(a), the reflectance loss has been suppressed to below 5% over a wide portion of the solar spectrum, from 400 nm up to 850 nm. Above 850 nm, the reflectance increases for both simulation and measurement results. This is because the optical absorption in c-Si is weak in this wavelength range [22]. The difference between simulation and experiment results at

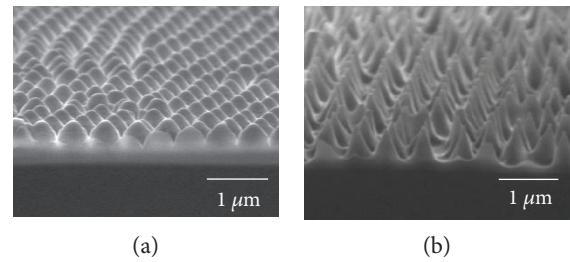


FIGURE 4: The SEM images of the fabricated NDL with (a) nanodome shape and (b) nanocone shape.

900 nm to 1000 nm mainly comes from the different bottom interface configuration. In simulation, the  $40\ \mu\text{m}$  c-Si thin layer is a free-standing thin film and the bottom surface is expose to air with large refractive index mismatch. Therefore, the unabsorbed light gets partially reflected at the bottom surface of c-Si. Such reflected light is reflected again at the front  $\text{SiN}_x$ /c-Si interface and the  $\text{SiN}_x$ /air interface. The  $40\ \mu\text{m}$  thin Si acts like a resonant cavity in this case, generating the resonant peaks between 900 nm to 1000 nm in Figure 5(a). On the other hand, in experiment, the sample was placed on a thick polymer layer ( $\sim 1$  mm) for handling. Therefore, the reflection from the back surface is not strong enough to generate such resonant peaks as in the simulation results. Figure 5(b) shows the measured integrated reflection at different incident angles. The spectral averaged reflection has been suppressed from  $\sim 30\%$  to below 10% up to 60-degree incident angle, demonstrating a wide-angle antireflection effect.

## 5. Nanostructured Dielectric Layer on Ultrathin c-Si Solar Cells

To better assess the performance of NDL, a c-Si solar cell with  $2.9\ \mu\text{m}$  ultrathin absorber was fabricated and integrated with NDL [23]. The fabrication process is shown in Figure 6.

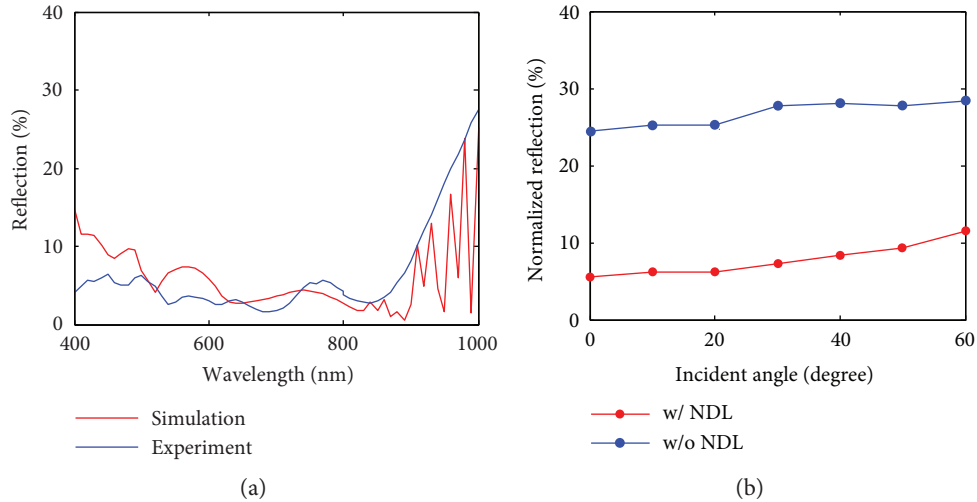


FIGURE 5: (a) The simulation and experiment results of reflection for NDL on  $40\ \mu\text{m}$  thick unpolished c-Si. The incident light is at normal direction with wavelength ranging from 400 nm to 1000 nm. (b) The dependence of spectral averaged reflection (400 nm to 1000 nm, AM 1.5G) on incident angle for fabricated NDL on unpolished  $40\ \mu\text{m}$  c-Si.

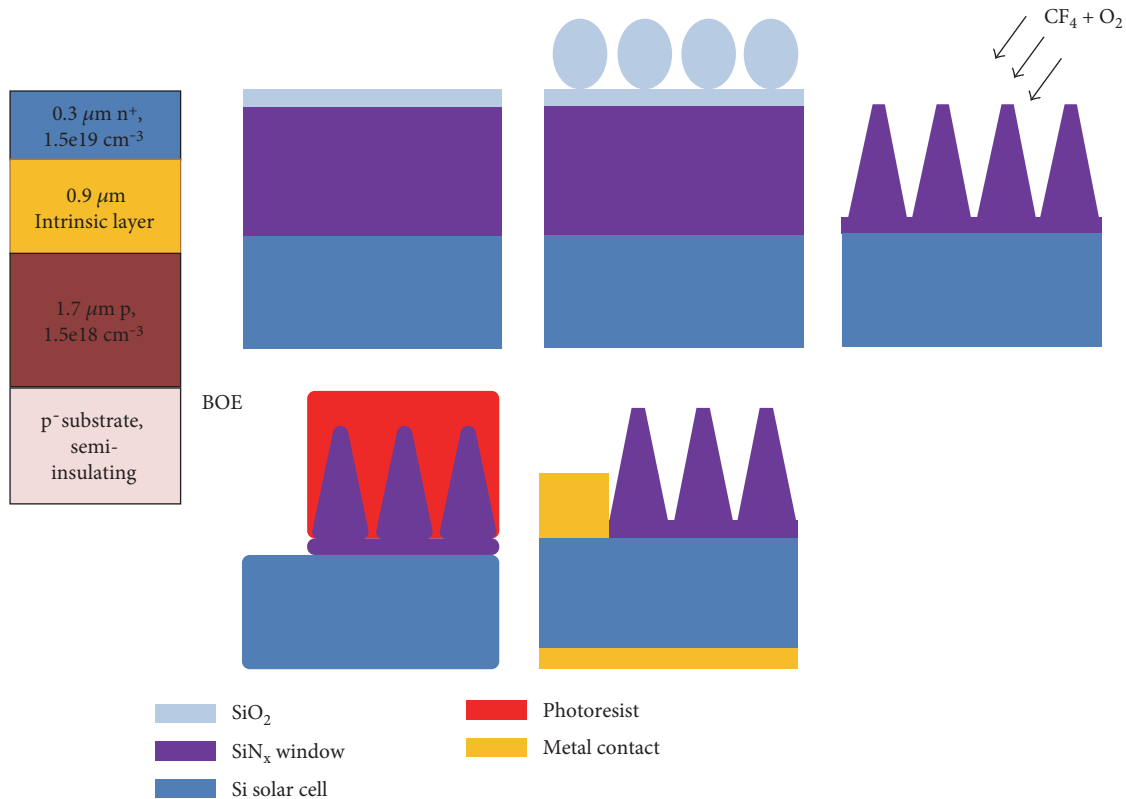


FIGURE 6: Schematics of the fabrication process of ultrathin c-Si solar cells with NDL on top. (a) Deposit a c-Si solar cell with ultrathin absorber on a semi-insulating substrate using RPCVD; (b) deposit the SiN<sub>x</sub> layer and thin SiO<sub>x</sub> layer on c-Si solar cell; (c) assemble a monolayer of silica nanospheres on top; (d) dry etch the SiN<sub>x</sub> layer to form the NDL; (e) use lithography and wet etching of SiN<sub>x</sub> in 6:1 BOE to define the top contact region; and (f) create front and back metal contacts.

For comparison, a control sample was fabricated using similar process but without the NDL on top.

First, the ultrathin c-Si solar cell was deposited on top of a  $\sim 100\ \Omega\cdot\text{cm}$  semi-insulating p<sup>-</sup> CZ substrate using reduced

pressure chemical vapor deposition (RPCVD) in an Applied Materials Epi2 system (Figure 6(a)). The deposition was at 1000°C using dichlorosilane (DCS), and phosphine (PH<sub>3</sub>) and diborane (B<sub>2</sub>H<sub>6</sub>) were used as the dopants. The solar cell

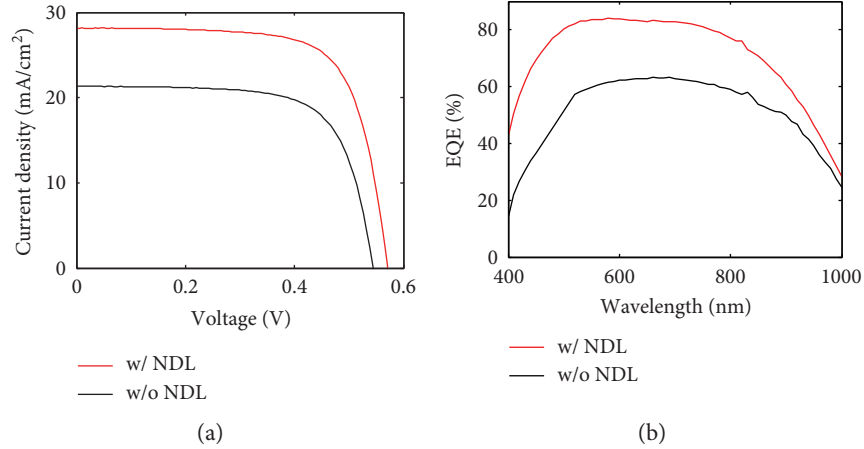


FIGURE 7: (a) J-V characteristics and (b) EQE characteristics of the solar cells with NDL (red) and without NDL (black).

contains three layers: a  $1.7 \mu\text{m}$   $1.5 \times 10^{18} \text{ cm}^{-3}$  boron-doped p-type base layer, a  $0.9 \mu\text{m}$   $10^{16} \text{ cm}^{-3}$  p<sup>-</sup> intrinsic layer, and a  $0.3 \mu\text{m}$   $1.5 \times 10^{19} \text{ cm}^{-3}$  phosphorus-doped n<sup>+</sup>-type emitter layer.

Second, the NDL was fabricated over the whole sample using the method described in Section 3. 700 nm SiN<sub>x</sub> layer was deposited at 350°C using PECVD with 10 nm SiO<sub>x</sub> layer on top (Figure 6(b)). Later, a monolayer of compact silica nanospheres was assembled on top of the SiO<sub>x</sub> thin film using LB method (Figure 6(c)). Next, a combination of CF<sub>4</sub> and O<sub>2</sub> was used to dry etch the SiN<sub>x</sub> with silica nanospheres as etching masks and followed by 50:1 HF dip to remove the remaining SiO<sub>x</sub> and silica (Figure 6(d)). The fabricated NDL has the nanodome shape as in Figure 4(a).

Standard 5X projection system optical lithography was used to define the contact region. The top contact region is formed by removing the PECVD SiN<sub>x</sub> with 6:1 buffered oxide etchant (BOE) (Figure 6(e)) and followed by evaporation of 200 nm thick aluminum for the contact. The front contact region is finally formed by lift-off process in acetone. The back contact was formed by directly aluminum evaporation on the back side of the wafer. The schematic of the fabricated solar cell with NDL is shown in Figure 6(f). To evaluate the performance of the NDL, control samples were also fabricated. The control samples have the similar cell structure and fabrication process, but without NDL on top.

The current density-voltage (J-V) characteristics of the fabricated  $2.9 \mu\text{m}$  cells were performed under AM 1.5G 1-sun illumination ( $1000 \text{ W/cm}^2$ ) at room temperature. A calibrated solar simulator was used to provide the illumination, and the light intensity was monitored using a NREL certificated solar cell. The J-V measurement results of the cells with and without the SiN<sub>x</sub> NDL structures are shown in Figure 7(a), and the key solar cell parameters including short-circuit current density, open-circuit voltage, efficiency, and fill factor are summarized in Table 1.

First of all, the solar cell with NDL achieved a  $J_{sc}$  of  $28.15 \text{ mA/cm}^2$ , which is 32% higher than the  $J_{sc}$  of the control cell without NDL. This is due to the antireflection and light-trapping effect of the NDL. Such effect could also be seen from the results of the external quantum efficiency (EQE)

TABLE 1: Summary of solar cell performance.

	$J_{sc}$ (mA/cm <sup>2</sup> )	$V_{oc}$ (mV)	Fill factor (%)	Efficiency (%)
w/ NDL	28.15	570	71.3	11.44
w/o NDL	21.32	540	69.4	8.08
Relative improvement	25%	6.5%	2.7%	44%

measurement in Figure 7(b), which was conducted using mechanically chopped monochromatic light with the photocurrent measured using a lock-in amplifier. With NDL, the EQE is improved from below 60% to ~80% over a wide range of solar spectrum (500 nm to 800 nm). However, EQE decreases at wavelength above 800 nm due to the weak absorption of c-Si at such wavelength range, and the improvement with NDL is also smaller there. The  $J_{sc}$  and EQE could be further improved by making a stand-alone ultrathin c-Si solar cell with integrated back reflector [24].

Second, the solar cell with NDL also achieved a  $V_{oc}$  of 570 mV, which is 30 mV higher than the  $V_{oc}$  of the control cell without NDL. As  $V_{oc}$  is related to the overall minority carrier recombination inside the solar cells, a higher  $V_{oc}$  indicates that the cell with NDL has a better surface passivation effect while still maintaining the same pn junction quality. Such a surface passivation effect could also be seen from the EQE enhancement at short wavelength (400 nm to 500 nm) in Figure 7(b). With NDL, the EQE is improved from below 20% to above 40% at 400 nm, which is more than 100% relative improvement. For photons at 400 nm wavelength, the absorption depth is only 82 nm [22], which means that most of the photons at 400 nm are absorbed near the surface and are highly affected by the surface recombination. Therefore, such a huge improvement at 400 nm EQE not only exhibits the antireflection effect but also demonstrates the surface passivation effect of NDL.

Overall, the solar cell with NDL has an energy conversion efficiency of 11.44%, which is 44% relatively higher than the efficiency of the control cell without NDL.

## 6. Summary

To summarize, we have demonstrated a systematical analysis of SiN<sub>x</sub> NDL for antireflection and light trapping in ultrathin c-Si solar cells. A complete large-area and whole-wafer process to form NDL on thin c-Si is also presented. Also, the NDL has been successfully integrated onto a 40 μm thin c-Si layer and an ultrathin c-Si solar cell with 2.9 μm absorber. From the simulation and experiment results, a wide-spectrum and wide-angle antireflection and light-trapping effect has been achieved using NDL. Together with the good surface passivation effect of SiN<sub>x</sub>, NDL exhibits great potential to produce high-efficiency and low-cost ultrathin c-Si solar cells.

## Conflicts of Interest

The authors declare that they have no conflicts of interest.

## Acknowledgments

This work was supported by the Bay Area Photovoltaic Consortium (BAPVC) and the Global Climate and Energy Project (GCEP) at Stanford University. The authors acknowledge the Stanford Nanofabrication Facility (SNF) for the use of the processing facilities, Center on Nanostructuring for Efficient Energy Conversion (CNEEC) for the use of characterization facilities, and Soixel Inc. for providing the 40 μm c-Si layer. Yusi Chen would like to acknowledge the funding support from Applied Materials Inc. through the SystemX FMA program. Jieyang Jia would like to acknowledge the funding support from the Stanford Graduate Fellowship (SGF).

## References

- [1] E. Garnett and P. D. Yang, "Light trapping in silicon nanowire solar cells," *Nano Letters*, vol. 10, no. 3, pp. 1082–1087, 2010.
- [2] P. J. Poole, D. Dalacu, J. Lefebvre, and R. L. Williams, "Selective epitaxy of semiconductor nanopillars for nanophotonics," *Nanotechnology*, vol. 21, no. 29, article 295302, 2010.
- [3] D. Liang, Y. Huo, Y. Kang et al., "Optical absorption enhancement in freestanding GaAs thin film nanopillar arrays," *Advanced Energy Materials*, vol. 2, no. 10, pp. 1254–1260, 2012.
- [4] J. Zhu, C. M. Hsu, Z. Yu, S. Fan, and Y. Cui, "Nanodome solar cells with efficient light management and self-cleaning," *Nano Letters*, vol. 10, no. 6, pp. 1979–1984, 2010.
- [5] J. Zhu, Z. Yu, G. F. Burkhard et al., "Optical absorption enhancement in amorphous silicon nanowire and nanodome arrays," *Nano Letters*, vol. 9, no. 1, pp. 279–282, 2009.
- [6] L. Dong, Y. Kang, Y. Huo, Y. Chen, Y. Cui, and J. S. Harris, "High-efficiency nanostructured window GaAs solar cells," *Nano Letters*, vol. 13, no. 10, pp. 4850–4856, 2013.
- [7] F. Khan, S. H. Baek, J. Kaur, I. Fareed, A. Mobin, and J. H. Kim, "Paraboloid structured silicon surface for enhanced light absorption: experimental and simulative investigations," *Nanoscale Research Letters*, vol. 10, no. 1, p. 376, 2015.
- [8] Y. Kang, D. Liang, Y. Huo et al., "Design and fabrication of nano-pyramid GaAs solar cell," in *Proceedings 39th IEEE Photovoltaic Specialists Conference*, pp. 3321–3323, Tampa, Florida, USA, 2013.
- [9] ITRPV Working Group, *International Technology Roadmap for Photovoltaic*, SEMI, 2014, <http://www.itrpv.net/>.
- [10] D. M. Powell, R. Fu, K. Horowitz, P. A. Basore, M. Woodhouse, and T. Buonassisi, "The capital intensity of photovoltaics manufacturing: barrier to scale and opportunity for innovation," *Energy & Environmental Science*, vol. 8, no. 12, pp. 3395–3408, 2015.
- [11] M. S. Branham, W. C. Hsu, S. Yerci et al., "15.7% efficient 10-μm-thick crystalline silicon solar cells using periodic nanostructures," *Advanced Materials*, vol. 27, no. 13, pp. 2182–2188, 2015.
- [12] S. Jeong, M. D. McGehee, and Y. Cui, "All-back-contact ultra-thin silicon nanodome solar cells with 13.7% power conversion efficiency," *Nature Communications*, vol. 4, no. 4, p. 2950, 2013.
- [13] K. J. Yu, J. S. Park, Y. R. Lee et al., "Light trapping in ultrathin monocrystalline silicon solar cells," *Advanced Energy Materials*, vol. 3, no. 11, pp. 1401–1406, 2013.
- [14] J. Oh, H.-C. Yuan, and H. M. Branz, "An 18.2%-efficient black-silicon solar cell achieved through control of carrier recombination in nanostructures," *Nature Nanotechnology*, vol. 7, no. 11, pp. 743–748, 2012.
- [15] L. M. Fraas and L. D. Partain, *Solar Cells and their Applications*, vol. 236, John Wiley & Sons, New York, USA, 2010.
- [16] A. G. Aberle, "Surface passivation of crystalline silicon solar cells: a review," *Progress in Photovoltaics: Research and Applications*, vol. 8, no. 5, pp. 473–487, 2000.
- [17] J. Schmidt, M. Kerr, and A. Cuevas, "Surface passivation of silicon solar cells using plasma-enhanced chemical-vapour-deposited SiN films and thin thermal SiO<sub>2</sub>/plasma SiN stacks," *Semiconductor Science and Technology*, vol. 16, no. 3, p. 164, 2001.
- [18] C. M. Hsu, S. T. Connor, M. X. Tang, and Y. Cui, "Wafer-scale silicon nanopillars and nanodomes by Langmuir–Blodgett assembly and etching," *Applied Physics Letters*, vol. 93, no. 13, pp. 133109–133109-3, 2008.
- [19] B. O. Dabbousi, C. B. Murray, M. F. Rubner, and M. G. Bawendi, "Langmuir–Blodgett manipulation of size-selected CdSe nanocrystallites," *Chemistry of Materials*, vol. 6, no. 2, pp. 216–219, 1994.
- [20] B. E. E. Kastenmeier, P. J. Matsuo, J. J. Beulens, and G. S. Oehrlein, "Chemical dry etching of silicon nitride and silicon dioxide using CF<sub>4</sub>/O<sub>2</sub>/N<sub>2</sub> gas mixtures," *Journal of Vacuum Science & Technology a*, vol. 14, no. 5, pp. 2802–2813, 1996.
- [21] C. Reyes-Betanzo, S. A. Moshkalyov, J. W. Swart, and A. C. S. Ramos, "Silicon nitride etching in high- and low-density plasmas using SF<sub>6</sub>/O<sub>2</sub>/N<sub>2</sub> mixtures," *Journal of Vacuum Science & Technology a: Vacuum, Surfaces, and Films*, vol. 21, no. 2, pp. 461–469, 2003.
- [22] M. A. Green and M. J. Keevers, "Optical properties of intrinsic silicon at 300 K," *Progress in Photovoltaics: Research and Applications*, vol. 3, no. 3, pp. 189–192, 1995.
- [23] Y. Chen, Y. Kang, Y. Huo et al., "Nanostructured dielectric layer—a new approach to design nanostructured solar cells," in *2014 IEEE 40th Photovoltaic Specialist Conference (PVSC)*, Denver, Colorado, USA, 2014.
- [24] K. X. Wang, Z. Yu, V. Liu, Y. Cui, and S. Fan, "Absorption enhancement in ultrathin crystalline silicon solar cells with antireflection and light-trapping nanodome gratings," *Nano Letters*, vol. 12, no. 3, pp. 1616–1619, 2012.

## Research Article

# Organic Dyes Containing Coplanar Dihexyl-Substituted Dithienosilole Groups for Efficient Dye-Sensitised Solar Cells

Ciaran Lyons,<sup>1</sup> Neelima Rathi,<sup>2</sup> Pratibha Dev,<sup>1</sup> Owen Byrne,<sup>1</sup> Praveen K. Surolia,<sup>1</sup> Pathik Maji,<sup>1</sup> J. M. D. MacElroy,<sup>1</sup> Aswani Yella,<sup>3</sup> Michael Grätzel,<sup>3</sup> Edmond Magner,<sup>2</sup> Niall J. English,<sup>1</sup> and K. Ravindranathan Thampi<sup>1</sup>

<sup>1</sup>SFI Strategic Research Cluster in Solar Energy Conversion, UCD School of Chemical and Bioprocess Engineering, University College Dublin, Dublin 4, Ireland

<sup>2</sup>SFI Strategic Research Cluster in Solar Energy Conversion, Department of Chemical Sciences and Bernal Institute, University of Limerick, Limerick, Ireland

<sup>3</sup>Laboratoire de Photonique et Interfaces (LPI), Ecole Polytechnique Fédérale de Lausanne, 1015 Lausanne, Switzerland

Correspondence should be addressed to Edmond Magner; edmond.magner@ul.ie, Niall J. English; niall.english@ucd.ie, and K. Ravindranathan Thampi; ravindranathan.thampi@ucd.ie

Received 20 October 2016; Accepted 20 February 2017; Published 4 May 2017

Academic Editor: Bill Pandit

Copyright © 2017 Ciaran Lyons et al. This is an open access article distributed under the Creative Commons Attribution License, which permits unrestricted use, distribution, and reproduction in any medium, provided the original work is properly cited.

A chromophore containing a coplanar dihexyl-substituted dithienosilole (CL1) synthesised for use in dye-sensitised solar cells displayed an energy conversion efficiency of 6.90% under AM 1.5 sunlight irradiation. The new sensitiser showed a similar fill factor and open-circuit voltage when compared with N719. Impedance measurements showed that, in the dark, the charge-transfer resistance of a cell using CL1 in the intermediate-frequency region was higher compared to N719 (69.8 versus 41.3  $\Omega$ ). Under illumination at AM 1.5G-simulated conditions, the charge-transfer resistances were comparable, indicative of similar recombination rates by the oxidised form of the redox couple. The dye showed instability in ethanol solution, but excellent stability when attached to TiO<sub>2</sub>. Classical molecular dynamics indicated that interactions between ethanol and the dye are likely to reduce the stability of CL1 in solution form. Time-dependent density functional theory studies were performed to ascertain the absorption spectrum of the dye and assess the contribution of various transitions to optical excitation, which showed good agreement with experimental results.

## 1. Introduction

Dye-sensitised solar cells (DSSCs) [1] have the distinct advantage of being responsive to low and diffuse light levels, as well as to the light incident under acute irradiation angles. This renders the technology particularly suitable for indoor situations and other similar applications where the incident light is confined to a select band in the visible spectrum, which may be the characteristic output of a certain light source. There, it is possible to tune the spectral sensitivity of DSSC as the light-harvesting function of the cell is separated from the semiconductor, unlike in inorganic solar cells, and is taken up by a sensitiser. The standard and most studied sensitisers for making DSSC are ruthenium dyes with

a reported maximum efficiency of 11.9% [2]. Although the DSSC is optimal for room interiors and vertical façade positions, its certified solar-to-electric power conversion efficiency (PCE) under standard air mass 1.5 (AM 1.5) reporting conditions (1000 W/m<sup>2</sup> solar light intensity and 298 K) is still a factor of 2 below that of Si solar cells. Much effort has been expended in developing more efficient dyes [3, 4]. However, Ru is expensive, has limited availability, and has an undesirable environmental impact when used in large amounts. A newer and increasingly emerging area of solar research lies in perovskite solar cells. One key challenge for perovskite commercialisation is stability. The light-sensitive material in these devices dissolves in the presence of water and decomposes at high temperature. Scientists must also address

the possibility of lead contamination before these cells can be commercialised at large scale [3].

The development of new organic dyes has been the subject of much interest lately, especially metal-free dyes [5–7]. Organic dyes can be more versatile in their light absorption properties, owing to a larger number of molecular structure variations possible and in principle cheaper for mass scale production. They also possess higher molar extinction coefficients allowing efficient light harvesting using thinner layers when compared to Ru dyes. Porphyrins and phthalocyanines containing inexpensive metal atoms also have attracted considerable attention in the recent years [8, 9]. Recent reports have described a porphyrin-based dye in combination with a Co-complex containing electrolyte, a redox mediator exhibiting higher reduction potentials than that of  $I_3^-$ , which has displayed the highest efficiency to date of 13%, as well as over 14% from a DSSC cophotosensitised with an alkoxy-silyl-anchor dye and a carboxy-anchor organic dye [5–7]. Another reason for developing organic dyes is the industrial and architectural preferences for specific dye colours such as green, bright red, golden, and blue, when conceiving new buildings with integrated photovoltaics and designing newer interior designs. Indeed, industry is even willing to compromise slightly on solar cell efficiency for desired colour characteristics. This confers to organic dye research a rather compelling new impetus and scope.

In general, organic dyes consist of three segments: a donor, a linker, and an acceptor group. Much research has been performed on altering the nature of each of these groups with the aim of tuning the dyes' absorption spectrum in the visible spectral region. Synthetic chemists increasingly turn to molecular structures based on the current understanding of dyes' structure-property relationships. The introduction of long-chain alkyloxy groups in the dye structure is suggested to generally retard the charge recombination process [10]. Donor- $\pi$ -bridge-acceptor (D- $\pi$ -A) sensitizers, endowed with such groups, recently reached open-circuit voltage ( $V_{oc}$ ) values exceeding 0.8 V when used with Co(II/III)tris(bipyridyl) redox electrolytes. However, the energy conversion efficiencies of these dyes remained in the 6.7 to 9.6% range because of their insufficient solar light harvesting, resulting in low photocurrents [10, 11]. The quest for newer dyes is therefore very challenging. In fact, dyes with narrower spectral bands still may find use in DSSC devices destined for indoor applications, where the available spectrum is usually influenced by indoor lighting systems.

Five-membered heterocycles containing silicon have also attracted attention recently, in particular, silole derivatives with a 2,2'-bithiophene group connected through a silicon atom. Si, an abundant tetravalent element like C and widely used in organic synthesis, is thus a natural choice for organic sensitizers. Dithienosilole derivatives have been used in many optoelectronic devices, such as light emitting diodes [12], whilst dithienosilole-based polymers have been used in polymer solar cells [13]. There have been a few reports on the use of these materials in DSSCs, too. Ko et al. described the synthesis of silole-spaced triarylamine derivatives containing combinations of phenyl and methyl groups attached to silicon, with a PCE of 7.50% [14, 15]. Lin et al. reported

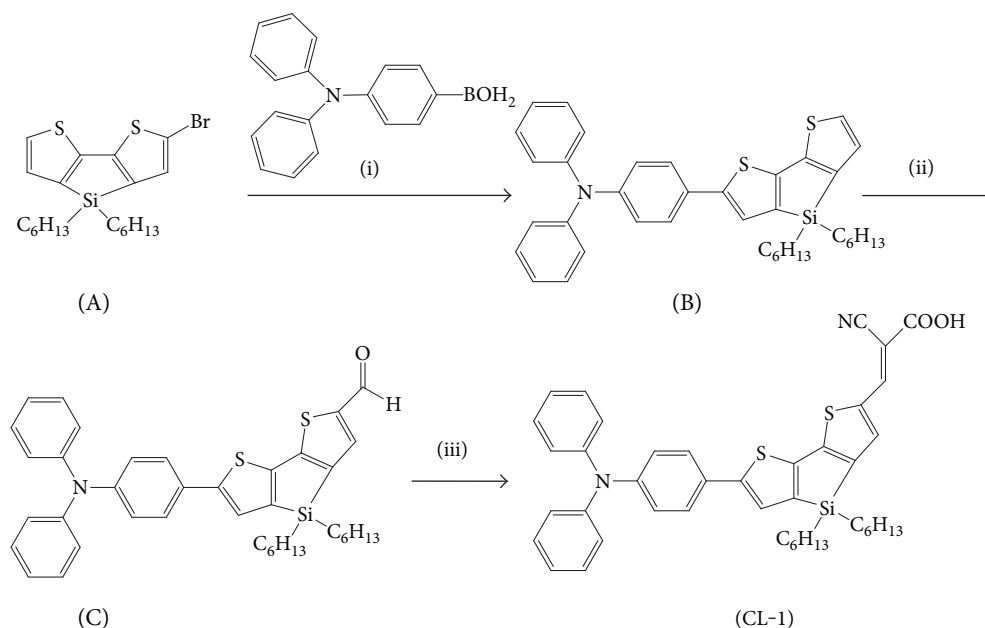
a coplanar diphenyl-substituted dithienosilole dye with an efficiency of 7.60%. The additional O-hexyl donor groups were added to the triphenylamine donor group to provide increased electron donor capabilities [14, 15]. However, these compounds possessed increased conjugation and lowered LUMO (lowest unoccupied molecular orbital) levels. Coplanarity of the  $\pi$ -spacer was obtained by bridging the two thiophene units with a silicon atom, leading to more effective rates of electron transfer. To our knowledge, there have been no reports to date on the effects of adding large alkyl chains to the silicon group.

Here, we report a dithienosilole dye (Scheme 1) containing alkyl chains to help prevent aggregation of the dye sensitizer. The brightly red-coloured dye showed a good power conversion efficiency of 6.90% under 1 sun, in the absence of any additional electron donor groups. Electrochemical impedance spectroscopy (EIS) was used to study the charge-transfer properties of the dye-sensitised solar cell [16–20]. Time-dependent density functional theory (TD-DFT) was used to calculate the absorption spectra and compare it with experimental spectra. On exposure to ethanol for a week in a dye bath, the dye showed a decrease in efficiency to 5.83% and the colour of the dye bath went from the bright fluorescent red to a dull brown. Cell performance and UV-Vis absorption tested over time are shown in Supporting Information available online at <https://doi.org/10.1155/2017/7594869>. However, DSSCs made using this dye and a standard iodide-tri-iodide electrolyte still showed a stable incident photon-to-current efficiency (IPCE) value even after a month. Computational studies using classical molecular dynamics (MD) were performed to provide an insight into solvent effects and investigate hydrogen bonding between the dye and the ethanol medium.

## 2. Experimental Section

**2.1. Materials.** The following materials were used as received: 1-butyl-3-methylimidazolium iodide (BMII, Merck 4.90187.0100) and guanidinium thiocyanate (GuSCN, Merck 8.20613.0250). Ethanol was purchased from Lennox, Dublin. All other chemicals were purchased and used as received from Sigma-Aldrich. Toluene was distilled under sodium benzophenone and stored under nitrogen. Dimethylformamide was dried using barium oxide. Titanium dioxide paste (Ti-Nanoxide D20), electrolyte (Iodolyte AN-50), Surlyn film (Meltonix 1170-60), and fluorine-doped tin oxide glass slides (TCO30-8, ~8 ohm/square) were purchased from Solaronix SA (Aubonne, Switzerland). A second "light scattering" paste of particle size 150–250 nm was purchased from DyeSol Ltd. (WER 2-0).

Three types of  $TiO_2$  pastes were used to make cells, including the commercially purchased samples. The first was a "transparent" type containing 20 nm particles of  $TiO_2$  prepared from Evonik P25 powder using a standard fabrication procedure [21]. Ethyl cellulose (Fluka, #46080) and anhydrous terpineol (Fluka, #46070) were used as received to make a paste. A second paste of particle size 150–250 nm and purchased from DyeSol Ltd. (WER 2-0) was used to form a light scattering layer. Both pastes were screen printed with a



SCHEME 1: Reagents and conditions: (i) 4-(diphenylamino) phenylboronic acid, palladium(II) acetate, cesium carbonate, toluene, reflux, 24 h, (ii)  $\text{POCl}_3$ , DMF,  $90^\circ\text{C}$ , 24 h, and (iii) 2-cyanoacetic acid, piperidine, acetonitrile, reflux, 4 h.

90T mesh to yield electrodes of approximately  $15\ \mu\text{m}$  thickness ( $10\ \mu\text{m}$  transparent layer and a  $5\ \mu\text{m}$  scattering layer). The standard liquid electrolyte used was labelled E1 [22] and was comprised of 0.03 M iodine, 0.1 M guanidinium thiocyanate, 0.5 M 4-*tert*-butylpyridine, and 0.6 M BMII in an acetonitrile : valeronitrile solvent mixture (85 : 15 by volume). The Solaronix paste was used without light scattering layers in certain experiments, where cell efficiencies were not considered the primary objective.

**2.2. Dye Characterisation.** Absorption and emission spectra of the dye were obtained, both in the dissolved form as well as in the chemisorbed state on  $\text{TiO}_2$  surface. For experiments with  $\text{TiO}_2$ , a mixture was prepared using  $100\ \mu\text{l}$  Ti-Nanoxide D20,  $35\ \mu\text{l}$  polyethylene glycol (PEG), and  $100\ \mu\text{l}$  of 1% Tween-80 in water, which were mixed together to obtain a gel. The gel was spread onto an FTO glass slide and left to dry for 30 min after which the electrode was calcined at  $450^\circ\text{C}$  for 30 minutes. The adsorption of CL1 dye was performed by immersing the  $\text{TiO}_2$  electrodes in CL1 (0.57 mM) solution in ethanol overnight (18 h). The electrodes were then rinsed with ethanol and dried in air. Solution-based absorption and emission spectra were recorded on a Varian Cary 300 UV-Visible and a Cary eclipse fluorescence spectrophotometer, respectively, using quartz cuvettes. The absorption spectrum of the anchored dye was obtained on a UV-1800 Shimadzu spectrophotometer.

A Perkin Elmer Spectrum 100 FT-IR spectrometer was used to record ATR-FTIR spectra at a resolution of  $2\ \text{cm}^{-1}$ . The spectra reported represent averages of 100 scans. A CHI800 potentiostat was used for cyclic-voltammetry measurements. Dye-immobilised  $\text{TiO}_2$ , Pt wire, and Ag/AgCl/KCl were used as the working, counter, and reference electrodes, respectively. Solutions were bubbled with  $\text{N}_2$  gas and kept under an  $\text{N}_2$  atmosphere during experiments.

Electrochemical impedance spectroscopy was performed using an impedance analyser (Solartron analytical, 1260) connected to a potentiostat (Solartron Analytical, 1287). EIS spectra were measured under illumination and at applied bias voltage equivalent to the open-circuit voltage ( $V_{oc}$ ) of the device in the dark over the frequency range of 0.1 to  $10^5$  Hz using a 10 mV amplitude AC signal. Impedance spectra were fitted to an equivalent circuit model using ZView software (Scribner Associates Inc.).

$^1\text{H}$  and  $^{13}\text{C}$  NMR spectra were recorded using Bruker 300 and 400 MHz instruments using the residual signals  $\delta = 7.26$  ppm and 77.0 ppm for  $\text{CDCl}_3$  and  $\delta = 2.50$  ppm and 39.4 ppm for  $[\text{D}_6]$ -DMSO.

**2.3. General Synthetic Procedure.** The synthetic procedure for the preparation of compound A has been described previously [23]. The synthesis of B was achieved through Suzuki coupling between the bromo-silole derivative and triphenylamine-boronic acid. Aldehyde addition was performed using Vilsmeier formylation using phosphorus oxychloride to yield C. Claisen condensation between cyano-2-acetic and the aldehyde in the presence of piperidine yielded CL-1 as a purple solid with a yield of 41%.

**2.4. 5-[N,N-Bis(phenylamino)phenyl]-3,3'-dihexylsilylene-2,2'-bithiophene (B).** Compound A (0.59 g, 1.34 mmol), 4-(diphenylamino) phenylboronic acid (0.469 g, 1.61 mmol), palladium(II) acetate (0.030 g, 0.134 mmol), and cesium carbonate (2.638 g, 8.09 mmol) were dissolved in toluene (75 ml). The reaction mixture was refluxed overnight. The organic layer was extracted using  $\text{CH}_2\text{Cl}_2$  and washed with  $\text{H}_2\text{O}$  and then dried over  $\text{Na}_2\text{SO}_4$ . The solvent was removed by rotary evaporation. The crude product obtained was then purified using column chromatography (petroleum ether/ $\text{CH}_2\text{Cl}_2 = 6/1$ ) to yield compound B as a yellow wax

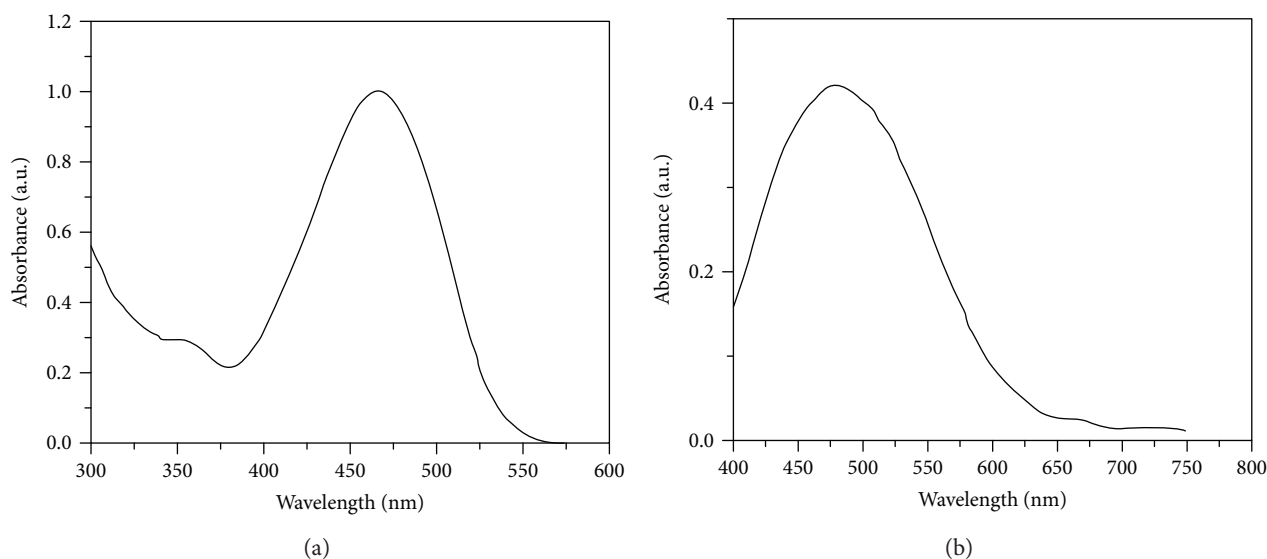


FIGURE 1: Absorption spectrum of CL1 dye showing an absorption band at 468 nm (a) in ethanol (0.057 mM) and (b) adsorbed on a TiO<sub>2</sub> film showing a red shift indicative of interactions between the dye molecule and the semiconductor.

with 61% yield. <sup>1</sup>H NMR (CDCl<sub>3</sub>, 400 MHz): δ ppm 7.46 (2H, *J* = 12 Hz, d), 7.29–6.97 (15H, m), 1.45–1.16 (16H, m), 0.95–0.87 (m, 4H), and 0.87–0.79 (6H, m); <sup>13</sup>C NMR ([D<sub>6</sub>]-DMSO, 100 MHz): δ ppm 149.42, 147.61, 147.51, 146.89, 144.78, 143.12, 141.05, 129.63, 129.27, 129.17, 128.90, 126.38, 124.95, 124.85, 124.39, 124.14, 123.90, 122.98, 122.64, 32.85, 31.42, 24.16, 22.55, 14.07, and 11.91.

2.5. 5-[*N,N*-Bis(phenylamino)phenyl]-5'-formyl-3,3'-hexylsilylene-2,2'-bithiophene (C). Compound B (0.50 g, 0.825 mmol) was dissolved in DMF (50.00 ml). At 0°C, POCl<sub>3</sub> (0.184 ml, 1.956 mmol) was added to this solution and the mixture was stirred at 90°C overnight. The organic layer was extracted using CH<sub>2</sub>Cl<sub>2</sub> and washed with H<sub>2</sub>O and before drying over Na<sub>2</sub>SO<sub>4</sub>. The solvent was removed by rotary evaporation. The crude product was then purified using column chromatography (petroleum ether/CH<sub>2</sub>Cl<sub>2</sub> = 4/1) to yield compound C as an orange wax in 74% yield. <sup>1</sup>H NMR (CDCl<sub>3</sub>, 400 MHz): δ ppm 9.85 (1H, s), 7.69 (1H, s), 7.47 (2H, *J* = 8 Hz, d), 7.30–7.21 (5H, m), 7.14–7.03 (8H, m), 1.44–1.19 (16H, m), 0.99–0.91 (4H, m), and 0.88–0.79 (6H, m); <sup>13</sup>C NMR (CDCl<sub>3</sub>, 100 MHz): δ ppm 181.41, 158.06, 148.15, 147.04, 146.77, 146.29, 145.03, 143.20, 140.68, 138.49, 132.94, 128.34, 126.75, 125.72, 124.00, 123.70, 122.34, 122.31, 119.94, 31.77, 30.34, 23.06, 21.49, 13.02, and 10.70.

2.6. 3-[5-[*N,N*-Bis(phenylamino)phenyl]-3,3'-dihexylsilylene-2,2'-bithiophene-5'-yl]-2-cyanoacrylic Acid (CL-1). At first, compound C (0.05 g, 0.883 mmol), 2-cyanoacetic acid (0.02 g, 0.258 mmol), and a drop of piperidine were dissolved in acetonitrile (10 ml). This mixture was then refluxed for 2.5 h. After removal of the solvent, the crude product was purified using column chromatography (CH<sub>2</sub>Cl<sub>2</sub>/MeOH = 30/1) to yield CL-1 as a purple solid with 41% yield. <sup>1</sup>H NMR (CDCl<sub>3</sub>, 400 MHz): δ ppm 8.05 (1H, s), 7.67 (1H, s), 7.59 (2H, *J* = 12 Hz, d), 7.52 (1H, s), 7.38–7.28

(4H, m), 7.12–6.94 (8H, m), 1.39–1.10 (16H, m), 0.99–0.89 (4H, m), and 0.84–0.73 (6H, m); HRMS (TOF-MS-ESI) *m/z*: 699.2535 [M<sup>+</sup>]; calculated for C<sub>42</sub>H<sub>43</sub>N<sub>2</sub>O<sub>2</sub>S<sub>2</sub>Si [M<sup>+</sup>]: 699.2535.

2.7. Cell Fabrication and Characterisation. DSSCs were manufactured as described previously [24]. Screen printing was used to deposit layers of TiO<sub>2</sub> on a fluorine-doped tin oxide (FTO) conducting transparent glass substrate. In all cases, a nonporous, dense blocking underlayer of TiO<sub>2</sub> was deposited first on the FTO substrate via TiCl<sub>4</sub> treatment [21] in order to reduce charge recombination, prior to screen printing. The TiO<sub>2</sub> paste was then printed on the TiCl<sub>4</sub> treated glass using a Tiflex Ltd., France, screen printer and involved several cycles. After deposition of each layer, the films were kept in an ethanol saturated chamber for 6 min followed by drying at 125°C for 6 min, whilst the final sintering involved gradual heating in an oven at 325°C (5 min), 375°C (5 min), 450°C (15 min), and 500°C (30 min). After sintering, a layer of TiCl<sub>4</sub> was deposited followed by sintering at 500°C for 30 min. The TiO<sub>2</sub> active area was 0.283 cm<sup>2</sup> (6 mm diameter circular spot). The sintered electrodes were placed in a dye bath of N719 (benchmark dye as supplied by Dyesol Ltd., without further purification) dissolved in an acetonitrile : tert-butyl alcohol: THF mixture (vol 4.5 : 4.5 : 1) or Si dye (CL-1) in ethanol at a concentration of 200 μM for 16–20 hours. The counter electrode was prepared with a thin film of Pt catalyst deposited via a drop of H<sub>2</sub>PtCl<sub>6</sub> solution (2 mg Pt content in 1 ml ethanol) and heat treated at 400°C for 15 minutes. The dye-coated TiO<sub>2</sub> electrode and Pt-coated counter electrode were sandwiched together and sealed using a Bynel polymer gasket (50 μm thick). Electrolyte was filled into the space between the two electrodes through a hole in the counter electrode via the vacuum back-filling method. The back hole was then heat sealed with a thin piece (0.1 mm thick) of glass, again with Bynel.

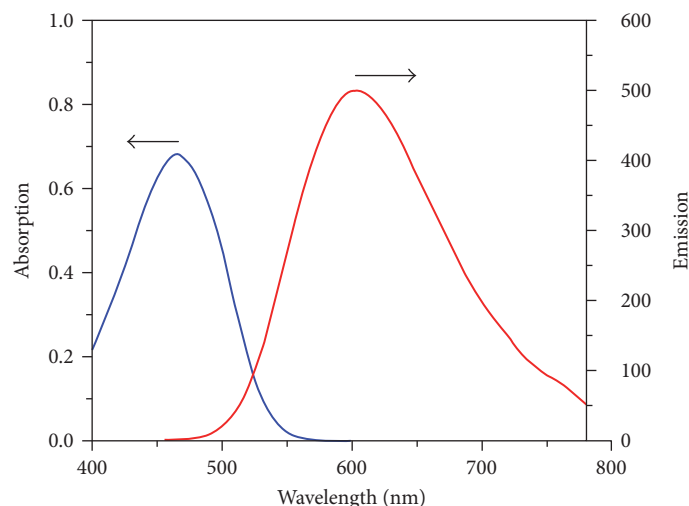


FIGURE 2: Absorption (blue line) and emission (red line) spectra of CL1 in ethanol in arbitrary units showing values of 468 nm and 618 nm, respectively.

**2.8. Electrooptical Characterisation.** Current/voltage ( $I$ - $V$ ) curves, open-circuit voltage ( $V_{oc}$ ), short-circuit current density ( $J_{sc}$ ), and the fill factor (FF) were measured using a Newport 91195A-1000 solar simulator and Newport 69920 Arc Lamp Power Supply. A Newport 81088A air mass filter was placed before the output of the solar simulator to simulate the AM 1.5 spectrum.  $I$ - $V$  measurements were recorded with a GAMRY Instruments potentiostat. Spectral response and incident photon-to-current efficiency (IPCE) measurements were made with using a solar cell spectral response/QE/IPCE measurement system (Solar Cell Scan 100 (SCS100)—Gilden Photonics Ltd.).

**2.9. Time-Dependent Density Functional Theory.** The CL-1 dye was modelled using Discovery Studio Visualizer package (Accelrys, San Diego, CA). Ground-state structural optimisation and excited-state calculations for the isolated dye and the dye in complex with a titania nanoparticle were then performed using Gaussian'09 using the linear response approach [25]. The two hexyl groups in the side chains were replaced by the methyl groups to reduce computational time. This should not affect the results, as these side chains do not participate in the photoexcitation of the dye. The transitions of interest are predominantly charge-transfer in character. Such excitations are better described by conventional hybrid and range-separated  $xc$ -functionals [26, 27]. For the CL1 dye, two approximations were used: (a) Becke-3 Lee-Yang-Parr (B3LYP) hybrid functional [28–30] and (b) Coulomb-attenuated functional, CAM-B3LYP [31]. The standard 6–31G\* basis set, which provides a very good compromise between the accuracy and computational time, was also used. The calculations were performed in two stages:

- (1) Structural optimisation was carried out for the isolated dye using both functionals. After geometry optimisation, TD-DFT was used to obtain the UV/Vis absorption spectra of the dye within the two functionals. The theoretical results were then compared

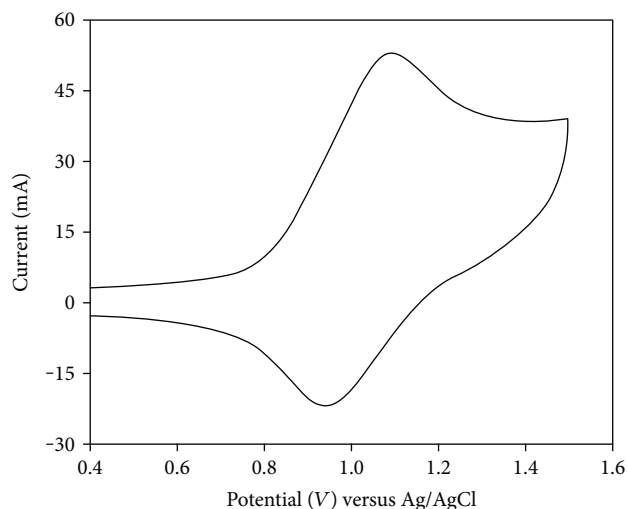


FIGURE 3: Cyclic voltammogram of adsorbed CL1 dye at a scan rate of 100 mV/s, in 0.1 M TBAPF<sub>6</sub> in acetonitrile showing quasi-reversible behaviour; the oxidation and reduction peaks can be attributed to the triphenylamine moieties and cyanoacrylic acid, respectively.

with experimental data to choose the most appropriate functional.

- (2) The ground- and excited-state properties of the dye-titania complex were characterised using the optimal functional. To compare theoretical results with their experimental counterparts, solvent (ethanol) effects were added using the polarisable continuum solvation model (C-PCM) [32] in all calculations. The complex was created by attaching the dye to a 114 atom-containing nanoparticle TiO<sub>2</sub> cut from an anatase (101) surface. This cluster geometry has been employed in earlier studies and demonstrated that the lowest excitation energy was in agreement with the experimental semiconductor bandgap [33–37].

TABLE 1: Experimental data of electrochemical and spectroscopic properties of the CL1 dye.

$\lambda_{\text{abs,max}}$ (nm)	$\epsilon$ ( $\text{M}^{-1} \text{cm}^{-1}$ )	$\lambda_{\text{em,max}}$ (nm)	$E_{\text{ox}}$ (V) (versus NHE)	${}^a E_{0-0}$ (eV)	$E_{\text{LUMO}}$ (V) (versus NHE)
468	30,000	618	1.28	2.29	-1.01

<sup>a</sup>The LUMO (lowest unoccupied molecular orbital) level of the dye was calculated using equation  $E_{\text{ox}} - E_{0-0}$  [47, 48], where  $E_{0-0}$  is the zeroth-zeroth transition energy of the dye estimated from the intersection between the absorption and emission spectra of the dye (Figure 2).

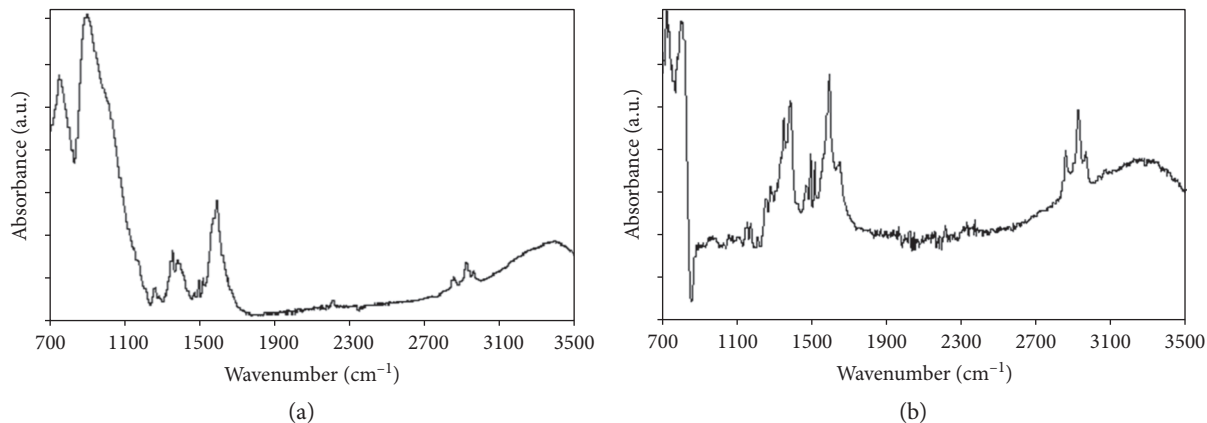


FIGURE 4: (a) ATR-FTIR spectrum of CL1 dye showing sharp phenyl and thiophene ring modes at 1517, 1491, 1375, and 1256  $\text{cm}^{-1}$ , whilst the C-N stretching mode of triarylamine appeared at 1348  $\text{cm}^{-1}$ . (b) ATR-FTIR spectrum of CL1 dye adsorbed on  $\text{TiO}_2$  showing the  $\nu_{\text{asym}}(\text{COO}^-)$  and  $\nu_{\text{sym}}(\text{COO}^-)$  stretching modes of carboxylate linker groups at 1590 and 1382  $\text{cm}^{-1}$ , respectively, whilst the  $\text{C}\equiv\text{N}$  stretch frequency was unchanged at 2209  $\text{cm}^{-1}$ .

Geometrical optimisation of the isolated titania cluster was performed under CAM-B3LYP. The ground-state structure of the nanoparticle was then used to create the CL1 dye-titania complex. Once the complexed structure was also optimised, TD-DFT calculations were performed to obtain the UV/Vis absorption spectra for the dye-titania complex.

**2.10. Molecular Dynamics.** Classical MD simulations were used to investigate and quantify hydrogen-bond lifetimes with ethanol as a solvent. Given the small-molecule nature of the dye, the MMFF94 force field was utilized [38]. All MD calculations were performed using the MOE software package [39]. Nonbonded interactions were treated using a twin-range method [40], with short and long cut-off radii of 10 and 12 Å, respectively, with reaction field electrostatics [41] with a cut-off radius of 15 Å. The dielectric constant was set at the experimental value of 24.3 [42]. Following gas-phase geometry optimisation, the dye was placed in the centre of a rectangular periodic box surrounded by 845 ethanol molecules under periodic boundary conditions (PBC) [43], relaxed via MD in the liquid state at 298 K and 1 atm. Prior to MD under PBC, the heavy atoms in the simulation box were fixed and the system was relaxed by energy minimization. This was followed by “heating” of the system to 300 K in 25 K increments by MD in stages of 10 ps duration in the NVT ensemble, using velocity assignments from the Maxwell-Boltzmann distribution at the start of each step. A production simulation was then carried out in the NPT ensemble for 100 ps, and bond lengths were constrained with a relative tolerance of  $10^{-8}$  [43]. A time step of 1 fs was used.

The period of the thermal and barostat reservoirs [43] was set to 1 and 5 ps, to allow for relatively weak coupling.

### 3. Results and Discussion

**3.1. Absorption and Emission Spectra.** The absorption spectrum of the CL1 dye in ethanol (Figure 1) showed a broad absorption band at 468 nm with a molar extinction coefficient ( $\epsilon$ ) of  $30 \times 10^3 \text{ M}^{-1} \text{ cm}^{-1}$ , which arises from  $\pi - \pi^*$  charge-transfer transition [15, 44, 45]. The absorption spectra of adsorbed dyes on  $\text{TiO}_2$  displayed a slight red shift in the absorption bands, indicative of interactions between the dye molecule and the semiconductor. The dye in solution exhibits considerable emission characteristics, when excited with light of suitable wavelengths. The fluorescence spectrum of the CL1 dye in ethanol shows an emission peak centred at 618 nm upon excitation at 468 nm. The absorption spectrum of CL1 dye in ethanol, shown in Figure 1(a), is presented together with its fluorescence spectrum in Figure 2, which shows a stoke shift of 150 nm.

**3.2. Cyclic Voltammetry.** Cyclic voltammetry was used to measure the ground-state oxidation potential ( $E_{\text{ox}}$ ) of the dye. The cyclic voltammogram (Figure 3) of the dye showed quasi-reversible behaviour; the oxidation and reduction peaks can be attributed to the triphenylamine moieties and cyanoacrylic acid, respectively [15]. The value of  $E_{\text{ox}}$  of the dye, 1.28 V (versus NHE), is more positive (Table 1) than the redox potential (0.4 V versus NHE) [46] of the iodide/triiodide couple. Thus, the oxidised dye can be regenerated by  $\text{I}^-$  in the electrolyte enabling efficient charge separation. The LUMO energy level of the dye, -1.01 V

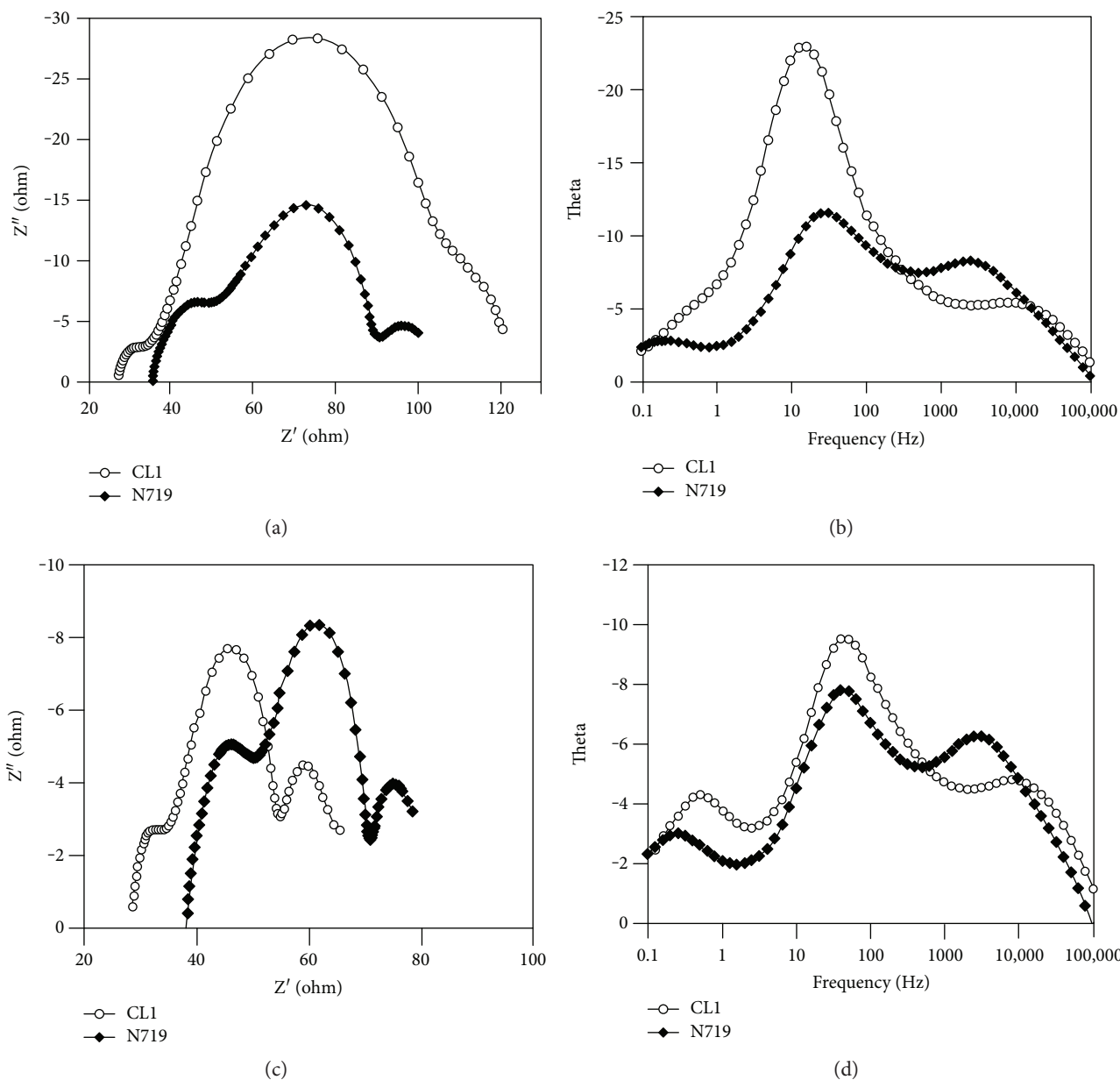


FIGURE 5: Nyquist ((a) and (c)) and Bode phase ((b) and (d)) plots of N719 and CL1 dye sensitised DSSCs in the dark ((a) and (b)) at  $-0.67$  V and under 1 sun illumination ((c) and (d)) at open-circuit voltages.

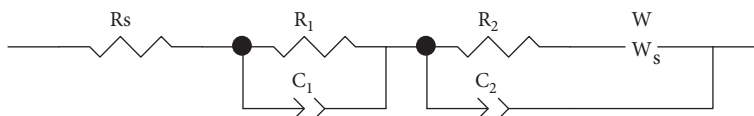


FIGURE 6: Equivalent circuit used to fit EIS data.

(versus NHE), is more negative than the conduction band edge ( $-0.5$  V versus NHE) [46] of  $\text{TiO}_2$  (Table 1), thus providing sufficient driving force to inject an electron from the excited dye to the conduction band of  $\text{TiO}_2$ .

**3.3. ATR-FTIR Spectra.** ATR-FTIR spectra of the dye (Figure 4(a)) showed sharp phenyl and thiophene ring

modes [42, 49, 50] at  $1517$ ,  $1491$ ,  $1375$ , and  $1256$   $\text{cm}^{-1}$ , whilst the C-N stretching mode of triarylamine appeared at  $1348$   $\text{cm}^{-1}$ . Stretching modes assigned to  $\nu$  (C=O),  $\nu$  (Si-C), and  $\nu$  (C-H) stretch were observed at  $1588$ ,  $886$ , and  $2957$   $\text{cm}^{-1}$ , respectively. The ATR-FTIR spectrum (Figure 4(b)) of adsorbed CL1 dye shows the  $\nu_{\text{asym}}(\text{COO}^-)$  and  $\nu_{\text{sym}}(\text{COO}^-)$  stretching modes of carboxylate linker

TABLE 2: Electronic device parameters obtained by fitting the EIS data to the equivalent circuit model (Figure 6).

DSC	$R_s$ ( $\Omega$ )	$R_1$ ( $\Omega$ )	$R_2$ ( $\Omega$ )	$\omega_{\max}$ (Hz)
AM 1.5 sunlight at an intensity of 1 sun (1000 W/m <sup>2</sup> )				
CL1	28.7	6.8	19.7	31.6
N719	38.1	10.7	22.6	39.8
In dark				
CL1	27.4	8.0	69.8	15.8
N719	35.7	12.9	41.3	19.9

groups at 1590 and 1382 cm<sup>-1</sup>, respectively [42, 49, 51]. The C≡N stretch frequency was unchanged at 2209 cm<sup>-1</sup>. Possible binding modes between the carboxylate group and TiO<sub>2</sub> can be either bidentate bridging or chelation [52]. As the chelation mode is known to be unstable [53], the bridging bidentate mode is more likely to occur.

**3.4. Impedance Analysis.** The electrochemical impedance spectra (Figure 5) were fitted to an equivalent circuit model [54–56], containing a constant phase element (CPE) and resistance ( $R$ ) (Figure 6).  $R_s$  is the resistance at the FTO/TiO<sub>2</sub> interface and  $R_1$  and  $C_1$  are the charge-transfer resistance and capacitance at the electrolyte/Pt-FTO interface. Variations in  $R_s$  arise from the electrical contacts and wiring of the device [57, 58].  $R_2$  and  $C_2$  are the charge recombination resistance and capacitance at the TiO<sub>2</sub>/dye/electrolyte interface. The parameters obtained upon fitting the spectra to the equivalent circuit (Figure 6) are shown in Table 2.

The impedance spectra of N719 and the CL1-DSSC measured at  $V_{oc}$  under illumination and in the dark at an applied bias voltage equivalent to  $V_{oc}$  of the cell are shown in Figure 6. Three semi-circles were observed in the Nyquist plots over the frequency range of 0.1–10<sup>5</sup> Hz. The smaller semicircle in the high-frequency region is associated with charge transfer at the electrolyte/Pt-FTO interface; the larger semicircle in the middle-frequency region, to the electron transport and recombination mechanism at the TiO<sub>2</sub>/dye/electrolyte interface, whilst the low-frequency region semicircle may be attributed to diffusion of  $I_3^-$  in the electrolyte. The impedance values of the TiO<sub>2</sub>/dye/electrolyte interface, represented by the semicircles at the intermediate-frequency region in the Nyquist plots, are much smaller under illumination than in the dark. Under illumination, and subject to solubility conditions [59],  $I_3^-$  is formed at the TiO<sub>2</sub>/electrolyte interface by dye regeneration, whilst in the dark,  $I_3^-$  is produced at the counter electrode. This indicates that recombination of CB electrons is accelerated under illumination hence decreasing the electron lifetime in the TiO<sub>2</sub> film. In the dark, the charge-transfer resistance of CL1 DSC (69.8  $\Omega$ ), in the intermediate frequency region, was higher compared to N719 (41.3  $\Omega$ ); under illumination, the charge-transfer resistances were similar (6.8 and 10.7  $\Omega$ , for CL1 and N719, respectively), indicative of similar recombination rates for both dyes.

EIS Bode phase plots also exhibited two characteristic peaks under 1 sun and in the dark; the peak at higher

TABLE 3: Photovoltaic parameters of DSSC cells fabricated using CL-1 and N719 dyes recorded under simulated AM 1.5 sunlight at an intensity of 1 sun (1000 W/m<sup>2</sup>).

Dye	$V_{oc}$ (V)	$J_{sc}$ (mA/cm <sup>2</sup> )	FF	$\eta$ (%)
Si dye	0.742	14.4	65	6.90
N719	0.745	17.4	62	8.05

frequency can be attributed to charge transfer at the counter electrode, whilst the peak in the middle-frequency region is associated with electron transfer at the TiO<sub>2</sub>/dye/electrolyte interface. The characteristic middle-frequency peak of the Bode plot can be used to provide a measure of the charge recombination rate [60]. For simple circuits, the reciprocal of this frequency peak is a direct measure of the electron lifetime in TiO<sub>2</sub>; however, the relationship is more complex for the Randles circuit described in Figure 6. Under illumination, the midfrequency peak of the CL1-based DSC (Figure 5(d)) is slightly shifted to higher frequency compared to that of the N719 DSC, indicative of a shorter electron lifetime. This suggests a slightly lower rate of electron injection and lower charge collection efficiency for the CL1-based cell compared to the N719 cell, hence leading to a lower overall value of  $J_{sc}$ .

**3.5. Cell Efficiency Analysis.** A PCE of 6.90% was achieved for the CL1-containing DSSC. The fill factor and open-circuit voltages ( $V_{oc}$ ) were similar to those of the N719 dye (cf. Table 3). The N719 dye achieved an efficiency of 8.05%, which is due to a higher cell current of 17.4 mA/cm<sup>2</sup> compared to the CL1 value of 14.4 mA/cm<sup>2</sup>. The difference in cell current can be rationalised in terms of the spectral response of each dye, as exhibited in the IPCE spectra in Figure 7. The N719 dye displayed an increased absorbance over the spectral region (500–750 nm), resulting in an increase in the overall photocurrent yield. Note that the Si dye has a higher absorbance than N719 in the 400–470 nm region, which may be advantageous depending on the desired DSSC application and lighting conditions, for example, under indoor lighting conditions. It is equally useful for tandem cell configurations, where the light management between the top and bottom cell need to be optimised for obtaining devices with maximum open-circuit voltage and photo-current density.

The possibility of CL1 showing considerable molecular aggregation on the surface of TiO<sub>2</sub> cannot be discounted. In fact, the dye-sensitised TiO<sub>2</sub> electrode surface shows a strong and attractive red colour, suggesting the possibility of molecular aggregation in a qualitative manner. However, with the limited architectural details available on the packing of the new dye in an adsorbed state over TiO<sub>2</sub> at this stage, no conclusive evidence is available to determine the magnitude of molecular aggregation and its dependence on the TiO<sub>2</sub>-dyeing process itself. Whether a neat monolayer could be obtained on TiO<sub>2</sub> surface without any molecular aggregation is also not clear as of now.

**3.6. Comparison of CL-1 with Other Silicon-Based Dyes.** Lin et al. synthesised a series of dithienosilole dyes (TPCADTS

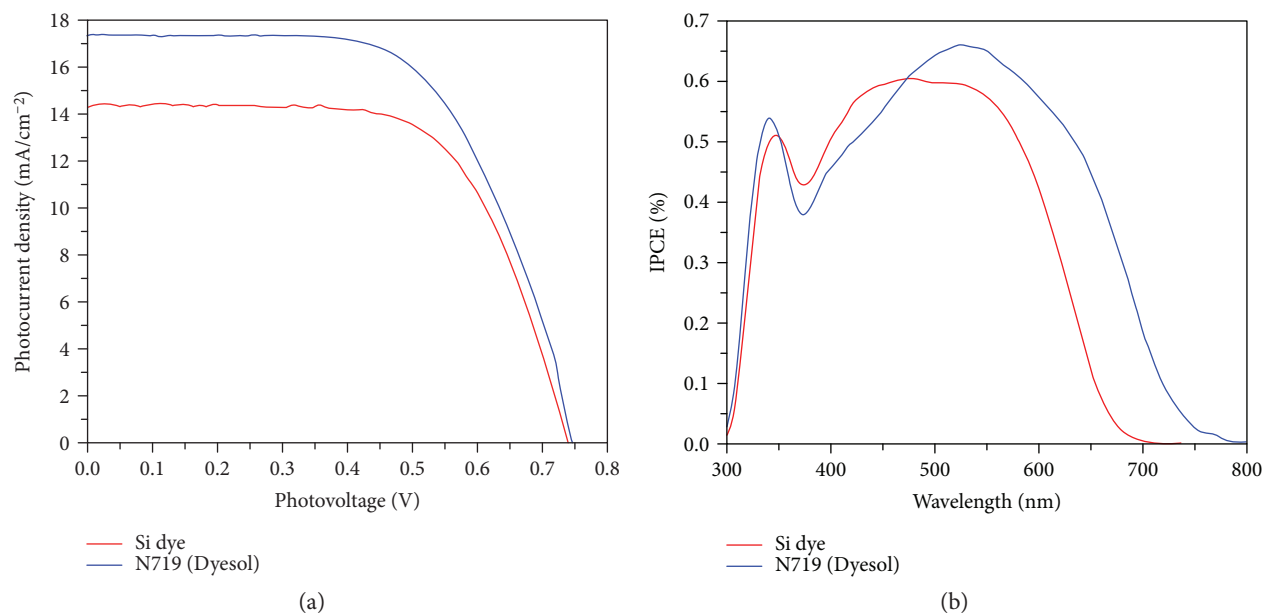


FIGURE 7: (a)  $J$ - $V$  characteristics of N719 and Si dye (CL-1)-sensitized DSSC under standard AM 1.5 testing conditions. Si dye showed a  $V_{oc}$ ,  $J_{sc}$ , FF, and  $\eta$  (%) of 0.742, 14.4, 65, and 6.90, respectively. N719 showed a  $V_{oc}$ ,  $J_{sc}$ , FF, and  $\eta$  (%) of 0.745, 17.4, 62, and 8.05, respectively. (b) IPCE spectra of these cells displayed an increased absorbance over the spectral region (500–750 nm) for N719, but a relatively lower absorbance in the 400–470 nm region compared with Si dye.

and TP6CADTS), which are structurally similar to CL-1 with comparable PCE values [15]. The structures are shown in Figure 8. TPCADTS contained diphenyl-substituted dithienosilole and showed a very similar efficiency of 6.65%. When extra electron donors were added by addition of O-hexyl groups, the efficiency increased to 7.60%. When comparing the more similar TPCADTS with CL-1, it is evident where the improvements lie. The largest improvement lay in the value of  $J_{sc}$  for CL-1 which increased from 12.7 to 14.4 mA/cm<sup>2</sup> on addition of the dihexyl-substituted dithienosilole core. The values obtained for  $V_{oc}$  remained very similar. It has been reported that on addition of alkyl chains,  $V_{oc}$  can increase; but, both the diphenyl and dihexyl cores had similar effects on the cell performance.

Ko et al. synthesised a series of silole-spaced triarylamine derivatives with an efficiency ranging from 6.73% to 7.50% [14]. These dyes also had similar structural features to CL-1. The one major difference which leads to the increase in efficiency in comparison to the CL-1 was that the added bulky electron donation was present in the form of a 3-5'-N,N-bis (9,9 dimethylfluorene-2-yl)-phenyl unit (DTS). This dye was named 7b. Diphenyl- rather than dihexyl-substituted dithienosilole was used, and, when combined with the DTS electron-donating group, it had a significantly greater efficiency of 7.50%. Surprisingly enough, the  $J_{sc}$  value decreased to 13.9 mA/cm<sup>2</sup> compared to 14.4 mA/cm<sup>2</sup> for CL-1. No significant difference was observed in the  $V_{oc}$ . The increased efficiency of 7b likely arises from the superior FF which increased by 9% compared with CL-1. When a dimethyl group (7a) was used instead of a diphenyl (7b), the efficiency value decreased to 6.73% which is lower than that of CL1. This suggests that lower aggregation levels were found with CL-1.

### 3.7. Molecular Modelling

**3.7.1. Hydrogen-Bonding Dynamics with Ethanol.** From the NPT production simulations of classical MD, the persistence times of hydrogen bonding events from hydrogen atoms in ethanol to the carboxylic acid's oxygen atom in the dye were measured. It was found that the hydrogen bonds were short lived and transient, occurring some 4-5% of the time overall on subpicosecond timescales; the average persistence time, between breakage and possible reformation, was  $0.072 \pm 0.023$  ps. As ethanol molecules underwent self-diffusion in the solvation layer of the dye, and rotational motion therein, the identities of the donors to the carboxylic group oxygen atom change. This underlines the key role of the interactions of the dye with ethanol and also on dye-solvent hydrogen bonding. These frequent dye-solvent hydrogen-bond rearrangements serve to rationalise the potential chemical transformation observed experimentally when placed in ethanol for several days or more.

**3.7.2. Spectra of Isolated Systems.** Turning to the use of TD-DFT to determine absorption spectra and the underlying transitions, the UV/Vis absorption spectra are provided in Figure 9 for the isolated dye (using the continuum solvation model for ethanol, as discussed earlier).

The experimental UV/Vis absorption spectrum has a maximum absorbance ( $\lambda_{max}$ ) at 468.0 nm. Figure 9 shows the theoretical UV/Vis absorption spectra of the isolated dye as calculated within the B3LYP and the CAM-B3LYP approximations. Using B3LYP, a charge-transfer excitation energy of 618.4 nm was obtained. On the other hand, the CAM-B3LYP calculation yielded a more accurate result of

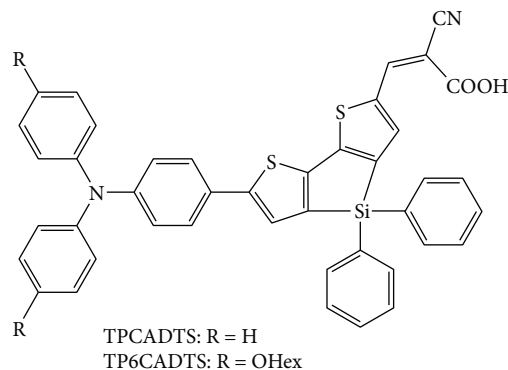
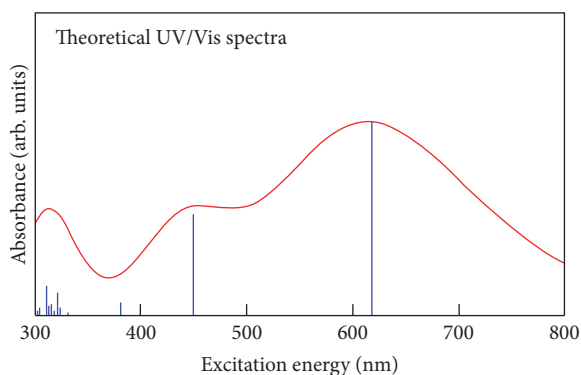
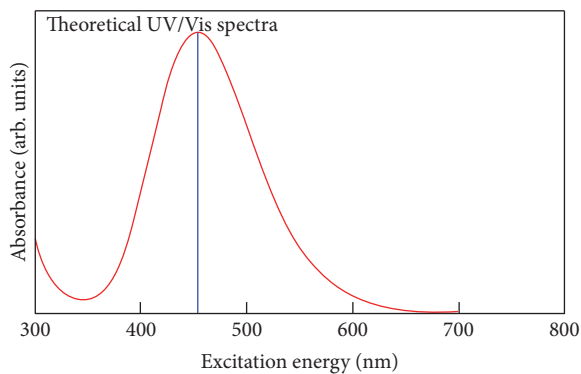


FIGURE 8: Molecular structures of TPCADTS and TP6CADTS.



(a) B3LYP



(b) CAM-B3LYP

FIGURE 9: Theoretical UV/Vis spectra of the CL1-dye calculated within the B3LYP approximations to  $xc$ -functional showing a charge-transfer excitation energy of 618.4 nm (a) and CAM-B3LYP approximations showing a more accurate result of 453.6 nm (b).

453.6 nm. Table 4 summarises these results, providing the values of  $\lambda_{\max}^{\text{Th}}$ , the positions of HOMO (H), LUMO (L), and the HL gaps,  $\Delta_{\text{HL}} = E_{\text{LUMO}} - E_{\text{HOMO}}$  for the dye. It also provides the values of valence band maximum (VBM), conduction band minimum (CBM), and the orbital energy bandgap ( $E_g$ ) for the nanoparticle.

Table 5 provides further details for the transition corresponding to  $\lambda_{\max}^{\text{Th}}$ . The B3LYP results displayed a large error in the excitation energy; therefore, we will focus mainly on CAM-B3LYP results. For CAM-B3LYP, the

TABLE 4: Relevant calculation details for the CL1-dye: wavelength at maximum absorbance ( $\lambda_{\max}^{\text{Th}}$ ) and HOMO (H), LUMO (L) positions and H-L gap ( $\Delta_{\text{HL}} = E_{\text{LUMO}} - E_{\text{HOMO}}$ ). For titania, we have reported the lowest transition valence band maximum (VBM) and the conduction band minimum (CBM) as well as the orbital-energy bandgap ( $E_g$ ).

System	Approx.	$\lambda_{\max}^{\text{Th}}$ eV (nm)	H (eV)	L (eV)	$\Delta_{\text{HL}}$ (eV)
CL1	B3LYP	2.0 (618.4)	-5.0	-2.8	2.3
	CAM-B3LYP	2.7 (453.6)	-6.2	-1.7	4.6
System	Approx.	1st trans. eV (nm)	VBM (eV)	CBM (eV)	$E_g$ (eV)
TiO <sub>2</sub>	B3LYP	3.8 (326.3)	-7.5	-3.0	4.5
	CAM-B3LYP	4.4 (279.9)	-9.2	-1.7	7.6

TABLE 5: Transition corresponding to  $\lambda_{\max}^{\text{Th}}$  for the CL1 dye within B3LYP and CAM-B3LYP: T.E.: transition energy ( $=\lambda_{\max}^{\text{Th}}$ ) in eV; O.S.: oscillator strength; and Coeff.: the magnitude of the configuration interaction singles coefficients. The most prominent transitions (indicated by the magnitude of the configuration interaction singles coefficients) are highlighted in bold.

Approx.	T.E. (O.S.) (eV)	Involved orbitals (Coeff.)
(1) B3LYP	2.0 (1.17)	<b>H <math>\rightarrow</math> L (0.71)</b>
(2) CAM-B3LYP	2.7 (1.65)	<b>H <math>\rightarrow</math> L (0.57)</b> , H-1 $\rightarrow$ L (0.37)
		H $\rightarrow$ L + 1 (0.14)

transition upon photoexcitation involves several promotions between the occupied and empty orbital pairs. However, the most prominent promotion (indicated by the magnitude of the configuration interaction singles coefficients) corresponds to the one from the highest occupied molecular orbital (HOMO) to the lowest unoccupied molecular orbitals (LUMO).

Figure 10 shows the isosurface plots (isovalue =  $0.2e/a.u.^3$ ) of the various MOs involved in the photoexcitation. The results show that the HOMO of the dye is delocalised over the entire molecule, with somewhat more localisation on the donor group compared to the acceptor group. In contrast, the LUMO of the dye is predominantly localised on the acceptor and the linker/spacer groups. In turn, this implies that there will be sufficient charge separation upon excitation, thereby, reducing the rate of charge recombination.

**3.7.3. Absorption Spectra of the CL1-TiO<sub>2</sub> Complex.** The excited-state properties of the dye-titania complex were modelled using the CAM-B3LYP approximation. CAM-B3LYP was utilised as it outperforms B3LYP in its description of the excited-state properties of the dye molecule, which is the photoactive subsystem in the complex; this superior performance of CAM-B3LYP was shown in the previous discussion of the isolated dye (cf. Tables 4 and 5 and Figures 10 and 11). To create a computer model of the dye-titania complex, the dye molecule was chemisorbed in silico onto the nanoparticle. This was accomplished by the removal of the hydrogen atom from the carboxylic acid anchor and

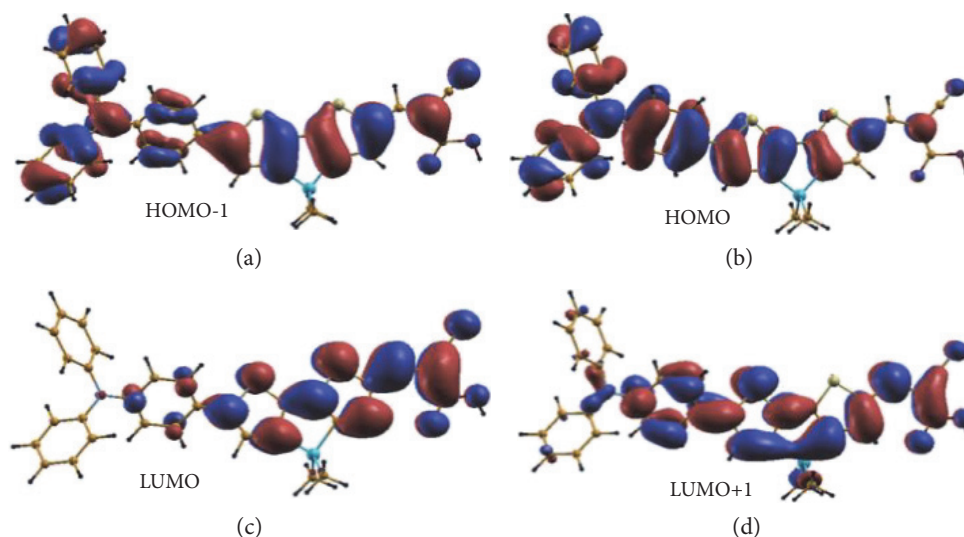


FIGURE 10: Isosurface plots (isovalue =  $0.2e/a.u.^3$ ) for the molecular orbitals involved in the photoexcitation of the CL1-dye. The orbitals were calculated within CAM-B3LYP.

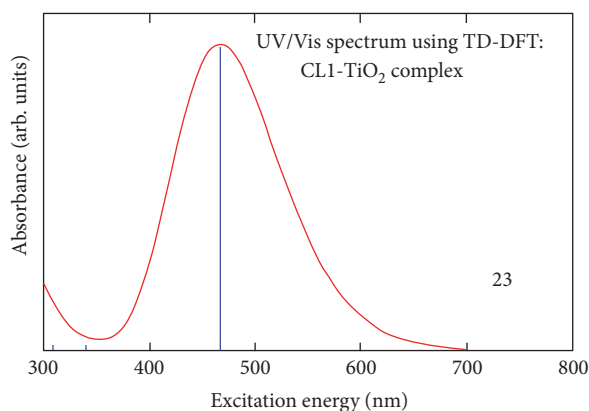


FIGURE 11: UV/Vis spectrum using TD-DFT of CL1-TiO<sub>2</sub> complex calculated within the CAM-B3LYP approximation, showing individual transitions as impulses with maximum absorbance values of 436.0 nm and 467.4 nm.

binding the two carboxylate oxygen atoms with two fivefold coordinated titanium atoms on the surface of the titania nanoparticle. The hydrogen atom removed was transferred to an undercoordinated oxygen atom on the titania surface to maintain the neutrality of the system, which was essential for the TD-DFT calculations. The resulting structure was relaxed within CAM-B3LYP. This optimised structure was then used to study the excited-state properties of the complex using TD-DFT.

Figure 11 shows the UV/Vis spectra for the complex as calculated using TD-DFT. The experimental and calculated values of the energy for maximum absorbance are in very good agreement at about 436.0 nm (2.8 eV) and 467.4 nm (2.7 eV), respectively.

Details of the most important transition corresponding to  $\lambda_{\max}^{\text{Th}}$  and the involved orbital pairs are provided in Table 6. Figure 12 shows the molecular orbitals of the complex involved in the transition (HOMO-1 orbital is not

TABLE 6: Details of the most important transition ( $=\lambda_{\max}^{\text{Th}}$ ) for the dye-titania complex. The calculations were done within the CAM-B3LYP approximation. Abbreviations and the use of bold font are as that of Table 5.

System	T.E. (eV) (O.S.)	Involved orbitals (Coeff.)
CL1-TiO <sub>2</sub>	2.7	H-1 → L (0.38)
	(1.77)	<b>H → L (0.55)</b>

shown here; it is mostly derived from the dye's HOMO-1). From the isosurface plots, both HOMO and LUMO are predominantly localised on the dye molecule itself. However, the LUMO does show some hybridisation between the dyes LUMO and the *d*-orbitals of the titanium atoms at the surface. Such a result, where the only empty state involved is the LUMO of the complex, may indicate that only a direct transition is possible for the complex. However, it is difficult to pinpoint the precise mechanism in this case. This is due to the fact that although CAM-B3LYP improves the description of the photophysics of the *isolated* dye, it overestimates the bandgap of the titania nanoparticle. In turn, this results in a misalignment of dye states with regard to the valence and conduction bands of the titania nanoparticle; hence, there is an absence of a titania-derived conduction band manifold below the dye's LUMO. Clearly, it is difficult to obtain an accurate value for the charge-transfer excitation energy of the isolated dye and the dye-titania complex, whilst also getting a reasonable level alignment (at least within the *xc*-functionals explored here). The latter is important for the accurate description of the charge-transfer mechanism(s), and this is discussed further in [61].

#### 4. Conclusions

The CL1 dye containing a silicon bridge showed a good light to electricity efficiency of 6.90%. The Si dye exhibited better

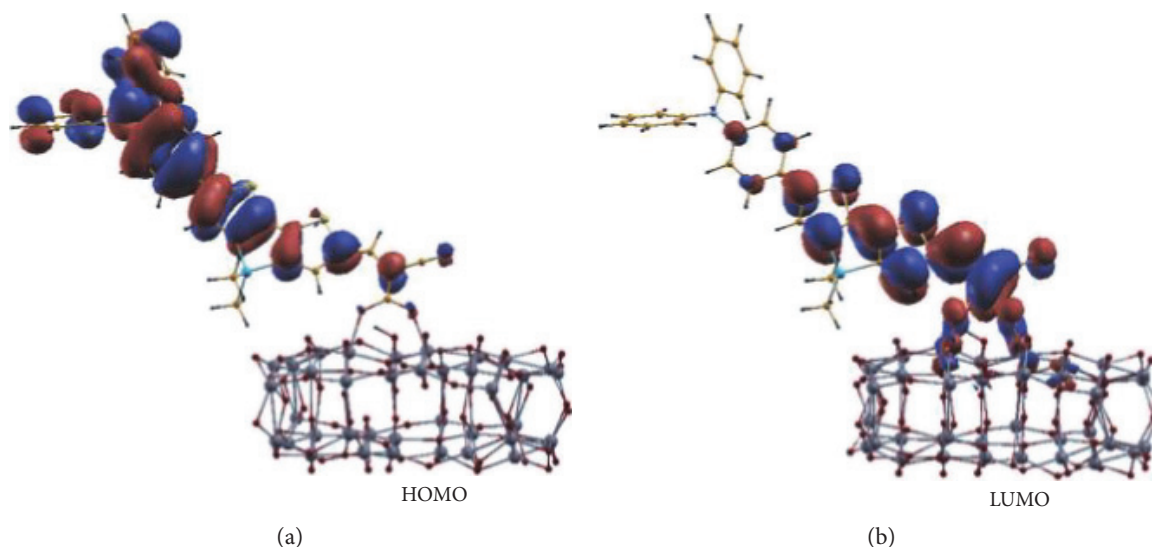


FIGURE 12: Molecular orbitals of CL1-TiO<sub>2</sub> complex involved in the most important transitions (HOMO and LUMO).

performance than N719 in the 400–470 nm region, which may be advantageous depending on the desired DSSC application and lighting conditions. CL-1 compares well with other Si-based dyes [9, 10], which achieve efficiencies of around 7.5%. Also, this is generally superior in performance than rival nanorod-based solar technologies [62] or DSSC approaches exploiting dye coverage with cobalt-based electrolytes [63]. From the view point of TD-DFT, the (conjectured) possibility that only a direct transition may take place due to some hybridisation between the LUMO of the dye and surface Ti atoms in the complexed state may limit the extent of photo-excited transition in the present dye—this may serve to rationalise why the observed overall energy conversion efficiency is not perhaps as high as the previously reported Si-based dyes. However, this conclusion is somewhat tentative, given that partial LUMO hybridisation does not necessarily preclude additional indirect transitions. These dyes are eventually useful for certain indoor applications where the spectral availability matches with the dye's absorption spectrum as well as for building tandem DSSC devices with optimal light management in order to obtain maximum short-circuit current densities. From classical MD simulations, it was evident that ethanol-formed hydrogen bonds and other dispersive and Coulombic interactions with the dye in dissolved state compromise its stability in solution form, whilst TD-DFT has provided a good agreement with the experimental data for prediction of optical absorption and identification of the underlying transitions responsible. Further work has been done on the addition of donor groups and will be presented in a later paper.

## Disclosure

Pratibha Dev's current address is at Department of Physics and Astronomy, Howard University, Washington, DC 20059, USA, and Praveen K. Surolia's current address is at Department of Chemistry, Manipal University Jaipur, Rajasthan, India.

## Conflicts of Interest

The authors declare that they have no conflicts of interest.

## Acknowledgments

This material is based upon work supported by the Science Foundation Ireland under Grant no. [07/SRC/B1160]. K. Ravindranathan Thampi acknowledges the support received under SFI-Airtricity-Funded SFI-Stokes professorship grant and the SMARTOP project (Grant no. 265769) financed by the EC-FP7 programme. The authors acknowledge the computational support provided by the Irish Centre for High-End Computing (ICHEC). Neelima Rathi and Edmond Magner acknowledge support from the HEA-funded PRTL14 programme, INSPIRE. Pratibha Dev and Praveen K. Surolia acknowledge the financial support for this work through EMPOWER fellowships granted by the Irish Research Council for Science and Engineering (IRCSET).

## References

- [1] B. O'Regan and M. Grätzel, "A low-cost, high-efficiency solar cell based on dye-sensitized," *Nature*, vol. 353, no. 6346, pp. 737–740, 1991.
- [2] R. Komiya, A. Fukui, N. Murofushi, N. Koide, R. Yamanaka, and H. Katayama, *Technical Digest, 21st International Photovoltaic Science and Engineering Conference*, Fukuoka, November 2011, 2 C-5O-08.
- [3] M. A. Green, K. Emery, Y. Hishikawa, W. Warta, and E. D. Dunlop, "Solar cell efficiency tables (version 45)," *Progress in Photovoltaics*, vol. 23, no. 1, pp. 1–9, 2015.
- [4] H. Imahori, T. Umeyama, and S. Ito, "Large  $\pi$ -aromatic molecules as potential sensitizers for highly efficient dye-sensitized solar cells," *Accounts of Chemical Research*, vol. 42, no. 11, pp. 1809–1818, 2009.
- [5] A. Yella, H. W. Lee, H. N. Tsao et al., "Porphyrin-sensitized solar cells with cobalt (II/III)-based redox electrolyte

- exceed 12 percent efficiency,” *Science*, vol. 334, no. 6056, pp. 629–634, 2011.
- [6] S. Mathew, A. Yella, P. Gao et al., “Dye-sensitized solar cells with 13% efficiency achieved through the molecular engineering of porphyrin sensitizers,” *Nature Chemistry*, vol. 6, no. 3, pp. 242–247, 2014.
- [7] K. Kakiage, Y. Aoyama, T. Yano, K. Oya, J. Fujisawa, and M. Hanaya, “Highly-efficient dye-sensitized solar cells with collaborative sensitization by silyl-anchor and carboxy-anchor dyes,” *Chemical Communications*, vol. 51, no. 88, pp. 15894–15897, 2015.
- [8] J. N. Clifford, G. Yahioğlu, L. R. Milgrom, and J. R. Durrant, “Molecular control of recombination dynamics in dye sensitised nanocrystalline TiO<sub>2</sub> films,” *Chemical Communications*, no. 12, pp. 1260–1261, 2002.
- [9] T. Bessho, S. M. Zakeeruddin, C. Y. Yeh, E. W. G. Diau, and M. Grätzel, “Highly efficient mesoscopic dye-sensitized solar cells based on donor-acceptor-substituted porphyrins,” *Angewandte Chemie, International Edition*, vol. 49, no. 37, pp. 6646–6649, 2010.
- [10] S. M. Feldt, E. A. Gibson, E. Gabriellson, L. Sun, G. Boschloo, and A. Hagfeldt, “Design of organic dyes and cobalt polypyridine redox mediators for high-efficiency dye-sensitized solar cells,” *Journal of the American Chemical Society*, vol. 132, no. 46, pp. 16714–16724, 2010.
- [11] H. N. Tsao, C. Yi, T. Moehl et al., “Cyclopentadithiophene bridged donor-acceptor dyes achieve high power conversion efficiencies in dye-sensitized solar cells based on the tris-cobalt bipyridine redox couple,” *ChemSusChem*, vol. 4, no. 5, pp. 591–594, 2011.
- [12] L. Liao, A. Cirpan, Q. Chu, F. E. Karasz, and Y. Pang, “Synthesis and optical properties of light-emitting  $\pi$ -conjugated polymers containing biphenyl and dithienosilole,” *Journal of Polymer Science Part A: Polymer Chemistry*, vol. 45, no. 10, pp. 2048–2058, 2007.
- [13] T.-Y. Chu, J. Lu, S. Beaupré et al., “Effects of the molecular weight and the side-chain length on the photovoltaic performance of dithienosilole/thienopyrrolodione copolymers,” *Advanced Functional Materials*, vol. 22, no. 11, pp. 2345–2351, 2012.
- [14] S. Ko, H. Choi, M.-S. Kang et al., “Silole-spaced triarylamine derivatives as highly efficient organic sensitizers in dye-sensitized solar cells (DSSCs),” *Journal of Materials Chemistry*, vol. 20, no. 12, pp. 2391–2399, 2010.
- [15] L.-Y. Lin, C.-H. Tsai, K.-T. Wong et al., “Organic dyes containing coplanar diphenyl-substituted dithienosilole core for efficient dye-sensitized solar cells,” *The Journal of Organic Chemistry*, vol. 75, no. 14, pp. 4778–4785, 2010.
- [16] M. J. Ross and K. R. William, *Impedance spectroscopy*, Wiley, New York, 1987.
- [17] J. Bisquert, “Theory of the impedance of charge transfer via surface states in dye-sensitized solar cells,” *Journal of Electroanalytical Chemistry*, vol. 646, no. 1–2, pp. 43–51, 2010.
- [18] L. Andrade, R. Cruz, H. Ribeiro, and A. Mendes, “Impedance characterization of dye-sensitized solar cells in a tandem arrangement for hydrogen production by water splitting,” *International Journal of Hydrogen Energy*, vol. 35, no. 17, pp. 8876–8883, 2010.
- [19] F. Fabregat-Santiago, J. Bisquert, E. Palomares et al., “Correlation between photovoltaic performance and impedance spectroscopy of dye-sensitized solar cells based on ionic liquids,” *Journal of Physical Chemistry C*, vol. 111, no. 17, pp. 6550–6560, 2007.
- [20] R. Kern, R. Sastrawan, J. Ferber, R. Stangl, and J. Luther, “Modeling and interpretation of electrical impedance spectra of dye solar cells operated under open-circuit conditions,” *Electrochimica Acta*, vol. 47, no. 26, pp. 4213–4225, 2002.
- [21] S. Ito, T. N. Murakami, P. Comte et al., “Fabrication of thin film dye sensitized solar cells with solar to electric power conversion efficiency over 10%,” *Thin Solid Films*, vol. 516, no. 14, pp. 4613–4619, 2008.
- [22] S. Ito, P. Chen, P. Comte et al., “Fabrication of screen-printing pastes from TiO<sub>2</sub> powders for dye-sensitized solar cells,” *Progress in Photovoltaics Research and Applications*, vol. 15, no. 7, pp. 603–612, 2007.
- [23] G. Lu, H. Usta, C. Risko et al., “Synthesis, characterization, and transistor response of semiconducting silole polymers with substantial hole mobility and air stability. Experiment and theory,” *Journal of the American Chemical Society*, vol. 130, no. 24, pp. 7670–7685, 2008.
- [24] J. M. Kroon, N. J. Bakker, H. J. P. Smit et al., “Nanocrystalline dye-sensitized solar cells having maximum performance,” *Progress in Photovoltaics Research and Applications*, vol. 15, no. 1, pp. 1–18, 2007.
- [25] M. Frisch, G. Trucks, H. Schlegel et al., “Semiempirical GGA-type density functional constructed with a long-range dispersion correction,” *Journal of Computational Chemistry*, vol. 27, no. 15, pp. 1787–1799, 2006.
- [26] M. J. G. Peach, P. Benfield, T. Helgaker, and D. J. Tozer, “Excitation energies in density functional theory: an evaluation and a diagnostic test,” *The Journal of Chemical Physics*, vol. 128, no. 4, p. 044118, 2008.
- [27] P. Dev, S. Agrawal, and N. J. English, “Determining the appropriate exchange-correlation functional for time-dependent density functional theory studies of charge-transfer excitations in organic dyes,” *The Journal of Chemical Physics*, vol. 136, no. 22, p. 224301, 2012.
- [28] A. D. Becke, “Density-functional thermochemistry. III. The role of exact exchange,” *The Journal of Chemical Physics*, vol. 98, no. 7, pp. 5648–5652, 1993.
- [29] R. Kavathekar, P. Dev, N. J. English, and J. M. D. MacElroy, “Molecular dynamics study of water in contact with TiO<sub>2</sub> rutile-110, 100, 101, 001 and anatase-101, 001 surfaces,” *Molecular Physics*, vol. 109, no. 13, pp. 1649–1656, 2011.
- [30] P. J. Stephens, F. J. Devlin, C. S. Ashvar, C. F. Chabalowski, and M. J. Frisch, “Theoretical calculation of vibrational circular dichroism spectra,” *Faraday Discussions*, vol. 99, pp. 103–119, 1994.
- [31] T. Yanai, D. P. Tew, and N. C. Handy, “A new hybrid exchange-correlation functional using the Coulomb-attenuating method (CAM-B3LYP),” *Chemical Physics Letters*, vol. 393, no. 1–3, pp. 51–57, 2004.
- [32] M. Cossi, N. Rega, G. Scalmani, and V. Barone, “Energies, structures, and electronic properties of molecules in solution with the C-PCM solvation model,” *Journal of Computational Chemistry*, vol. 24, no. 6, pp. 669–681, 2003.
- [33] P. Persson, R. Bergström, and S. Lunell, “Quantum chemical study of photoinjection processes in dye-sensitized TiO<sub>2</sub> nanoparticles,” *The Journal of Physical Chemistry. B*, vol. 104, no. 44, pp. 10348–10351, 2000.
- [34] F. De Angelis, A. Tilocca, and A. Selloni, “Time-dependent DFT study of [Fe (CN)<sub>6</sub>] 4-sensitization of TiO<sub>2</sub>

- nanoparticles," *Journal of the American Chemical Society*, vol. 126, no. 46, pp. 15024–15025, 2004.
- [35] F. De Angelis, "Direct vs. indirect injection mechanisms in perylene dye-sensitized solar cells: a DFT/TDDFT investigation," *Chemical Physics Letters*, vol. 493, no. 4–6, pp. 323–327, 2010.
- [36] S. Agrawal, P. Dev, N. J. English, K. R. Thampi, and J. MacElroy, "First-principles study of the excited-state properties of coumarin-derived dyes in dye-sensitized solar cells," *Journal of Materials Chemistry*, vol. 21, no. 30, pp. 11101–11108, 2011.
- [37] S. Agrawal, P. Dev, N. J. English, K. R. Thampi, and J. MacElroy, "A TD-DFT study of the effects of structural variations on the photochemistry of polyene dyes," *Chemical Science*, vol. 3, no. 2, pp. 416–424, 2012.
- [38] T. A. Halgren, "Merck molecular force field. I. Basis, form, scope, parameterization, and performance of MMFF94," *Journal of Computational Chemistry*, vol. 17, no. 5–6, pp. 490–519, 1996.
- [39] MOE, *The Molecular Operating Environment from Chemical Computing Group Inc.*
- [40] N. J. English and J. M. D. MacElroy, "Atomistic simulations of liquid water using Lekner electrostatics," *Molecular Physics*, vol. 100, no. 23, pp. 3753–3769, 2002.
- [41] N. J. English, "Effect of electrostatics techniques on the estimation of thermal conductivity via equilibrium molecular dynamics simulation: application to methane hydrate," *Molecular Physics*, vol. 106, no. 15, pp. 1887–1898, 2008.
- [42] M. Xu, S. Wenger, H. Bala et al., "Tuning the energy level of organic sensitizers for high-performance dye-sensitized solar cells," *Journal of Physical Chemistry C*, vol. 113, no. 7, pp. 2966–2973, 2009.
- [43] M. P. Allen and D. J. Tildesley, *Molecular Simulation of Liquids*, Clarendon, Oxford.
- [44] S. Roquet, A. Cravino, P. Leriche, O. Alévêque, P. Frère, and J. Roncali, "Triphenylamine–thienylenevinylene hybrid systems with internal charge transfer as donor materials for heterojunction solar cells," *Journal of the American Chemical Society*, vol. 128, no. 10, pp. 3459–3466, 2006.
- [45] J. H. Yum, D. P. Hagberg, S. J. Moon et al., "A light-resistant organic sensitizer for solar-cell applications," *Angewandte Chemie (International Edition in English)*, vol. 48, no. 9, pp. 1576–1580, 2009.
- [46] A. Hagfeldt and M. Gratzel, "Light-induced redox reactions in nanocrystalline systems," *Chemical Reviews*, vol. 95, no. 1, pp. 49–68, 1995.
- [47] C. Klein, M. K. Nazeeruddin, P. Liska et al., "Engineering of a novel ruthenium sensitizer and its application in dye-sensitized solar cells for conversion of sunlight into electricity," *Inorganic Chemistry*, vol. 44, no. 2, pp. 178–180, 2004.
- [48] C. Teng, X. Yang, C. Yang et al., "Influence of triple bonds as  $\pi$ -spacer units in metal-free organic dyes for dye-sensitized solar cells," *Journal of Physical Chemistry C*, vol. 114, no. 25, pp. 11305–11313.
- [49] D. Shi, Y. Cao, N. Pootrakulchote et al., "New organic sensitizer for stable dye-sensitized solar cells with solvent-free ionic liquid electrolytes," *Journal of Physical Chemistry C*, vol. 112, no. 44, pp. 17478–17485, 2008.
- [50] R. M. Silverstein, G. C. Bassler, and T. C. Morrill, *Spectrometric identification of organic compounds*, 1974.
- [51] M. K. Nazeeruddin, R. Humphry-Baker, D. L. Officer, W. M. Campbell, A. K. Burrell, and M. Gratzel, "Application of metalloporphyrins in nanocrystalline dye-sensitized solar cells for conversion of sunlight into electricity," *Langmuir*, vol. 20, no. 15, pp. 6514–6517, 2004.
- [52] G. B. Deacon and R. J. Phillips, "Relationships between the carbon-oxygen stretching frequencies of carboxylate complexes and the type of carboxylate coordination," *Coordination Chemistry Reviews*, vol. 33, no. 3, pp. 227–250, 1980.
- [53] A. Vittadini, A. Selloni, F. P. Rotzinger, and M. Gratzel, "Formic acid adsorption on dry and hydrated TiO<sub>2</sub> anatase (101) surfaces by DFT calculations," *The Journal of Physical Chemistry. B*, vol. 104, no. 6, pp. 1300–1306, 2000.
- [54] J. Bisquert, F. Fabregat-Santiago, I. Mora-Sero, G. Garcia-Belmonte, and S. Giménez, "Electron lifetime in dye-sensitized solar cells: theory and interpretation of measurements," *Journal of Physical Chemistry C*, vol. 113, no. 40, pp. 17278–17290, 2009.
- [55] Q. Wang, J.-E. Moser, and M. Grätzel, "Electrochemical impedance spectroscopic analysis of dye-sensitized solar cells," *The Journal of Physical Chemistry B*, vol. 109, no. 31, pp. 14945–14953, 2005.
- [56] L. Han, N. Koide, Y. Chiba, and T. Mitate, "Modeling of an equivalent circuit for dye-sensitized solar cells," *Applied Physics Letters*, vol. 84, no. 13, pp. 2433–2435, 2004.
- [57] J. Halme, P. Vahermaa, K. Miettunen, and P. Lund, "Device physics of dye solar cells," *Advanced Materials*, vol. 22, no. 35, pp. 22E210–E234, 2010.
- [58] L.-L. Li, Y.-C. Chang, H.-P. Wu, and E. W.-G. Diau, "Characterisation of electron transport and charge recombination using temporally resolved and frequency-domain techniques for dye-sensitized solar cells," *International Reviews in Physical Chemistry*, vol. 31, no. 3, pp. 420–467, 2012.
- [59] N. J. English and D. G. Carroll, "Prediction of Henry's Law constants by a Quantitative Structure Property Relationship and neural networks," *Journal of Chemical Information and Computer Sciences*, vol. 41, no. 5, pp. 1150–1161, 2001.
- [60] M. Adachi, M. Sakamoto, J. Jiu, Y. Ogata, and S. Isoda, "Determination of parameters of electron transport in dye-sensitized solar cells using electrochemical impedance spectroscopy," *The Journal of Physical Chemistry. B*, vol. 110, no. 28, pp. 13872–13880, 2006.
- [61] P. Dev, S. Agrawal, and N. J. English, "Functional assessment for predicting charge-transfer excitations of dyes in complexed state: a study of triphenylamine-donor dyes on titania for dye-sensitized solar cells," *The Journal of Physical Chemistry. A*, vol. 117, no. 10, pp. 2114–2124, 2013.
- [62] A. Singh, N. J. English, and K. M. Ryan, "Highly ordered nanorod assemblies extending over device scale areas and in controlled multilayers by electrophoretic deposition," *The Journal of Physical Chemistry. B*, vol. 117, no. 6, pp. 1608–1615, 2013.
- [63] M. Pazoki, P. W. Lohse, N. Taghavinia, A. Hagfeldt, and G. Boschloo, "The effect of dye coverage on the performance of dye-sensitized solar cells with a cobalt-based electrolyte," *Physical Chemistry Chemical Physics*, vol. 16, no. 18, pp. 8503–8508, 2014.

## Research Article

# Influence of the Porosity of the TiO<sub>2</sub> Film on the Performance of the Perovskite Solar Cell

Xiaodan Sun,<sup>1</sup> Jia Xu,<sup>2</sup> Li Xiao,<sup>1</sup> Jing Chen,<sup>1,2</sup> Bing Zhang,<sup>1,3</sup>  
Jianxi Yao,<sup>1,2</sup> and Songyuan Dai<sup>1,3</sup>

<sup>1</sup>State Key Laboratory of Alternate Electrical Power System with Renewable Energy Sources, North China Electric Power University, Beijing 102206, China

<sup>2</sup>Beijing Key Laboratory of Energy Safety and Clean Utilization, North China Electric Power University, Beijing 102206, China

<sup>3</sup>Beijing Key Laboratory of Novel Film Solar Cell, North China Electric Power University, Beijing 102206, China

Correspondence should be addressed to Jianxi Yao; [jianxiyao@ncepu.edu.cn](mailto:jianxiyao@ncepu.edu.cn) and Songyuan Dai; [sydai@ipp.ac.cn](mailto:sydai@ipp.ac.cn)

Received 8 October 2016; Accepted 19 December 2016; Published 1 February 2017

Academic Editor: Pushpa Pudasaini

Copyright © 2017 Xiaodan Sun et al. This is an open access article distributed under the Creative Commons Attribution License, which permits unrestricted use, distribution, and reproduction in any medium, provided the original work is properly cited.

The structure of mesoporous TiO<sub>2</sub> (mp-TiO<sub>2</sub>) films is crucial to the performance of mesoporous perovskite solar cells (PSCs). In this study, we fabricated highly porous mp-TiO<sub>2</sub> films by doping polystyrene (PS) spheres in TiO<sub>2</sub> paste. The composition of the perovskite films was effectively improved by modifying the mass fraction of the PS spheres in the TiO<sub>2</sub> paste. Due to the high porosity of the mp-TiO<sub>2</sub> film, PbI<sub>2</sub> and CH<sub>3</sub>NH<sub>3</sub>I could sufficiently infiltrate into the network of the mp-TiO<sub>2</sub> film, which ensured a more complete transformation to CH<sub>3</sub>NH<sub>3</sub>PbI<sub>3</sub>. The surface morphology of the mp-TiO<sub>2</sub> film and the photoelectric performance of the perovskite solar cells were investigated. The results showed that an increase in the porosity of the mp-TiO<sub>2</sub> film resulted in an improvement in the performance of the PSCs. The best device with the optimized mass fraction of 1.0 wt% PS in TiO<sub>2</sub> paste exhibited an efficiency of 12.69%, which is 25% higher than the efficiency of the PSCs without PS spheres.

## 1. Introduction

Perovskite solar cells based on CH<sub>3</sub>NH<sub>3</sub>PbI<sub>3</sub> have attracted much attention. Tremendous progress has been made since the seminal work of Kojima et al. in 2009 [1]. In just six years, power conversion efficiencies (PCEs) of PSCs have increased sharply from 3.8% [1] to 22.1% [2], which exceeds the PCEs of polycrystalline silicon solar cells [3–5]. Moreover, their solution processability and low cost endow them with high potential for next generation solar cells [4, 6].

Two typical PSC structures are widely used, including the planar heterojunction architectures [7] and the mesoporous structures [8–10]. Planar perovskite solar cells are advantageous because they have simple and scalable cell configurations [11]. In mesoporous structured PSCs, semiconductors, including TiO<sub>2</sub>, ZnO, insulating Al<sub>2</sub>O<sub>3</sub> and ZrO<sub>2</sub>, are employed as the electron transporting layer (ETL) or the scaffold of the perovskite layer [12]. Due to its

excellent physicochemical properties, such as large band gap, chemical stability, photostability, nontoxicity, and low cost [13], mesoporous TiO<sub>2</sub> is the most widely used electron transporting material in PSCs. The mp-TiO<sub>2</sub> film acts as not only the scaffold of the perovskite layer but also as the pathway for electron transport [14].

It has been reported that the structural properties of the mp-TiO<sub>2</sub> layer, such as particle size [15], thickness [16–18] and porosity, have a significant influence on the performance of PSCs [19]. Highly porous mp-TiO<sub>2</sub> films promote the easy infiltration of perovskite which subsequently fills the pores. A higher deposition of perovskites in mp-TiO<sub>2</sub> film results in increased light absorption and a higher current density [12, 14]. Moreover, the interface between the mp-TiO<sub>2</sub> film and perovskite film plays a key role in determining the overall conversion efficiency of PSCs [20]. Increasing the specific surface area and porosity of mp-TiO<sub>2</sub> film can promote a deeper infiltration of perovskites in TiO<sub>2</sub> films. This superior

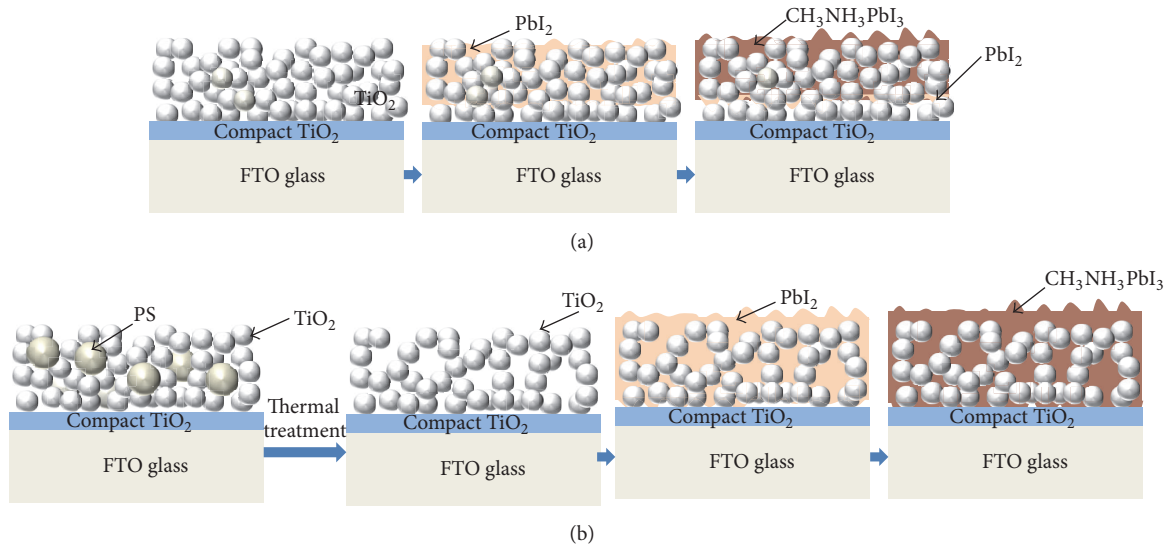


FIGURE 1: Schematic illustration of the distribution of  $\text{PbI}_2$  and  $\text{TiO}_2$  in mp- $\text{TiO}_2$  film (a) without and (b) with PS spheres.

infiltration is thought as an effective way to decrease the contact barrier between the  $\text{TiO}_2/\text{CH}_3\text{NH}_3\text{PbI}_3$  interfaces, which could improve the transport of carriers in the PSCs. Dharani et al. [21] used electrospinning to prepare  $\text{TiO}_2$  nanofibers as the ETL for PSCs. The  $\text{TiO}_2$  nanofiber formed a highly porous structure. The excellent porous network resulted in improved loading of  $\text{PbI}_2$ . Therefore, the  $\text{CH}_3\text{NH}_3\text{I}$  can infiltrate through the pores to completely react with  $\text{PbI}_2$ . Sarkar et al. [22] prepared well-organized mesoporous  $\text{TiO}_2$  photoelectrodes with enlarged pores by block copolymer-induced sol-gel assembly.  $\text{TiO}_2$  photoelectrodes with larger pores are favorable for filling of perovskite in the mp- $\text{TiO}_2$  film. Within a certain range, devices based on larger pores showed a higher  $J_{sc}$  and superior performance. Rapsomanikis et al. [19] synthesized highly meso-macroporous  $\text{TiO}_2$  thin films as ETLs of PSCs using a sol-gel process and Pluronic P-123 block copolymer as the organic template. Their results showed that the high porosity enabled the  $\text{TiO}_2$  thin film to act as an ideal host for perovskite. The efficient contact between mp- $\text{TiO}_2$  and perovskite enhanced the electron transport.

Methods of controlling the mesoporous networks of mp- $\text{TiO}_2$  include changing the size of  $\text{TiO}_2$  nanoparticles, using amphiphilic block copolymers [14, 22] and using templates. Many researchers reported that polystyrene (PS) spheres can be used as a mesostructured template to fabricate macro and mesoporous  $\text{TiO}_2$  films in dye-sensitized solar cells (DSSC) because of its size tunability [23, 24]. By using various preparation method and PS spheres with different sizes, the morphology of the films can be easily controlled. Dionigi et al. [25] used PS spheres as structure-directing agents and coated the PS spheres with titanium dihydroxide to fabricate porous  $\text{TiO}_2$  films with ordered pore architectures. Du et al. [24] fabricated hierarchically ordered macro-mesoporous  $\text{TiO}_2$  films as the interfacial layer of DSSC using PS spheres

as a template. Because of the periodically ordered structure and large specific surface of the macro-mesoporous  $\text{TiO}_2$  films, a higher  $J_{sc}$  and a PCE enhanced by 83% were obtained.

However, to our knowledge, there have been no reports on the use of PS spheres to change the mesoporous networks of mp- $\text{TiO}_2$  film in PSCs. In this study, we present a facile method of controlling the porosity of mp- $\text{TiO}_2$  by introducing PS spheres into  $\text{TiO}_2$  paste, which can be an effective strategy for the development of mesoporous PSCs. Figure 1 shows the schematic representation of the reaction process studied in this work. As shown in Figure 1(a),  $\text{TiO}_2$  nanoparticles are close to each other. There are only few pores between the particles.  $\text{PbI}_2$  cannot fully infiltrate into the narrow pores of mp- $\text{TiO}_2$  without the introduction of PS spheres during the preparation process; instead,  $\text{CH}_3\text{NH}_3\text{I}$  would react with the superficial  $\text{PbI}_2$ , which results in a large amount of residual  $\text{PbI}_2$  in the  $\text{TiO}_2$  film. In Figure 1(b), PS spheres can be observed in the  $\text{TiO}_2$  film before heat treatment. Then PS spheres were removed by heat treatment and a large amount of pores were formed in mesoporous  $\text{TiO}_2$  film. Therefore, more  $\text{PbI}_2$  infiltrated into the film. The subsequently deposited  $\text{CH}_3\text{NH}_3\text{I}$  reacted more completely with  $\text{PbI}_2$ , which reduced the amount of the residual  $\text{PbI}_2$ . By adjusting the mass fraction of PS spheres in  $\text{TiO}_2$  paste, a controllable porous mp- $\text{TiO}_2$  film was obtained. The incorporation of the macropores in mp- $\text{TiO}_2$  films increased the perovskite loading in the film and improved the contact between the  $\text{TiO}_2$  and perovskite interface, which effectively suppressed charge recombination in the interface. X-ray diffraction and fluorescence lifetime measurements confirmed that the increased porosity ensured an adequate reaction between  $\text{PbI}_2$  and  $\text{CH}_3\text{NH}_3\text{I}$ , thus decreasing the amount of residual  $\text{PbI}_2$  and enhancing the electron injection from the perovskite to mp- $\text{TiO}_2$  film. The PSCs with the

porous TiO<sub>2</sub> films showed an enhanced short-circuit current density and higher efficiency.

## 2. Materials and Methods

**2.1. Materials.** Titanium dioxide paste (18-RT) was purchased from Yingkou OPV Tech New Energy Co., Ltd. Ethanol (99.8%) and hydrochloric acid (36%) were purchased from Beijing Chemical Plant (Beijing, China). The 100 nm PS spheres (Mw ~ 100000) were purchased from Janus New-Materials Co., Ltd. PbI<sub>2</sub> (99%) was purchased from Acros. CH<sub>3</sub>NH<sub>3</sub>I (99.5%) and 2,2',7,7'-tetrakis-(N,N-dimethoxyphenylamine)-9,9'-spirobifluorene (Spiro-OMeTAD) (99.7%) were purchased from Borun Chemicals (Ningbo, China). Tris(2-(1H-pyrazol-1-yl)-4-tert-butylpyridine)-cobalt(III)tris(bis(trifluoromethylsulfonyl)imide) (FK209-cobalt(III)-TFSI) was purchased from MaterWin Chemicals (Shanghai, China). N,N-dimethylformamide (DMF) was purchased from Alfa Aesar. Isopropanol was purchased from J&K Scientific Co., Ltd. All chemicals were used as received. Glass substrates with a transparent fluorine-doped tin oxide (FTO, sheet resistance 15 Ω/square) layer were used for the PSCs.

The solution of the compact TiO<sub>2</sub> is prepared by mixing titanium isopropoxide, HCl, and ethanol with a volume ratio of 7:22:100. In the solution of compact TiO<sub>2</sub>, the concentrations of HCl and ethanol are 70.24% and 8.48%, respectively. For the preparation of the TiO<sub>2</sub> paste, we first diluted the TiO<sub>2</sub> paste in ethanol with a ratio of 1:3.5. Then, the mixture was added to 100 nm PS spheres with various wt% (0 wt%, 1.0 wt%, and 1.5 wt%) and stirred for 12 h. The spiro-MeOTAD solution was prepared by dissolving 72.3 mg spiro-MeOTAD in 1 mL chlorobenzene, and then 28.8 μL TBP and an 8 μL solution of LiTFSI (520 mg/mL LiTFSI in acetonitrile) were added.

**2.2. Device Fabrication.** Devices were fabricated on FTO glass substrates with a dimension of 1.5 cm × 1.3 cm. First, FTO was partially etched with Zn powder and HCl. Then, the etched FTO was cleaned using potassium sulfate solution, soap, deionized water, and ethanol, and, finally, it was sintered at 500 °C for 30 minutes. A compact TiO<sub>2</sub> layer was prepared by spin coating compact TiO<sub>2</sub> solution, followed by annealing at 500 °C for 30 min. The mesoporous TiO<sub>2</sub> film was prepared by spin coating 35 μL TiO<sub>2</sub> paste at 5000 r.p.m. for 30 s. Then, the films were heated to 450 °C for 2 hours with a heating rate of 5 °C/min. 462 mg of PbI<sub>2</sub> was dissolved in 1 mL DMF under stirring at 70 °C for 12 hours. 40 μL PbI<sub>2</sub> solution was spin-coated on the mp-TiO<sub>2</sub> films at 3000 r.p.m. for 30 s. After loading was performed for 4 min, the substrates were dried at 70 °C for 30 min. After the films were cooled to room temperature, 90 μL CH<sub>3</sub>NH<sub>3</sub>I solution in 2-propanol (8 mg/mL) was sprayed on the PbI<sub>2</sub> films, and the films were spun at 4000 r.p.m. for 30 s and then dried at 70 °C for 30 min. The hole transporting layer (HTL) was prepared by spinning spiro-MeOTAD on the TiO<sub>2</sub>/CH<sub>3</sub>NH<sub>3</sub>PbI<sub>3</sub>

film at 3000 r.p.m. for 30 s. Finally, 70 nm gold electrodes were deposited on top of the device by thermally evaporation.

**2.3. Characterization and Measurement.** The surface morphology of the films was observed with a field emission scanning electron microscope (SEM, SU8010, Hitachi, 20.0 kV, 10.5 μA). The AFM images were obtained by An AC Mode III (Agilent 5500) atomic force microscope (AFM). X-ray diffraction (XRD) patterns were obtained by using a Bruker X-ray diffractometer with a Cu-Kα radiation source (40 kV, 400 mA). The 2θ diffraction angle was scanned from 10° to 80°, with a scanning speed of 1 second per step. The incident-photon-to-electron conversion efficiency (IPCE) curves were measured under ambient atmosphere using a QE-R measurement system (Enli Technology). The current-voltage characteristics (*J-V* curves) were obtained with a Keithley 2400 source meter and a sunlight simulator (XES-300T1, SAN-EI Electric, AM 1.5), which was calibrated using a standard silicon reference cell.

## 3. Results and Discussion

**3.1. Morphology of the Porous TiO<sub>2</sub> Film.** The size and mass fraction of PS spheres are crucial in determining the porosity and uniformity of the TiO<sub>2</sub> mesoporous layer. The surface morphology of the TiO<sub>2</sub> films was analyzed by scanning electron microscopy. The SEM images of sample PS-1.0 before and after heat treatment are shown in Figure S1 in Supplementary Material available online at <https://doi.org/10.1155/2017/4935265>. As observed in Figure 2, unlike the TiO<sub>2</sub> layer formed by spinning the paste without PS spheres (PS-0), pores can be observed in the mp-TiO<sub>2</sub> film prepared by TiO<sub>2</sub> paste with PS spheres. For a low mass fraction of 0.5 wt% PS spheres in the paste (PS-0.5), a few pores with an average size of 70 nm (the statistic numbers and histogram of pore size distribution are shown in Table S1 and Figure S2) are formed on the surface of the mp-TiO<sub>2</sub> layer. When the mass fraction of the PS spheres in TiO<sub>2</sub> paste increased to 1.0 wt%, (PS-1.0), lots of pores with an average size of 80 nm are formed. The average pore sizes for both PS-0.5 and PS-1.0 are almost the same, and the pore distribution is uniform. As the mass fraction of PS spheres increases to 1.5 wt% (PS-1.5), pores with relative larger pores (94 nm) were formed due to the high mass fraction of PS spheres and the agglomeration of PS spheres in the TiO<sub>2</sub> paste. The pore distribution is inhomogeneous compared to the PS-1.0 sample. The pore structure could be clearly observed in the cross-sectional SEM images of samples PS-0 and PS-1.0 (Figures 2(e) and 2(f)). As observed in Figures 2(e) and 2(f), the thickness of samples PS-0 and PS-1.0 is 260 nm and 360 nm, respectively. Moreover, the porous structure of sample PS-1.0 is looser than that of sample PS-0. The TiO<sub>2</sub> nanoparticles are densely packed and there are almost no pores among the nanoparticles in sample PS-0. However, pores can be observed from the cross-sectional SEM image in PS-1.0 (Figure 2(f)). The pores emerged not only on the surface of mp-TiO<sub>2</sub> film but also throughout the film. Sample

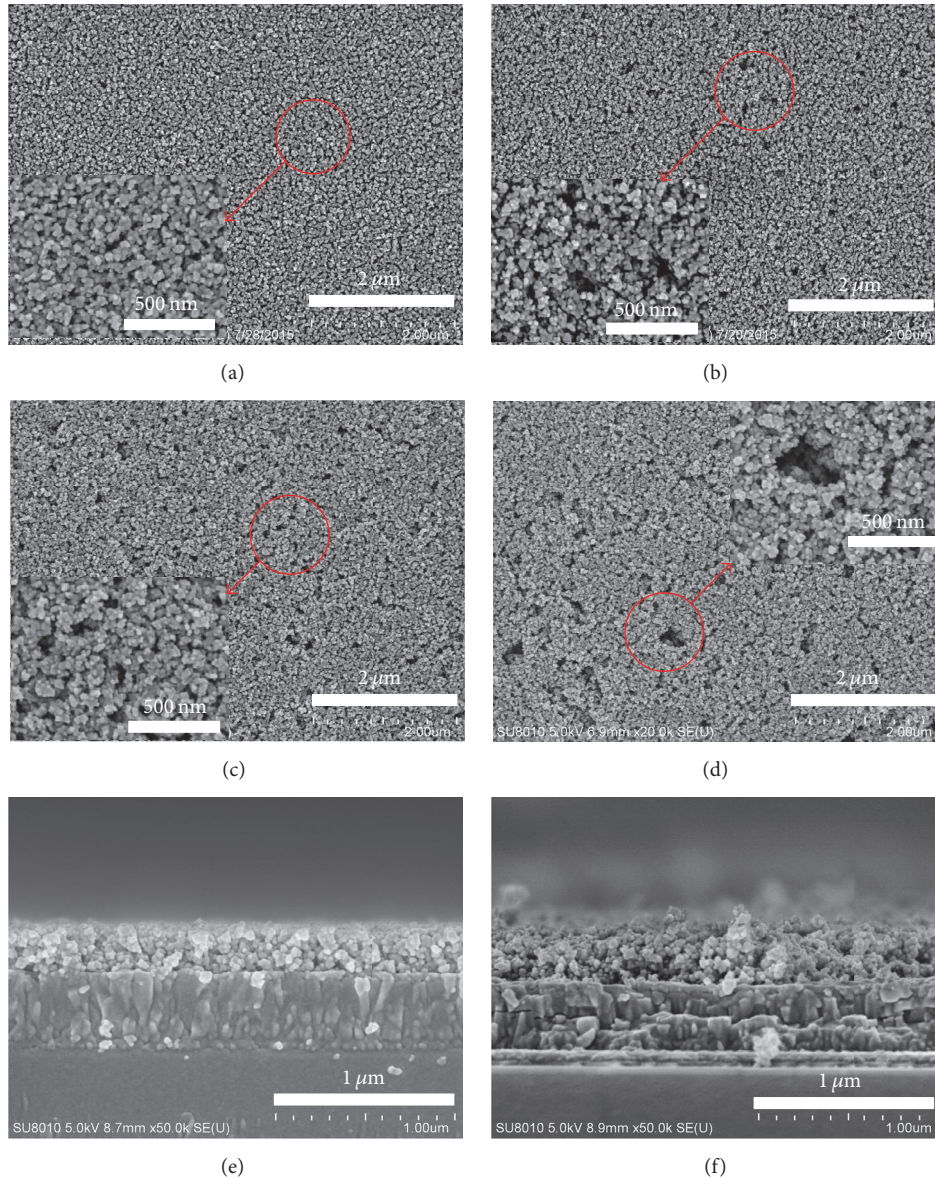


FIGURE 2: Plane-view SEM images of (a) PS-0, (b) PS-0.5, (c) PS-1.0, and (d) PS-1.5. Cross-sectional SEM images under high magnification of (e) PS-0 and (f) PS-1.0.

PS-1.0 is thicker than sample PS-0 due to the presence of more pores in the film.

**3.2. Effect of  $\text{TiO}_2$  Porosity on the Growth of Perovskite.** The mp- $\text{TiO}_2$  film plays a key role in determining the structure of the perovskite layer. SEM and AFM images of the perovskite layer were obtained for mp- $\text{TiO}_2$  films prepared by  $\text{TiO}_2$  paste with different mass fraction PS spheres. As shown in Figure 3, the average size of the perovskite is 300 nm regardless of if PS spheres were used in the mp- $\text{TiO}_2$  paste or not. The root-mean-square (RMS) roughness values of the  $\text{CH}_3\text{NH}_3\text{PbI}_3$  films based on samples PS-0, PS-0.5, PS-1.0, and PS-1.5 obtained for a  $5\ \mu\text{m} \times 5\ \mu\text{m}$  area were evaluated as 53.3 nm, 55.6 nm, 53.2 nm, and 58.2 nm, respectively. This means that the amount of pores in the mp- $\text{TiO}_2$  films does

not change the morphology and roughness of the perovskite film.

To better understand the distribution of perovskite in the mp- $\text{TiO}_2$  film, energy dispersive X-ray (EDX) mapping was performed. The EDX mapping of the cross-sectional area shows the distribution of two elements, Ti and Pb, along the mp- $\text{TiO}_2$  film thickness. As observed in Figure 4(a), a small amount of Pb is deposited in the sample PS-0. Figure 4(b) shows that more Pb is deposited at deeper levels in the sample PS-1.0 and the distribution of Pb is more uniform along the thickness of the  $\text{TiO}_2$  film. In addition,  $\text{CH}_3\text{NH}_3\text{PbI}_3$  was uniformly distributed in the mp- $\text{TiO}_2$  film owing to the presence of more pores.

Moreover, the perovskite crystallinity and the amount of residual  $\text{PbI}_2$  are crucial to the performance of perovskite solar cells. It is well known that the residual  $\text{PbI}_2$  layer exists

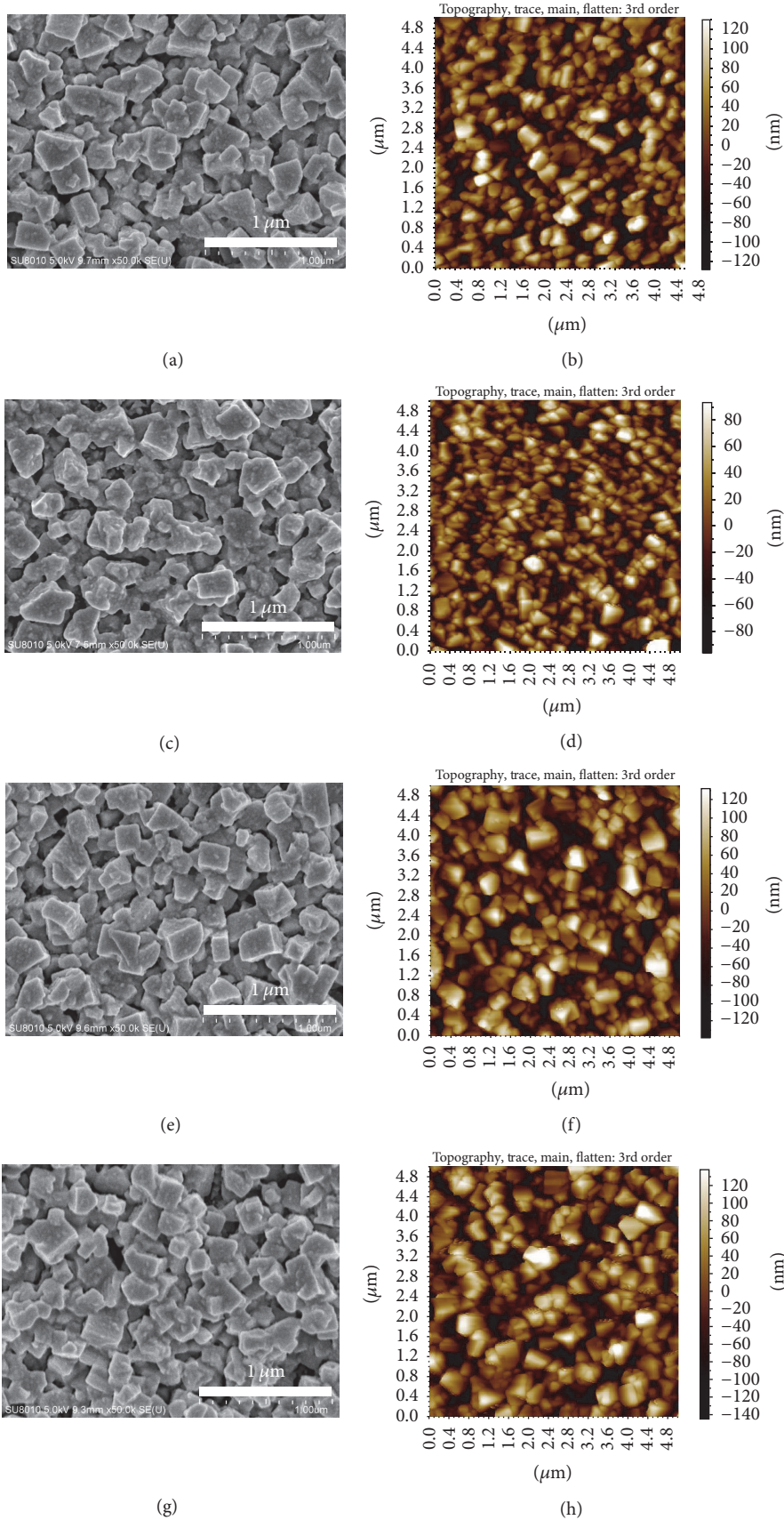


FIGURE 3: SEM and AFM images ( $5 \mu\text{m} \times 5 \mu\text{m}$ ) of the perovskite films based on the mesoporous TiO<sub>2</sub>: (a), (b) PS-0; (c), (d) PS-0.5; (e), (f) PS-1.0; and (g), (h) PS-1.5.

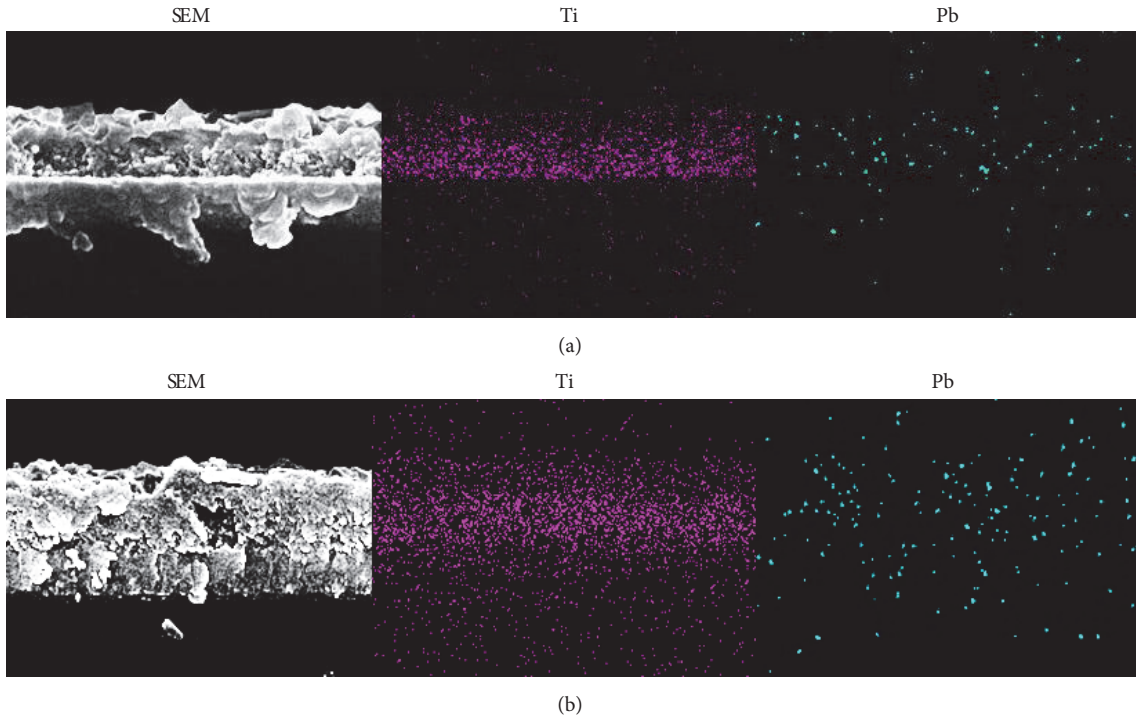


FIGURE 4: SEM-EDX mapping along the mp-TiO<sub>2</sub> film thickness to show the change in the distribution of Ti and Pb in CH<sub>3</sub>NH<sub>3</sub>PbI<sub>3</sub> loaded on (a) PS-0 and (b) PS-1.0.

between the interface of the mp-TiO<sub>2</sub> film and perovskite layer due to the incomplete reaction of PbI<sub>2</sub> and CH<sub>3</sub>NH<sub>3</sub>I [26]. Excessive amounts of residual PbI<sub>2</sub> will block the electron injected from the perovskite to mp-TiO<sub>2</sub> film, which deteriorates the cell performance of PSCs [27, 28]. However, a trace amount of residual PbI<sub>2</sub> acts as a passivation layer and reduces charge recombination at the interface between mp-TiO<sub>2</sub> film and the perovskite layer. To investigate the influence of the porosity of TiO<sub>2</sub> substrate on the growth of perovskite, X-ray diffraction was performed. In Figure 5, the peaks at 26.8°, 38.1°, and 51.8° correspond to the (110), (200), and (211) planes of FTO. The diffraction peaks marked by stars represent the PbI<sub>2</sub> (001) lattice plane, which conforms well with the literature data [29]. The Bragg peaks at 14.08°, 19.92°, 28.40°, 31.85°, 40.46°, and 43.02°, respectively, represent the reflections from the (110), (112), (220), (310), (224), and (314) crystal planes of the tetragonal perovskite structure [30, 31], which means that the change in porosity of the TiO<sub>2</sub> mesoporous layer has no influence on perovskite crystallinity. However, as the mass fraction of PS spheres in the TiO<sub>2</sub> paste increases, the intensity of the PbI<sub>2</sub> peaks reduces. There is only a little residual PbI<sub>2</sub> in the sample PS-1.0. By introducing PS spheres in TiO<sub>2</sub> paste, more pores were formed in the mp-TiO<sub>2</sub> film. The presence of more pores enables a deeper infiltration of PbI<sub>2</sub> and CH<sub>3</sub>NH<sub>3</sub>I solution, which endows complete reaction to CH<sub>3</sub>NH<sub>3</sub>PbI<sub>3</sub>.

**3.3. Photovoltaic Characterization of PSCs.** The current density versus voltage (*J-V*) characteristics of PSCs based on the mp-TiO<sub>2</sub> layer prepared by TiO<sub>2</sub> paste with and without PS

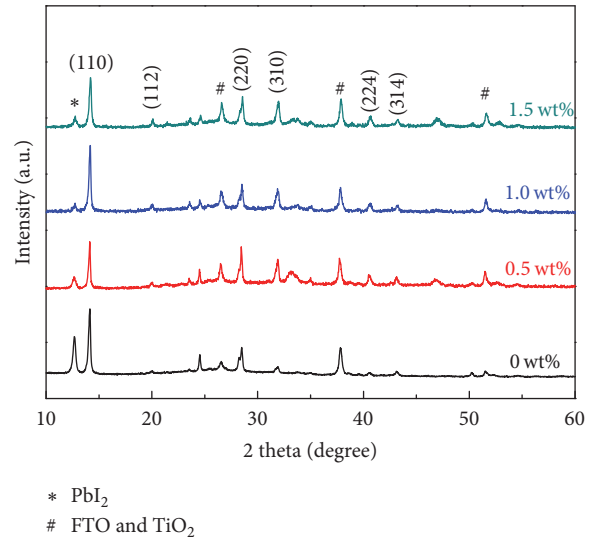


FIGURE 5: X-ray diffraction patterns of CH<sub>3</sub>NH<sub>3</sub>PbI<sub>3</sub> films based on TiO<sub>2</sub> mesoporous layers with different mass fractions of PS spheres.

spheres are shown in Figure 6. The photovoltaic parameters of the devices are summarized in Table 1. PSCs based on the mp-TiO<sub>2</sub> film PS-0 showed a reasonable PCE of 10.07% with an open-circuit voltage (*V*<sub>oc</sub>) of 0.91 V, a short-circuit current (*J*<sub>sc</sub>) of 19.07 mA/cm<sup>2</sup>, and a fill factor (FF) of 57.99%. A relatively higher performance was exhibited by the device with PS spheres. After doping 0.5 wt% PS spheres, *J*<sub>sc</sub>, *V*<sub>oc</sub>,

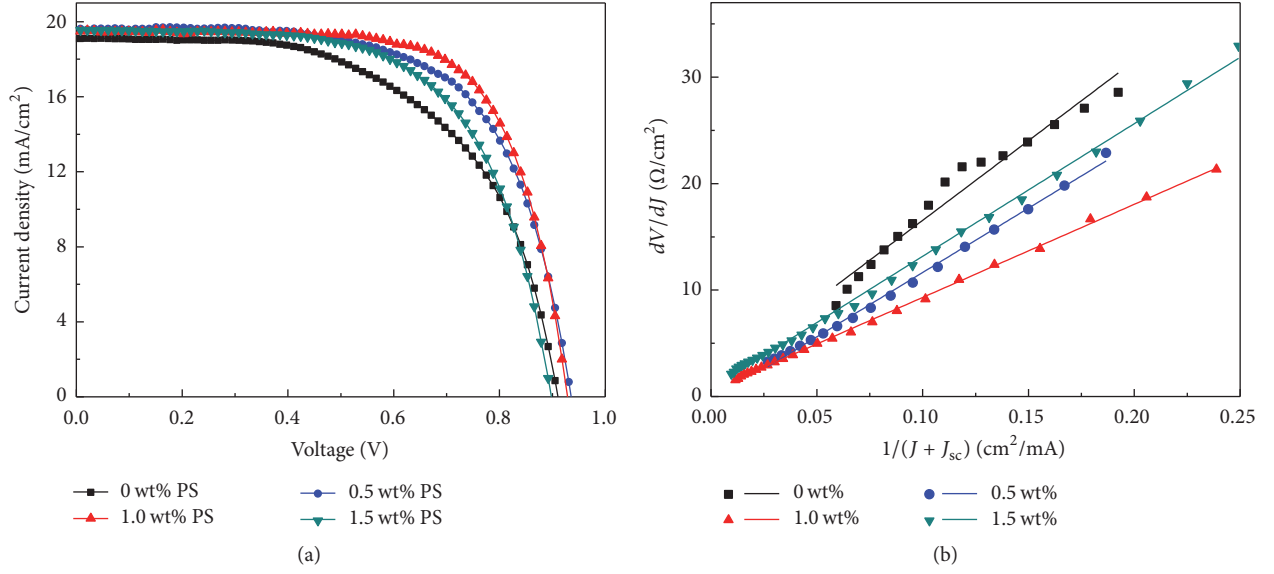


FIGURE 6: (a) Current density-voltage curves and the best-performing solar cells based on mp-TiO<sub>2</sub> film with different wt% of PS. (b) Plots of  $dV/dJ$  versus  $1/(J + J_{sc})$  and the linear fitting curves.

TABLE 1: Photovoltaic performance of CH<sub>3</sub>NH<sub>3</sub>PbI<sub>3</sub> based devices as a function of different wt% of PS.

wt% of PS	$R_{sh}$ (Ω)	$R_s$ (Ω·cm <sup>2</sup> )	$J_{sc}$ (mA/cm <sup>2</sup> )	$V_{oc}$ (V)	Fill factor (%)	Efficiency (%)
0	1220	1.57	19.07	0.91	57.99	10.07
0.5	3860	0.43	19.64	0.94	64.91	11.92
1.0	5320	0.56	19.44	0.93	69.91	12.62
1.5	3700	0.71	19.54	0.90	63.47	11.14

FF, and PCE increased to 19.64 mA/cm<sup>2</sup>, 0.94 V, 64.91% and 11.92%, respectively. For a 1.0% mass fraction of PS spheres, the best PCE ( $V_{oc}$  of 0.93,  $J_{sc}$  of 19.44 mA/cm<sup>2</sup>, FF of 69.91%, and PCE of 12.62%) was achieved. When the mass fraction of PS spheres increased to 1.5 wt%, the PCS exhibits  $J_{sc}$  of 19.54 mA/cm<sup>2</sup>,  $V_{oc}$  of 0.90 V, FF of 63.47%, and PCE of 11.14%. The decrease in the residual PbI<sub>2</sub> contributes to rapid electron injection from the perovskite to TiO<sub>2</sub> and higher  $J_{sc}$ . The improvements in the performance for the PSCs are mainly due to the increase of FF. Generally, FF depends largely on the series resistance ( $R_s$ ) and shunt resistance ( $R_{sh}$ ).

The equivalent circuit of the perovskite solar cell is shown in Figure 7. The output current density  $J$  can be expressed by the following equation:

$$J = J_0 \left( e^{q(V - JR_s)/kT} - 1 \right) + \frac{V - JR_s}{R_{sh}} - J_{sc}, \quad (1)$$

where  $J_0$  represent the reverse saturation current density,  $A$  is ideality factor,  $k$  is Boltzmann's constant,  $T$  represent the temperature, and  $q$  represent electron charge. When  $R_s \ll R_{sh}$ , (1) can be expressed as

$$\frac{dV}{dJ} = R_s + \frac{AkT}{q} \frac{1}{J + J_{sc}}. \quad (2)$$

It is found that, from (2),  $dV/dJ$  has a linear relation with  $(J_{sc} - J)^{-1}$ . The intercept of the linear fitting curve gives

the value of series resistance. Figure 6(b) shows the plot of  $dV/dJ$  versus  $1/(J + J_{sc})$  and the linear fitting curve. As can be seen in Figure 6(b), the fitting curves are more linear by doping PS spheres in TiO<sub>2</sub> paste. Slightly decreased values of  $R_s$  from 1.57 Ω·cm<sup>2</sup> to 0.43 Ω·cm<sup>2</sup>, 0.56 Ω·cm<sup>2</sup>, and 0.71 Ω·cm<sup>2</sup> were evaluated after doping 0.5 wt%, 1.0 wt%, and 1.5 wt% PS spheres in the mp-TiO<sub>2</sub> paste. The smaller  $R_s$  values are due to the reduction in both the contact resistance and bulk resistance, which means a higher photocurrent will be generated [32]. However, when the mass fraction of PS spheres is 1.5 wt%, the increased  $R_s$  is attributed to the higher resistance caused by more pores and the negative contact with TiO<sub>2</sub> nanoparticles. The device based on TiO<sub>2</sub> mesoporous layer prepared by TiO<sub>2</sub> paste with PS spheres showed larger  $R_{sh}$  ( $R_{sh}$  values of the PSCs are 1220 Ω, 3860 Ω, 5320 Ω, and 3700 Ω for doping with 0 wt%, 0.5 wt%, 1.0 wt%, and 1.5 wt% PS spheres, resp.). A higher  $R_{sh}$  can improve FF and electron mobility [33], which is consistent with the results of the  $J$ - $V$  test.

$R_{sh}$  is closely related to the charge recombination at interfaces inside solar cells. A lower charge recombination contributes to a higher  $R_{sh}$  [34]. To better understand the separation of light-induced charge at the TiO<sub>2</sub>/CH<sub>3</sub>NH<sub>3</sub>PbI<sub>3</sub> interface, we performed time-resolved photoluminescence (PL) decay measurements on the CH<sub>3</sub>NH<sub>3</sub>PbI<sub>3</sub> perovskite-filled mp-TiO<sub>2</sub> films prepared by TiO<sub>2</sub> paste with different

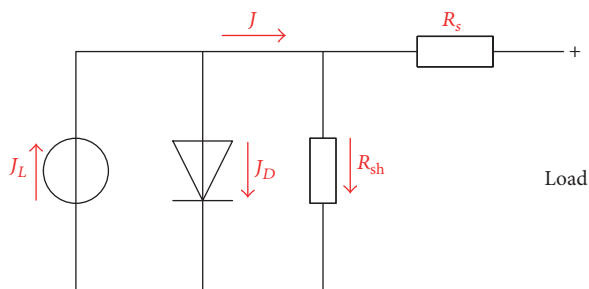


FIGURE 7: Equivalent circuit of the perovskite solar cell.

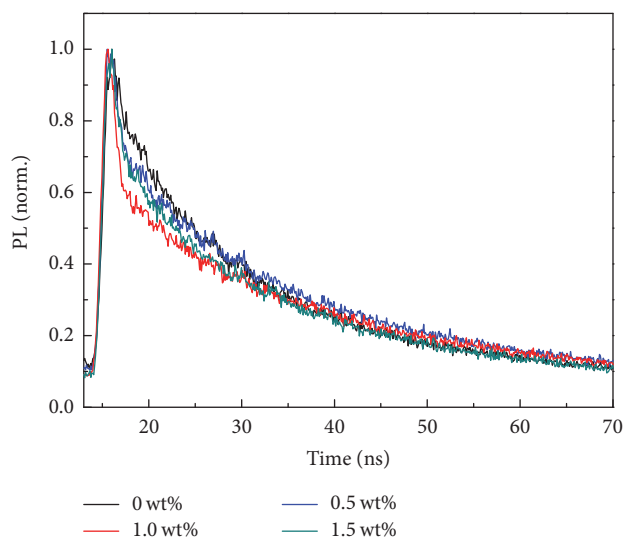


FIGURE 8: Normalized transient PL decay profiles of the perovskites based on  $\text{TiO}_2$  with different wt% PS.

mass fractions of PS spheres, which are presented in Figure 8. Using global biexponential fits, the PL decay of the  $\text{CH}_3\text{NH}_3\text{PbI}_3$  perovskite in the mp- $\text{TiO}_2$  films without PS spheres and with 0.5 wt%, 1.0 wt% and 1.5 wt% PS spheres exhibits  $\tau_1$  values of 22.53 ns, 17.57 ns, 17.71 ns, and 18.93 ns, respectively. By doping PS spheres into the  $\text{TiO}_2$  paste, the rate of electron injection from the perovskite into  $\text{TiO}_2$  film becomes faster, which results in lower charge recombination at the  $\text{TiO}_2/\text{CH}_3\text{NH}_3\text{PbI}_3$  interfaces. This could be attributed to the better filling of the  $\text{CH}_3\text{NH}_3\text{PbI}_3$  perovskite in the mp- $\text{TiO}_2$  film and the more complete contact between the  $\text{TiO}_2$ /perovskite as more pores emerge in the mp- $\text{TiO}_2$  film.

The photon-to-electron conversion efficiency (IPCE) spectra with mp- $\text{TiO}_2$  doping for different mass fractions of PS spheres are shown in Figure 9. The convolution of the spectral response with the photon flux of the AM 1.5G spectrum provided the estimated  $J_{sc}$  values of 15.537  $\text{mA}/\text{cm}^2$ , 16.994  $\text{mA}/\text{cm}^2$ , 16.825  $\text{mA}/\text{cm}^2$ , and 16.397  $\text{mA}/\text{cm}^2$ . The calculated  $J_{sc}$  values from the IPCE spectrum are well matched with the  $J_{sc}$  values obtained from the  $J$ - $V$  curves. In addition, the PCSs from mp- $\text{TiO}_2$  films with PS spheres exhibited a higher and broader spectrum from 450 nm to 700 nm. Here, an IPCE of  $\sim 80\%$  was obtained at the

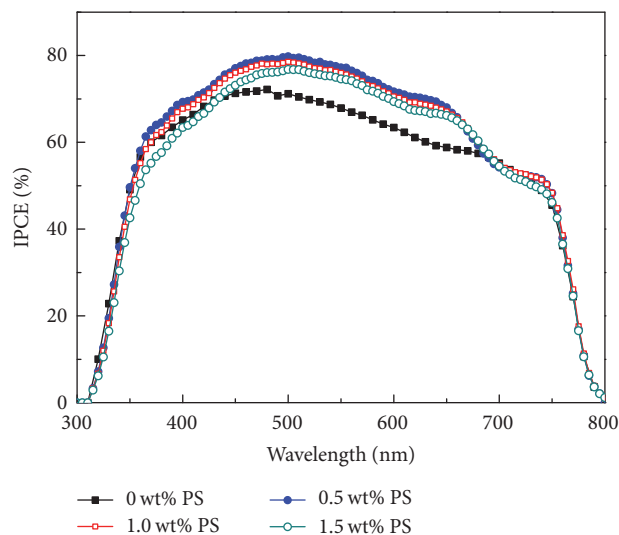


FIGURE 9: IPCE spectra of the best-performing solar cells based on different mass fractions of PS spheres.

maximum peak, while the device based on mp- $\text{TiO}_2$  films without PS spheres exhibited a lower IPCE of  $\sim 70\%$ .

To further determine the influence of the porosity of mp- $\text{TiO}_2$  films on the fabricated solar cells, we showed the statistic results of the cells based on the mp- $\text{TiO}_2$  film prepared by  $\text{TiO}_2$  paste with different mass fractions of PS spheres in Figure 10. The deviations of  $J_{sc}$ ,  $V_{oc}$ , FF, and PCE have been shown in Table S2. As observed in Figure 10,  $J_{sc}$  and FF increase as the mass fraction of the PS spheres increases and they attain their highest values at the mass fraction of 1.0 wt%, which contributes to the increase in the PCE.

## 4. Conclusions

In conclusion, mp- $\text{TiO}_2$  films with tunable porosities were fabricated by doping PS spheres in  $\text{TiO}_2$  paste and applied as the ETL of perovskite solar cells. The results indicate that the porosity of mp- $\text{TiO}_2$  films not only affects the infiltration and residual amounts of  $\text{PbI}_2$  but also significantly influences the contact between the mp- $\text{TiO}_2$  film and perovskite layer. By adjusting the mass fraction of PS spheres, the perovskite solar cell based on mp- $\text{TiO}_2$  film prepared by  $\text{TiO}_2$  paste with 1.0 wt% PS spheres exhibits the highest power conversion efficiency of 12.62% under a simulated standard AM 1.5 condition.

## Competing Interests

The authors declare that they have no competing interests.

## Acknowledgments

This work was supported by the National High Technology Research and Development Program of China (863 Program) (no. 2015AA050602), the National Natural Science Foundation of China (no. 51372083), Jiangsu Province Science and

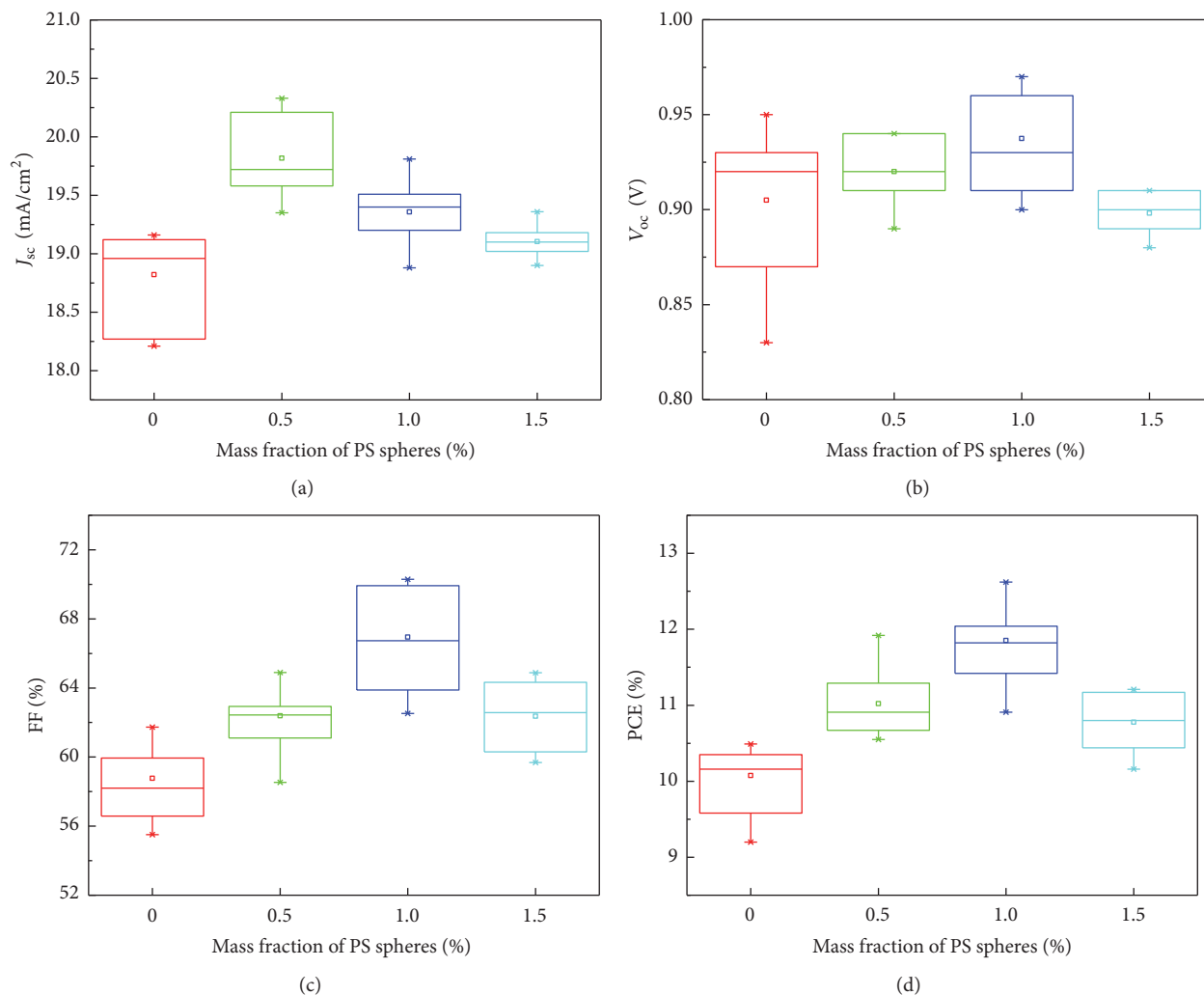


FIGURE 10: Statistic results of the cells based on the mp-TiO<sub>2</sub> film with different mass fractions of PS spheres.

Technology Support Program, China (BE2014147-4), and the Fundamental Research Funds for the Central Universities (nos. 2014ZZD07 and 2015ZD11).

## References

- [1] A. Kojima, K. Teshima, Y. Shirai, and T. Miyasaka, "Organometal halide perovskites as visible-light sensitizers for photovoltaic cells," *Journal of the American Chemical Society*, vol. 131, no. 17, pp. 6050–6051, 2009.
- [2] "Best Research-Cell Efficiency," national renewable energy laboratory, [http://www.nrel.gov/pv/assets/images/efficiency\\_chart.jpg](http://www.nrel.gov/pv/assets/images/efficiency_chart.jpg).
- [3] W. S. Yang, J. H. Noh, N. J. Jeon et al., "High-performance photovoltaic perovskite layers fabricated through intramolecular exchange," *Science*, vol. 348, no. 6240, pp. 1234–1237, 2015.
- [4] J. Qing, H.-T. Chandran, H.-T. Xue et al., "Simple fabrication of perovskite solar cells using lead acetate as lead source at low temperature," *Organic Electronics: physics, materials, applications*, vol. 27, article no. 3243, pp. 12–17, 2015.
- [5] M. I. Ahmed, A. Habib, and S. S. Javaid, "Perovskite solar cells: potentials, challenges, and opportunities," *International Journal of Photoenergy*, vol. 2015, Article ID 592308, 13 pages, 2015.
- [6] Q. Chen, H. Zhou, Z. Hong et al., "Planar heterojunction perovskite solar cells via vapor-assisted solution process," *Journal of the American Chemical Society*, vol. 136, no. 2, pp. 622–625, 2014.
- [7] M. Liu, M. B. Johnston, and H. J. Snaith, "Efficient planar heterojunction perovskite solar cells by vapour deposition," *Nature*, vol. 501, no. 7467, pp. 395–398, 2013.
- [8] L. Etgar, P. Gao, Z. Xue et al., "Mesoscopic CH<sub>3</sub>NH<sub>3</sub>PbI<sub>3</sub>/TiO<sub>2</sub> heterojunction solar cells," *Journal of the American Chemical Society*, vol. 134, no. 42, pp. 17396–17399, 2012.
- [9] H.-S. Kim, C.-R. Lee, J.-H. Im et al., "Lead iodide perovskite sensitized all-solid-state submicron thin film mesoscopic solar cell with efficiency exceeding 9%," *Scientific Reports*, vol. 2, article 591, 2012.
- [10] M. M. Lee, J. Teuscher, T. Miyasaka, T. N. Murakami, and H. J. Snaith, "Efficient hybrid solar cells based on meso-structured organometal halide perovskites," *Science*, vol. 338, no. 6107, pp. 643–647, 2012.

- [11] Y. Li, J. K. Cooper, R. Buonsanti et al., "Fabrication of planar heterojunction perovskite solar cells by controlled low-pressure vapor annealing," *Journal of Physical Chemistry Letters*, vol. 6, no. 3, pp. 493–499, 2015.
- [12] H. Liu, Z. Huang, S. Wei, L. Zheng, L. Xiao, and Q. Gong, "Nano-structured electron transporting materials for perovskite solar cells," *Nanoscale*, vol. 8, no. 12, pp. 6209–6221, 2016.
- [13] M. He, D. Zheng, M. Wang, C. Lin, and Z. Lin, "High efficiency perovskite solar cells: from complex nanostructure to planar heterojunction," *Journal of Materials Chemistry A*, vol. 2, no. 17, pp. 5994–6003, 2014.
- [14] H. Lu, K. Deng, N. Yan et al., "Efficient perovskite solar cells based on novel three-dimensional TiO<sub>2</sub> network architectures," *Science Bulletin*, vol. 61, no. 10, pp. 778–786, 2016.
- [15] Y. Yang, K. Ri, A. Mei et al., "The size effect of TiO<sub>2</sub> nanoparticles on a printable mesoscopic perovskite solar cell," *Journal of Materials Chemistry A*, vol. 3, no. 17, pp. 9103–9107, 2015.
- [16] S. Aharon, S. Gamliel, B. E. Cohen, and L. Etgar, "Depletion region effect of highly efficient hole conductor free CH<sub>3</sub>NH<sub>3</sub>PbI<sub>3</sub> perovskite solar cells," *Physical Chemistry Chemical Physics*, vol. 16, no. 22, pp. 10512–10518, 2014.
- [17] Y. Zhao, A. M. Nardes, and K. Zhu, "Solid-state mesostructured perovskite CH<sub>3</sub>NH<sub>3</sub>PbI<sub>3</sub> solar cells: charge transport, recombination, and diffusion length," *Journal of Physical Chemistry Letters*, vol. 5, no. 3, pp. 490–494, 2014.
- [18] H.-S. Kim and N.-G. Park, "Parameters affecting I–V hysteresis of CH<sub>3</sub>NH<sub>3</sub>PbI<sub>3</sub> perovskite solar cells: effects of perovskite crystal size and mesoporous TiO<sub>2</sub> layer," *Journal of Physical Chemistry Letters*, vol. 5, no. 17, pp. 2927–2934, 2014.
- [19] A. Rapsomanikis, D. Karageorgopoulos, P. Lianos, and E. Stathatos, "High performance perovskite solar cells with functional highly porous TiO<sub>2</sub> thin films constructed in ambient air," *Solar Energy Materials and Solar Cells*, vol. 151, pp. 36–43, 2016.
- [20] W. Wang, Z. Zhang, Y. Cai et al., "Enhanced performance of CH<sub>3</sub>NH<sub>3</sub>PbI<sub>3-x</sub>Cl<sub>x</sub> perovskite solar cells by CH<sub>3</sub>NH<sub>3</sub>I modification of TiO<sub>2</sub>-perovskite layer interface," *Nanoscale Research Letters*, vol. 11, no. 1, article 316, 2016.
- [21] S. Dharani, H. K. Mulmudi, N. Yantara et al., "High efficiency electrospun TiO<sub>2</sub> nanofiber based hybrid organic–inorganic perovskite solar cell," *Nanoscale*, vol. 6, no. 3, pp. 1675–1679, 2014.
- [22] A. Sarkar, N. J. Jeon, J. H. Noh, and S. I. Seok, "Well-organized mesoporous TiO<sub>2</sub> photoelectrodes by block copolymer-induced sol–Gel assembly for inorganic–organic hybrid perovskite solar cells," *Journal of Physical Chemistry C*, vol. 118, no. 30, pp. 16688–16693, 2014.
- [23] Y. J. Kim, Y. H. Lee, M. H. Lee et al., "Formation of efficient dye-sensitized solar cells by introducing an interfacial layer of long-range ordered mesoporous TiO<sub>2</sub> thin film," *Langmuir*, vol. 24, no. 22, pp. 13225–13230, 2008.
- [24] J. Du, X. Lai, N. Yang et al., "Hierarchically ordered macro–mesoporous TiO<sub>2</sub>–graphene composite films: improved mass transfer, reduced charge recombination, and their enhanced photocatalytic activities," *ACS Nano*, vol. 5, no. 1, pp. 590–596, 2011.
- [25] C. Dionigi, P. Greco, G. Ruani, M. Cavallini, F. Borgatti, and F. Biscarini, "3D hierarchical porous TiO<sub>2</sub> films from colloidal composite fluidic deposition," *Chemistry of Materials*, vol. 20, no. 22, pp. 7130–7135, 2008.
- [26] S. Wang, W. Dong, X. Fang et al., "Credible evidence for the passivation effect of remnant PbI<sub>2</sub> in CH<sub>3</sub>NH<sub>3</sub>PbI<sub>3</sub> films in improving the performance of perovskite solar cells," *Nanoscale*, vol. 8, no. 12, pp. 6600–6608, 2016.
- [27] Y. H. Lee, J. Luo, R. Humphry-Baker, P. Gao, M. Grätzel, and M. K. Nazeeruddin, "Unraveling the reasons for efficiency loss in perovskite solar cells," *Advanced Functional Materials*, vol. 25, no. 25, pp. 3925–3933, 2015.
- [28] J. Jiang, H. J. Tao, S. Chen et al., "Efficiency enhancement of perovskite solar cells by fabricating as-prepared film before sequential spin-coating procedure," *Applied Surface Science*, vol. 371, pp. 289–295, 2016.
- [29] D. H. Cao, C. C. Stoumpos, C. D. Malliakas et al., "Remnant PbI<sub>2</sub>, an unforeseen necessity in high-efficiency hybrid perovskite-based solar cells? A)," *APL Materials*, vol. 2, no. 9, Article ID 091101, 2014.
- [30] Y. Zhao and K. Zhu, "Charge transport and recombination in perovskite (CH<sub>3</sub>NH<sub>3</sub>)PbI<sub>3</sub> sensitized TiO<sub>2</sub> solar cells," *The Journal of Physical Chemistry Letters*, vol. 4, no. 17, pp. 2880–2884, 2013.
- [31] T. Baikie, Y. Fang, J. M. Kadro et al., "Synthesis and crystal chemistry of the hybrid perovskite (CH<sub>3</sub>NH<sub>3</sub>)PbI<sub>3</sub> for solid-state sensitised solar cell applications," *Journal of Materials Chemistry A*, vol. 1, no. 18, pp. 5628–5641, 2013.
- [32] Y. Tu, J. Wu, M. Zheng et al., "TiO<sub>2</sub> quantum dots as superb compact block layers for high-performance CH<sub>3</sub>NH<sub>3</sub>PbI<sub>3</sub> perovskite solar cells with an efficiency of 16.97%," *Nanoscale*, vol. 7, no. 48, pp. 20539–20546, 2015.
- [33] W. Ke, G. Fang, J. Wan et al., "Efficient hole-blocking layer-free planar halide perovskite thin-film solar cells," *Nature Communications*, vol. 6, article 6700, 2015.
- [34] W. Ke, G. Fang, Q. Liu et al., "Low-temperature solution-processed tin oxide as an alternative electron transporting layer for efficient perovskite solar cells," *Journal of the American Chemical Society*, vol. 137, no. 21, pp. 6730–6733, 2015.

## Research Article

# Impedance Spectroscopic Investigation of the Degraded Dye-Sensitized Solar Cell due to Ageing

Parth Bhatt,<sup>1</sup> Kavita Pandey,<sup>1,2</sup> Pankaj Yadav,<sup>3</sup> Brijesh Tripathi,<sup>4</sup> and Manoj Kumar<sup>4</sup>

<sup>1</sup>Department of Solar Energy, School of Technology, Pandit Deendayal Petroleum University, Gandhinagar 382007, India

<sup>2</sup>Inorganic Chemistry Laboratory, University of Oxford, South Parks Road, Oxford OXI 3QR, UK

<sup>3</sup>Department of Electrical Engineering, Incheon National University, Incheon 406772, Republic of Korea

<sup>4</sup>Department of Science, School of Technology, Pandit Deendayal Petroleum University, Gandhinagar 382007, India

Correspondence should be addressed to Manoj Kumar; [manoj.kspv@gmail.com](mailto:manoj.kspv@gmail.com)

Received 19 July 2016; Accepted 9 November 2016

Academic Editor: Francisco R. Zepeda

Copyright © 2016 Parth Bhatt et al. This is an open access article distributed under the Creative Commons Attribution License, which permits unrestricted use, distribution, and reproduction in any medium, provided the original work is properly cited.

This paper investigates the effect of ageing on the performance of dye-sensitized solar cells (DSCs). The electrical characterization of fresh and degraded DSCs is done under AM1.5G spectrum and the current density-voltage ( $J$ - $V$ ) characteristics are analyzed. Short circuit current density ( $J_{SC}$ ) decreases significantly whereas a noticeable increase in open circuit voltage is observed. These results have been further investigated electroanalytically using electrochemical impedance spectroscopy (EIS). An increase in net resistance results in a lower  $J_{SC}$  for the degraded DSC. This decrease in current is mainly due to degradation of  $TiO_2$ -dye interface, which is observed from light and dark  $J$ - $V$  characteristics and is further confirmed by EIS measurements. A reduction in the chemical capacitance of the degraded DSC is observed, which is responsible for the shifting of Fermi level with respect to conduction band edge that further results in an increase of open circuit voltage for the degraded DSC. It is also confirmed from EIS that the degradation leads to a better contact formation between the electrolyte and Pt electrode, which improves the fill factor of the DSC. But the recombination throughout the DSC is found to increase along with degradation. This study suggests that the DSC should be used under low illumination conditions and around room temperature for a longer life.

## 1. Introduction

The metal oxide based dye-sensitized solar cells (DSCs) have attracted significant attention of researchers in recent years, because of their economic fabrication process and efficient working under diffuse illumination. The highest certified device efficiency has reached 11.9% [1]. A DSC module of large area ( $100\text{ cm}^2$ ) has been demonstrated with an efficiency of 8.4% [2]. The DSC was explicated by O'Regan and Grätzel [3], which operates by exposing dye molecules to light that releases excited electrons to oxidize the dye, which is then restored by electron donation from the redox couples (iodide/triiodide,  $I^-/I_3^-$ ) in the electrolyte. The redox couples are then revived by counter electrode with electrons extracted from the working electrode via the external load circuitry. Though the DSCs have demonstrated a highly promising performance instantly, the long term performance

plays a major role in the commercialization of a solar PV technology. The poor stability of DSC is mainly directed by the degradation mechanism occurring at different layers of the device after prolonged operation. So, the analysis of the degradation mechanisms within DSC is of great interest to explore the factors affecting the performance of DSCs. Only a few papers present the stability studies of DSC [4–9]. Different techniques have been used to analyze the degradation mechanisms in DSCs; Uam et al. [10] used UV-vis absorption spectroscopy to identify that the desorption of dye on the  $TiO_2$  surface was the reason for current density reduction in an aged cell. Additionally, Tatay et al. [11] accompanied the UV-vis absorption spectroscopy with luminescence and cyclic voltammetry and observed that organic dyes formed molecular aggregates which could deteriorate the device efficiency. Also, there are few studies which used electrochemical impedance spectroscopy (EIS)

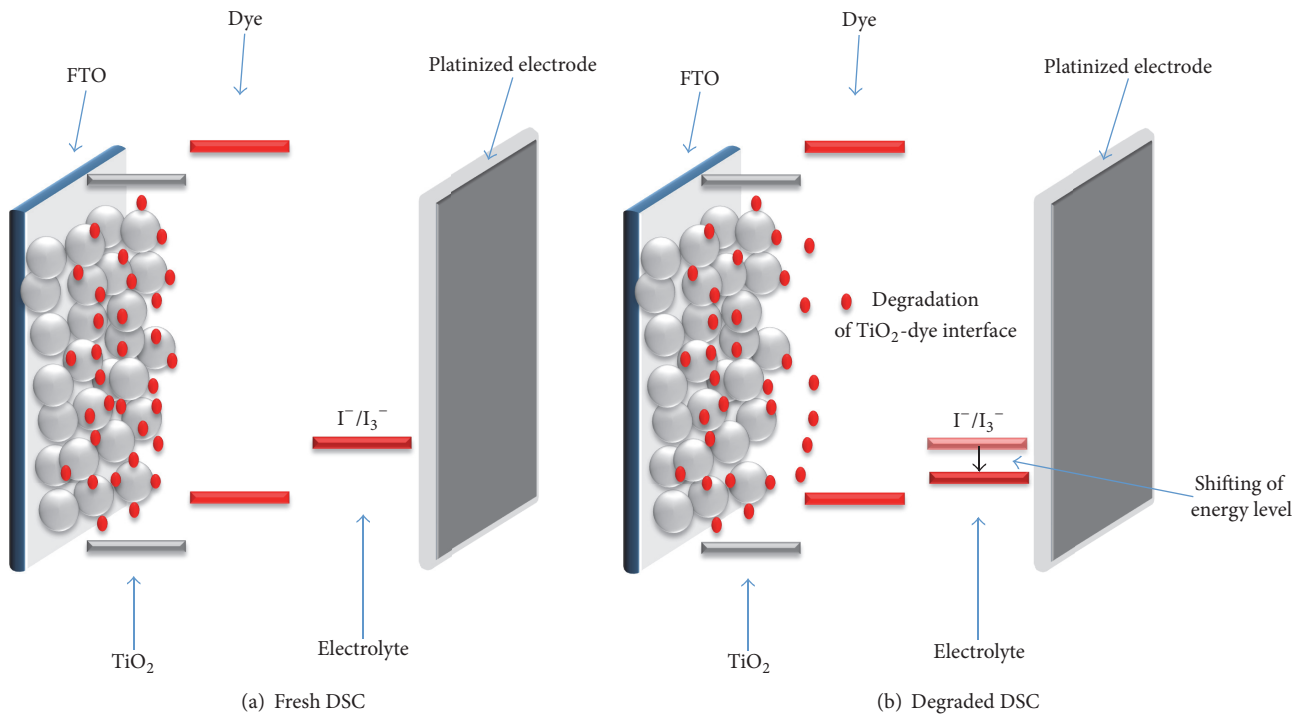


FIGURE 1: Schematic diagram representing the components of (a) fresh DSC and (b) degraded DSC.

to investigate degradations in ageing DSCs [4, 8] but they lack in-depth understanding on the correlation of electron kinetics with the device performance.

In our previous report, we have analyzed the interfacial losses in large area DSCs [12]. In continuation with previous studies, this article reports the electroanalytical analysis of various degradation mechanisms within DSC of comparatively larger area ( $= 3.78 \text{ cm}^2$ ) for a gap of 45 days using the EIS technique. A schematic diagram to show the mechanisms of degradation in the reported DSC is shown in Figure 1.

## 2. Experimental

The details of the fabrication of DSCs are discussed in our previous work [12]. In short, FTO thin films, about 1 mm thick, were spray-deposited on Corning glass sheets. Silver grid lines (with 12 mm intervals) were deposited on the above FTO using Ag paste. Mesoporous TiO<sub>2</sub> was deposited between silver grids after which the samples were dipped into a 3 mM solution of N719 dye for 12 h. Counter electrodes were prepared by lightly sputtering Pt (50 nm) on 1.1 mm thick titanium metal plates. For each cell, photoelectrodes and counter electrodes were sandwiched, and UV was irradiated to cure the sealant while using a mask to cover the dye coated area. The active area of the fabricated cell is  $3.78 \text{ cm}^2$  (fabricated by SPD laboratory, Japan).

The photovoltaic measurements were carried out using a solar simulator (Photoemission Tec SS80AAA with 1.5AM-G filter) and a source measuring unit (U2722A, Agilent). A three-electrode potentiostat (CHI 660D) equipped with a general purpose software was used for the EIS measurements.

The working electrode was connected to the positive terminal of the cell whereas the counter electrode and reference electrode were shorted and connected to the negative terminal of the DSC. An AC perturbation signal of 10 mV (root-mean-square voltage) was applied in the frequency range of 10 mHz to 1000 kHz during the EIS measurements. The inductive effect between the connecting leads and the potentiostat were taken care of during the experiments.

## 3. Results and Discussion

**3.1. J-V Analysis.** Figures 2(a) and 2(b) depict the light and dark *J-V* characteristics of a fresh and degraded DSC, respectively. As received DSC shows a power conversion efficiency ( $\eta$ ) of 4.0%, short circuit current density ( $J_{SC}$ ) of  $9.92 \text{ mA/cm}^2$ , open circuit voltage ( $V_{OC}$ ) of 0.65 V, and fill factor (FF) of 60.9%, but after degradation  $\eta$  reduces to 3.6% with  $J_{SC}$  of  $7.74 \text{ mA/cm}^2$ ,  $V_{OC}$  of 0.685 V, and FF of 67%. From the above observation, it is clear that the drop in  $J_{SC}$  has played a vital role in degradation of the device. This significant loss in  $J_{SC}$  in the degraded cell may be attributed to the increased recombination and resistive losses in the device. In DSCs, the recombination loss is mainly associated with (i) electron recombination from TiO<sub>2</sub> conduction band and deep and shallow level traps to the electrolyte and (ii) electron recombination from the uncovered layer of FTO to the electrolyte [13]. Conversely, the resistive losses are mainly linked to the resistance at FTO-TiO<sub>2</sub> interface, resistance due to the diffusion of redox species in the electrolyte, the charge transfer resistance at platinized counter electrode-electrolyte interface, and sheet resistance of FTO [14, 15].

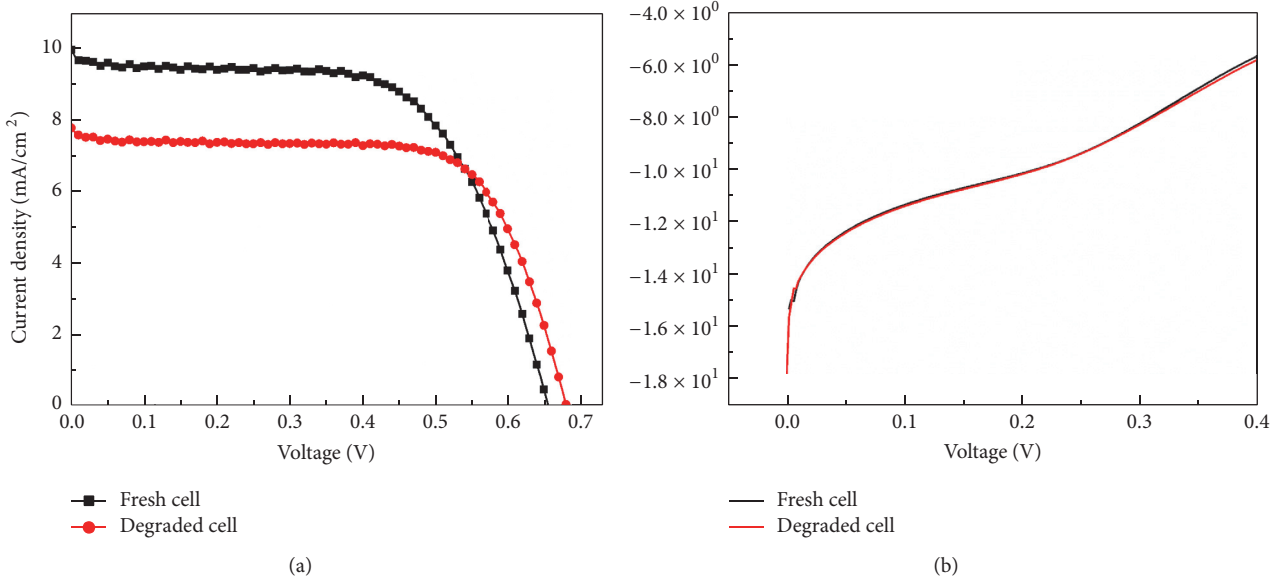


FIGURE 2: (a) Current density-voltage ( $J$ - $V$ ) characteristics of fresh DSC and degraded DSC. (b) Dark  $J$ - $V$  for fresh and degraded DSC.

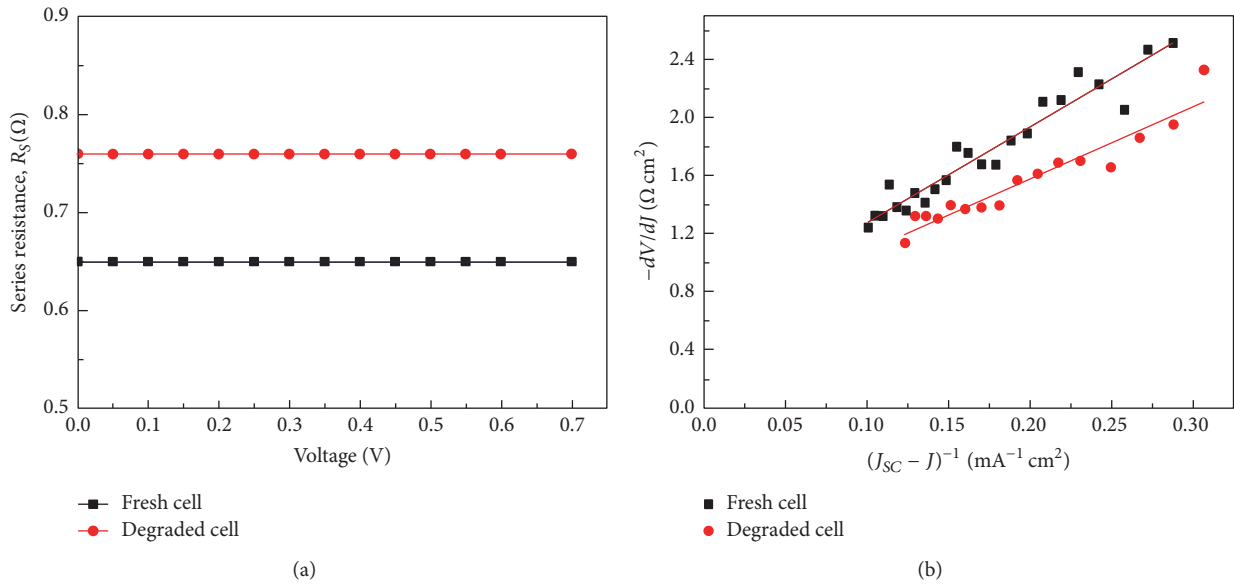


FIGURE 3: (a)  $R_s$  of both cells calculated by EIS. (b)  $R_s$  of both cells calculated by light  $J$ - $V$ .

$V_{OC}$  and FF have been surprisingly observed to improve along with the degradation of the cell. The improvement in FF can be ascribed to the formation of better contact between the electrolyte and Pt electrode along with degradation [16]. The increase in  $V_{OC}$  of degraded DSC has been observed by Lai et al. [4]. The increase can also be attributed to greater photon flux received by the dye, the reduction of  $\text{I}^{3-}$  concentration, or reduction of dye cation concentration.

To get further understanding about the degradation of DSC, the  $J$ - $V$  characteristics are calculated by  $J = J_0 \exp((qV + JR_s)/mk_B T) - J_{SC}$ , where  $J_0$  is the dark exchange current,  $R_s$  is the series resistance,  $m$  is the diode ideality factor which depends on the rate of recombination reaction of electrons,

oxidized species in the electrolyte, and the distribution of recombination sites [17], and  $q$ ,  $k_B$ , and  $T$  represent the electronic charge, Boltzmann's constant, and cell temperature, respectively. The equation above can be reduced as (considering  $J_0$  as negligible to  $J_{SC}$ )  $dV/dJ = R_s + (mk_B T/q) \cdot (1/(J_{SC} - J))$  [18, 19].

Figure 3(a) shows plot of  $-dV/dJ$  versus  $(J_{SC} - J)^{-1}$  for fresh and degraded DSCs in which a linear fit is made to the experimental data to estimate the values of  $m$  and  $R_s$ . For fresh DSC  $m$  and  $R_s$  are obtained to be 1.18 and  $0.65 \Omega \text{cm}^2$  and for degraded DSC they are obtained as 1.22 and  $0.76 \Omega \text{cm}^2$ , respectively. Figure 3(b) shows plot of  $R_s$  versus voltage for fresh and degraded DSCs. The increase in

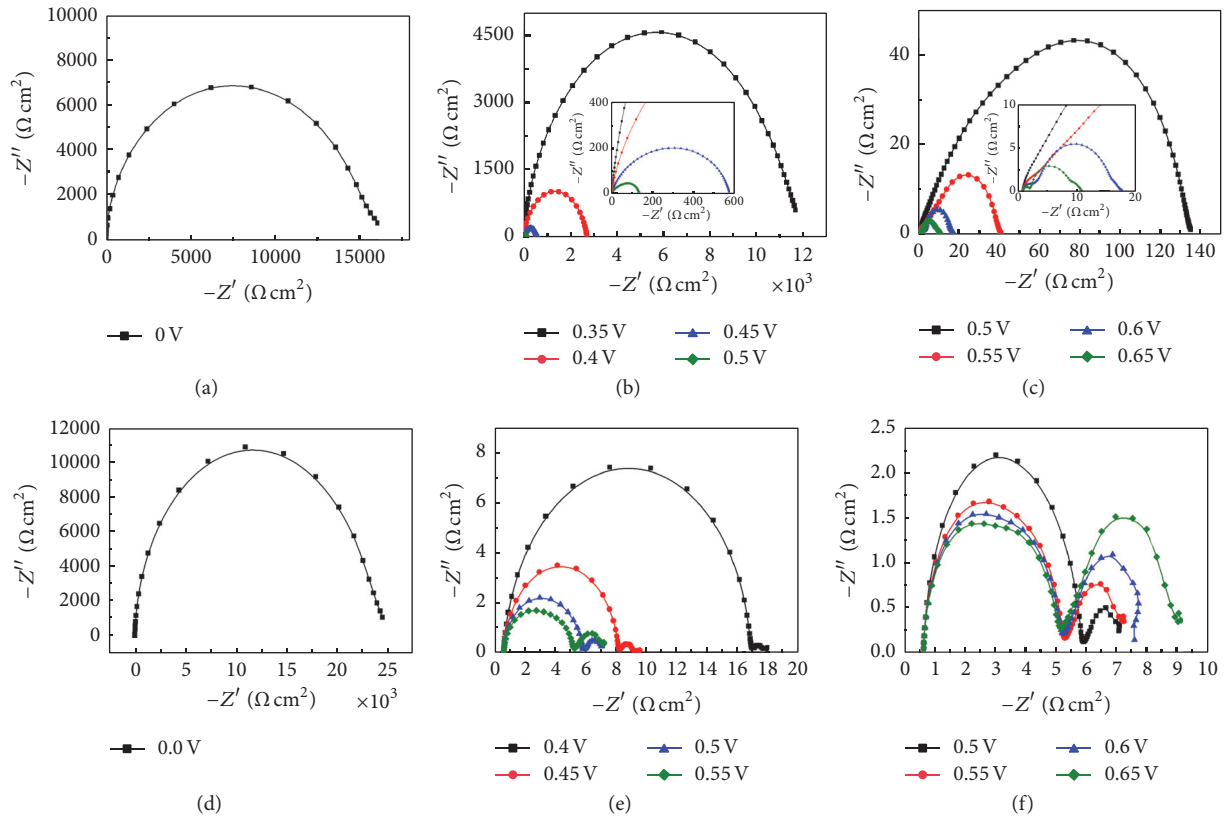


FIGURE 4: Nyquist plot for fresh DSC (a) at 0 bias, (b) near knee voltage, and (c) near  $V_{OC}$ , respectively. Nyquist plot for degraded DSC (d) at 0 bias, (e) near knee voltage, and (f) near  $V_{OC}$ , respectively.

$R_S$  of  $0.12 \Omega \text{ cm}^2$  for the degraded DSC can be considered as one of the possible reasons for increase in resistive losses resulting in lower  $J_{SC}$  in degraded cells. Furthermore, the shunt resistance for the fresh and degraded DSCs is obtained as  $1552 \Omega \text{ cm}^2$  and  $2845 \Omega \text{ cm}^2$ , respectively. The increased shunt resistance due to degradation is responsible for improvement in the FF and  $V_{OC}$  of the degraded DSC.

No conclusive evidence for the cause of degradation can be identified solely with analysis of  $J$ - $V$  characteristics, as the DSCs have a complex device structure, nonlinear recombination mechanism, and indivisible device parameters. So, in order to have a conclusive evidence for the observed degradation the DC and AC characterizations, that is, impedance spectroscopy (IS) and  $J$ - $V$ , are combined together.

**3.2. EIS Analysis.** Electrochemical impedance spectroscopy (EIS) is used to identify the performance limiting factors leading to degradation of DSCs. Using EIS the various physical processes can be modelled (under the appropriate conditions) in terms of resistive and capacitive elements [20]. The aim of this article is to compare the fresh DSC and degraded DSC, which can be done on the basis of selected crucial parameters with a simplified model as compared to the transmission line model. The transmission line model is generally used to describe the working of a DSC in detail, which was not required in this case. The

characteristic impedance spectroscopic data measured under dark conditions of the fresh and degraded DSCs depicts the contribution from various charge transport layers as shown in Figure 4. In order to analyze the data the Nyquist plot is used, which shows different arcs to represent different processes occurring within the device with respect to frequency. This method helps in quantifying the dynamic features of the system to compare their values. From the Nyquist plot ( $Z'$  versus  $Z''$ ) the value of resistance can be estimated by the width of the arc in the real axis. As described in device operation, several interfaces in the DSC involve high level of electron transfer and transport. These processes include charge transport through porous  $\text{TiO}_2$  layer, electron transfer at  $\text{TiO}_2$ -dye/electrolyte interface,  $\text{I}_3^-$  diffusion region in electrolytic medium, and electron transfer at electrolyte/Pt interface. Another important representation is the Bode plot, that is,  $|Z|$  versus frequency and phase versus frequency plots. The resistances can be obtained from the plateaus. The important aspect of this plot is that  $\omega$  information is not lost.

**3.2.1. At 0 Bias.** Figures 4(a)–4(f) show the Nyquist plot of the fresh and degraded cells under various bias in dark conditions. The line following the experimental data in Figure 4 represents the theoretical fit. Figures 5(a)–5(f) represent the Bode plots for the fresh and degraded DSCs. The fitting of the experimental data is done using the equivalent circuit as shown in Figure 6(a). At zero bias, that is, when the

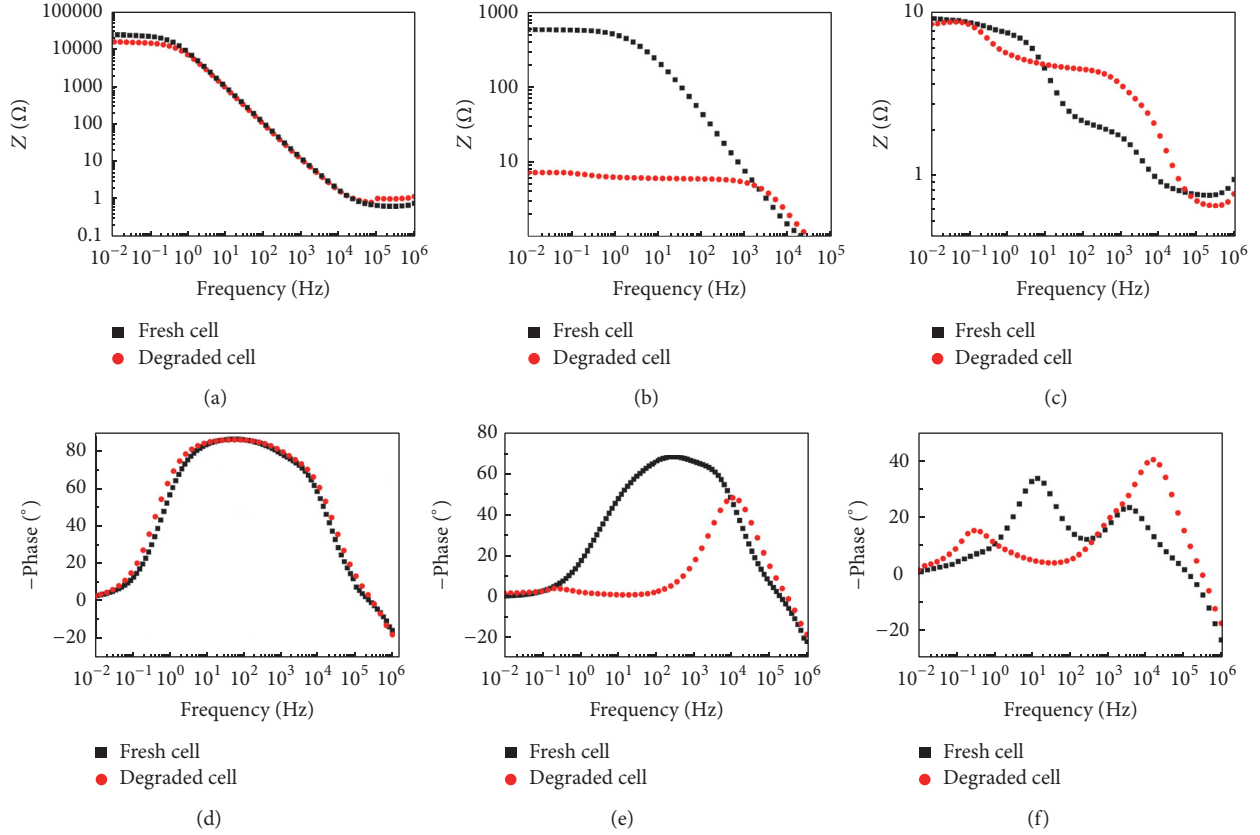


FIGURE 5: Bode plots for fresh and degraded DSC (a–d) at 0 bias, (b–e) at knee voltage, and (c–f) at  $V_{OC}$ , respectively.

device is under nonconducting state, a standard Nyquist plot is observed for fresh DSC [21]. But, for a degraded DSC there is an increase in magnitude of impedance, which can be attributed to increase in  $R_1$  (at FTO-TiO<sub>2</sub> interface).  $R_s$  for the fresh and degraded DSC from the EIS measurements are estimated to be  $0.63 \Omega \text{ cm}^2$  and  $0.78 \Omega \text{ cm}^2$ , respectively, which are well in agreement with that obtained from  $J$ - $V$  measurements. Figure 5(a), that is, the Bode plot at zero bias, shows the change in  $R_s$ . The height of the plateau region for the degraded cell has increased which depicts change in  $R_1$  as observed in impedance. Also the change in height of the plateau shows change in  $R_1$ . Xue et al. [8] have showed that increase in resistance  $R_1$  is caused due to formation of cracks in TiO<sub>2</sub> photoelectrode. The Bode plot of phase versus frequency follows almost a similar trend for both the fresh and degraded DSCs.

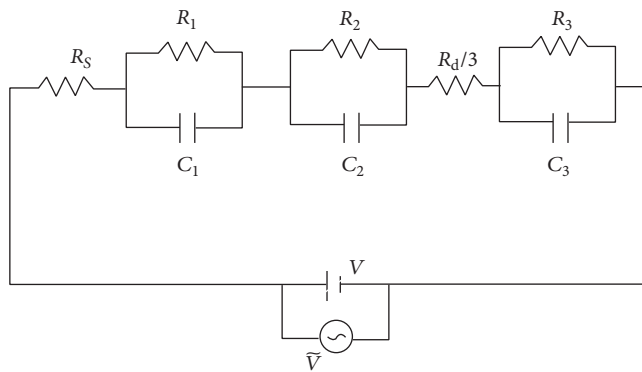
### 3.2.2. At Knee Voltage (the Voltage at Maximum Power Point).

The EIS for the DSCs near knee yields two semicircles with their frequencies corresponding to TiO<sub>2</sub>-dye/electrolyte and electrolyte/Pt, but the dominant semicircle represents TiO<sub>2</sub>-dye/electrolyte medium which depicts the Nyquist feature of Gerischer element and overall impedance of the cell decreases with increase in bias [22, 23]. The Gerischer element originates from the FB reduction of  $\text{I}_3^-$  ions by electrons from the conduction band of  $\text{TiO}_2(1/2)\text{I}_3^- + e^-(\text{TiO}_2) = (3/2)\text{I}^-$  [24]. It can be clearly observed from the EIS for the fresh

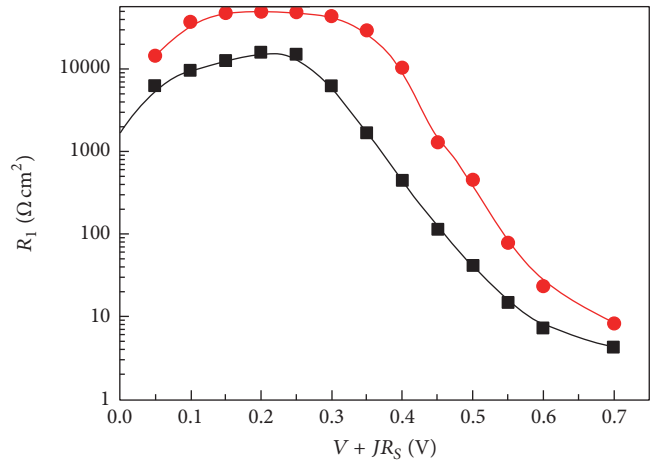
and degraded cells that resistance  $R_2$  (resistance at TiO<sub>2</sub>-dye/electrolyte interface) has reduced dramatically for the degraded devices. This reduction in  $R_2$  can be attributed to reduction in electron collection from TiO<sub>2</sub> to FTO electrode. In the Bode plot at knee voltage (Figure 5(b)), the slope for degraded cell changes dynamically, which shows the increase in  $R_2$ . Furthermore, electron lifetime ( $\tau_e$ ) can be estimated from Figure 5(e) using the relation  $\tau_e = 1/2\pi f_{\text{max}}$  [24, 25], where  $f_{\text{max}}$  represents peak frequency.  $\tau_e$  for fresh DSCs is observed to be higher than that for degraded samples. This reduction in  $\tau_e$  reduces the diffusion of the  $\text{I}^{3-}$  ions in electrolyte, which increases the concentration of  $\text{I}^{3-}$  ions at the TiO<sub>2</sub>-dye/electrolyte interface, which further increases the recombination leading to degradation in performance of DSCs.

### 3.2.3. Near Open Circuit Voltage.

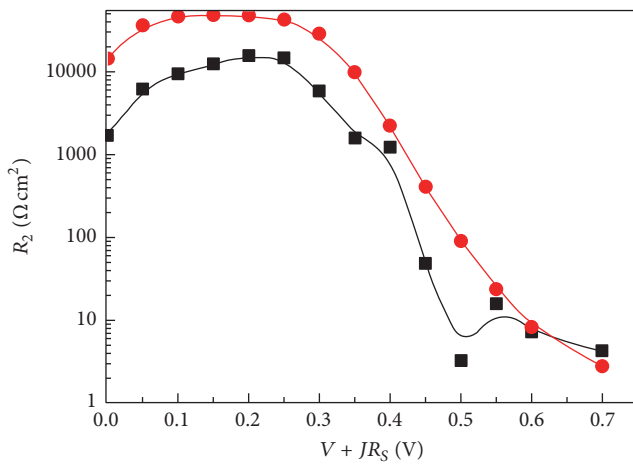
The Nyquist plot near  $V_{OC}$  shows three semicircles representing all three regions within the device. Interestingly for the degraded DSCs with increasing bias the circle representing TiO<sub>2</sub>-dye/electrolyte interface decreases and that for electrolyte/Pt interface increases. In the Bode plot we observe two characteristic peaks: the peak at lower frequency corresponds to the TiO<sub>2</sub>-dye/electrolyte interface and that at high frequency corresponds to electrolyte/Pt interface. The peak for TiO<sub>2</sub>-dye/electrolyte interface is lower for degraded DSC as compared to fresh ones corresponding to reduction in charge transfer at the interface.



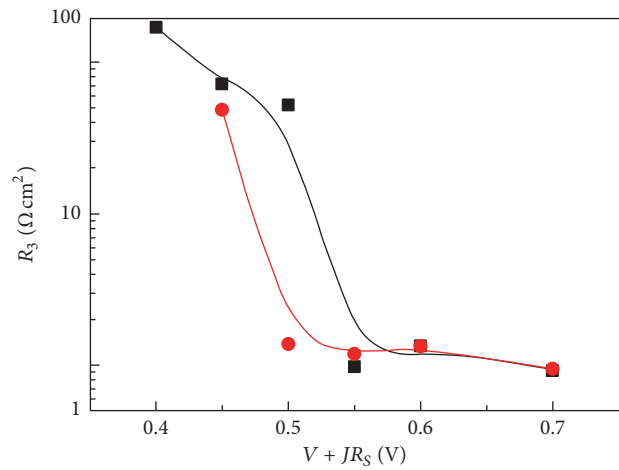
(a)



(b)



(c)



(d)

FIGURE 6: (a) Equivalent circuit used for fitting EIS. Variation of resistances (b)  $R_1$ , (c)  $R_2$ , and (d)  $R_3$  as a function of applied bias, respectively.

While comparing the Nyquist plots for fresh and degraded DSC for electrolyte/Pt interface, we observe a higher peak for the degraded DSC, which validates better charge transfer at the interface. Hence we can say that degradation of DSC leads to better contact formation between the electrolyte and Pt. This better contact formation is further responsible for higher FF and  $V_{OC}$  for the degraded DSC [16].

Figures 6(b)–6(d) show the plots for  $R_1$ ,  $R_2$ , and  $R_3$  versus voltage for the fresh and degraded cells. The lower value of  $R_1$  for degraded cell throughout the bias in Figure 6(b) is one of the reasons for the reduction in  $J_{SC}$ .  $R_2$  for degraded cell is higher than fresh cell till  $V_{OC}$ , beyond which it decreases, which signifies low charge transfer within the device for the degraded DSCs. Interestingly,  $R_3$  (resistance at electrolyte/Pt-FTO interface) for the degraded cells is observed to be lower than that for the fresh ones. This reduction in  $R_3$  may be

attributed to better charge transfer between the electrolyte and Pt, which validates the observation in Bode plot and further justifies the enhancement in FF and  $V_{OC}$  due to degradation. The sum of all resistances,  $R_1 + R_2 + R_3$ , gives rise to higher net series resistance resulting in lower  $J_{SC}$ . With increasing resistance a drop in chemical capacitance,  $C_2$ , is observed within the device signifying lower electron injection into the conduction band of  $TiO_2$ . Bisquert [20] showed a direct dependence of  $C_2$  on the difference between the positions of electron Fermi level with respect to the conduction band. The lower value of  $C_2$  results in shifting of the Fermi level towards the conduction band edge, which further results in increase in  $V_{OC}$  due to degradation.

Bisquert and Mora-Seró [25] have indicated that the electron back recombination rate ( $U$ ) is nonlinear in a DSC. This nonlinear nature of the recombination can be represented

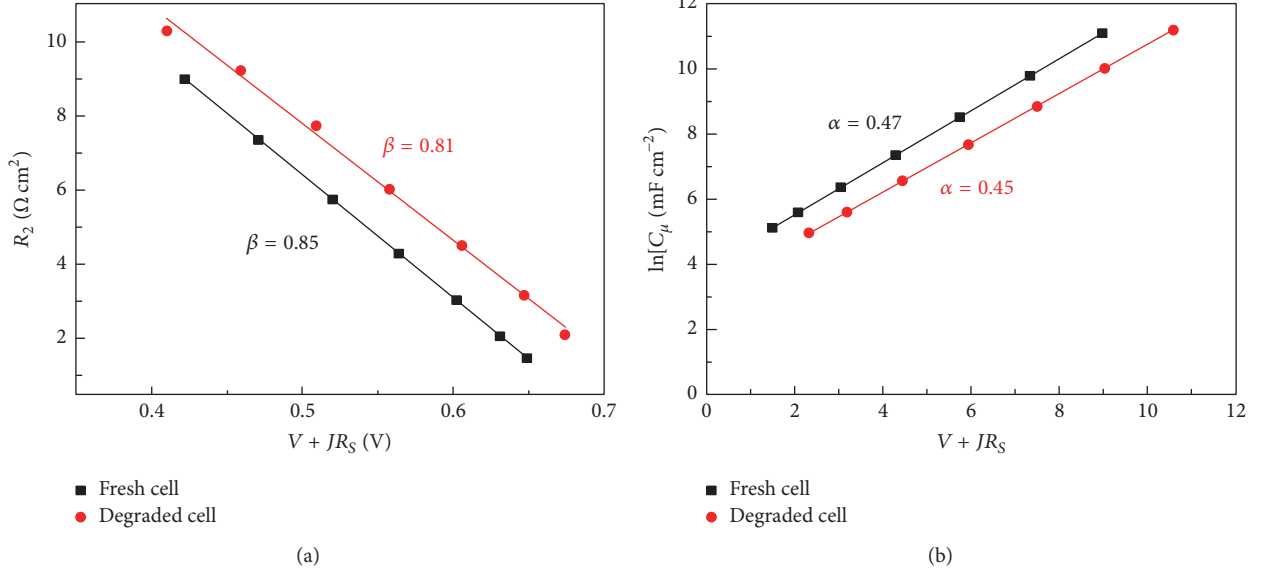


FIGURE 7: Comparative plot for (a) recombination resistance and (b) chemical capacitance for fresh and degraded DSC, respectively. The line indicates theoretical fit.

using the reaction rate  $\beta$ , which is expressed as  $U = k_r n^\beta$ , where  $k_r$  is a constant and  $n$  is free electron density. The order of recombination,  $\beta$ , ranges from 0 and 1. A recombination order of 1 indicates a simple unimolecular recombination via conduction band states. Generally, for DSCs a recombination order of the range between 0.6 and 0.8 is observed [26, 27]. The detailed role and estimation of  $\beta$  in DSCs are reported in our previous work [12]. The plot for estimation of  $\beta$  is shown in Figure 7(a). The  $\beta$  values for fresh and degraded DSCs are estimated as 0.85 and 0.81, respectively. Sarker et al. [27] have expressed the dependence of  $V_{OC}$  on  $\beta$  as  $V_{OC} = (k_B T / q\beta) \ln(J_{PH} / J_0)$ . From the above equation it can be stated that the decrease in  $\beta$  along with degradation is responsible for the decrease in charge collection due to recombination and also for increase in  $V_{OC}$ .

As reported by Wang et al. [21], the chemical capacitance  $C_2$  can be expressed as  $C_2 = C_0 \exp(-\alpha q V_F / k_B T) = C_0 \exp(-q V_F / k_B T_0)$ , where  $\alpha$  is related to the exponential trap distribution of electrons below the conduction band or it is simply a band gap modulation factor. The plot of  $\ln C_2$  versus applied bias for the fresh and degraded DSC is shown in Figure 7(b). The linear fit of the graph provides the value of  $\alpha$ . The value of  $\alpha$  for fresh and degraded DSC is obtained as 0.47 and 0.45, respectively. The decrease in  $\alpha$  again proves the shifting of Fermi level as observed in EIS, which is responsible for increase in  $V_{OC}$  and fill Factor along with the degradation of DSC.

The net terminal  $J$ - $V$  characteristic of DSC is given by [28]

$$J_{\text{cell}} = J_{\text{ph}} - J_0 \left[ \exp \left( \frac{q\beta(V + j_{\text{cell}}R_S)}{k_B T} \right) - 1 \right] - \frac{V_{\text{cell}} + j_{\text{cell}}R_S}{R_{\text{SH}}}, \quad (1)$$

TABLE 1: Parameters used for simulating the experimental  $J$ - $V$  curve for fresh and degraded DSC.

Parameters	Fresh DSC	Degraded DSC
Series resistance, $R_S$ ( $\Omega \text{ cm}^2$ )	0.65	0.76
Photocurrent density, $J_{\text{ph}}$ ( $\text{mA/cm}^2$ )	9.73	7.64
Order of recombination, $\beta$	0.85	0.81
Reverse saturation current, $J_0$ ( $\text{A/cm}^2$ )	$2.23E - 07$	$1.59E - 07$

where the term  $J_0[\exp(q\beta V_j / k_B T) - 1]$  indicates the dependence of charge transfer current on the applied voltage and can be approximated through simplified Butler-Volmer equation [22, 29] which is essentially the same as the diode equation describing the dark  $J$ - $V$  characteristics. The parameters extracted from the EIS measurements of the fresh and degraded DSCs are listed in Table 1. Using these parameters and equation above the simulated  $J$ - $V$  was generated and fitted on the experimental data. The fitting of simulated and experimental  $J$ - $V$  for fresh and degraded DSC is shown in Figure 8. A good fit of the experimental data suggests a very good evaluation of the performance parameters from the EIS measurements, which further validates the conclusions driven.

#### 4. Conclusions

This paper investigates the effect of environmental parameters on the performance degradation of DSC. The electrical characterization of fresh and degraded DSC is done under AM1.5G spectrum and the current-voltage characteristics

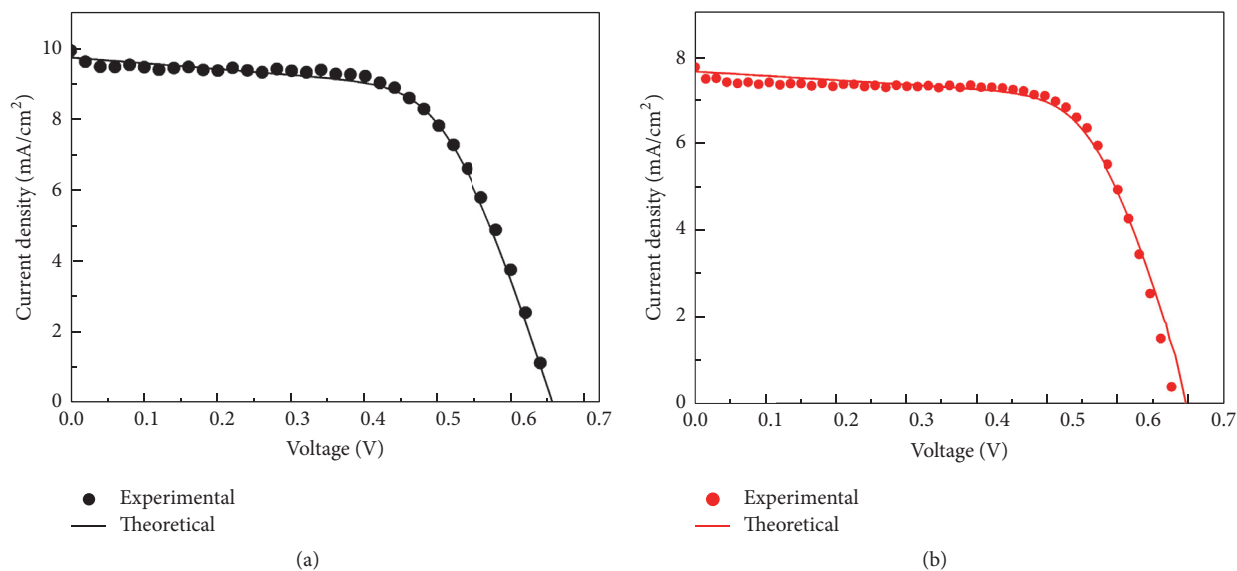


FIGURE 8: Experimental and theoretical fit for  $J$ - $V$  characteristics of (a) fresh and (b) degraded DSC, respectively.

are analyzed. The short circuit current decreases significantly whereas a noticeable increase in open circuit voltage is observed. These results have been further investigated using electrochemical impedance spectroscopic techniques. It is found that the decrease in current is mainly due to dissociation of dye molecules with respect to exposure to ambient environmental conditions, which is confirmed by dark I-V analysis. The increase in  $V_{OC}$  is attributed to Fermi level realignment which is investigated by impedance spectroscopy in the range of applied bias from  $-0.7$  V to  $0$  V. It is found that recombination increases along with ageing of DSC. The study suggests that DSC should be used under low illumination conditions and around room temperature.

## Competing Interests

The authors declare that they have no competing interests.

## Acknowledgments

The authors Parth Bhatt and Kavita Pandey would like to acknowledge Solar Research and Development Centre (SRDC), School of Solar Energy, PDP, and Department of Science and Technology INSPIRE fellowship program for providing financial support, respectively. The authors would like to acknowledge S. Kaneko, SPD laboratories (Hamamatsu, Japan), for providing DSC used in this article.

## References

- [1] M. A. Green, K. Emery, Y. Hishikawa, W. Warta, and E. D. Dunlop, "Solar cell efficiency tables (version 47)," *Progress in Photovoltaics: Research and Applications*, vol. 24, no. 1, pp. 3–11, 2016.
- [2] F.-T. Kong, S.-Y. Dai, and K.-J. Wang, "Review of recent progress in dye-sensitized solar cells," *Advances in OptoElectronics*, vol. 2007, Article ID 75384, 13 pages, 2007.
- [3] B. O'Regan and M. Grätzel, "A low-cost, high-efficiency solar cell based on dye-sensitized colloidal  $TiO_2$  films," *Nature*, vol. 353, no. 6346, pp. 737–740, 1991.
- [4] S. C. Lai, K. N. P. Connor, and L. Ke, "Degradation mechanisms and electron kinetics analysis in aging dye sensitized solar cell using electrochemical impedance spectroscopy," *Journal of the Electrochemical Society*, vol. 158, no. 12, pp. H1193–H1200, 2011.
- [5] P. D. Lund, G. Hashmi, Y. Ma, J. Patakangas, and Y. Jing, "Degradation and stability of nanostructured energy devices," *Microelectronic Engineering*, vol. 126, pp. 49–53, 2014.
- [6] U. Opara Krašovec, M. Bokalič, and M. Topič, "Ageing of DSSC studied by electroluminescence and transmission imaging," *Solar Energy Materials and Solar Cells*, vol. 117, pp. 67–72, 2013.
- [7] D. Pumiglia, M. Giustini, D. Dini et al., "Photoelectrochemical response of DSSCs under prolonged reverse bias and conduction band lowering in Ru-complex-sensitized  $TiO_2$ ," *ChemElectroChem*, vol. 1, no. 8, pp. 1388–1394, 2014.
- [8] G. Xue, Y. Guo, T. Yu et al., "Degradation mechanisms investigation for long-term thermal stability of dye-sensitized solar cells," *International Journal of Electrochemical Science*, vol. 7, no. 2, pp. 1496–1511, 2012.
- [9] F. Li, J. R. Jennings, N. Mathews, and Q. Wang, "Evolution of charge collection/separation efficiencies in dye-sensitized solar cells upon aging: a case study," *Journal of The Electrochemical Society*, vol. 158, no. 9, pp. B1158–B1163, 2011.
- [10] H.-S. Uam, Y.-S. Jung, Y. Jun, and K.-J. Kim, "Relation of Ru(II) dye desorption from  $TiO_2$  film during illumination with photocurrent decrease of dye-sensitized solar cells," *Journal of Photochemistry and Photobiology A: Chemistry*, vol. 212, no. 2-3, pp. 122–128, 2010.
- [11] S. Tatay, S. A. Haque, B. O'Regan et al., "Kinetic competition in liquid electrolyte and solid-state cyanine dye sensitized solar

- cells,” *Journal of Materials Chemistry*, vol. 17, no. 29, pp. 3037–3044, 2007.
- [12] P. Yadav, K. Pandey, B. Tripathi, P. V. V. Jayaweera, S. Kaneko, and M. Kumar, “Electroanalytical investigation of the losses during interfacial charge transport in dye-sensitized solar cell,” *Solar Energy*, vol. 129, pp. 207–216, 2016.
- [13] X. Xu, K. Cao, D. Huang, Y. Shen, and M. Wang, “Disulfide/thiolate based redox shuttle for dye-sensitized solar cells: An Impedance Spectroscopy Study,” *Journal of Physical Chemistry C*, vol. 116, no. 48, pp. 25233–25241, 2012.
- [14] T. Hoshikawa, M. Yamada, R. Kikuchi, and K. Eguchi, “Impedance analysis of internal resistance affecting the photoelectrochemical performance of dye-sensitized solar cells,” *Journal of the Electrochemical Society*, vol. 152, no. 2, pp. E68–E73, 2005.
- [15] M. S. Góes, E. Joanni, E. C. Muniz et al., “Impedance spectroscopy analysis of the effect of TiO<sub>2</sub> blocking layers on the efficiency of dye sensitized solar cells,” *Journal of Physical Chemistry C*, vol. 116, no. 23, pp. 12415–12421, 2012.
- [16] Q. Wang, J.-E. Moser, and M. Grätzel, “Electrochemical impedance spectroscopic analysis of dye-sensitized solar cells,” *The Journal of Physical Chemistry B*, vol. 109, no. 31, pp. 14945–14953, 2005.
- [17] H. Tian, E. Gabrielsson, P. W. Lohse et al., “Development of an organic redox couple and organic dyes for aqueous dye-sensitized solar cells,” *Energy & Environmental Science*, vol. 5, no. 12, pp. 9752–9755, 2012.
- [18] D. J. Crain, S. E. Rock, J. E. Garland, and D. Roy, “Comparison of D.C. and A.C. electro-analytical methods for measuring diode ideality factors and series resistances of silicon solar cells,” *Current Applied Physics*, vol. 13, no. 9, pp. 2087–2097, 2013.
- [19] J. Shi, J. Dong, S. Lv et al., “Hole-conductor-free perovskite organic lead iodide heterojunction thin-film solar cells: high efficiency and junction property,” *Applied Physics Letters*, vol. 104, no. 6, Article ID 063901, 2014.
- [20] J. Bisquert, “Chemical capacitance of nanostructured semiconductors: its origin and significance for nanocomposite solar cells,” *Physical Chemistry Chemical Physics*, vol. 5, no. 24, pp. 5360–5364, 2003.
- [21] Q. Wang, S. Ito, M. Grätzel et al., “Characteristics of high efficiency dye-sensitized solar cells,” *The Journal of Physical Chemistry B*, vol. 110, no. 50, pp. 25210–25221, 2006.
- [22] J. E. Garland, D. J. Crain, and D. Roy, “Utilization of electrochemical impedance spectroscopy for experimental characterization of the diode features of charge recombination in a dye sensitized solar cell,” *Electrochimica Acta*, vol. 148, pp. 62–72, 2014.
- [23] Á. Pitarch, G. Garcia-Belmonte, I. Mora-Seró, and J. Bisquert, “Electrochemical impedance spectra for the complete equivalent circuit of diffusion and reaction under steady-state recombination current,” *Physical Chemistry Chemical Physics*, vol. 6, no. 11, pp. 2983–2988, 2004.
- [24] M. Adachi, M. Sakamoto, J. Jiu, Y. Ogata, and S. Isoda, “Determination of parameters of electron transport in dye-sensitized solar cells using electrochemical impedance spectroscopy,” *Journal of Physical Chemistry B*, vol. 110, no. 28, pp. 13872–13880, 2006.
- [25] J. Bisquert and I. Mora-Seró, “Simulation of steady-state characteristics of dye-sensitized solar cells and the interpretation of the diffusion length,” *The Journal of Physical Chemistry Letters*, vol. 1, no. 1, pp. 450–456, 2010.
- [26] S. Sarker, H. W. Seo, and D. M. Kim, “Electrochemical impedance spectroscopy of dye-sensitized solar cells with thermally degraded N719 loaded TiO<sub>2</sub>,” *Chemical Physics Letters*, vol. 585, pp. 193–197, 2013.
- [27] S. Sarker, H. W. Seo, and D. M. Kim, “Calculating current density—voltage curves of dye-sensitized solar cells: a straightforward approach,” *Journal of Power Sources*, vol. 248, pp. 739–744, 2014.
- [28] B. Tripathi, P. Yadav, and M. Kumar, “Charge transfer and recombination kinetics in dye-sensitized solar cell using static and dynamic electrical characterization techniques,” *Solar Energy*, vol. 108, pp. 107–116, 2014.
- [29] S. E. Rock, X. Shi, J. E. Garland, and D. Roy, “Experimental considerations for temperature controlled measurements of fast charge recombination times in dye sensitized solar cells using open circuit voltage decay and impedance spectroscopy,” *Measurement*, vol. 53, pp. 71–82, 2014.

## Research Article

# Photoelectric Properties of DSSCs Sensitized by Phloxine B and Bromophenol Blue

Penghui Ren,<sup>1</sup> Yuanzuo Li,<sup>1</sup> Yuehua Zhang,<sup>2</sup> Hongshuai Wang,<sup>1</sup> and Qungui Wang<sup>1</sup>

<sup>1</sup>College of Science, Northeast Forestry University, Harbin 150040, China

<sup>2</sup>College of Science, Jiamusi University, Jiamusi 154007, China

Correspondence should be addressed to Yuanzuo Li; yuanzuo.li@gmail.com and Yuehua Zhang; yuehuazhangjd@sina.cn

Received 30 June 2016; Revised 12 September 2016; Accepted 5 October 2016

Academic Editor: Francisco R. Zepeda

Copyright © 2016 Penghui Ren et al. This is an open access article distributed under the Creative Commons Attribution License, which permits unrestricted use, distribution, and reproduction in any medium, provided the original work is properly cited.

Phloxine B and bromophenol blue as the sensitizers of dye-sensitized solar cells were investigated via UV-Vis spectra, FT-IR spectra, fluorescence spectra, and current-voltage characteristics. The frontier molecular orbital, vibration analysis, and the first hyperpolarizability were calculated with DFT/6-31G(d). The dipole moment, light harvesting efficiency (LHE), and larger absolute value of driving force of electron injection ( $\Delta G^{\text{inject}}$ ) were also discussed. The calculated results were compared with the experimental results of phloxine B and bromophenol blue. It was found that, compared with bromophenol blue, bigger dipole moment of phloxine B results in larger open circuit voltage ( $V_{oc}$ ) according to the correlation between dipole moment and  $V_{oc}$ . At the same time, for configuration of phloxine B, it has higher LHE and  $\Delta G^{\text{inject}}$ , which are helpful to enhance the abilities of absorbing sunlight and electron injection. Therefore, higher LHE and  $\Delta G^{\text{inject}}$  for phloxine B produced a larger value of  $J_{sc}$ .

## 1. Introduction

With gradually aggravated environmental problem, it is hoped that more energies can be found to replace traditional fossil energy. Solar energy as the clean and renewable source has aroused extensive attention. Since O'Regan and Graetzel [1] developed dye-sensitized solar cells (DSSCs), the photo-to-electric conversion efficiency ( $\eta$ ) of this type of solar cells has achieved 7.1–7.9%. Due to their friendliness and low cost of production [2–5], more attention has been paid to investigate the relationship between structure and performance and to design new DSSCs.

The band engineering of the solar cells devices is shown in Figure 1, which indicates the complete energy levels of the different materials used on the DSSCs devices. DSSCs have the characteristics of the following five aspects [6–9]: (1) Dye molecules absorb sunlight energy, and they are excited from ground state to excited state. (2) After the dye molecules are excited, the electrons are injected into the conduction band of semiconductor and moved into the conducting glass. (3) The electrons diffuse into the external circuit. (4) The dye molecules in oxidation state are deoxidized by the electrolyte in reduction. (5) The electrolyte in oxidation state

is deoxidized after receiving the electron at the conducting glass, thereby completing a cycle.

The DSSCs are mainly composed of a nanocrystalline porous semiconductor electrode-absorbed dye, a counter electrode, and an electrolyte containing iodide and triiodide ions [10]. The dye as a sensitizer plays a key factor in absorbing sunlight and conversion solar energy into electric energy. DSSCs mainly are divided into organic dyes and inorganic dyes [11–13]. Inorganic dyes such as N3 and N719 polypyridine complexes [14] have been used as sensitizer in DSSCs. Although DSSCs of inorganic dyes have provided a relatively high efficiency, there are several shortcomings of using inorganic dyes in DSSCs. For example, some inorganic dyes are considered as resources that are limited in amount, which result in more expensive cost in the field of DSSC. By contrast, organic dyes not only are cheaper, but also have been reported to reach efficiency as high as 9.8% [15]. Nevertheless, the conversion efficiency  $\eta$  of organic dyes was still lower than that of inorganic dyes, and it was not suitable for commercial production in comparison with silicon cell [3]. Torchani et al. [16] studied the henna and mallow (Mloukhya) as the sensitizers of DSSCs. The results showed that the filling factor

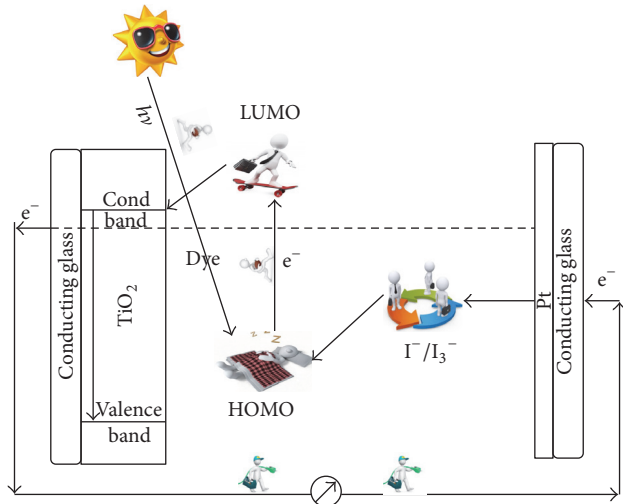


FIGURE 1: Schematic of band edge engineering to electron transfer.

of mallow solar cells is 55%, and  $\eta$  is 0.215%. Zhou et al. [17] studied twenty natural dyes, extracted from natural materials (such as flowers, leaves, fruits, traditional Chinese medicines, and beverages), and the results showed that the open circuit voltage and  $\eta$  of mangosteen pericarp are the highest, which are 0.686 V and 1.17%, respectively. Now several organic dyes have been utilized as sensitizers in DSSCs, such as coumarin [18], porphyrins [19–21], triphenylmethane [22, 23], indoline [24, 25], and cyanine [26, 27].

In recent years, quantum chemistry method has provided a reliable theoretical basis for the rapid screening of high efficiency dye molecules [28–32]. Kumara et al. [33] reported the black tea waste extract (BTE) as a sensitizer for DSSCs in experimental and theoretical studies. The BTE has four theaflavin analogues, and they are calculated via density functional theory (DFT) and time-dependent density functional theory (TD-DFT). The results showed that theaflavin and theaflavin digallate as sensitizers have well performance among four analogues. Beni and Zarandi [34] analyzed the 3-amino-4-nitrofurazan molecule using functional theory (DFT) and MP2 methods. The geometry of the molecule in the gas phase was optimized and compared with that of the crystal. According to DFT and MP2 methods, they obtain the stable gaseous form. El-Shishtawy et al. [35] studied electronic absorption spectra, ground state geometries, and electronic structures of symmetric and asymmetric squaraine dyes with DFT method, and they found that absorption of squaraine dyes can extend into NIR region by straightforward structural modification, and there are well energy match between dye and  $\text{TiO}_2$ . Sun et al. [36] investigated the optical and electrical properties of two dyes, purpurin and alizarin complexone, as sensitizers by using UV-Vis spectrum, FT-IR spectrum, cyclic voltammetry,  $I$ - $V$  characteristics, and DFT calculation, and the results indicated that the side chain has an interesting effect on the optical and electrical properties of sensitizers. Li and coworkers [37] investigated the ground state and excited state properties of polymers BSeTT, QTT, BDT-DTBTBPz (Pz), and BDT-DTBTBQx (Qx) and their

derivatives D1, D2, and D3 via DFT and TD-DFT methods, which indicated that the molecule BDT-DTBTBPz and designed molecule (D2) had the best optical and electronic properties among the investigated system. Song et al. [38] reported that electron transfer is a key process of light driven charge separation reaction in organic solar cell.

In this work, phloxine B and bromophenol blue were selected as sensitizers to investigate the optical and electrical properties of DSSCs experimentally, and the UV-Vis spectra, fluorescence spectra, and FT-IR spectra are calculated with density functional theory (DFT) and time-dependent density functional theory (TD-DFT). At the same time, the absorption spectra, infrared spectra, and fluorescence spectra of phloxine B and bromophenol blue are analyzed and compared. In addition, the radiative lifetime ( $\tau$ ) and total static first hyperpolarizability of the two dyes are calculated. Combined study of experiment and theory provides deep insight into the relationship between structure and performance for two DSSCs.

## 2. Methods

UV-Vis spectra were measured with TU-1900 spectrometer (Beijing, China), and the FT-IR spectra were measured with FT-IR 360 spectrometer (Nicolet, Madison, WI, USA). Solar energy conversion efficiency measurements were done with a solar simulation instrument (Pecell-15, Japan), and light intensity was adjusted via a reference standard Si-solar cell at sunlight intensity of  $100 \text{ mW cm}^{-2}$ . The ground state structures of phloxine B and bromophenol blue were optimized with DFT [39] using B3LYP [40] functional at the 6-31G(d) basis set. Based on the optimized ground state structures, the highest occupied molecular orbital (HOMO), the lowest unoccupied molecular orbital (LUMO), and energy gaps of the two dye molecules were computed, and vibration frequencies were done at the same level. There was no imaginary vibration frequency in the minimum energy structure in the potential energy landscape. Simulation of absorption spectra was done with TD-DFT at the same level. The total static first hyperpolarizability can be written as follows [41]:

$$\beta = \sqrt{\beta_x^2 + \beta_y^2 + \beta_z^2}. \quad (1)$$

Individual static components in the above equation are calculated from

$$\beta_i = \beta_{iii} + \frac{1}{3} \sum_{i \neq j} (\beta_{ijj} + \beta_{jij} + \beta_{jji}), \quad (2)$$

where  $\beta_{ijk}$  ( $i, j, k = x, y, z$ ) are tensor components of hyperpolarizability. Due to the Kleinman symmetry, we finally obtain the equation that has been employed:

$$\beta_{\text{tot}} = \left[ (\beta_{xxx} + \beta_{xyy} + \beta_{xzz})^2 + (\beta_{yyy} + \beta_{yzz} + \beta_{yxx})^2 + (\beta_{zzz} + \beta_{zxx} + \beta_{zyy})^2 \right]^{1/2}. \quad (3)$$

All of the calculations were performed by using Gaussian 09 package [42].

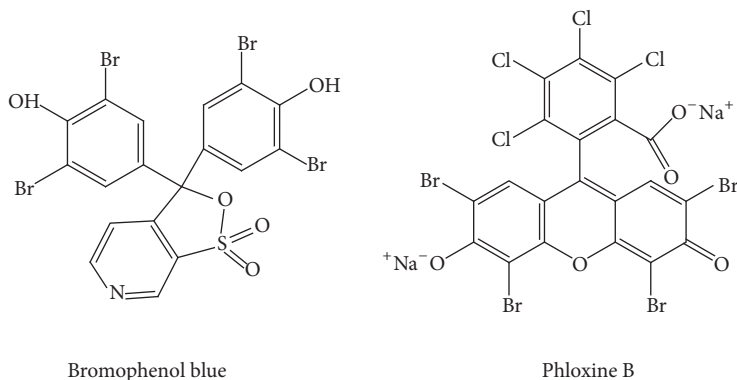


FIGURE 2: Chemical structures of bromophenol blue and phloxine B.

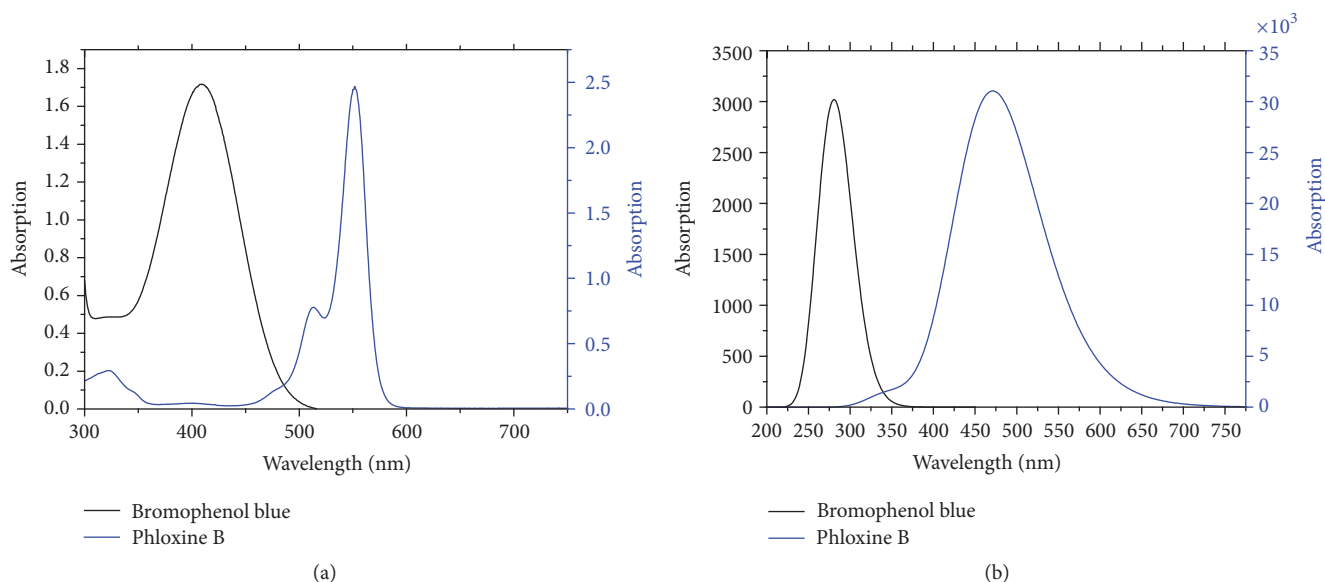


FIGURE 3: (a) Measured UV-Vis absorption spectra of bromophenol blue and phloxine B in experiment. (b) Simulated UV-Vis absorption spectra of bromophenol blue and phloxine B in solvent by using TD-DFT/6-31G(d).

### 3. Results and Discussion

**3.1. The Optical Properties of the Dye.** The chemical structures of bromophenol blue and phloxine B are shown in Figure 2. The experimental absorption spectra of two dyes in ethanol are presented in Figure 3(a). Absorption spectra of phloxine B showed that the absorption range was 450–600 nm, with maximum absorption peak ( $\lambda_{\max}$ ) at around 550 nm. Absorption spectra of bromophenol blue were displayed within the range of 300–500 nm, and  $\lambda_{\max}$  was 410 nm, and bromophenol blue had no other obvious absorption peaks (see Figure 3(a)).

In addition, absorption spectra of bromophenol blue and phloxine B were computed via TD-DFT/6-31G(d) in solvent (see Figure 3(b)), and the data are listed in Table 1. Phloxine B showed the absorption region in 300–700 nm, with a  $\lambda_{\max}$  of 472 nm. Bromophenol blue absorption range was 230–330 nm, while  $\lambda_{\max}$  was 289 nm. The absorptions in visible and near-UV area were important areas for photovoltaic performance, so there are two important factors (the oscillator

strength larger than 0.1 and absorption bands with the wavelength longer than 300 nm). The oscillator strength of the first excited state S1 of phloxine B was 0.7582 (at 472 nm), in which the oscillator strength was the strongest among the six excited states. The maximum absorption in absorption spectra was dominated by HOMO  $\rightarrow$  LUMO transition (contribution is about 0.70069), and the corresponding transition energy was 2.63 eV. Meanwhile, for bromophenol blue, at the first excited state S1, the oscillator strength was 0.0322. The oscillator strength of S1 was the strongest in the states, and this state is composed of HOMO  $\rightarrow$  LUMO electron transition.

For more in-depth understanding of the electronic structure of the two dyes, the isodensity plots of the frontier molecular orbitals (MOs) of two dyes were shown in Figure 4. Phloxine B consists of two parts, namely, sodium-2,3,4,5-tetrachlorobenzene and sodium-2,4,5,7-tetrabromo-6-oxo-xanthen-3-olate, respectively. The electron density of HOMO was located on the sodium-2,4,5,7-tetrabromo-6-oxo-xanthen-3-olate group, and that of LUMO was located

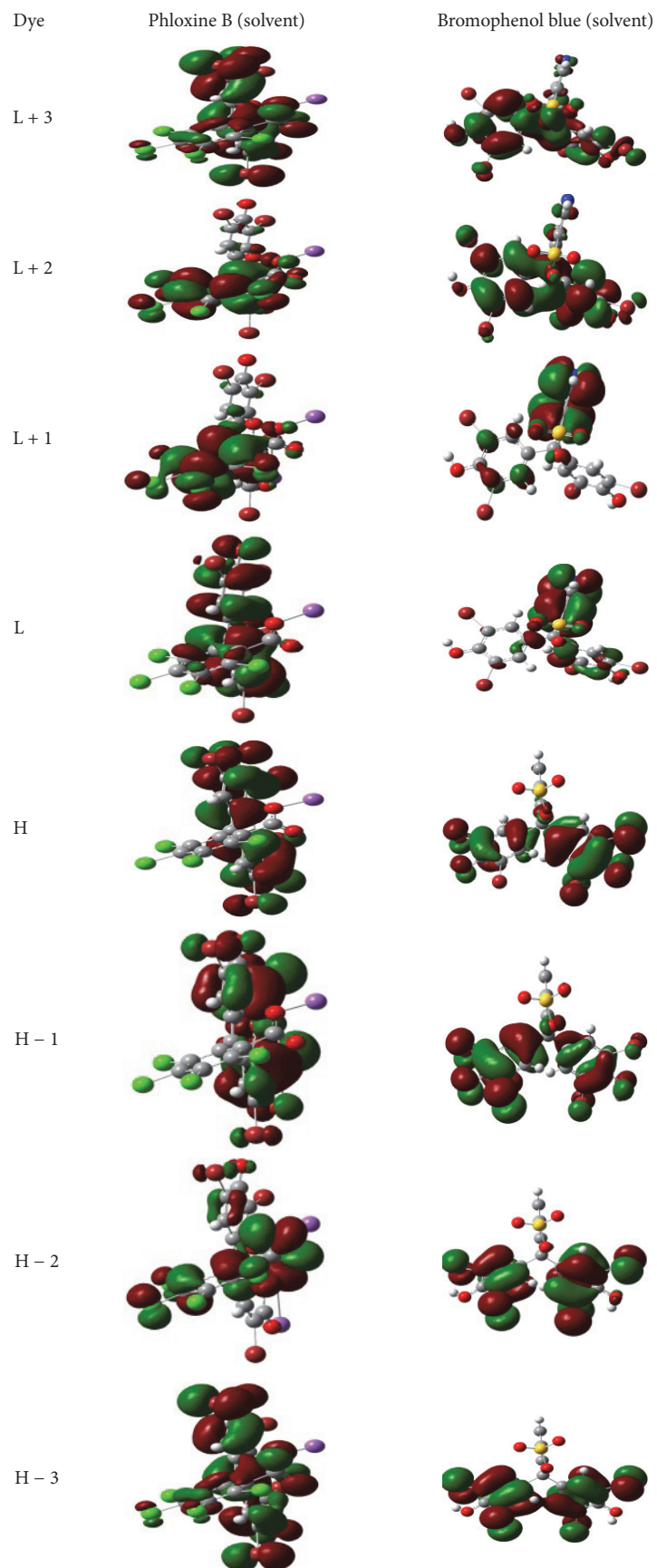


FIGURE 4: Electron densities of the selected HOMO and LUMO of the two dyes.

TABLE 1: Transition energy and oscillator strength of phloxine B and bromophenol blue in solvent were calculated by using TD-DFT/6-31(d) in the solvent.

Dyes	State	$E$ (eV)	Absorption peak $\lambda$ (nm)	Contribution MO	Strength $f$
Phloxine B	S1	2.63	472	(0.70069)H $\rightarrow$ L	0.7582
	S2	3.00	413	(0.69801)H - 1 $\rightarrow$ L	0.0187
	S3	3.30	376	(0.49261)H - 4 $\rightarrow$ L	0.0015
	S4	3.32	373	(0.53756)H - 2 $\rightarrow$ L	0.0039
	S5	3.56	349	(0.70249)H $\rightarrow$ L + 1	0.0243
	S6	3.64	340	(0.49354)H $\rightarrow$ L + 2	0.0079
Bromophenol blue	S1	4.28	289	(0.69468)H $\rightarrow$ L	0.0322
	S2	4.36	284	(0.69221)H - 1 $\rightarrow$ L	0.0206
	S3	4.53	273	(0.69343)H $\rightarrow$ L + 1	0.0021
	S4	4.61	269	(0.52434)H - 1 $\rightarrow$ L + 1	0.0127
	S5	4.62	231	(0.48364)H - 2 $\rightarrow$ L	0.0148
	S6	4.72	263	(0.60405)H - 3 $\rightarrow$ L	0.0037

on conjugated bridge and sodium-2,4,5,7-tetrabromo-6-oxo-xanthen-3-olate group. From the distribution of the above molecular orbitals of HOMO and LUMO, electron transfer was most likely to occur from sodium-2,4,5,7-tetrabromo-6-oxo-xanthen-3-olate group unit to conjugated bridge. Electron densities of other MOs were shown in Figure 4, corresponding to the HOMO - 1, HOMO - 2, HOMO - 3, LUMO + 1, LUMO + 2, and LUMO + 3, respectively.

Bromophenol blue is composed of three parts, namely, two identical 2,6-dibromophenol groups and pyridine, respectively. The electron density of HOMO was located on two identical 2,6-dibromophenol groups and conjugated bridge, and that of LUMO was located on pyridine and conjugated bridge. As the electron transition is from HOMO to LUMO, it was found that a tiny fraction of MOs for HOMO and LUMO was loaded in conjugated bridge, and more electrons were moved to pyridine. Therefore, excitation should result in electron transfer from two identical 2,6-dibromophenol groups to pyridine. The HOMOs and LUMOs in the dyes indicated that the transitions at maximum absorptions had intramolecular charge transfer (ICT) character, and they played an important role in DSSCs.

**3.2. Fourier Transforms Infrared Spectra.** Fourier transforms infrared (FT-IR) spectra of phloxine B and bromophenol blue were recorded in the 500–4000  $\text{cm}^{-1}$  range using KBr pellets and calculated at DFT/B3LYP methods with the 6-31G(d) basis set. The experimental FT-IR spectra were shown in Figures 5(a) and 5(b), and calculated FT-IR spectra were given in Figures 5(c) and 5(d). For absorption peak vibration of bromophenol blue, the absorption peaks were distributed in ranges of 1000–2000  $\text{cm}^{-1}$  and 3000–4000  $\text{cm}^{-1}$ . They were 1398.75, 1472.31, 1634.19, 3440.26  $\text{cm}^{-1}$ , and 3851.47  $\text{cm}^{-1}$  (see Figure 5(a)), respectively. Swing vibration of two C-H bonds of 2,6-dibromophenol group for bromophenol blue was observed at 3243.83  $\text{cm}^{-1}$  (see Figure 5(c)). Swing vibration of two O-H bonds of two 2,6-dibromophenol groups was

observed at 1389.36  $\text{cm}^{-1}$ . Stretching vibration of two C-H bonds of pyridine group was observed at 1452.16  $\text{cm}^{-1}$  and 3652.02  $\text{cm}^{-1}$ , respectively. Pyridine group swing vibration was observed at 1632.13  $\text{cm}^{-1}$ .

C-H vibrations were studied as follows: C-H swing and stretching vibration in unit 2,6-dibromophenol groups were calculated in the range of 681.42, 868.79–934.34, 974.53, 1085.05–1087.63, 1205.43–1209.30, 1232.40, 1333.11–1338.06, 1388–1445.35, 1519.36–1609.41, and 1641.86–1644.21  $\text{cm}^{-1}$  and at 3234.68–3443.83  $\text{cm}^{-1}$ . C-H swing and stretching in pyridine group were calculated in range of 718.94, 765.71–766.86, 842.82–863.99, 944.66, 993.54–999.10, 1057.47, 1108.78–1171.92, and 1452.16–1513.01  $\text{cm}^{-1}$  and at 3192.57–322.58  $\text{cm}^{-1}$ , respectively.

For S-O, OH, and ring vibrations, results showed that S-O stretching vibration was observed at 746.58  $\text{cm}^{-1}$ , and S=O symmetric stretching was observed at 1171.92 and 1357.69  $\text{cm}^{-1}$  in FT-IR, respectively. OH swing and stretching vibration occurred in the range of 613.14, 1205.43–1209.30, 1295.17–1301.14, 1338.06–1388.22–1445.35, 1519.36–1609.41, and 3651.80–3652.02  $\text{cm}^{-1}$ . Benzene rings stretching vibration often occurred in range of 718.94–742.42, 766.86, and 1606.85–1641.80  $\text{cm}^{-1}$ . Benzene rings twisting vibration was found to be 765.71  $\text{cm}^{-1}$ .

For absorption peak vibration of phloxine B, the main absorption peaks of FT-IR spectra focus on 1000–2000  $\text{cm}^{-1}$ . They were 1242.93, 1355.36, 1463.41, 1558.18  $\text{cm}^{-1}$ , and 1634.31  $\text{cm}^{-1}$  (see Figure 5(b)), respectively. Swing vibration of sodium-2,4,5,7-tetrabromo-6-oxo-xanthen-3-olate group was observed at 1453.18  $\text{cm}^{-1}$  and 1548.97  $\text{cm}^{-1}$  (see Figure 5(d)), respectively. Two C-H bonds' stretching vibrations of sodium-2,4,5,7-tetrabromo-6-oxo-xanthen-3-olate group were observed at 1228.48  $\text{cm}^{-1}$  and 1356.04  $\text{cm}^{-1}$ , respectively. C=O bond stretching vibration of sodium-2,4,5,7-tetrabromo-6-oxo-xanthen-3-olate group was observed at 1642.66  $\text{cm}^{-1}$ .

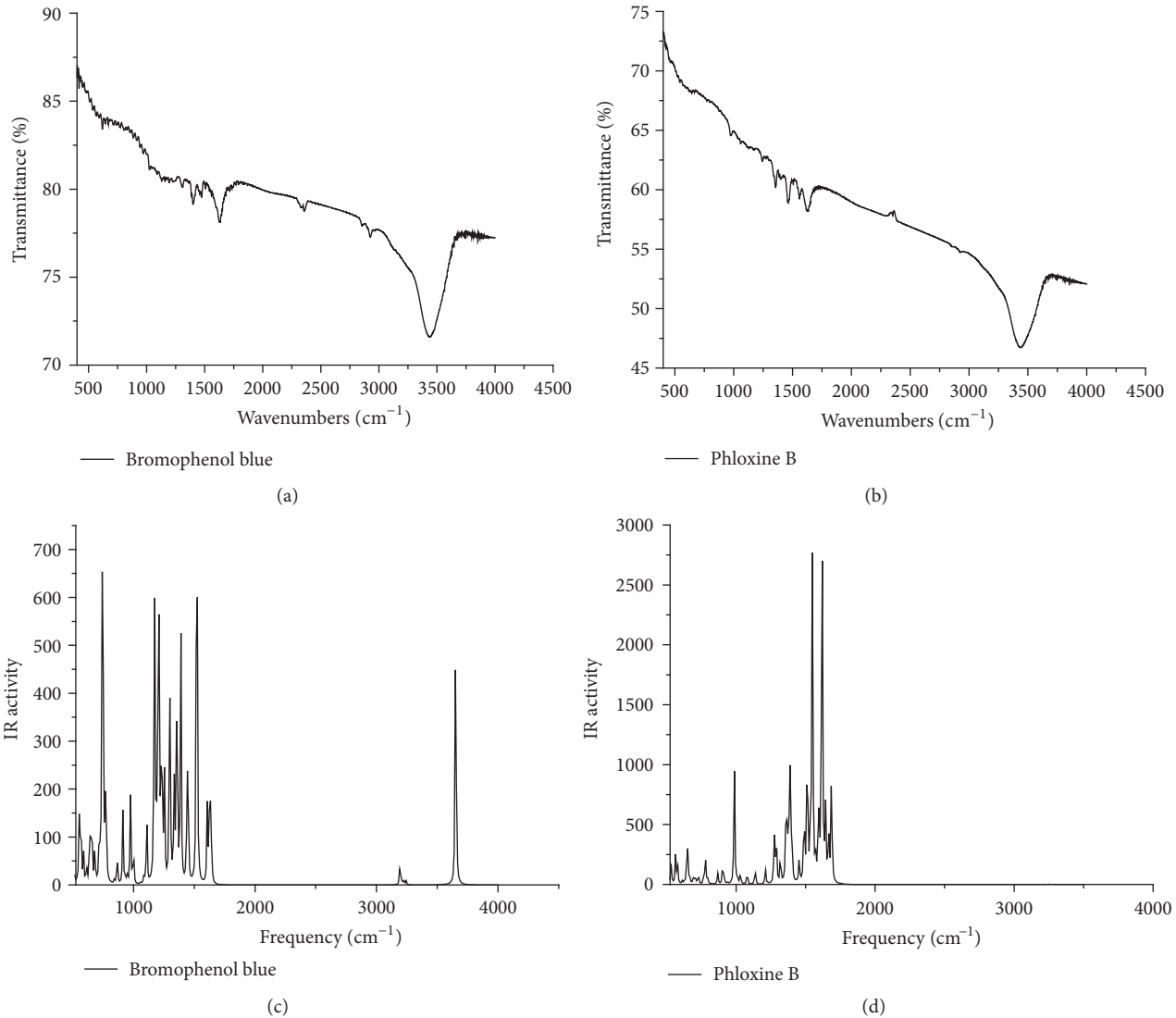


FIGURE 5: (a) Measured FT-IR spectra of bromophenol blue in experiment. (b) Measured FT-IR spectra of phloxine B in experiment. (c) Simulated IR spectra of bromophenol blue in theory. (d) Simulated IR spectra of phloxine B in theory.

For C-H, COONa, and O-Na vibrations, it was found that C-H swing and stretching vibration in sodium-2,4,5,7-tetrabromo-6-oxo-xanthen-3-olate group were assigned in the region of 936.95, 987.30, 1008.72, 1030.88, 1204.51–1511.59, 1545.61, 1617.78, and 1665.48 cm<sup>-1</sup>, respectively. The COONa symmetric stretching vibration of sodium-2,4,5,7-tetrabromo-6-oxo-xanthen-3-olate group occurred at 910.95 and 1686.27 cm<sup>-1</sup>, respectively. O-Na stretching vibration was observed at 1593.03 cm<sup>-1</sup>.

Furthermore, there are three benzene rings in the phloxine B. Benzene ring symmetric stretching vibration was observed in the region of 910.95–987.30, 1030.88, 1388.10, 1453.18, 1532.61, and 1572.03 cm<sup>-1</sup> and at 1665.48 cm<sup>-1</sup>, respectively. Benzene ring asymmetric stretching vibration was calculated in range of 1008.72, 1136.98–1204.51, 1272.62, 1290.53, 1356.04, 1382.82, 1488.37, 1511.59, and 1545.61 cm<sup>-1</sup>, and in-plane bending vibration was computed at 1211.25 cm<sup>-1</sup>.

**3.3. Photovoltaic Characterization.** The following formula is used to calculate the maximum power photo-to-electric conversion efficiency ( $\eta$ ) [43]:

$$\eta = \frac{J_{sc} \cdot V_{oc} \cdot FF}{P} \quad (4)$$

Here,  $P$  was the intensity of the incident light;  $J_{sc}$ ,  $V_{oc}$ , and  $FF$  represent short circuit density, open circuit voltage, and fill factor, respectively.

The  $FF$  was defined as the ratio of the maximum power  $P_{max}$  obtained from the DSSCs and the theoretical maximum power of it [44]. Hence,

$$FF = \frac{I_m \cdot V_m}{J_{sc} \cdot V_{oc}} \quad (5)$$

Here,  $I_m$  and  $V_m$  were current and voltage related to the maximum power. In the experiment, we used the phloxine B

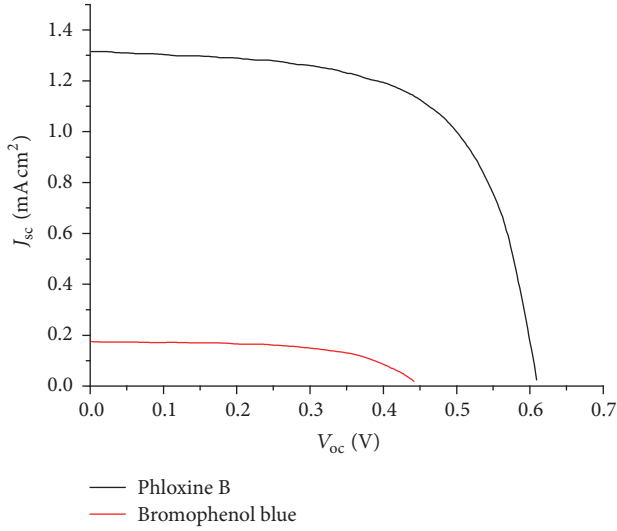


FIGURE 6: The photocurrent-potential ( $I$ - $V$ ) characteristics of the DSSCs with  $\text{TiO}_2$  film electrode sensitized by phloxine B and bromophenol blue.

TABLE 2: Current-voltage characteristics of phloxine B and bromophenol blue.

	$V_{oc}$ (V)	$J_{sc}$ ( $\text{mA}/\text{cm}^2$ )	FF	$\eta\%$
Phloxine B	0.61	1.31	0.65	0.52
Bromophenol blue	0.44	0.17	0.68	0.05

and bromophenol blue as sensitizers, to measure the current-voltage ( $I$ - $V$ ) under sunlight intensity of  $100 \text{ mW cm}^{-2}$ . And the results are shown in Figure 6, and measured  $I$ - $V$  characteristics of the DSSCs sensitized for the two dyes are listed in Table 2.

The DSSCs sensitized with phloxine B showed  $\eta$  of 0.52%, with  $V_{oc}$  of 0.61 V,  $J_{sc}$  of  $1.31 \text{ mA cm}^{-2}$ , and FF of 0.65, while the DSSCs sensitized with bromophenol blue showed  $\eta$  of 0.05%, with  $V_{oc}$  of 0.44 V,  $J_{sc}$  of  $0.17 \text{ mA cm}^{-2}$ , and FF of 0.68. The results showed that photovoltaic performance of phloxine B is greater than that of bromophenol blue. Then  $V_{oc}$  of the DSSCs using the phloxine B as sensitizer was more suitable. The photovoltaic performance of the phloxine B was higher than that of bromophenol blue. This improvement in the photovoltaic performance of the DSSCs with phloxine B could be attributed to the absorption spectra of solar radiations (450–600 nm) (see Figure 3(a)) [43]. This result indicated that the range of absorption spectra affected  $\eta$  of DSSCs.

To analyze the difference of two dyes, we performed theoretical calculation to explain the well photoelectric properties (larger  $V_{oc}$  and  $J_{sc}$ ) of phloxine B. The value of  $V_{oc}$  was viewed as the difference between the quasi-Fermi level of semiconductor conduction band edge value and the electrolyte oxygen reductions. Because the electrolyte was typically  $\text{I}^-/\text{I}_3^-$ , the redox electrolyte can be considered constant. The value of  $V_{oc}$  has a direct dependence on the shift

of the reduction potential of the semiconductor conduction band ( $\Delta E_{CB}$ ), and  $\Delta E_{CB}$  is expressed [45]:

$$\Delta E_{CB} = \frac{-q\mu_{\text{normal}}\gamma}{\epsilon_0\epsilon}, \quad (6)$$

where  $\gamma$  is adsorbed on the surface concentration and  $\mu_{\text{normal}}$  is the dipole moment component perpendicular to the direction of  $\text{TiO}_2$  surface (where  $\mu_{\text{normal}}$  was the  $x$ -axis direction),  $\epsilon_0$  is the gas permittivity, and  $\epsilon$  is the dielectric constant of the organic monolayer. Obviously, according to (6), the larger the value of  $\mu_{\text{normal}}$ , the bigger the value of  $\Delta E_{CB}$ . The change of  $\Delta E_{CB}$  has direct influence on  $V_{oc}$ . In order to analyze and compare  $V_{oc}$ , we calculated  $\mu_{\text{normal}}$ , as shown in Figure 7.  $\mu_{\text{normal}}$  of phloxine B was 19.80 D, and  $\mu_{\text{normal}}$  of bromophenol blue was  $-1.29$  D.  $\mu_{\text{normal}}$  of phloxine B was much larger than that of bromophenol blue. Therefore, the increasing  $\mu_{\text{normal}}$  for phloxine B results in the larger  $V_{oc}$  [46, 47].

For the dye sensitizers, the light harvesting efficiency (LHE) and oscillator strength had correlated relationship [48], which is expressed as follows:

$$\text{LHE} = 1 - 10^{-f}. \quad (7)$$

Here,  $f$  is the oscillator strength. According to Table 1, we found that the first excited state of phloxine B and bromophenol blue corresponds to a dominant position in absorption, and the oscillator strength of phloxine B was larger than that of bromophenol blue. The LHE of phloxine B was 0.8255, and that of bromophenol blue was 0.0714. So the correlated relationship between the oscillator strength and light harvesting efficiency (LHE) implied that the dye with larger oscillator strength made more LHE, and thus phloxine B has well utilities of sunlight.

The sunlight absorption and electron injection were important process in DSSCs, which obviously affect the efficiency of  $J_{sc}$  [49]. Driving force of electron injection ( $\Delta G^{\text{inject}}$ ) means that the excited dye provided electron into semiconductor conduction band. Electron injection occurred from the excited state;  $\Delta G^{\text{inject}}$  could be calculated by the following equation [50]:

$$\Delta G^{\text{inject}} = E_{\text{OX}}^{\text{dye}^*} - E_{\text{CB}}^{\text{SC}}, \quad (8)$$

where  $E_{\text{OX}}^{\text{dye}^*}$  is the oxidation potential of the excited state of the dye, and  $E_{\text{CB}}^{\text{SC}}$  is the reduction potential of the semiconductor conduction band. The reported  $E_{\text{CB}}^{\text{SC}} = 4.0 \text{ eV}$  [51] for  $\text{TiO}_2$  was adopted in this work.  $E_{\text{OX}}^{\text{dye}^*}$  could be calculated as follows [52]:

$$E_{\text{OX}}^{\text{dye}^*} = E_{\text{OX}}^{\text{dye}} - \lambda_{\text{max}}. \quad (9)$$

Here  $E_{\text{OX}}^{\text{dye}}$  is the redox potential of the ground state, and  $\lambda_{\text{max}}$  was the absorption maximum with ICT character.

The data of phloxine B and bromophenol blue were listed in Table 3. According to the calculation results,  $\Delta G^{\text{inject}}$  of phloxine B ( $-1.82 \text{ eV}$ ) was higher than bromophenol blue ( $-1.49 \text{ eV}$ ), meaning that  $\Delta G^{\text{inject}}$  of phloxine B was easier than bromophenol blue.  $\Delta G^{\text{inject}}$  was an important influence

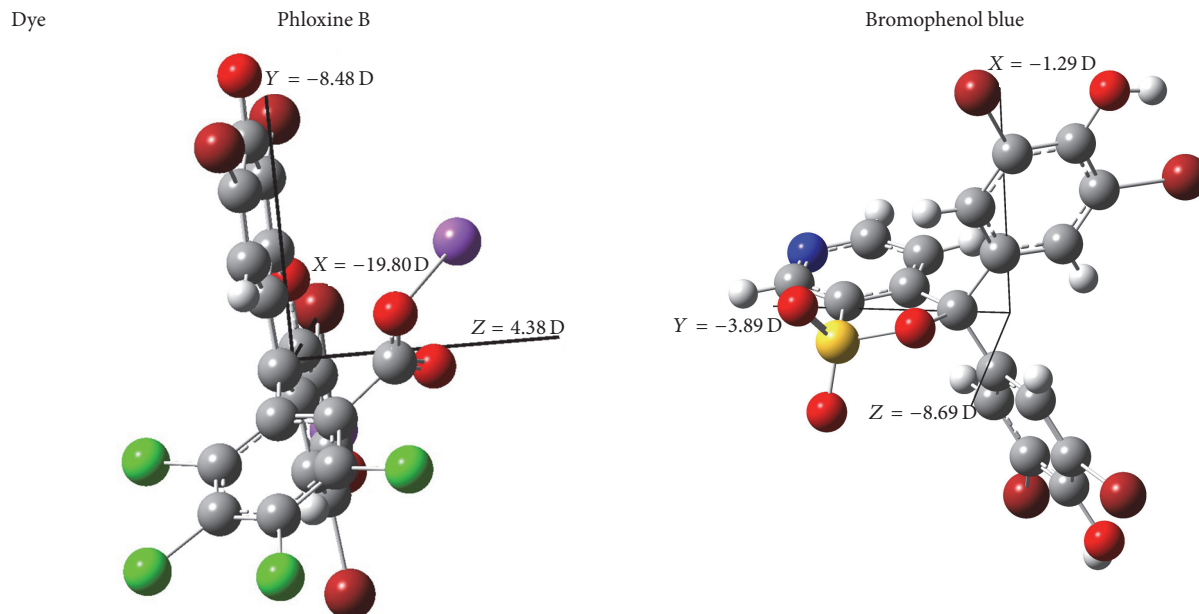


FIGURE 7: Dipole moment of phloxine B and bromophenol blue (gray for C, deep red for Br, red for O, green for Cl, blue for N, purple for Na, yellow for S, and white for H).

TABLE 3: The driving force of electron injection  $\Delta G^{\text{inject}}$  (in eV) for the phloxine B and bromophenol blue in the solvent.

Dye	$E_{\text{OX}}^{\text{dye}}$	$E_{\text{OX}}^{\text{dye}^*}$	$\Delta G^{\text{inject}}$
Phloxine B	5.44	2.83	-1.82
Bromophenol blue	6.63	2.35	-1.49

TABLE 4: Energy levels of HOMO, LUMO, and energy gaps in solvent (eV).

	Phloxine B	Bromophenol blue
H	-5.44	-6.63
L	-2.64	-1.77
Gap	-2.80	-4.86

factor for the electron injection efficiency. At the same time, the LHE showed that phloxine B was stronger than bromophenol blue, as discussed above. Therefore, phloxine B has improved absorption and injection abilities in comparison with bromophenol blue, which cause the larger value of  $J_{\text{sc}}$ .

**3.4. Ground and Excited State Properties.** To ensure that electrons could be effectively injected into the conduction band of  $\text{TiO}_2$  (about  $-4.0$  eV) [51], LUMO energy level must be higher than the edge of the conduction band of the  $\text{TiO}_2$ , and HOMO energy level must be below  $\text{I}^-/\text{I}_3^-$  electrolyte (about  $-4.85$  eV) [46]. Energy levels of MOs and energy gaps in solvent were studied by using DFT/B3LYP/6-31G(d) method. Energy levels and HOMO-LUMO gap are presented in Figure 8, and the calculated data are listed in Table 4. For phloxine B, the highest occupied MO (HOMO) was  $-5.44$  eV and the lowest unoccupied MO (LUMO) was  $-2.64$  eV. For bromophenol blue, the HOMO was  $-6.63$  eV and the LUMO

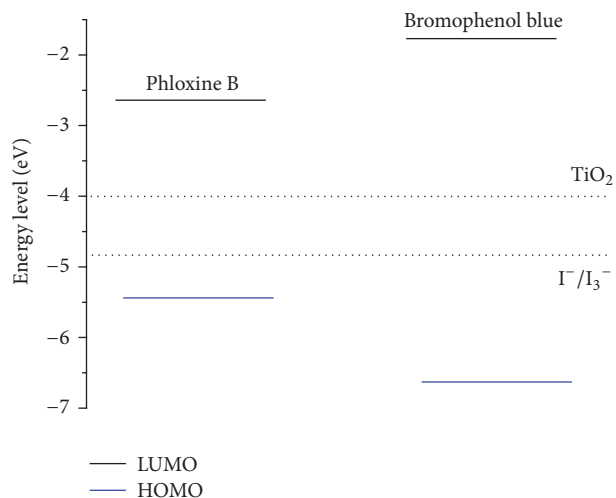


FIGURE 8: Energy levels of phloxine B and bromophenol blue in solvent.

was  $-1.77$  eV. The band gap of phloxine B was smaller than that of bromophenol blue, meaning there is a red-shifted absorption for phloxine B. From Figure 8, it seems that the LUMOs of phloxine B and bromophenol blue were all higher than the conduction band of  $\text{TiO}_2$ , meaning that the electron injection can occur from excited dyes into  $\text{TiO}_2$ , and

TABLE 5: Hyperpolarizability of phloxine and bromophenol blue.

	$\beta_{xxx}$	$\beta_{xyx}$	$\beta_{xyy}$	$\beta_{yyy}$	$\beta_{xxz}$	$\beta_{xyz}$	$\beta_{yyz}$	$\beta_{xzz}$	$\beta_{yzz}$	$\beta_{zzz}$	$\beta_{tot}$
Phloxine B	1056.816	1811.374	-176.166	-1358.839	303.029	103.036	-151.766	-220.581	194.588	-334.674	942.390
Bromophenol blue	-166.629	263.472	-97.931	430.917	-91.126	-74.537	-118.993	37.162	73.307	-204.705	901.746

TABLE 6: The calculated electron radiative lifetime ( $\tau$ ) for the phloxine B and bromophenol blue in the solvent.

Dye	$E$ (eV)	$\lambda$ (nm)	Strength $f$	$\tau$ (s)
Phloxine B	2.45	507	0.6268	$6.14 \times 10^{-9}$
Bromophenol blue	3.22	385	0.0085	$2.61 \times 10^{-7}$

the HOMOs of two dyes were lower than  $I^-/I_3^-$  (see Figure 8); therefore, two dyes can obtain electron to recovery.

Molecular nonlinear optical properties have a close relationship with external electric field. It reflects the characteristics of the intramolecular charge transfer (ICT), which can affect the electron injection efficiency and the light current. The first hyperpolarizability ( $\beta$ ) is directly proportional to the difference in the dipole moment ( $\Delta\mu_{eg}$ ) between the ground state and the excited state and the transition dipole moment ( $\mu_{eg}$ ), and it is inversely proportional to the transition energy. The first hyperpolarizabilities could be written as follows [53]:

$$\beta \propto \frac{\Delta\mu_{eg} (\mu_{eg})^2}{E_{eg}^2}, \quad (10)$$

where  $\Delta\mu_{eg}$  and  $\mu_{eg}$  are difference in the dipole moment for ground state and excited state and the transition dipole,  $E_{eg}$  is transition energy. The first hyperpolarizabilities were calculated, as listed in Table 5. The  $\beta_{tot}$  of phloxine B was higher than that of bromophenol blue. Table 1 and Figure 7 support the results of hyperpolarizabilities. Figure 7 showed that the value of  $\mu_{eg}$  for phloxine B is larger than that of bromophenol blue; at the same time, phloxine B has smaller excitation energy, so phloxine B has larger hyperpolarizabilities with obvious ICT.

**3.5. Fluorescence Spectroscopy of Dyes.** Radiative lifetime ( $\tau$ ) played an important role in DSSCs, and it could affect charge recombination [54].  $\tau$  could be calculated as follows [55]:

$$\tau = \frac{ac^3u^2}{2fe^2}. \quad (11)$$

Here,  $c$  is the speed of light,  $f$  is the oscillator strength, and  $e$  is the fluorescent energy. The experimental spectra of the phloxine B and bromophenol blue are shown in Figure 9, and the calculated fluorescence maxima  $\lambda$ , oscillator strength ( $f$  in a.u.), and relative radiative lifetime are listed in Table 6. The maximum absorption peak of phloxine B was 507 nm. The fluorescence energy, oscillator strength, and radiative lifetime were 2.45 eV, 0.6268, and  $6.14 \times 10^{-9}$  s, respectively. The absorption peak of bromophenol blue was 385 nm. The fluorescence energy, oscillator strength, and radiative lifetime were 3.22 eV, 0.0085, and  $2.61 \times 10^{-7}$  s, respectively. The radiative lifetime of bromophenol blue was higher ( $2.61 \times 10^{-7}$  s). But phloxine B was propitious to charge recombination [54].

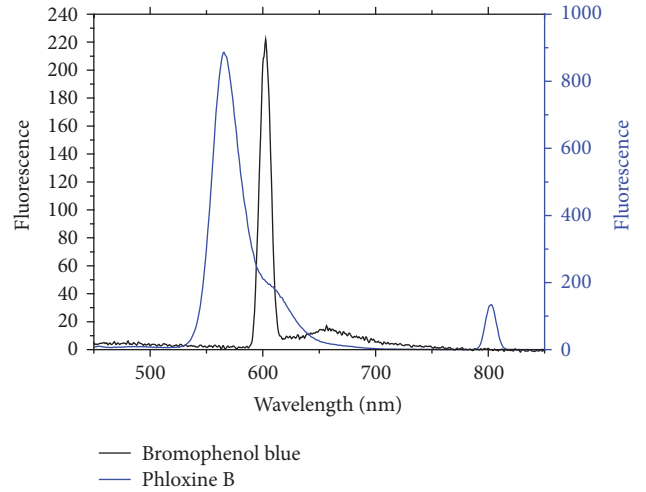


FIGURE 9: Fluorescence spectra of phloxine B and bromophenol blue.

## 4. Conclusion

The absorption, molecular orbital energies, radiative lifetimes, LHE, and  $\Delta G^{\text{inject}}$  were addressed. The oscillator strength (0.7582), vertical dipole moment (19.80 D), and  $\Delta G^{\text{inject}}$  (-1.82 eV) for phloxine B were higher than those of bromophenol blue. The  $J_{sc}$ ,  $V_{oc}$ , and  $\eta$  of phloxine B were 0.61 V, 1.31 mA/cm<sup>2</sup>, and 0.52%, respectively, which were higher than those of bromophenol blue. The results showed that higher dipole moment of phloxine B corresponds to larger  $V_{oc}$ . This means that enlarging dipole moment was a possible way to increase  $V_{oc}$  of DSSCs. The larger oscillator strength, higher LHE, and larger absolute value of  $\Delta G^{\text{inject}}$  correspond to larger  $J_{sc}$ . This means increasing oscillator strength and LHE and larger absolute value of  $\Delta G^{\text{inject}}$  were a possible way to increase  $J_{sc}$ . A similar trend between theory and experiment was observed. Photovoltaic performance of phloxine B was significantly higher than that of bromophenol blue.

## Competing Interests

The authors declare that they have no competing interests.

## Acknowledgments

This work was supported by the Fundamental Research Funds for the Central Universities (Grant no. 2572014CB31), the Heilongjiang Provincial Youth Science Foundation (Grant no. QC2013C006), the National Natural Science Foundation of China (Grant nos. 11404055 and 11374353), China Postdoctoral Science Foundation (2016M590270), Heilongjiang Postdoctoral Grant (LBH-Z15002), National Undergraduate Innovative and Entrepreneurial Training Program (Grant no. 201610225099), and Academic Research Training of NEFU for Undergraduate (Grant no. KY2015020).

## References

- [1] B. O'Regan and M. Graetzel, "A low-cost, high-efficiency solar cell based on dye-sensitized colloidal titanium dioxide films," *Nature*, vol. 353, no. 6346, pp. 737–740, 1991.
- [2] M. Grätzel, "Photoelectrochemical cells," *Nature*, vol. 414, no. 6861, pp. 338–344, 2001.
- [3] D. Wei, "Dye sensitized solar cells," *International Journal of Molecular Sciences*, vol. 11, no. 3, pp. 1103–1113, 2010.
- [4] M. K. Nazeeruddin, C. Klein, P. Liska, and M. Grätzel, "Synthesis of novel ruthenium sensitizers and their application in dye-sensitized solar cells," *Coordination Chemistry Reviews*, vol. 249, no. 13–14, pp. 1460–1467, 2005.
- [5] B. Li, L. Wang, B. Kang, P. Wang, and Y. Qiu, "Review of recent progress in solid-state dye-sensitized solar cells," *Solar Energy Materials and Solar Cells*, vol. 90, no. 5, pp. 549–573, 2006.
- [6] N. Robertson, "Optimizing dyes for dye-sensitized solar cells," *Angewandte Chemie*, vol. 45, no. 15, pp. 2338–2345, 2006.
- [7] A. Sasani, A. Baktash, K. Mirabbaszadeh, and B. Khoshnevisan, "Structural and electronic properties of Mg and Mg-Nb co-doped TiO<sub>2</sub> (101) anatase surface," *Applied Surface Science*, vol. 384, pp. 298–303, 2016.
- [8] S. E. Gledhill, B. Scott, and B. A. Gregg, "Organic and nano-structured composite photovoltaics: an overview," *Journal of Materials Research*, vol. 20, no. 12, pp. 3167–3179, 2005.
- [9] M. Magni, P. Biagini, A. Colombo, C. Dragonetti, D. Roberto, and A. Valore, "Versatile copper complexes as a convenient springboard for both dyes and redox mediators in dye sensitized solar cells," *Coordination Chemistry Reviews*, vol. 322, pp. 69–93, 2016.
- [10] M. Grätzel, "The advent of mesoscopic injection solar cells," *Progress in Photovoltaics: Research and Applications*, vol. 14, no. 5, pp. 429–442, 2006.
- [11] A. Mishra, M. K. R. Fischer, and P. Büuerle, "Metal-free organic dyes for dye-sensitized solar cells: from structure: property relationships to design rules," *Angewandte Chemie*, vol. 48, no. 14, pp. 2474–2499, 2009.
- [12] Z. Ning and H. Tian, "Triarylamine: a promising core unit for efficient photovoltaic materials," *Chemical Communications*, vol. 45, no. 37, pp. 5483–5495, 2009.
- [13] S. M. Zakeeruddin and M. Grätzel, "Solvent-free ionic liquid electrolytes for mesoscopic dye-sensitized solar cells," *Advanced Functional Materials*, vol. 19, no. 14, pp. 2187–2202, 2009.
- [14] H. Chang and Y.-J. Lo, "Pomegranate leaves and mulberry fruit as natural sensitizers for dye-sensitized solar cells," *Solar Energy*, vol. 84, no. 10, pp. 1833–1837, 2010.
- [15] G. Zhang, H. Bala, Y. Cheng et al., "High efficiency and stable dye-sensitized solar cells with an organic chromophore featuring a binary  $\pi$ -conjugated spacer," *Chemical Communications*, no. 16, pp. 2198–2200, 2009.
- [16] A. Torchani, S. Saadaoui, R. Gharbi, and M. Fathallah, "Sensitized solar cells based on natural dyes," *Current Applied Physics*, vol. 15, no. 3, pp. 307–312, 2015.
- [17] H. Zhou, L. Wu, Y. Gao, and T. Ma, "Dye-sensitized solar cells using 20 natural dyes as sensitizers," *Journal of Photochemistry and Photobiology A: Chemistry*, vol. 219, no. 2–3, pp. 188–194, 2011.
- [18] Z.-S. Wang, Y. Cui, K. Hara, Y. Dan-Oh, C. Kasada, and A. Shinpo, "A high-light-harvesting-efficiency coumarin dye for stable dye-sensitized solar cells," *Advanced Materials*, vol. 19, no. 8, pp. 1138–1141, 2007.
- [19] C.-L. Wang, C.-M. Lan, S.-H. Hong et al., "Enveloping porphyrins for efficient dye-sensitized solar cells," *Energy and Environmental Science*, vol. 5, no. 5, pp. 6933–6940, 2012.
- [20] M. J. Griffith, K. Sunahara, P. Wagner et al., "Porphyrins for dye-sensitized solar cells: new insights into efficiency-determining electron transfer steps," *Chemical Communications*, vol. 48, no. 35, pp. 4145–4162, 2012.
- [21] W. M. Campbell, A. K. Burrell, D. L. Officer, and K. W. Jolley, "Porphyrins as light harvesters in the dye-sensitized TiO<sub>2</sub> solar cell," *Coordination Chemistry Reviews*, vol. 248, no. 13–14, pp. 1363–1379, 2004.
- [22] K. Kudo, H. Yageta, S. Kuniyoshi, and K. Tanaka, "Surface pressure variation in triphenylmethane dye adsorbed merocyanine monolayers at the air-water interface," *Japanese Journal of Applied Physics*, vol. 32, no. 4, pp. 1775–1778, 1993.
- [23] S. Cleinmensen, J. C. Jensen, N. J. Jensen, O. Meyer, P. Olsen, and G. Würtzen, "Toxicological studies on malachite green: a triphenylmethane dye," *Archiv Für Toxikologie*, vol. 56, no. 1, pp. 43–45, 1984.
- [24] G. Li, M. Liang, H. Wang et al., "Significant enhancement of open-circuit voltage in indoline-based dye-sensitized solar cells via retarding charge recombination," *Chemistry of Materials*, vol. 25, no. 9, pp. 1713–1722, 2013.
- [25] H. W. Ham and Y. S. Kim, "Theoretical study of indoline dyes for dye-sensitized solar cells," *Thin Solid Films*, vol. 518, no. 22, pp. 6558–6563, 2010.
- [26] X. Ma, J. Hua, W. Wu et al., "A high-efficiency cyanine dye for dye-sensitized solar cells," *Tetrahedron*, vol. 64, no. 2, pp. 345–350, 2008.
- [27] J. Tang, W. Wu, J. Hua, J. Li, X. Li, and H. Tian, "Starburst triphenylamine-based cyanine dye for efficient quasi-solid-state dye-sensitized solar cells," *Energy & Environmental Science*, vol. 2, no. 9, pp. 982–990, 2009.
- [28] Y. Li, T. Pullerits, M. Zhao, and M. Sun, "Theoretical characterization of the PC60BM:PDDTT model for an organic solar cell," *The Journal of Physical Chemistry C*, vol. 115, no. 44, pp. 21865–21873, 2011.
- [29] Ü. Ceylan, G. Ö. Tari, H. Gökce, and E. Ağar, "Spectroscopic (FT-IR and UV-Vis) and theoretical (HF and DFT) investigation of 2-Ethyl-N-[(5-nitrothiophene-2-yl)methylidene]aniline," *Journal of Molecular Structure*, vol. 1110, pp. 1–10, 2016.
- [30] E. B. Sas, M. Kurt, M. Can, N. Horzum, and A. Atac, "Spectroscopic studies on 9H-carbazole-9-(4-phenyl) boronic acid pinacol ester by DFT method," *Journal of Molecular Structure*, vol. 1118, pp. 124–138, 2016.

- [31] S. Soleimani Amiri, S. Makarem, H. Ahmar, and S. Ashenagar, "Theoretical studies and spectroscopic characterization of novel 4-methyl-5-((5-phenyl-1,3,4-oxadiazol-2-yl)thio)benzene-1,2-diol," *Journal of Molecular Structure*, vol. 1119, pp. 18–24, 2016.
- [32] A. G. Al-Sehemi, A. Irfan, A. M. Asiri, and Y. A. Ammar, "Synthesis, characterization and DFT study of methoxybenzylidene containing chromophores for DSSC materials," *Spectrochimica Acta Part A: Molecular and Biomolecular Spectroscopy*, vol. 91, pp. 239–243, 2012.
- [33] N. T. R. N. Kumara, M. R. R. Kooh, A. Lim et al., "DFT/TDDFT and experimental studies of natural pigments extracted from black tea waste for DSSC application," *International Journal of Photoenergy*, vol. 2013, Article ID 109843, 8 pages, 2013.
- [34] A. S. Beni and M. Zarandi, "Application of DFT and MP2 calculations on structural and water-assisted proton transfer in 3-amino-4-nitrofurazan," *Russian Journal of Physical Chemistry A*, vol. 90, no. 2, pp. 374–382, 2016.
- [35] R. M. El-Shishtawy, S. A. Elroby, A. M. Asiri, and K. Mullen, "Optical absorption spectra and electronic properties of symmetric and asymmetric squaraine dyes for use in DSSC solar cells: DFT and TD-DFT studies," *International Journal of Molecular Sciences*, vol. 17, no. 4, p. 487, 2016.
- [36] C. F. Sun, Y. Z. Li, D. W. Qi, H. X. Li, and P. Song, "Optical and electrical properties of purpurin and alizarin complexone as sensitizers for dye-sensitized solar cells," *Journal of Materials Science: Materials in Electronics*, vol. 27, no. 8, pp. 8027–8039, 2016.
- [37] Y. Z. Li, C. F. Sun, D. W. Qi, P. Song, and F. C. Ma, "Effects of different functional groups on the optical and charge transport properties of copolymers for polymer solar cells," *RSC Advances*, vol. 6, no. 66, pp. 61809–61820, 2016.
- [38] P. Song, Y. Li, F. Ma, T. Pullerits, and M. Sun, "Photoinduced electron transfer in organic solar cells," *Chemical Record*, vol. 16, no. 2, pp. 734–753, 2016.
- [39] W. Kohn and L. J. Sham, "Quantum density oscillations in an inhomogeneous electron gas," *Physical Review*, vol. 137, no. 6, pp. A1697–A1705, 1965.
- [40] C. Lee, W. Yang, and R. G. Parr, "Development of the Colle-Salvetti correlation-energy formula into a functional of the electron density," *Physical Review B: Condensed Matter*, vol. 37, no. 2, pp. 785–789, 1988.
- [41] D. A. Kleinman, "Nonlinear dielectric polarization in optical media," *Physical Review*, vol. 126, no. 6, pp. 1977–1979, 1962.
- [42] M. J. Frisch, G. W. Trucks, H. B. Schlegel et al., *Gaussian 09*, Gaussian Inc., Wallingford, Conn, USA, 2009.
- [43] S. Kushwaha and L. Bahadur, "Enhancement of power conversion efficiency of dye-sensitized solar cells by co-sensitization of Phloxine B and Bromophenol blue dyes on ZnO photoanode," *Journal of Luminescence*, vol. 161, pp. 426–430, 2015.
- [44] W. Li, J. Wang, J. Chen, F.-Q. Bai, and H.-X. Zhang, "Theoretical investigation of triphenylamine-based sensitizers with different  $\pi$ -spacers for DSSC," *Spectrochimica Acta Part A: Molecular and Biomolecular Spectroscopy*, vol. 118, pp. 1144–1151, 2014.
- [45] M. Liang and J. Chen, "Arylamine organic dyes for dye-sensitized solar cells," *Chemical Society Reviews*, vol. 42, no. 8, pp. 3453–3488, 2013.
- [46] S. Rühle, M. Greenshtein, S.-G. Chen et al., "Molecular adjustment of the electronic properties of nanoporous electrodes in dye-sensitized solar cells," *The Journal of Physical Chemistry B*, vol. 109, no. 40, pp. 18907–18913, 2005.
- [47] Z. Ning, Y. Fu, and H. Tian, "Improvement of dye-sensitized solar cells: what we know and what we need to know," *Energy & Environmental Science*, vol. 3, no. 9, pp. 1170–1181, 2010.
- [48] J. Preat, D. Jacquemin, and E. A. Perpète, "Towards new efficient dye-sensitized solar cells," *Energy and Environmental Science*, vol. 3, no. 7, pp. 891–904, 2010.
- [49] T. Marinado, D. P. Hagberg, M. Hedlund et al., "Rhodanine dyes for dye-sensitized solar cells: spectroscopy, energy levels and photovoltaic performance," *Physical Chemistry Chemical Physics*, vol. 11, no. 1, pp. 133–141, 2009.
- [50] J. Preat, C. Michaux, D. Jacquemin, and E. A. Perpète, "Enhanced efficiency of organic dye-sensitized solar cells: triphenylamine derivatives," *Journal of Physical Chemistry C*, vol. 113, no. 38, pp. 16821–16833, 2009.
- [51] J. B. Asbury, Y.-Q. Wang, E. Hao, H. N. Ghosh, and T. Lian, "Evidences of hot excited state electron injection from sensitizer molecules to TiO<sub>2</sub> nanocrystalline thin films," *Research on Chemical Intermediates*, vol. 27, no. 4–5, pp. 393–406, 2001.
- [52] R. Katoh, A. Furube, T. Yoshihara et al., "Efficiencies of electron injection from excited N<sub>3</sub> dye into nanocrystalline semiconductor (ZrO<sub>2</sub>, TiO<sub>2</sub>, ZnO, Nb<sub>2</sub>O<sub>5</sub>, SnO<sub>2</sub>, In<sub>2</sub>O<sub>3</sub>) Films," *Journal of Physical Chemistry B*, vol. 108, no. 15, pp. 4818–4822, 2004.
- [53] G. Olbrechts, T. Munters, K. Clays, A. Persoons, O.-K. Kim, and L.-S. Choi, "High-frequency demodulation of multi-photon fluorescence in hyper-Rayleigh scattering," *Optical Materials*, vol. 12, no. 2, pp. 221–224, 1999.
- [54] C.-R. Zhang, L. Liu, J.-W. Zhe et al., "The role of the conjugate bridge in electronic structures and related properties of tetrahydroquinoline for dye sensitized solar cells," *International Journal of Molecular Sciences*, vol. 14, no. 3, pp. 5461–5481, 2013.
- [55] T. Le Bahers, T. Pauporté, G. Scalmani, C. Adamo, and I. Ciofini, "A TD-DFT investigation of ground and excited state properties in indoline dyes used for dye-sensitized solar cells," *Physical Chemistry Chemical Physics*, vol. 11, no. 47, pp. 11276–11284, 2009.